A Balloon Measurement of the Isotopic Composition of Galactic Cosmic Ray Iron

Thesis by

Jon Eric Grove

In Partial Fulfillment of the Requirements

for the Degree of

Doctor of Philosophy

California Institute of Technology

Pasadena, California

1989

(Submitted April 21, 1989)

SRL 89-02

Acknowledgements

I would like to thank my advisor, Dr. Edward Stone, for his direction. His dedication and clarity of thought are an inspiration. Dr. Richard Mewaldt's guidance and encouragement, especially at the end, are much appreciated. Dr. Stephen Schindler has been a good friend. I am indebted to Dr. Andrew Buffington, who is primarily responsible for the design of the HEIST instrument. Dr. Ib Rasmussen, of the Danish Space Research Institute, provided the aerogels that made this experiment possible.

Steen Laursen, of the Danish Space Research Institute, Bill Althouse, Dan Burke, and James Weger have provided able engineering support, as well as countless hours of entertainment and encouragement. Marty Gould's great skill as a machinist has enabled us to make a working whole out of pieces gathered from around the world. Deeby Kadrie, Louise Sartain, and Carmen Silva have willingly provided secretarial assistance, usually on a moment's notice.

I am grateful to Dr. Eric Christian for his years of work on the HEIST project and, in particular, his development of the position algorithm. He, Dr. Koon Lau, David Palmer, and Andrea Ghez have made the office a good place to be. Andrea's friendship and fresh perspective have brightened my last two years here.

I am grateful to my parents for their ceaseless confidence in me, and for providing a home in which education was an important ingredient. My brother, Dr. J. Russell Grove, and my sister, Debra Maher, continue to be inspirational, each in his or her own way.

Most of all, I would like to thank my wife, Lisa, for her constant love, encouragement, and understanding. She has made everything easier.

Abstract

We have measured the isotopic composition of galactic cosmic ray iron in the energy interval ~1550-2200 MeV/nucleon using a balloon-borne mass spectrometer. The instrument was flown from Palestine, Texas, in May 1984 for >35 hours at an atmospheric depth of ~6 g/cm^2. Masses were derived by the Cerenkov-Energy technique. The Cerenkov counter employed a silica aerogel radiator with index of refraction n = 1.1. Particle energies were measured in a stack of NaI(Tl) scintillators, which also provided particle trajectories. The calibration of the detectors is discussed, along with the algorithms we have used to calculate velocities, energies, and masses. The limitations of aerogels as Cerenkov radiators, particularly the stability of their light yield, are considered. A detailed discussion of the sources of mass uncertainty is presented, including an analytic model of the contribution from fluctuations in the Cerenkov yield from knock-on electrons. The achieved mass resolution is ~0.65 amu, which is consistent with the theoretical estimate. We report an $^{54}Fe/^{56}Fe$ abundance ratio of $0.14^{+0.18}_{-0.11}$ and an 84% confidence upper limit of $^{58}Fe/^{56}Fe \leq 0.07$ at the top of the atmosphere. Combining our data with those of previous measurements of the composition of iron at lower energies, and using a model of the galactic propagation, we derive cosmic-ray source abundance ratios of $^{54}Fe/^{56}Fe = 0.064^{+0.032}_{-0.027}$ and $^{58}Fe/^{56}Fe \leq 0.062$. These values are consistent with the composition of solar-system iron and place restrictions on the conditions under which cosmic-ray iron is synthesized.

Table Of Contents

Chapter 1
Introduction

1.1. Purpose of Cosmic Ray Isotope Studies

Theories of stellar nucleosynthesis are constrained primarily by measurements of isotopic abundances taken from samples of the Earth, the Moon, and meteorites. Such local abundances, however, reflect primarily a restricted sample of the composition that was frozen-in as the solar system condensed out of the proto-solar nebula some $\sim 4.5 \times 10^9$ years ago; hence they may not be representative of conditions throughout the galaxy at that time. In addition, reprocessing of material elsewhere in the galaxy in succeeding stellar generations may have significantly modified the abundance of heavy nuclides since then. It is of interest, therefore, to measure the isotopic composition of newer material from other sources. Any observed differences in composition would further our understanding of stellar nucleosynthesis and galactic evolution.

The galactic cosmic rays are a directly accessible contemporary sample of matter ($\sim 10^7$ years; e.g., Wiedenbeck and Greiner, 1980) from outside the solar system. The isotopic composition contains a record of the nuclear history of the cosmic rays, including their synthesis and subsequent modification by nuclear interactions during propagation through the interstellar medium (ISM). Chemical fractionation effects are known to have a large effect on the observed *elemental* composition of the cosmic rays. For example, there exists a strong correlation between elemental abundance and first ionization potential (Cassé and Goret, 1978), perhaps indicating preferential acceleration of species which are more readily ionized. However, such selection effects are significantly reduced when abundance ratios of isotopes of the same element are considered. In addition, the abundances of many nuclides are sufficiently large that contributions from spallation of heavier nuclides during propagation through the ISM are small. Thus the interpretation of observed abundances of such species is possible with simple corrections for propagation effects.

An understanding of the isotopic composition of the Fe-group elements ($24 \leq Z \leq 28$; Cr, Mn, Fe, Co, and Ni) is particularly important to theories of nucleosynthesis, as these elements represent the end of the exothermic nucleosynthetic chain that occurs in stellar interiors. In addition, because of the negligible contribution from spallation of the much rarer, heavier cosmic rays, the isotopic composition of Fe accurately reflects the nature of the source. The relative abundances of the isotopes of Fe and Ni are strongly dependent on the parameters of nucleosynthesis and therefore are sensitive probes of extreme stellar conditions (§5.6).

Studies of isotopic composition can also yield information on the acceleration mechanism and the propagation of cosmic rays in the galaxy. One of the remaining fundamental questions of cosmic-ray astrophysics is whether the cosmic rays are a sample of freshly synthesized material, e.g., from recent supernovae, or a sample of older material stored in the ISM for some time until being accelerated to cosmic-ray energies. The relative abundance of the electron-capture species ^{59}Ni, ^{56}Ni, and ^{57}Co can be used to measure this time delay between nucleosynthesis and acceleration (Cassé and Soutoul, 1975). Current observations of the elemental abundance ratios Ni/Fe and Co/Fe indicate that the delay is at least one year (Soutoul *et al.*, 1978); however, further refinement must await a measurement of the isotopic composition.

Cosmic-ray clocks such as ^{10}Be and ^{26}Al have been used to measure the confinement time of cosmic rays in the galaxy (Garcia-Munoz *et al.*, 1977; Wiedenbeck and Greiner, 1980; Wiedenbeck, 1983). Measurements of ^{54}Mn and ^{60}Fe abundances would test the confinement time of the heavy nuclei, and measurements of the abundances of stable isotopes that are assumed to be rare at the source but produced by the spallation of abundant heavier species would test the distribution of cosmic-ray pathlengths in the galaxy (e.g., Protheroe *et al.*, 1981; Ormes and Protheroe, 1983; and Garcia-Munoz *et al.*, 1987).

1.2. Status of Cosmic Ray Isotope Spectroscopy

Observations over the last decade have demonstrated that the isotopic composition of matter at the galactic cosmic ray source (GCRS) differs from that of typical solar-system material. Indeed, in every case in which the isotopic composition has been measured to better than 30%, the composition of the two samples differs. Table 1.1 and Figure 1.1, both adapted from Mewaldt (1988), summarize the observed abundance ratios for several species. Also included in the figure are the expected enhancements from two cosmic-ray source models (see below and §5.6). It is apparent that the abundances of the neutron-rich isotopes of Ne, Mg, and Si are enhanced at the GCRS relative to the solar system (SS).

Table 1.1: Cosmic-Ray Source Composition
Mewaldt (1988)

Isotope Ratio	GCRS/SS
$^{13}C/^{12}C$	1.6 ± 0.9
$^{18}O/^{16}O$	≤ 4
$^{22}Ne/^{20}Ne$	3.5 ± 0.6
$^{25}Mg/^{24}Mg$	$1.6^{+0.4}_{-0.3}$
$^{26}Mg/^{24}Mg$	1.6 ± 0.25
$^{29}Si/^{28}Si$	$1.5^{+0.4}_{-0.35}$
$^{30}Si/^{28}Si$	$1.5^{+0.4}_{-0.3}$
$^{34}S/^{32}S$	≤ 4
$^{54}Fe/^{56}Fe$	≤ 1.7
$^{57}Fe/^{56}Fe$	≤ 4
$^{58}Fe/^{56}Fe$	≤ 10
$^{60}Ni/^{58}Ni$	$1.9^{+1.1}_{-1.2}$

Note that there is some controversy over the correct solar-system abundance ratio for $^{22}Ne/^{20}Ne$. The enhancement factor of 3.5 given in the table is in reference to the value

Figure 1.1

Summary of observed abundance ratios of several nuclides in the cosmic rays. The data are gathered from a variety of balloon-borne and spacecraft instruments and are summarized in Mewaldt (1988). The enhancement factor of 3.5 for $^{22}Ne/^{20}Ne$ is in reference to the "neon-A" ratio $^{22}Ne_{\odot}/^{20}Ne_{\odot}=0.122$ derived from meteoritic inclusions and adopted as the solar standard by Cameron (1973), while the enhancement factor of 5.8 is in reference to the solar wind value of $^{22}Ne_{\odot}/^{20}Ne_{\odot}=0.073$ adopted as the standard by Anders and Ebihara (1982). For a recent summary of the various measurements of local Ne composition, see Mewaldt and Stone (1989).

Also shown are the expected enhancement factors from the Supermetallicity model (Woosley and Weaver, 1981) and the Wolf-Rayet model (Casse´ and Paul, 1982). The Wolf-Rayet enhancements are taken from the calculations of Prantzos (1984).

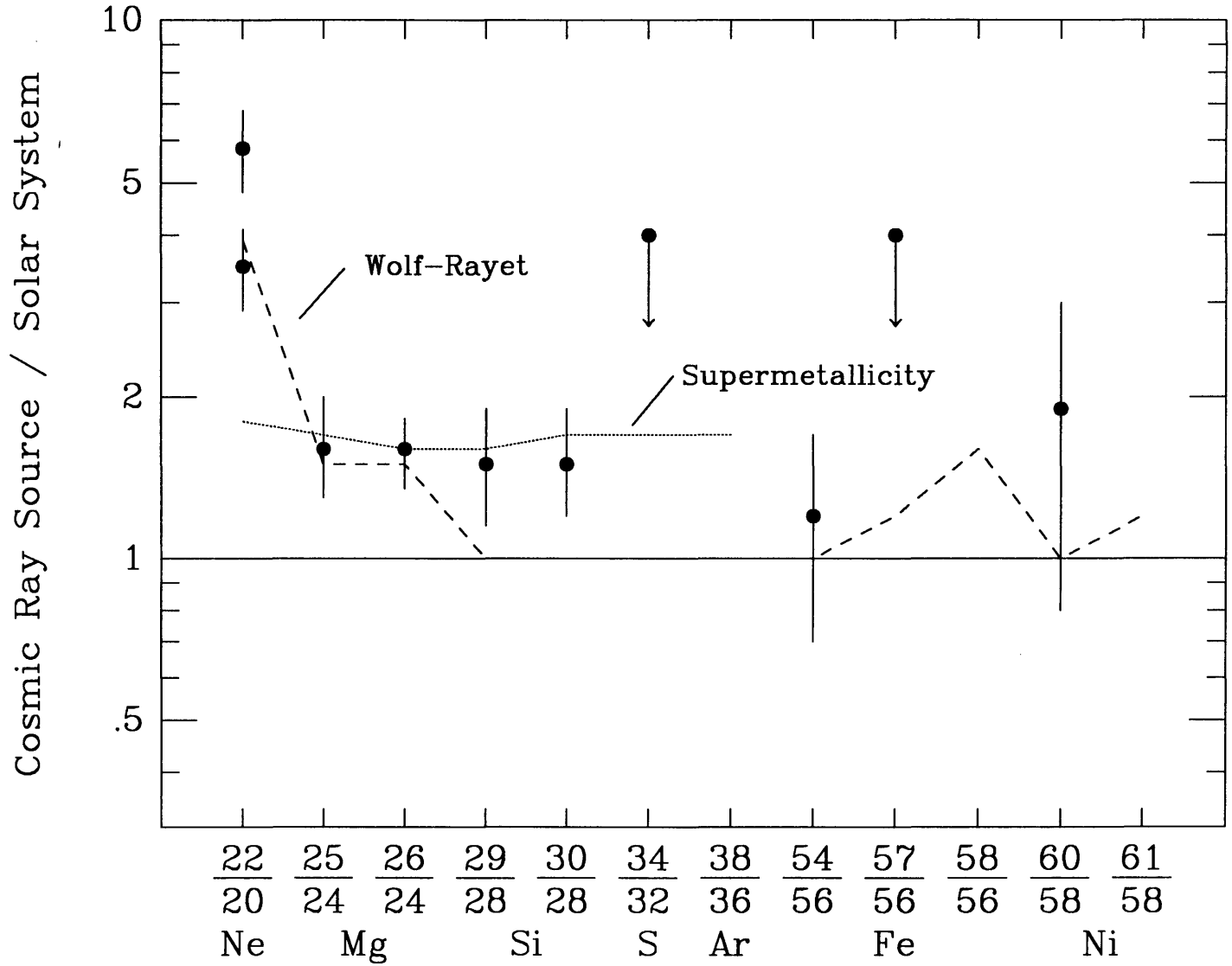
Cosmic Ray Source / Solar System
10
5
2
1
.5
Wolf–Rayet
Supermetallicity
22/20 Ne
25/24 Mg
26/24 Mg
29/28 Si
30/28 Si
34/32 S
38/36 Ar
54/56 Fe
57/56 Fe
58/56 Fe
60/58 Ni
61/58 Ni

Figure 1.1

of $^{22}Ne_{\odot}/^{20}Ne_{\odot}=0.122$ derived from meteoritic inclusions. This "neon-A" component has been adopted as the solar-system standard by Cameron (1973). The ratio observed in the solar energetic particles is consistent with the neon-A value, while the ratio observed in the solar wind and in lunar rock implantations of solar-wind particles ("neon-B") is significantly smaller ($^{22}Ne_{\odot}/^{20}Ne_{\odot}=0.073$). If the solar wind value is adopted as the standard, as it has by Anders and Ebihara (1982), the observed enhancement in the cosmic rays rises to 5.8 ± 1.0. For a recent summary of the various measurements of local Ne composition, see Mewaldt and Stone (1989).

Models proposed to account for the observed excess of neutron-rich isotopes in the cosmic rays fall generally into three categories: first, those that propose that the cosmic ray source material has been repeatedly processed in massive stars, causing an evolutionary increase in the abundance of neutron-rich species (e.g., the Supermetallicity model of Woosley and Weaver, 1981); second, those that propose that a fraction of the cosmic rays are produced in stars whose characteristics differ from those that produced the material from which the solar system formed (e.g., the Wolf-Rayet model of Cassé and Paul, 1982); and third, those that propose that the cosmic rays are a true sample of the interstellar medium and that events preceding the formation of the solar system modified the composition of the solar nebula, making the solar-system abundances anomalous with respect to typical galactic material (e.g, the OB Association model of Olive and Schramm, 1980). We outline examples of the first two categories below and discuss them in more detail in §5.6.

The Supermetallicity model of Woosley and Weaver (1981) suggests that cosmic rays are synthesized in Type II supernovae that are typically metal-rich by a factor of about two relative to the solar system. The metallicity Z is defined as the mass fraction of all elements in the star heavier than He; the Sun has $Z_{\odot}=0.020$ (Anders and Ebihara, 1982). The essence of this model is that the production of the neutron-rich isotopes is proportional to the initial metallicity (see §5.6.1.1). The Supermetallicity model can account for the observed enhancements of the neutron-rich isotopes of Mg and Si as well as a portion of the enhancement of ^{22}Ne by assuming a source with metallicity $Z \approx 1.8\,Z_{\odot}$ (Figure 1.1). The model also predicts an enhancement in the $^{54}Fe/^{56}Fe$ ratio; however, because the enhancement factor is strongly dependent on the

mass cut and on the degree to which β-decays have modified the composition of the stellar core, the magnitude of the enhancement is uncertain (see §5.6.1.2).

Wolf-Rayet stars are the exposed helium-burning cores of massive stars ($M \sim 50\,M_\odot$) undergoing rapid mass-loss ($\dot{M} > 10^{-5}\,M_\odot$/yr) to a high-speed stellar wind ($v_{WR} \sim 2000$ km/s $\sim 5\,v_{\text{solar wind}}$) (e.g., de Loore and Willis, 1982). A subclass of these stars, the WC stars, have spectra dominated by emission lines of He, C, and O, indicating that the freshly processed nuclear material is available at the stellar surface (e.g., Willis and Wilson, 1978). Assuming an initial solar metallicity in the WC stars, Cassé and Paul (1982) have proposed that the ^{22}Ne formed by the helium-burning of ^{14}N (see §5.6.1.2) should be enhanced at the surface of WC stars to a value $(^{22}\text{Ne})_{WR}/(^{22}\text{Ne})_\odot = (\text{CNO})_\odot/(^{22}\text{Ne})_\odot \sim 120$ relative to the solar-system value. At the end of helium-burning, neutrons from $^{22}\text{Ne}(\alpha,\text{n})^{25}\text{Mg}$ can drive some s-process nucleosynthesis, leading in particular to an enhancement of ^{57}Fe and ^{58}Fe. The substantial overproduction of ^{22}Ne led Cassé and Paul to propose that the contribution to the cosmic-ray composition from WC stars was diluted with a material assumed to have solar-system composition: for example, if WC stars were entirely responsible for the ^{22}Ne enhancement of a factor of 3.5, their total contribution to cosmic-ray ^{20}Ne would be one particle in 50. The Wolf-Rayet model can account for the observed excesses of neutron-rich isotopes of Ne and Mg, but fails to produce excess ^{29}Si and ^{30}Si.

The expected enhancement factors for the Supermetallicity and Wolf-Rayet models are shown in Figure 1.1. They are discussed in more detail in §5.6.1.2 and §5.6.1.3.

1.3. Fe Measurements to Date

Four previous measurements of the isotopic composition of Fe (Tarlé *et al.*, 1979; Mewaldt *et al.*, 1980; Webber, 1981; and Young *et al.*, 1981) have established that ^{56}Fe is the dominant isotope in the cosmic rays and that the composition is consistent with solar-system composition at the source. However, since the uncertainties are large, the measurements do not rule out an enhancement of a factor of two in ^{54}Fe and set only an upper limit of a factor of ten on the enhancement of ^{58}Fe. The measurement of Mewaldt *et al.* was made on-board the *ISEE 3* spacecraft and covered the energy range

from 83-284 MeV/nucleon. This measurement showed very good mass resolution ($\sigma < 0.4$ amu); however it suffered from poor statistics. The remaining three measurements were made with balloon-borne instruments covering the energy range from ~600-900 MeV/nucleon. Although the statistics of these measurements were much better, the resolution was inadequate to resolve isotopes of Fe separated by a single mass unit (§5.5).

The instrument from which the current measurements were obtained was designed to cover a higher energy regime. Because the cosmic-ray intensity falls approximately as a power law in total energy, it is more difficult to obtain a statistically significant sample. However, when the design of the instrument was begun in 1980, it was considered a prototype of an instrument to be carried on the Space Transportation System. The balloon instrument was expected to test techniques for mass spectroscopy at high energies, such as those accessible from a Shuttle orbit with 56° inclination. In addition, there are several scientific advantages to investigating this regime. First, the energy-dependence of the cross sections for nuclear interactions is small above ~1000 MeV/nucleon. Second, the solar modulation of cosmic-ray intensity decreases with increasing energy, with the result that at high energies simple models of modulation are more likely to account properly for any effects on isotopic abundance ratios. Third, ionization energy losses in propagating through the interstellar medium are small above ~1000 MeV/nucleon, again reducing any bias in the abundance ratios. Finally, we note that balloon flights are most easily and inexpensively carried out at the National Scientific Balloon Facility (NSBF) in Palestine, Texas, where the geomagnetic cutoff limits observations to rigidities greater than ~4.2 GV/c, or ~1250 MeV/nucleon for $A = 2Z$ particles.

1.4. Required Resolution

Stone (1973) and Wiedenbeck (1977) address the question of the mass resolution required to resolve isotopes separated by a single mass unit as a function of the abundance ratio. They find, for example, that a resolution of ≤ 0.3 amu is required to observe an inflection point between two Gaussian distributions with relative abundance of 1:10. This is a reasonable design goal for an instrument intended to measure the

composition of cosmic-ray Fe. However, we note that achieving such resolution is a difficult prospect, because the isotopes of Fe are separated by just ~2% in mass.

Because ^{54}Fe is expected to be roughly twice as abundant as ^{55}Fe (e.g., Table 5.5) and is separated by two mass units from the dominant isotope, a resolution of 0.5 amu will give an inflection point between ^{54}Fe and ^{56}Fe. Mass resolution of this magnitude is more readily attainable.

1.5. Instrument

The discrete nature of nuclear charge and mass permit the nuclear species of a high-energy charged particle to be determined by simultaneous measurement of two physical processes that depend on nuclear charge Z, nuclear mass M, and velocity β. In particular, a mass spectrometer can be constructed from detectors that measure the Cerenkov emission, $C = C(Z,\beta)$, and the total energy, $E = E(M,\beta)$.

A collaborative effort of the California Institute of Technology and the Danish Space Research Institute (DSRI), the High Energy Isotope Spectrometer Telescope (HEIST) is a balloon-borne mass spectrometer designed to measure the isotopic abundance of the cosmic rays from Ne to Ni ($10 \leq Z \leq 28$) at energies from ~1300 MeV/nucleon to ~2000 MeV/nucleon at the instrument. Particle masses can be measured by the Cerenkov-ΔE-Cerenkov, Cerenkov-Energy, Cerenkov-Range, and Range-Energy techniques, although only the Cerenkov-Energy technique was employed in this analysis (§2.2).

The instrument employs several innovative features, which are described in detail in §2.1. Particle velocities are measured in a Cerenkov counter employing a silica aerogel radiator with index of refraction $n = 1.1$. This novel substance, with its Cerenkov threshold energy of ~1300 MeV/nucleon, allows the exploration of a new, high-energy regime. Particle positions are measured in a stack of NaI(Tl) scintillators that also measures particle energy loss, obviating the need for external position-sensitive detectors such as gas-filled multiwire proportional counters (§3.2). The added complexities of operating such gas-filled counters make them less attractive for use aboard a spacecraft than detectors employing only solid materials. The division of the NaI(Tl) into twelve separate layers also permits the identification of events that undergo nuclear

interactions (§4.3.11). The NaI(Tl) is maintained in an isothermal environment by an evaporative cooling system (§2.1.1), eliminating the need for temperature-dependent corrections to the scintillator response.

The instrument was calibrated at the Lawrence Berkeley Laboratory Bevalac in November 1982. The calibration data were used to map the position-dependence of the detector response and to develop the algorithms required for the mass calculation. The instrument was flown in May 1984 from Palestine, Texas. More than 430,000 cosmic-ray nuclei were collected during the $35^h\ 32^m$ it spent at a typical float altitude of ~115,000 feet.

1.6. Summary

Chapter 2 contains a description of the HEIST instrument (§2.1), as well as a discussion of the several techniques of mass determination (§2.2) and the contributions to mass resolution (§2.3). Because the resolution of the top Cerenkov counter had degraded by the time of the flight (§3.6.3), and because the accelerator calibration of the instrument was not adequate to map the bottom Cerenkov counter (§3.1), the resolution of events that penetrate the NaI(Tl) stack was expected to be poor. Consequently, only events that stop in the NaI(Tl) have been analyzed. Since the Ne, Mg, and Si nuclei penetrate the stack, and only elements from the Fe group stop in relatively large numbers, only Fe isotope abundances have been measured. The mass resolution for stopping Fe events by the Cerenkov-Energy technique is calculated to be 0.65 amu, which is not adequate to resolve isotopes separated by a single mass unit.

The greater part of Chapter 3 concerns the algorithms used to calculate positions (§3.2), energy loss (§3.3 and §3.5), and velocity (§3.6). It also includes a discussion of the degradation of the aerogel Cerenkov yield with time, along with a comparison of the degradation observed by other experimenters (§3.6.3). It is this decrease that is the source of much of the mass uncertainty.

Chapter 4 contains a summary of the flight (§4.1) and presents a detailed discussion of the data selection for the final mass analysis (§4.3). The final Fe data set contains 32 events, which is fewer than the expected number, 54±8, from a Monte Carlo simulation of the instrument in flight (§4.2).

Because isotopes are not individually resolved, successful deconvolution of the mass histogram requires an accurate understanding of the resolution function. An estimate of the resolution function is developed in Chapter 5, where we account for nuclear interactions in the atmosphere and the instrument (§5.2). We have used a maximum-likelihood technique (§5.3) to estimate the composition of Fe at the top of the atmosphere. The propagation of the cosmic rays in the interstellar medium is discussed in §5.4, where we derive correction factors to estimate the isotopic composition at the GCRS. We find an abundance ratio of $^{54}\mathrm{Fe}/^{56}\mathrm{Fe} = 0.12^{+0.18}_{-0.11}$ and set an upper limit of $^{58}\mathrm{Fe}/^{56}\mathrm{Fe} \leq 0.07$. Both ratios are consistent with the previous measurements (§5.5) and with a solar-system composition—as well as with significant enhancements—at the GCRS. We discuss the implications of these observations for the nucleosynthesis of the elements in the Fe group (§5.6).

We conclude by discussing some of the limitations of the aerogels as Cerenkov radiators (§6.2) and the enhancements to the HEIST instrument that followed the flight considered here (§6.3).

Chapter 2
Instrumentation, Mass Algorithms, and Mass Resolution

2.1. Instrument

The Caltech/DSRI High Energy Isotope Spectrometer Telescope (HEIST) is a balloon-borne mass spectrometer designed to measure the isotopic abundance of the cosmic rays from Ne to Ni ($10 \leq Z \leq 28$) at energies from ~1300 MeV/nucleon to ~2000 MeV/nucleon. Particle masses can be measured by the Cerenkov-ΔE-Cerenkov, Cerenkov-Energy, Cerenkov-Range, and Range-Energy techniques, although only the Cerenkov-Energy technique was employed in this analysis.

Figure 2.1 shows a schematic of the HEIST instrument, which consists of a stack of twelve NaI(Tl) scintillators (L1 through L12), two Cerenkov counters (C1 and C2), and two plastic scintillators (S1 and S2). The geometry factor of the instrument varies with particle depth in the stack, ranging from 0.27 to 0.17 m^2sr. Such a large area is necessary to provide sufficient statistics during a typical flight time. The instrument has been described in detail by Lau (1985) (see also Buffington *et al.*, 1983), and we describe here only the major features.

The stack of NaI(Tl) scintillators, each nominally 52 cm in diameter and 2 cm thick, comprising a total thickness of 87.2 g/cm^2, provides a direct measurement of energy loss ΔE. Because NaI(Tl) is hygroscopic, the stack is hermetically sealed in a dry environment. Each NaI(Tl) layer is mounted in an annular plexiglass lightpipe and viewed by six 1.5" photomultipliers (Amperex XP 2008/UB) symmetrically positioned around the periphery. The layers are separated by light shields of black-painted aluminum foil. The photomultipliers are individually digitized, and their combined outputs measure the scintillation light yield in the layer. Shortly after the stack was placed in its hermetic can, one of the photomultipliers on layer 3 failed. The resulting degradation in resolution in that layer is small.

The thickness of the ends of the hermetic can that holds the NaI(Tl) has been minimized to reduce the amount of passive material in the instrument. They consist of 0.41 cm (1.1 g/cm^2) of Al; however, the center 3.8 cm in radius has been reinforced with an Al plug 1.6 cm (4.3 g/cm^2) thick. These center plugs were intended as additional attachment points for the two Cerenkov counters but were not used in the final design.

Particle position information, which is used in the HEIST instrument primarily to correct for the variation of detector response with position and angle, is provided by the NaI(Tl) stack. While traditionally such information is provided by gas-filled multiwire proportional counters, such counters can place additional burdens on the design, operation, and maintenance of a balloon-borne or spacecraft instrument that might otherwise consist entirely of solid detector materials. Progress in the use of scintillators as position-sensitive detectors in the years preceding the design of the HEIST instrument (Arens, 1974; Rogers *et al.*, 1974; Arens *et al.*, 1978; and Zych *et al.*, 1979) implied that the desired resolution of <0.5 cm was attainable with minor improvements in the techniques. The position algorithm, which is described in detail in §3.2 and Appendix B, relies on the fact that the amount of scintillation light collected in each photomultiplier depends on the position at which it was generated in the scintillator. The fundamental limit on position resolution with such a technique is statistical fluctuations in the number of photoelectrons collected in the viewing system. While this limit is $\sim$1 mm for the systems listed above (Buffington, 1981), systematic errors of various kinds have limited the actual performance of these systems to $\sim$1 cm resolution. We have succeeded in reducing some of these systematic errors by careful preparation of all optical surfaces and by thoroughly mapping the detector response (§3.2).

The total thickness of the stack was chosen to stop $\sim$2000 MeV/nucleon ^{56}Fe incident at typical angles of 30° and to provide sufficient slowing of ^{20}Ne so that its velocity could be measured in the second Cerenkov counter. The thickness, and therefore the number, of individual NaI(Tl) layers was chosen to provide good angular resolution for particle trajectories (Buffington, 1980).

The top Cerenkov counter C1 contains a silica aerogel radiator with index of refraction $n \approx 1.1$, corresponding to a Cerenkov threshold energy of $\sim$1300

Figure 2.1

Schematic representation of the HEIST instrument, which consists of a stack of twelve NaI(Tl) scintillators, two Cerenkov counters (C1 and C2), and two plastic scintillators (S1 and S2). The C1 Cerenkov radiator is silica aerogel ($n = 1.1$). The C2 radiator is a sandwich of Teflon ($n = 1.33$) and Pilot-425 ($n = 1.50$). The geometry factor of the instrument is ~ 0.25 $m^2 sr$.

Figure 2.1

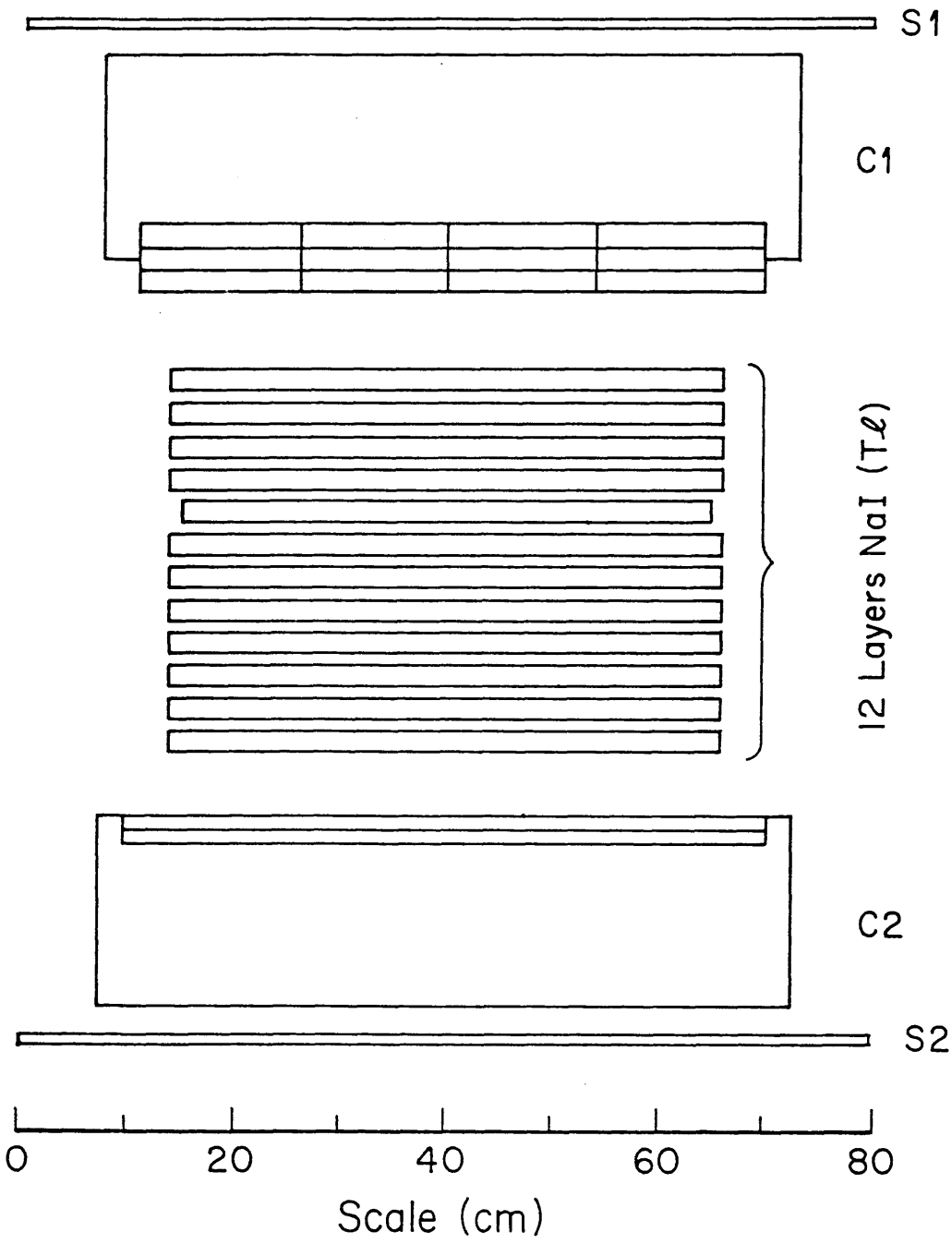

MeV/nucleon. As shown in Figure 2.2, the radiator is a matrix of 48 blocks—36 square and 12 triangular—each 2.0 cm thick and 14.0 cm on a side forming a mosaic 6.0 cm thick and more than 58 cm in diameter. The individual blocks are precision-machined to within 50 μm of the nominal size, and grouped in threes according to average index of refraction. The indices are listed in Figure 2.3. The maximum deviation in index among the blocks in a given group of three is $\Delta n = 0.0166$. The radiator mosaic is mounted in the bottom of a light-integration box whose inner surfaces are coated with a high-reflectance $BaSO_4$ paint to diffuse the light. The counter is viewed by twelve individually digitized 5" EMI 9709 photomultipliers, covering $\sim$14% of the area of the counter.

Note that because of the large number of block edges, a large fraction of the number of possible particle trajectories will intersect or pass near an edge. Particles with such trajectories are rejected, since the pathlength through the groups of blocks cannot be accurately determined, because of the finite trajectory resolution available from the NaI(Tl) stack, and the appropriate corrections for index and response differences cannot be properly applied. This results in a decrease of $\sim$33% in the effective geometry factor of the instrument (see §4.2 and §4.3.8).

One selects the energy region of a Cerenkov detector's sensitivity with the selection of the medium of index of refraction n. High-pressure gas-filled counters can provide indices up to $\sim$1.05, while liquid and conventional solid radiators have indices of $\sim$1.23 and higher, leaving the physically interesting region between 2000 MeV/nucleon and $\sim$1000 MeV/nucleon uncovered. Solid silica aerogels, which have been produced with indices from 1.02 to 1.25, can fill this gap. Solid aerogels with indices between 1.02 and 1.05 have been used by the high-energy physics community (e.g., Burkhardt *et al.*, 1981; Fernandez *et al.*, 1984) and astrophysics community (e.g., Cantin *et al.*, 1981) since the mid-1970s; however, this is the first use of aerogels with an index as high as $n = 1.1$.

The bottom Cerenkov counter contains a sandwich of 1.3 cm thick Teflon ($n = 1.33$) and 1.2 cm thick Pilot-425 ($n = 1.49$) radiators, each 60 cm in diameter. The Cerenkov threshold energies are $\sim$480 MeV/nucleon and $\sim$325 MeV/nucleon, respectively. The radiators are mounted at the top of a $BaSO_4$-covered light-

integration box and viewed by twelve 5" EMI 9709 photomultipliers. Two radiators with differing index values were chosen to extend the range of energies at which velocities can be accurately determined. For example, a ^{20}Ne nucleus entering the instrument at the aerogel Cerenkov threshold energy of ~1300 MeV/nucleon at a typical angle for penetrating particles (~20°) passes through the bottom Cerenkov counter with an energy ~575 MeV/nucleon, in the sensitive range for the Teflon radiator, and a ^{32}S nucleus entering at ~1550 MeV/nucleon passes through the bottom counter at ~350 MeV/nucleon, in the sensitive range for Pilot.

The top and bottom scintillators are NE110 plastic, each nominally 1 cm thick and 79 cm in diameter, and wrapped in aluminum foil and black paper tape. Each is viewed on its edge by six individually digitized 1.5" photomultipliers identical to those in the NaI(Tl) stack. Also mounted on the top scintillator are two 1.5" EMI D550 photomultipliers, which are not digitized but whose analog outputs form part of the trigger subsystem (see §2.2.1).

2.1.1. Electronic and Thermal Subsystems

A detailed description of the HEIST electronic subsystems also appears in Lau (1985), but we repeat here some of the more important features for completeness.

The entire HEIST detector system contains 110 photomultipliers, and associated with each of 108 of these are analog and digital circuits for pulse-height analysis. The analog-to-digital converters (ADCs) provide 12-bit resolution (4096 channels) with good linearity (deviations $<5\times10^{-4}$ near mid-scale) and low power consumption (~0.7 W each) (Althouse *et al.*, 1981). Each ADC has a zero offset, a non-zero output at zero input signal level, which we term the ADC "pedestal" value. The ADCs can operate in two modes: a normal mode for accelerator calibration and flight in which the anode output of each photomultiplier is digitized, and a high-gain mode for use with sea-level cosmic-ray muons in which the output of the final dynode of each photomultiplier is digitized after passing through a preamplifier with a gain of ~70.

The trigger subsystem identifies valid events through a two-step process. The first step is a fast coincidence between the two timing photomultipliers T1 and T2 in the top plastic scintillator. These photomultipliers are not digitized; rather, their outputs

Figure 2.2

Oblique view of the aerogel mosaic. The 48 blocks are each 2.0 cm thick and 14.0 cm on a side.

Figure 2.2

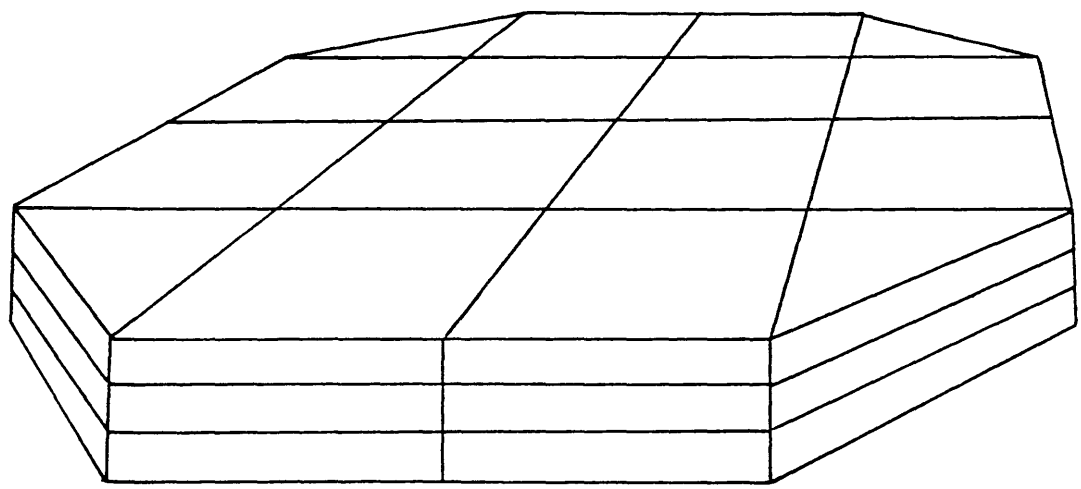

Figure 2.3

Plan view of the aerogel mosaic. Each group of three blocks is labeled by its ordinal number, and the orientation of the mosaic relative to Cerenkov photomultiplier A is noted. The number in boldface is the effective index of refraction (Equation (3.16)) of the group. The numbers in parentheses are the refractive indices of the individual blocks in the group, listed from top to bottom in the order they appear in the group.

Figure 2.3

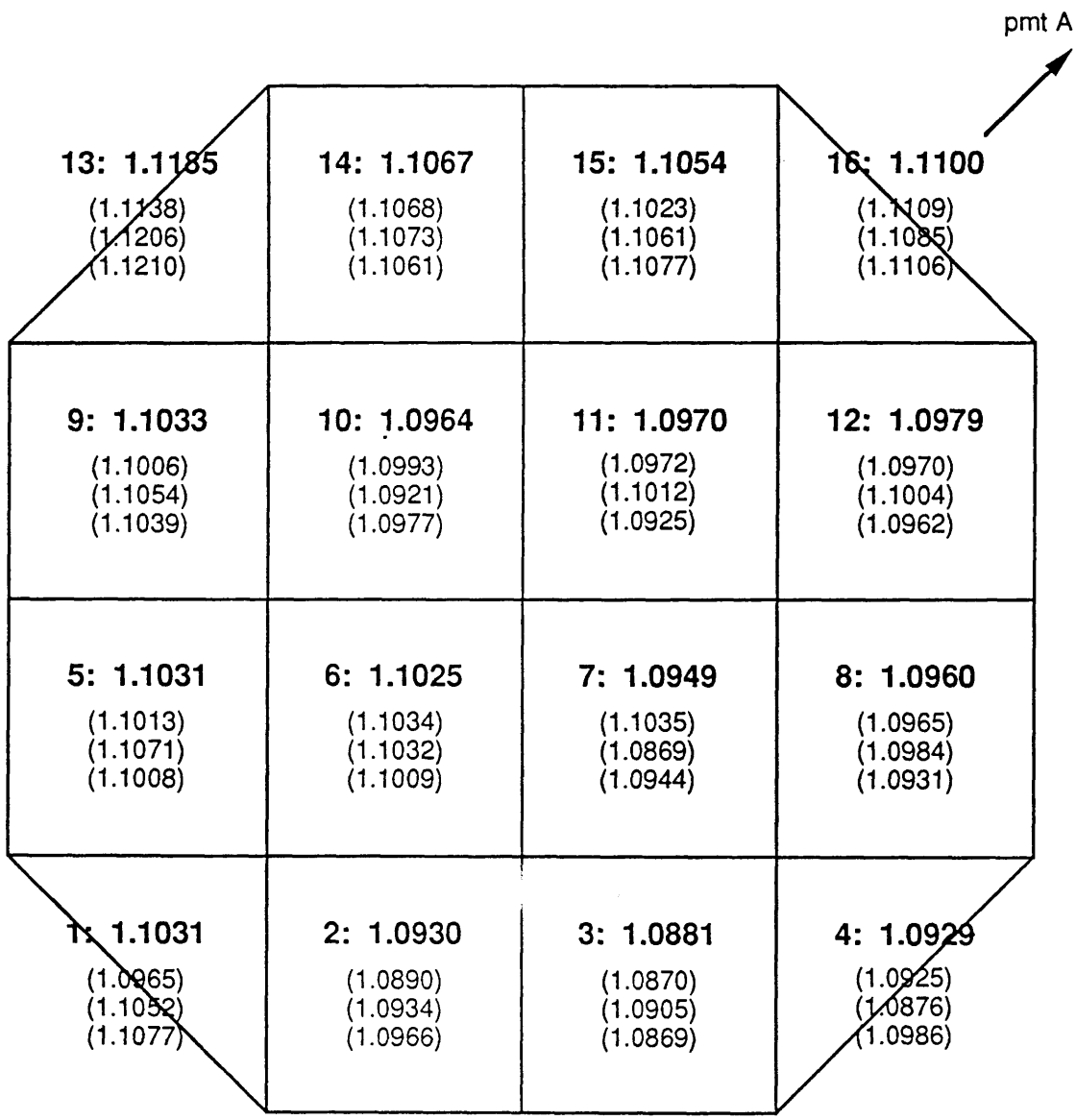
pmt A
13: 1.1185
(1.1138)
(1.1206)
(1.1210)
14: 1.1067
(1.1068)
(1.1073)
(1.1061)
15: 1.1054
(1.1023)
(1.1061)
(1.1077)
16: 1.1100
(1.1109)
(1.1085)
(1.1106)
9: 1.1033
(1.1006)
(1.1054)
(1.1039)
10: 1.0964
(1.0993)
(1.0921)
(1.0977)
11: 1.0970
(1.0972)
(1.1012)
(1.0925)
12: 1.0979
(1.0970)
(1.1004)
(1.0962)
5: 1.1031
(1.1013)
(1.1071)
(1.1008)
6: 1.1025
(1.1034)
(1.1032)
(1.1009)
7: 1.0949
(1.1035)
(1.0869)
(1.0944)
8: 1.0960
(1.0965)
(1.0984)
(1.0931)
1: 1.1031
(1.0965)
(1.1052)
(1.1077)
2: 1.0930
(1.0890)
(1.0934)
(1.0966)
3: 1.0881
(1.0870)
(1.0905)
(1.0869)
4: 1.0929
(1.0925)
(1.0876)
(1.0986)

are tested by analog comparators against threshold values that correspond to approximately one-half the nominal signal from a minimum-ionizing proton in the high-gain muon mode, and ~10 times minimum-ionizing in the flight mode. The T1T2 coincidence condition is commandable in flight into four states: T1+T2, T1&T2, T1 only, or T2 only. Throughout most of the May 1984 flight, the fast coincidence condition was T1+T2. If the fast coincidence condition is satisfied, the second step is begun, a slow coincidence among sums of photomultipliers in the top scintillator, S1, and the fifth NaI(Tl) stack layer, L5. The outputs of the six photomultipliers are grouped into two analog sums of three for redundancy, and a separate commandable discriminator threshold corresponding to ~1 to ~50 times minimum ionizing is provided for each triplet of photomultipliers. The default slow-coincidence condition is the logical AND of all four triplets. Other trigger conditions are available (Lau, 1985) but were not used during the flight. If the slow coincidence is also satisfied, a valid trigger is generated and the 108 photomultiplier outputs are digitized.

Valid triggers can also be generated by an external pulser for electronic calibration of the ADCs or by the trigger logic itself. Such EXTERNAL TRIGGER events are flagged in the data stream. EXTERNAL TRIGGERs are generated by the trigger logic normally under two conditions. First, the trigger logic design calls for an EXTERNAL TRIGGER to be generated every 33 seconds to provide a means of checking the stability of the ADC pedestals during flight; however, a wiring error disabled this function for the May 1984 flight. Second, to protect against a particular failure mode in the data recording system, the trigger logic generates an EXTERNAL TRIGGER if a valid trigger has not occurred in the previous 1.5 seconds. The 1.5 second timeout occurred with sufficient frequency during the flight to provide an adequate check of the ADC stability (see §4.1.1 and §4.3.2).

The baseline-restoration time of the pulse-shaping circuitry associated with the stack photomultipliers can be as long as ~200μs. To provide some protection against pulse pile-up, the trigger logic flags as a HAZARD event any event whose T1T2 coincidence is preceded by an additional T1T2 coincidence within 256μs. Because of the large area of the top scintillator, the fast coincidence rate during the flight averaged ~500 s^{-1}, with ~12% of the flight events tagged as HAZARD events.

Data handling on board the gondola is managed by a TMS 9901 microprocessor system. Valid events are time-stamped and read into a buffer along with housekeeping data including on-board temperatures, pressures, power-supply voltages, magnetometers, and altitude information. Each event forms a block of 256 bytes, and the buffer has a capacity of 200 events.

The primary flight data storage is on board. When the 200-event buffer is full, the data are translated into video format and stored on either one or two commercial video cassette recorders, each providing $\sim$250 MB of storage. The video formatter, which was designed at Caltech, places two copies of each event into a single video frame of 251 horizontal scan lines of 16 bits. The quality of the data recording can be verified by comparing the two copies or by comparing with a checksum, which is recorded in each copy of the event. The data can therefore be recorded four times on board, as was done throughout most of the flight. A 20 kbit/s telemetry data stream provides a nine event-per-second downlink to the ground support computer for real-time monitoring of the housekeeping and science data, and for additional backup data recording. The ground support equipment is described in sufficient detail in Lau (1985), and the description will not be repeated here.

The scintillation yield of NaI(Tl) is temperature-dependent, and therefore it is desirable to maintain the stack at a constant temperature throughout a flight, a period of $\sim$40 hours. The on-board electronics dissipates a total of $\sim$260 W of heat, which must be removed. The evaporative cooling system consists of an aluminum torus containing 20 liters of water and a redundant system of valves that allow the water to be vented to the upper atmosphere. The valves can be operated on command from the ground or automatically, based on temperatures recorded on board. The cooling system maintained the NaI(Tl) temperature constant to within $\pm 0.6\,^{\circ}$C during the flight (§4.1).

2.2. Techniques for Cosmic-Ray Mass Spectroscopy

2.2.1. Cerenkov Radiation

A charged particle that passes through a medium with index of refraction n at a velocity $v = \beta c$ greater than the local group-velocity of light, c/n, generates Cerenkov radiation according to the following relation (Jelly, 1958):

$$C(\beta) = \frac{Z^2 e^2}{\hbar c^2} \int\int_{n\beta>1} \left[1 - \frac{1}{n^2(\omega)\beta^2} \right] d\omega \, dx \,, \tag{2.2}$$

where ω is the angular frequency of the radiation, and $n(\omega)$ is the index of refraction of the Cerenkov radiator. Note also that the efficiency of escape of Cerenkov photons from the radiator and of collection in the detector optics will be frequency-dependent. It is customary to approximate this relation with an effective index of refraction n_{eff} and integrate over both the frequency and the radiator thickness such that the Cerenkov emission collected in a detector system for a particle with velocity greater than the Cerenkov threshold from a radiator of unit thickness is

$$C(\beta) = Z^2 N_\mu \sec\theta \left[\frac{1 - 1/(n_{eff}^2 \beta^2)}{1 - 1/n_{eff}^2} \right], \tag{2.3}$$

where N_μ is the number of photoelectrons collected in the viewing system from a particle of charge $Z = 1$ and velocity $\beta = 1$, and $\sec\theta$ is the pathlength correction. Note that the expression in brackets asymptotically approaches unity as the particle approaches $\beta = 1$ and is frequently known as the "fraction of relativistic light." Throughout the remainder of this document, the effective index of refraction will be denoted "n" without the subscript. The Cerenkov formula can, of course, be inverted and solved for velocity; thus, with a suitable choice of normalization, the Cerenkov response provides a direct measure of particle velocity.

The fraction of relativistic light is depicted in Figure 2.4 as a function $f(\gamma)$ of Lorentz factor $\gamma = (1-\beta^2)^{-1/2}$ for three values of effective index: $n = 1.10$, $n = 1.33$, $n = 1.50$. The fraction rises rapidly from the Cerenkov threshold $\gamma_{th} = (1-n^{-2})^{-1/2}$, then

flattens to its asymptotic unit value. In the region of large slope, a small change in velocity will correspond to a large change in Cerenkov response, and the Cerenkov formula will provide a sensitive measure of particle velocity. It is apparent from the figure that the selection of the radiator material with its associated index of refraction sets the sensitive energy range of a Cerenkov counter.

2.2.1.1. Cerenkov Response Model

The Cerenkov emission of the incident nucleus is not the sole contributor to the signal in the aerogel counter. The high-energy "knock-on" electrons which the incident particle ejects from both the radiator and the material above also emit Cerenkov radiation. We have followed a procedure similar to that of Lezniak (1976) to calculate the average added Cerenkov radiation produced by the knock-on electrons. The details appear in Appendix A. We find that the average Cerenkov component $K(\gamma)$ from knock-on electrons in the aerogel counter typically has a magnitude of $\sim 2\%$ of Z^2N_μ, where Z^2N_μ is the Cerenkov signal generated by a particle of charge Z at velocity $\beta = 1$, and has the following approximate functional form in the velocity interval $2.0 \leq \gamma \leq 3.5$,

$$K(\gamma) \;=\; Z^2 N_\mu \sec\theta \; k(\gamma) \;=\; Z^2 N_\mu \sec\theta \; (\; 0.0136\,(\gamma - 1) + 0.00547 \;) \; . \qquad (2.4)$$

Other background sources of light also exist. For example, Ahlen and Salamon (1979) have shown that $BaSO_4$, which lines the aerogel light-integration box, behaves as a Cerenkov radiator with index $n = 1.61$. In addition, the dry N_2 that fills the counter may act as a scintillator, and there may be some low-level residual scintillation in the aerogel itself. Note that such Cerenkov emission will be slowly increasing with increasing energy, while such scintillation will be slowly decreasing as the particle energy approaches its minimum-ionizing value. The data from the accelerator calibration of the instrument described in §3.1 covered an insufficient number of energies below the Cerenkov threshold to measure the separate contributions to the signal in the aerogel counter, so we have assumed a constant background contribution and modeled the total response in the aerogel counter for a particle of charge Z and Lorentz factor γ as the sum of three sources,

Figure 2.4

The fraction of relativistic Cerenkov light as a function of Lorentz factor for the three values of index of refraction represented in the HEIST instrument: $n = 1.10$, $n = 1.33$, and $n = 1.49$. The Cerenkov response is a sensitive function of particle velocity in the regions where these curves are steeply rising.

Figure 2.4

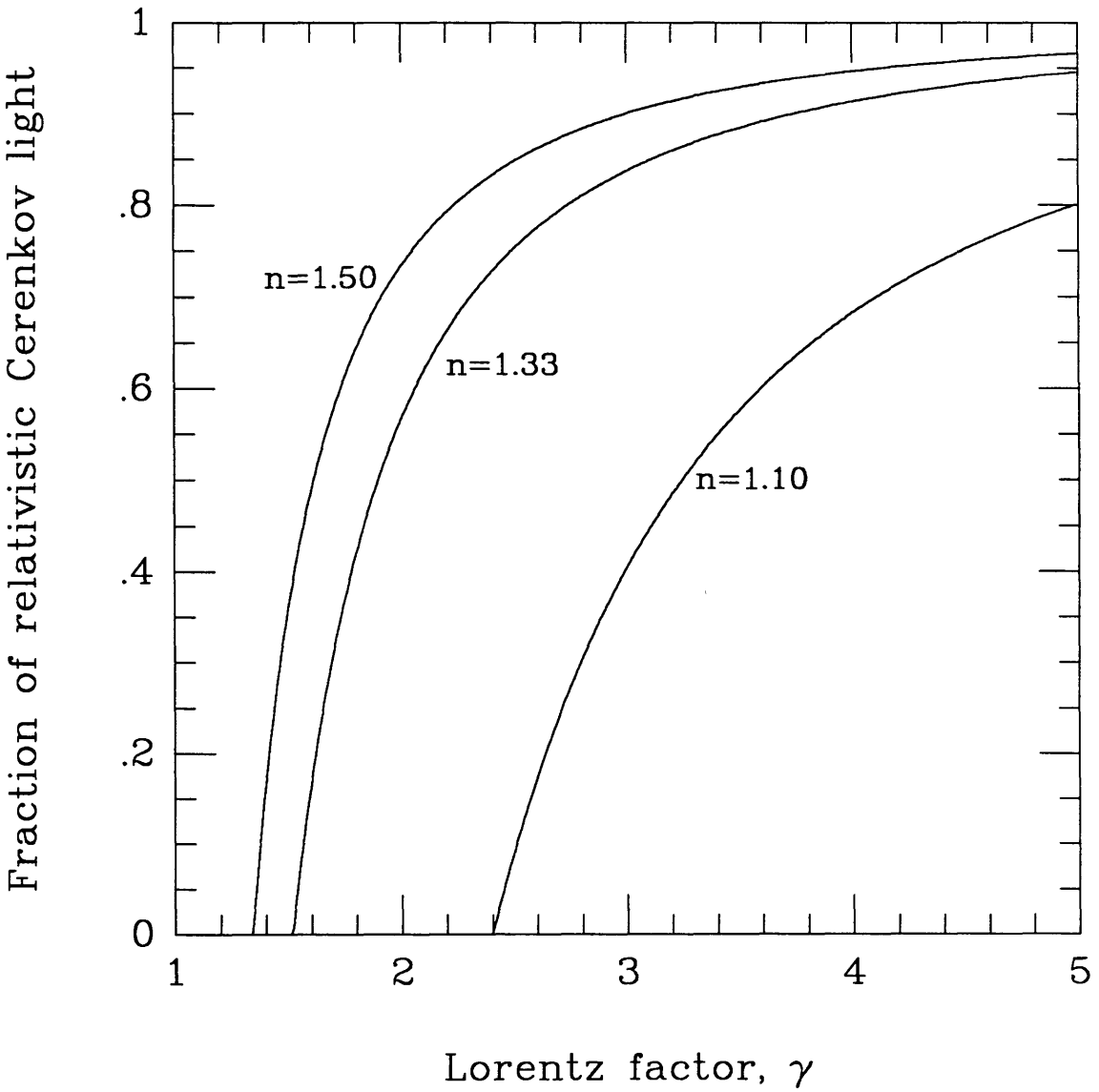
Fraction of relativistic Cerenkov light
1
.8
.6
.4
.2
0
1
2
3
4
5
n=1.50
n=1.33
n=1.10
Lorentz factor, γ

$$C = Z^2 N_\mu \sec\theta \, (f(\gamma) + k(\gamma) + b) , \tag{2.5}$$

where

$$f(\gamma) = \frac{\gamma^2(n^2-1) - n^2}{(n^2-1)(\gamma^2-1)} \tag{2.6}$$

is the fraction of relativistic Cerenkov light generated by the primary particle, expressed in this instance as a function of γ; N_μ is the number of photoelectrons generated by a β=1, Z=1 particle; $k(\gamma)$ is the Cerenkov light generated by knock-on electrons produced above and within the aerogel, modeled in Appendix A; and b is a constant background light level that accounts for the other sources of light in the counter. For the aerogel counter at the full accelerator beam energy (~1650 MeV/nucleon, $\gamma = 2.77$), we had $f(2.77) \sim 0.29$, $k(2.77) \sim 0.02$, and $b \sim 0.02$. Because of the decline in the Cerenkov yield from the aerogel blocks (§3.6.3), the relative contribution from the background had increased to a value of $b = 0.04$ by the time of the flight (§3.6.4). We have used this latter value for the calculation of mass resolution in §2.3.

2.2.2. Ionization Energy Loss

As a particle of charge Z and mass number A passes through matter, it loses energy, predominantly through collision with atomic electrons in the medium. The specific ionization energy loss for heavy charged particles is well described by the following relation (Ahlen, 1980 and 1982),

$$\frac{dE}{dx} = \frac{4\pi e^4 N_A \rho_T}{m_e c^2} \frac{Z_T}{A_T} \frac{Z_{eff}^2}{\beta^2} \left[\ln\left(\frac{2m_e c^2 \beta^2 \gamma^2}{I_{adj}}\right) - \beta^2 - S - D + G - B + R_B \right], \tag{2.7}$$

where

β is the particle velocity,

$\gamma = (1-\beta^2)^{-½}$, is the Lorentz factor,

Z_T, A_T, and ρ_T are the mean atomic number, atomic weight, and density of the target material,

$N_A = 6.02\times10^{23}$ is Avogadro's number,

I_{adj} is the logarithmic mean ionization potential of the target material, and

$m_e c^2 = 0.511$ MeV is the rest energy of the electron.

The effective charge of the projectile is given by the semiempirical expression of Pierce and Blann (1968),

$$Z_{eff} = Z \left[1 - \exp(-130\beta Z^{-2/3}) \right], \tag{2.8}$$

which accounts for electron pickup by the incident nucleus as it slows to a velocity comparable to atomic electron velocities.

$S = S(\beta, I_{adj})/Z_T$ is the atomic shell-effect correction as expressed by Barkas and Berger (1964), which becomes significant when the particle velocity is comparable to the atomic electron velocity. Note, however, that this expression is not valid for $\beta < 0.13$ ($E < 8$ MeV/nucleon), and Equation (2.7) must not be applied below this velocity.

$D = \delta(Z_T, A_T, \beta, I_{adj})/2$ is the relativistic density-effect correction (Fermi, 1939 and 1940). This accounts for the screening of the electric field of the projectile by atoms of the medium, which reduces the effect of distant collisions. The correction becomes appreciable only above a few GeV/nucleon in solids.

$G = G(Z_{eff}, \beta, I_{adj})/2$ is the correction for Mott scattering of the atomic electrons by the distributed charge on the projectile. It has been derived to order Z_{eff}^7.

$B = B(\alpha Z_{eff}/\beta)$, where $\alpha = 1/137$ is the fine-structure constant, is the non-relativistic Bloch (1933) correction, which arises from modeling the bound atomic electrons as wave packets rather than plane waves.

$R_B = R_B(Z_{eff}, \beta, \theta_0, \lambda)$ is the relativistic Bloch correction as derived in the third Born approximation by Ahlen (1982). Parameters θ_0 and λ are free to range within bounds given by Ahlen. At energies above ~500 MeV/nucleon, R_B has a magnitude on the order of the non-relativistic correction B, and the two terms tend to cancel.

Waddington *et al.* (1985) provide evidence for the use of all terms of Equation (2.7) from the measured ranges of Xe, Ho, Au, and U beams at energies between 900 MeV/nucleon and 1200 MeV/nucleon in nuclear emulsion.

Newport, Klarmann, and Waddington have developed a software algorithm based on that of Salamon (1980), which calculates dE/dx in arbitrary materials using Equation (2.7) (e.g., Newport, 1986). For example, for the useful energy interval in the first stack layer (~1200 MeV/nucleon to ~2000 MeV/nucleon), we find that we can approximate the specific ionization energy loss in NaI(Tl) for a particle of charge Z and Lorentz factor γ by

$$\frac{dE}{dx} = 1.375\ Z^2\ (\ 2.19 - 1.12\gamma + 0.348\gamma^2 - 0.0362\gamma^3\ )\ \text{MeVcm}^2/\text{g}\ . \qquad (2.9)$$

The polynomial term in parentheses has a magnitude ~1.0 and varies by ~3% over the energy interval, monotonically decreasing with increasing energy. The minimum-ionizing energy for ^{56}Fe in NaI(Tl) is approximately 2050 MeV/nucleon. We have chosen a polynomial approximation to simplify the algebra in the calculations of mass resolution (see §2.3).

The total energy loss in the HEIST instrument is therefore the integrated specific ionization over the pathlength R of particle in the NaI(Tl),

$$\Delta E = \int_0^R \frac{dE}{dx}\, dx\ . \qquad (2.10)$$

2.2.3. Scintillation Efficiency and the NaI(Tl) Response Model

It would be ideal if our detectors were perfectly linear, that is, if the scintillation light yield were strictly proportional to the ionization energy loss. We note, however, that the light output of NaI(Tl) is not proportional to dE/dx for heavy nuclei, but exhibits a saturation so that the light output per unit energy loss dL/dE decreases slowly with increasing dE/dx. Salamon and Ahlen (1981) measured this effect in NaI(Tl) with heavy ions at the Lawrence Berkeley Laboratory Bevalac at energies up to 550 MeV/nucleon and found that the scintillation efficiency dL/dE was primarily a function only of dE/dx at these velocities and not the charge or mass of the beam. Our accelerator calibration data are in good agreement with their results. Figure 2.5, which is taken from Schindler *et al.* (1983), shows the results of Salamon and Ahlen as vertical

error bars connected by solid lines, and data from the HEIST stack as solid circles, normalized such that the measured ^{55}Mn response in layer 1 agrees with an extrapolation of their data to the energy loss appropriate for the Bevalac beam in the first layer. The four data points at larger values of dE/dx are from the responses in layers 8 through 11 for a beam that passed through the hermetic can center plug, and the points at smaller values of dE/dx are layer 1 responses of lower Z particles generated in a target upstream of the instrument. We fit a simple logarithmic curve to our data, showing that the scintillation efficiency for elements in the Fe group ($24 \leq Z \leq 28$) can be approximated as

$$<h\nu> \frac{dL}{dE} = 0.273 - 0.0251 \ln(\frac{dE}{dx}) , \qquad (2.11)$$

where $<h\nu>$ is the average energy of scintillation photons in NaI(Tl), and dE/dx is expressed in MeV cm^2/g. We have rescaled the arbitrary units of Salamon *et al.* such that their measured relative scintillation efficiency for a minimum-ionizing proton equals the absolute measurement of (14.1±0.7)% given by van Sciver and Bogart (1957). It is apparent from Figure 2.5 that the scintillation yield for typical Fe nuclei with $dE/dx \sim 10^3$MeV cm^2/g should be ~2/3 of that expected by Z^2 scaling from the muon response. Inserting the polynomial expression for dE/dx into Equation (2.11), we find that dL/dE varies only by ~0.8% over the energy interval from 1200 MeV/nucleon to 2000 MeV/nucleon.

We therefore model the scintillation response S in a single stack layer as the integrated specific ionization energy loss dE/dx in the layer weighted by the scintillation efficiency dL/dE,

$$S = \int \frac{dE}{dx} \frac{dL}{dE} dx . \qquad (2.12)$$

Near the top of the NaI(Tl) stack, the incident nuclei do not slow appreciably in a single layer, so we can approximate dE/dx and dL/dE with their average values and write the model scintillation response in the following form,

$$S = \alpha_S Z^2 \sec\theta \, s(Z,\gamma) , \qquad (2.13)$$

where

Figure 2.5

Scintillation efficiency of NaI(Tl), taken from Schindler *et al.*, (1983). The data of Salamon and Ahlen (1981) for ^{56}Fe, ^{40}Ar, and ^{20}Ne are shown as solid lines. The arrow indicates the scintillation efficiency for relativistic muons given by Salamon and Ahlen. The data of Schindler *et al.* from the HEIST NaI(Tl) stack using a ^{55}Mn accelerator beam are shown as filled circles, and are normalized such that the observed response in the first stack layer agrees with an extrapolation of the data of Salamon and Ahlen. Also shown are the observed efficiencies in the first stack layer for individual charges between Mg and Mn created by fragmentation interactions in a polyethylene absorber.

Figure 2.5

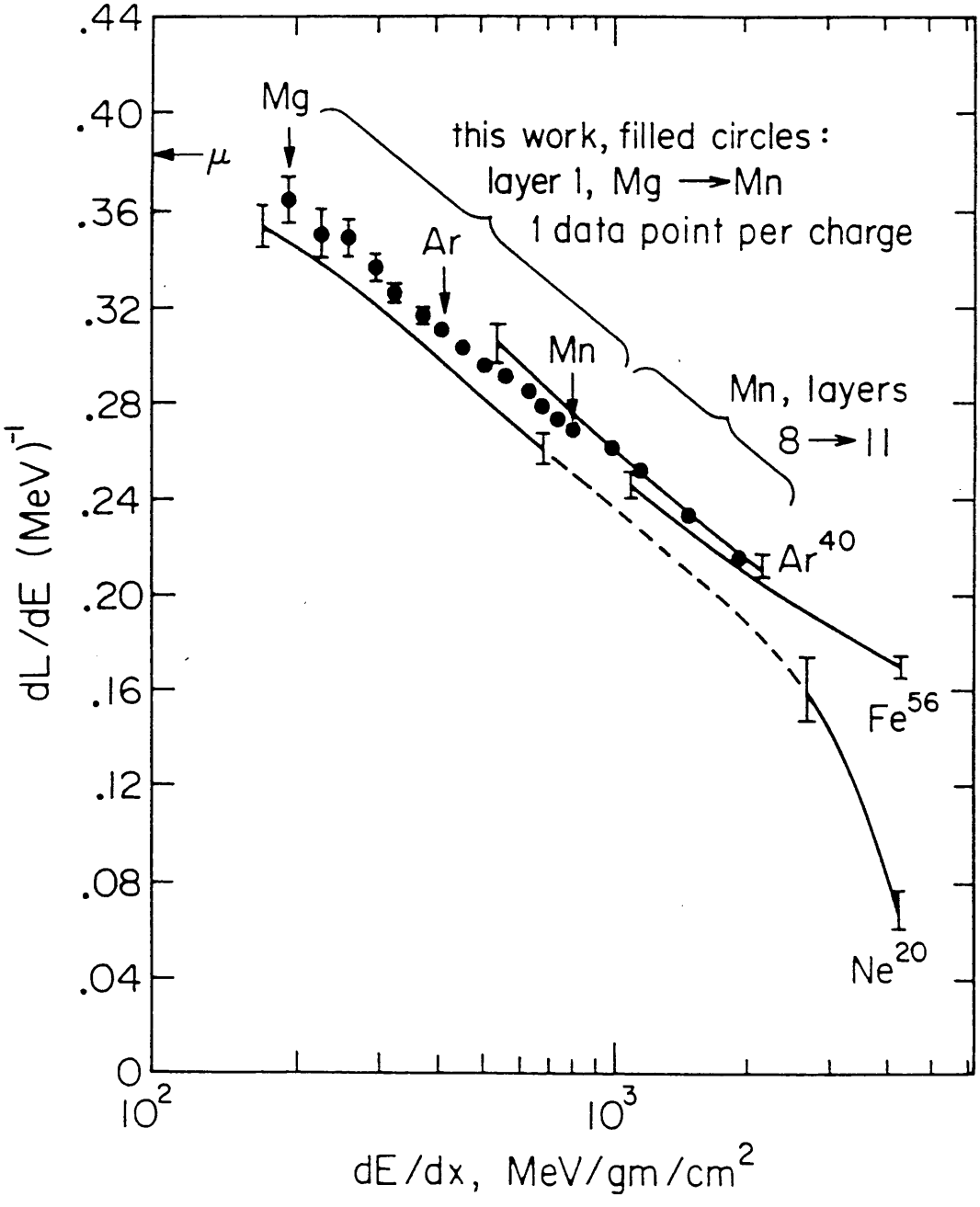
.44
.40
.36
.32
.28
.24
.20
.16
.12
.08
.04
0
10^2
10^3
dL/dE (MeV)$^{-1}$
dE/dx, MeV/gm/cm^2
←μ
Mg
Ar
Mn
this work, filled circles:
layer 1, Mg → Mn
1 data point per charge
Mn, layers
8 → 11
Ar^{40}
Fe^{56}
Ne^{20}

$$s(Z,\gamma) = h_3(\gamma) \left\{ 1 - 0.249 \ln \left[\left(\frac{Z}{26}\right)^2 h_3(\gamma) \right] \right\}, \tag{2.14}$$

where $h_3(\gamma)$ is the third-order polynomial term from Equation (2.9) for dE/dx. However, in the final few layers of a particle's range, where the deceleration within a layer becomes significant, the integral must be evaluated more precisely, and Equation (2.13) is not valid.

2.2.4. The Range-Energy Relation

The range of a charged particle can be derived from the specific ionization energy loss by integrating from the incident energy down to stopping,

$$R = \int_0^E \frac{dE}{dE/dx} . \tag{2.15}$$

It is apparent from the form of Equation (2.7) that the specific ionization of a heavy nucleus is larger by a factor of Z^2 than that of a proton with the same velocity, that is, with the same kinetic energy per nucleon E/A; thus the range will scale as A/Z^2. The velocity dependence of the above integral can be approximated with reasonable accuracy as a power law in energy per nucleon an any limited energy interval, and therefore the range is given by

$$R = k \frac{A}{Z^2} (\gamma - 1)^{\alpha} . \tag{2.16}$$

Table 4.1 in §4.3.11 lists power-law coefficients and index values in NaI(Tl) and the energy intervals over which they are valid.

The NaI(Tl) scintillator stack provides the range measurement for those particles that stop in the HEIST instrument. No range measurement is possible for particles that penetrate the stack. Although the range relation has not been used here to calculate particle masses, it has been used to select Fe events (§4.3.11).

2.2.5. Mass by Cerenkov-ΔE-Cerenkov and Cerenkov-Energy

The kinetic energy E of a particle of mass M and Lorentz factor $\gamma = (1-\beta^2)^{-½}$ is given by

$$E = (\gamma - 1)\,Mc^2 \,. \tag{2.17}$$

Thus a particle that loses an energy ΔE undergoes a corresponding change in Lorentz factor $\Delta\gamma$, and the mass can be derived from

$$M = \frac{\Delta E}{c^2 \Delta\gamma} \,. \tag{2.18}$$

The Cerenkov-ΔE-Cerenkov technique is used to determine the masses of particles that penetrate the HEIST NaI(Tl) stack. For penetrating particles, ΔE is given by the total energy loss measured in the NaI(Tl), and $\Delta\gamma$ is given by the difference in velocities measured above and below the stack, $\Delta\gamma = \gamma_{C1} - \gamma_{C2}$. The Cerenkov-Energy technique is used for particles that stop in the stack. Stopping particles have $\Delta\gamma = \gamma_{C1} - 1$. This technique was pioneered by W. R. Webber (e.g., Webber *et al*, 1973).

Success of the Cerenkov-ΔE-Cerenkov technique for penetrating particles requires that two precise measurements of velocity be made, making the resolution inherently poorer than that for the Cerenkov-Energy technique. In addition, it requires that the thickness of the ΔE detector and the index value of the bottom radiator be carefully matched such that the energy lost by the particles places them in the sensitive energy range of the bottom radiator. Because the resolution of the top Cerenkov counter had degraded by the time of the 1984 HEIST flight (see §3.6.3), and because the 1982 accelerator calibration of the instrument was not adequate to map the bottom Cerenkov counter (see §3.1), the resolution of penetrating events during the flight was expected to be rather poor. Consequently, penetrating events have not been analyzed, and the Cerenkov-ΔE-Cerenkov technique has not been employed. Since the Ne, Mg, and Si nuclei that have energies above the aerogel threshold penetrate the stack, and only elements from the Fe group stop in the stack in large numbers, only Fe isotope abundances have been measured with the flight data.

Before proceeding, we will make a change of notation. The mass of a nucleus can be expressed as

$$M = Zm_p + (A-Z)m_n - B/c^2 , \tag{2.19}$$

where $m_p = 938.28$ MeV/c^2 and $m_n = 939.57$ MeV/c^2 are the masses of the proton and neutron, respectively, Z and A are the nuclear charge and mass number, and B is the nuclear binding energy. For elements in the Fe group, the binding energy is approximately a constant 8.7 MeV/nucleon, and we can approximate the kinetic energy as

$$E = (\gamma - 1)Am_u c^2, \tag{2.20}$$

where $m_u = 931.50$ MeV/c^2 is the mass per atomic mass unit. We then re-express the mass determined by the Cerenkov-Energy technique as

$$A_{CE} = \frac{\Delta E}{m_u c^2 \Delta\gamma} , \tag{2.21}$$

where $\Delta\gamma = \gamma_{C1} - 1$.

2.2.6. Mass by Range-Energy and Cerenkov-Range

For stopping particles, mass can also be determined from the range of the particle between the point at which the velocity measurement is made to the point at which it stops. We stated above that the range-energy relation can be approximated as a power law in energy per nucleon,

$$R = k\frac{A}{Z^2}\left[\frac{\Delta E}{Am_u c^2}\right]^{\alpha} \tag{2.22}$$

$$= k\frac{A}{Z^2}(\gamma - 1)^{\alpha} . \tag{2.23}$$

Equation (2.24) gives the mass determined by the Range-Energy technique,

$$A_{RE} = \left[\frac{k}{Z^2 m_u c^2}\frac{(\Delta E)^{\alpha}}{R}\right]^{1/(\alpha-1)} , \tag{2.24}$$

and Equation (2.25) gives the mass by the Cerenkov-Range technique,

$$A_{CR} = \frac{Z^2}{k}\frac{R}{(\gamma-1)^{\alpha}} . \tag{2.25}$$

As we will see below, the mass resolution of both techniques is unacceptably large, primarily because of the inadequate accuracy of the range measurement. Neither technique has been used in this analysis.

2.3. Contributions to Mass Resolution

Because the isotopes of Fe are separated in mass by only ~2%, determination of the mass depends on precise measurements of ΔE and $\Delta\gamma$. The equation for mass determination by Cerenkov-Energy is easily differentiated to give the resolution,

$$\delta A_{CE} = A_{CE} \left[\left(\frac{\delta \Delta E}{\Delta E}\right)^2 + \left(\frac{\delta \Delta \gamma}{\Delta \gamma}\right)^2 \right]^{1/2} . \tag{2.26}$$

For the contribution to mass resolution from each measurement to be 0.25 amu for ^{56}Fe, the measurements of ΔE and $\Delta\gamma$ must be precise to ~0.5%.

Similarly, the mass resolution for the Cerenkov-Range and Cerenkov-Energy techniques is calculated by differentiating Equations (2.24) and (2.25),

$$\delta A_{CR} = A_{CR} \left[\left(\frac{\delta R}{R}\right)^2 + \left(\alpha \frac{\delta \Delta \gamma}{\Delta \gamma}\right)^2 \right]^{1/2} \tag{2.27}$$

$$\delta A_{RE} = A_{RE} \left[\left(\frac{1}{\alpha - 1} \frac{\delta R}{R}\right)^2 + \left(\frac{\alpha}{\alpha - 1} \frac{\delta \Delta E}{\Delta E}\right)^2 \right]^{1/2} . \tag{2.28}$$

For the Range-Energy technique, the multiplicative factors of $1/(\alpha-1)$ and $\alpha/(\alpha-1)$ in Equation (2.28) with $\alpha \sim 1.25$ (see Table 4.1, §4.3.11) imply that the measurements of range and kinetic energy must be precise to ~0.1% in order to reduce the contribution from each to 0.25 amu or less. Because these large multiplicative factors do not appear in Equation (2.27), and instead only the velocity resolution is multiplied by α, the Cerenkov-Range technique is less sensitive to uncertainties in the velocity and range measurements.

In §3.2.3 we show that the angular resolution for a typical Fe event ($\theta = 30^\circ$) is $\sigma_{\sec\theta} \sim 0.02$. The range is given by $R = X \sec\theta$, where X is the vertical distance through the instrument to the particle's stopping point. Thus the fractional range uncertainty is $\delta R/R = \delta \sec\theta / \sec\theta \sim 2\%$, which is clearly much too large to permit

isotope resolution by either method that relies on a range measurement.

Before discussing the contributions to mass resolution in detail, we make the following conclusion about the method we will use to calculate velocity. It is apparent from the Cerenkov formula (Equation (2.5)) that in order to derive the velocity from the Cerenkov response C, we must correct the measured response for the pathlength through the radiator. The uncertainty in the pathlength correction $\delta \sec\theta$ will therefore contribute to the uncertainty in the mass as follows,

$$\delta A_\theta = \frac{\partial A}{\partial \gamma}\frac{\partial \gamma}{\partial C}\frac{\partial C}{\partial \sec\theta}\delta\sec\theta \tag{2.29}$$

$$= \frac{A}{\Delta\gamma}\frac{f(\gamma)+k(\gamma)+b}{f'(\gamma)+k'(\gamma)}\tan\theta\,\delta\theta\,, \tag{2.30}$$

where $f'(\gamma)$ and $k'(\gamma)$ denote the derivatives with respect to γ. We note that the resolution is proportional to $\tan\theta\,\delta\theta$, and therefore the resolution degrades as the angle of incidence increases. In §3.2.3 we will find that the angular resolution for a typical Fe event during flight (1500 MeV/nucleon, $\theta = 30^\circ$) is $\delta\theta \sim 0.8^\circ$; thus the contribution to mass resolution for a typical Fe is ~0.25 amu and rises to ~0.4 amu at 45°. This contribution is rather large, but it can be eliminated. We note that the response in both the aerogel counter and the first stack layer are proportional to the pathlength $\sec\theta$. The ratio of the two responses, C/S, should therefore be independent of pathlength, yet still be a function of γ.

Taking the ratio of the Cerenkov response model (Equation (2.5)) to the scintillation response model (Equation (2.13)), we find

$$\Omega \equiv \frac{C}{S} = \frac{N_\mu}{\alpha_S}\frac{f(\gamma)+k(\gamma)+b}{s(Z,\gamma)}\,. \tag{2.31}$$

We therefore can measure the Lorentz factor γ without explicitly including pathlength corrections. We note, however, that the uncertainty in the measured scintillator response now contributes to the uncertainty in velocity. In §2.3.1.2 we will see that this contribution is smaller than the contribution from the pathlength correction.

Contributions to mass resolution from the velocity measurement include those that are due to (1) photoelectron statistical fluctuations in the aerogel Cerenkov

counter; (2) fluctuations in energy loss in the first NaI(Tl) stack layer; (3) fluctuations in the aerogel Cerenkov response from knock-on electrons; (4) multiple Coulomb scattering between the aerogel and the first stack layer; (5) uncertainty in the normalization of the aerogel blocks; (6) uncertainty in the level of background light in the aerogel counter; variations in (7) the light-collection efficiency and (8) the index of refraction not accounted for in the maps of the response of the aerogel counter; and (9) errors in the calculation of velocity that are due to uncertainty in the particle positions. Contributions from the energy measurement include (1) photoelectron statistical fluctuations in the NaI(Tl), (2) errors in the calculation of energy losses that are due to uncertainty in the particle positions, and (3) errors in the maps of scintillator response generated from the accelerator calibration data.

Additional sources of mass uncertainty exist that are not discussed in §2.3.1 and §2.3.2 below; however, they are expected to be relatively small. Errors in modeling the Cerenkov and NaI(Tl) scintillator responses can contribute to mass uncertainty. However we note, for example, that the variation in the correction for average scintillation efficiency (§2.2.3) is sufficiently small that errors in the correction are unlikely to be significant. Additional instrumental contributions include those from (1) errors in measured photomultiplier gains and layer-to-layer gains in the stack; (2) high-voltage noise; and (3) finite channel width in the ADCs. The assignment of photomultiplier gains for the flight data is discussed in §4.1.1. (1) Since the uncertainty in the gain for an individual photomultiplier is estimated to be $\sim$0.3% and a typical Fe nucleus stops in the eighth or ninth stack layer, the uncertainty in the total energy loss is $\sim$0.04%, which is negligible. The statistical uncertainty in the layer-to-layer gain balancing is estimated to be $\sim$0.4% for each layer. Because the trigger condition requires that each event pass through at least five layers, the error in the total energy loss is in all cases $<$0.2% and typically $\sim$0.1%. (2) Noise in the photomultiplier high-voltage system causes the signal to fluctuate. Noise distributions collected just prior to flight show an rms variation of $\sim$0.01% of a typical Fe response in the NaI(Tl) and $\sim$0.1% in the aerogel counter. (3) The contribution from the width of an ADC channel amounts to $\sim$0.02% of a typical Fe response in the NaI(Tl) and $\sim$0.1% in the aerogel counter. These contributions are all negligible in comparison with the those listed in §2.3.1 and §2.3.2.

We discuss first the contributions from the velocity measurement, then those from the energy loss measurement. Figure 2.6 depicts the various contributions to mass uncertainty associated with the flight data by the Cerenkov-Energy technique as a function of particle energy for an ^{56}Fe nucleus at an angle of incidence of $\theta = 30°$. Detailed inspection of the largest contributions shows that the resolution has only a small dependence on angle, improving with increasing angle less quickly than $1/\sec^{1/2}\theta$. We have assumed an index of refraction $n = 1.1$ and a photoelectron yield of $N_\mu = 9$. All curves begin at the Cerenkov threshold velocity. Note that velocity measurement is possible below the threshold; however, the resolution is significantly worse since the slope of the total response in the Cerenkov counter is significantly smaller. In this case the contributions to velocity resolution can be calculated from the expressions given below by nullifying the Cerenkov response, $f(\gamma) = f'(\gamma) = 0$.

2.3.1. Contributions to Velocity Uncertainty

In the following discussion, for those contributions for which an analytic expression can be calculated, we list the fractional velocity uncertainty first as a product of partial derivatives, then in symbolic form as evaluated for the Cerenkov and scintillator response models, and finally as an approximate function of γ, with the secondary Cerenkov sources neglected ($k(\gamma) \equiv 0$ and $b \equiv 0$) and the functional dependence of the scintillation correction set to unity ($s(Z,\gamma) \equiv 1$). The approximate form makes apparent the velocity and index dependence to leading order. The curves of Figure 2.6 are calculated from the complete expressions.

2.3.1.1. Photoelectron Statistical Fluctuations

The dominant fundamental source of velocity uncertainty is statistical fluctuations in the number of photoelectrons collected in the photomultipliers viewing the Cerenkov counters. Photoelectron statistical fluctuations, $\delta C = \sqrt{C}$, contribute to velocity resolution as

$$\frac{\delta\Delta\gamma_{pe}}{\Delta\gamma} = \frac{1}{\Delta\gamma}\frac{\partial\gamma}{\partial\Omega}\frac{\partial\Omega}{\partial C}\delta C \tag{2.32}$$

$$= \frac{1}{\Delta\gamma} \frac{[f(\gamma) + k(\gamma) + b]^{\frac{1}{2}}}{f'(\gamma) + k'(\gamma) - \frac{s'(Z,\gamma)}{s(Z,\gamma)}[f(\gamma) + k(\gamma) + b]} \frac{1}{Z N_\mu^{\frac{1}{2}} \sec^{\frac{1}{2}}\theta} \quad (2.33)$$

$$\sim \left\{ \frac{(n^2-1)(\gamma^2-1)^3}{\gamma^2(\gamma-1)^2} [\gamma^2(n^2-1) - n^2] \right\}^{\frac{1}{2}} \frac{1}{2Z N_\mu^{\frac{1}{2}} \sec^{\frac{1}{2}}\theta} . \quad (2.34)$$

Note that velocity resolution is inversely proportional to $N_\mu^{\frac{1}{2}}$, the square root of the number of photoelectrons collected. Thus statistical fluctuations make a smaller contribution to the velocity resolution in a counter with a high light yield and an efficient light-collection system, as one would expect. By the time of the flight, the aerogel counter had a relatively poor light yield ($N_\mu \approx 9$, see §3.6.3). This accounts for the magnitude of the photoelectron contribution presented in Figure 2.6.

Note also that the velocity resolution is inversely proportional to Z. Since the mass $A \approx 2Z$, the photoelectron contribution to mass resolution is approximately independent of the nuclear species.

2.3.1.2. Energy Loss Fluctuations

Dividing the Cerenkov response by the NaI(Tl) response eliminated the need for pathlength corrections, but it introduced fluctuations in energy loss into the calculation of γ and thus the calculation of the mass. In §3.3.1 we find that the measured energy-loss resolution of Fe-group events is typically ~1.1%. The ionization energy loss of heavy charged particles is the result of a large number of collisions with atomic electrons in the target material, and since each collision is an independent event, energy loss is a statistical process. Thus particles of a given energy do not lose the same amount of energy in traversing an absorber of given thickness. However, in §3.3.1 we find that such fluctuations cannot account for the entirety of the observed resolution, and other contributions must be invoked.

Because the energy resolution as measured in §3.3.2 is approximately linearly dependent on Z, we will write it as $\delta S = \alpha_L Z \sec^{\frac{1}{2}}\theta$, where α_L is a scale factor which we take to be independent of velocity. Thus the measured energy resolution, δS, contributes to an uncertainty in velocity as

Figure 2.6

Summary of contributions to mass resolution for ^{56}Fe at a 30° angle of incidence. The energy shown is the kinetic energy per nucleon in the center of the aerogel counter. The resolution has only a small dependence on angle. The legend lists the nine contributions to mass resolution from the aerogel counter, the three contributions from the NaI(Tl) stack, and the total mass resolution, as described in the text. The curves start at the Cerenkov threshold energy. Mass measurement is possible below the threshold; however, the resolution is significantly worse since the slope of the Cerenkov response is significantly smaller.

Figure 2.6

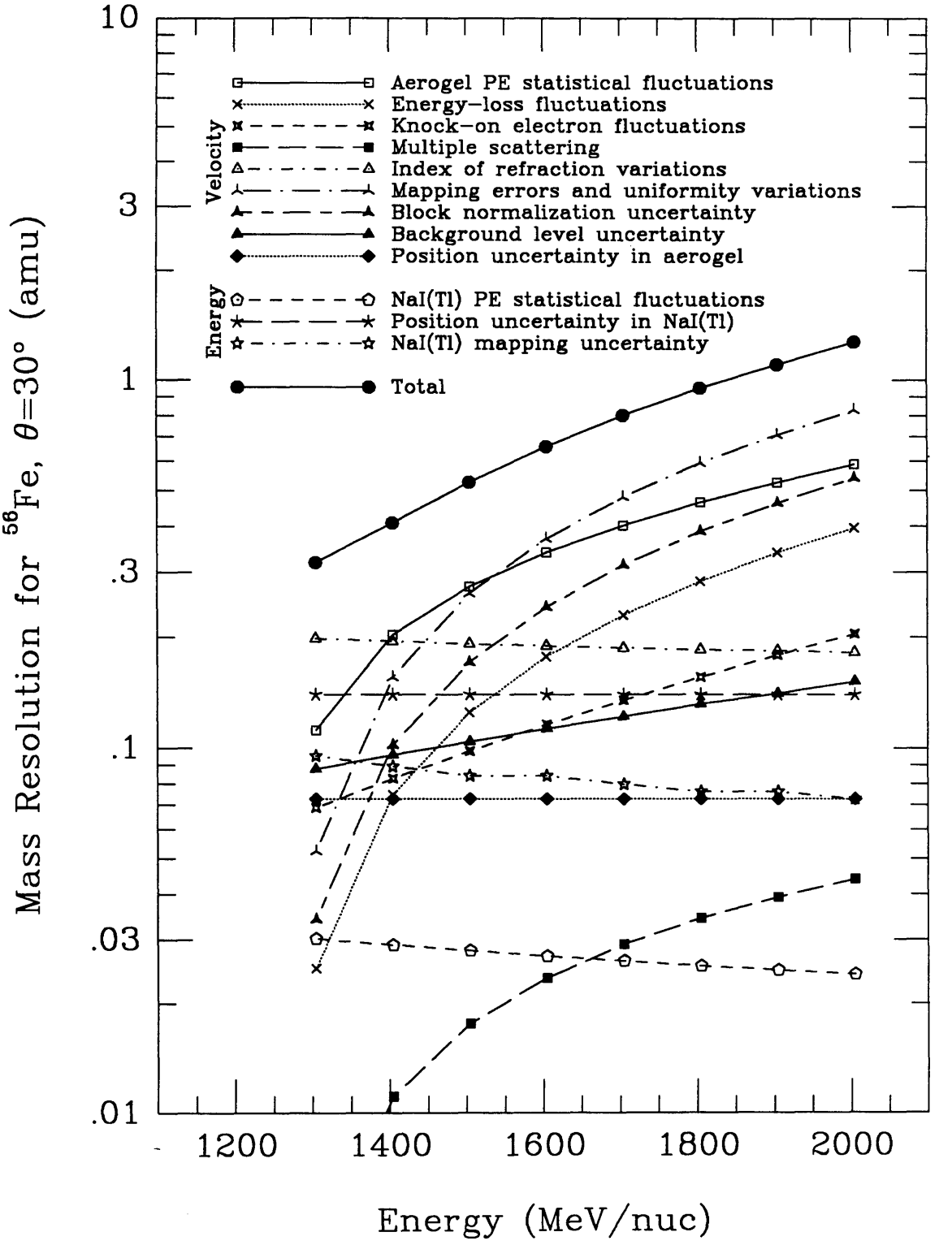
Mass Resolution for ^{56}Fe, θ=30° (amu)
10
3
1
.3
.1
.03
.01
1200
1400
1600
1800
2000
Energy (MeV/nuc)
Velocity
Energy
Aerogel PE statistical fluctuations
Energy-loss fluctuations
Knock-on electron fluctuations
Multiple scattering
Index of refraction variations
Mapping errors and uniformity variations
Block normalization uncertainty
Background level uncertainty
Position uncertainty in aerogel
NaI(Tl) PE statistical fluctuations
Position uncertainty in NaI(Tl)
NaI(Tl) mapping uncertainty
Total

$$\frac{\delta\Delta\gamma_L}{\Delta\gamma} = \frac{1}{\Delta\gamma}\frac{\partial\gamma}{\partial\Omega}\frac{\partial\Omega}{\partial S}\delta S \tag{2.35}$$

$$= \frac{1}{\Delta\gamma}\frac{f(\gamma)+k(\gamma)+b}{s(Z,\gamma)[f'(\gamma)+k'(\gamma)]-s'(Z,\gamma)[f(\gamma)+k(\gamma)+b]}\frac{\alpha_L}{\alpha_S}\frac{1}{Z\sec^{1/2}\theta}$$

$$\sim \frac{\gamma+1}{\gamma}[\gamma^2(n^2-1)-n^2]\frac{\alpha_L}{\alpha_S}\frac{1}{2Z\sec^{1/2}\theta}. \tag{2.37}$$

We find that to the extent that the energy resolution in a single layer scales linearly with charge, the velocity resolution is inversely proportional to Z. In Figure 2.6, we have used the measured resolution of 1.1%. This contribution is typically ~0.2 amu and is smaller than the contribution from pathlength uncertainty for most angles of incidence.

2.3.1.3. Knock-on Electrons

In Appendix A we calculate the mean added Cerenkov component from knock-on electrons generated in and above the aerogel, and by expanding on the method of Lezniak (1976), we also calculate the rms variation in the Cerenkov emission from the knock-ons. This variation, which is caused by fluctuations in the number and energies of the knock-ons, contributes to the velocity uncertainty. The parameterization of the rms variation in the added Cerenkov signal, $\sigma_K(Z,\gamma) = ZN_\mu\sec^{1/2}\theta\,\sigma_k(\gamma)$, can be found in Appendix A.

$$\frac{\delta\Delta\gamma_k}{\Delta\gamma} = \frac{1}{\Delta\gamma}\frac{\partial\gamma}{\partial\Omega}\frac{\partial\Omega}{\partial K}\sigma_K(Z,\gamma) \tag{2.38}$$

$$= \frac{1}{\Delta\gamma}\frac{\sigma_k(\gamma)}{f'(\gamma)+k'(\gamma)-\frac{s'(Z,\gamma)}{s(Z,\gamma)}[f(\gamma)+k(\gamma)+b]}\frac{1}{Z\sec^{1/2}\theta} \tag{2.39}$$

$$\sim \frac{(n^2-1)(\gamma^2-1)^2}{\gamma(\gamma-1)}\frac{\sigma_k(\gamma)}{2Z\sec^{1/2}\theta}. \tag{2.40}$$

The contribution to mass resolution is relatively small, typically ~0.1 amu. Again,

since the velocity resolution is inversely proportional to Z, the mass resolution is approximately independent of the nuclear species.

2.3.1.4. Multiple Coulomb Scattering

As a charged particle traverses a medium of finite thickness, it undergoes a large number of collisions with the atomic electrons of the medium, most of which cause a small deflection in the trajectory of the particle. Such multiple Coulomb scattering between the aerogel and the bottom of the first NaI(Tl) stack layer causes the average angle in each detector to differ. If the angle of incidence in the aerogel is θ_C and the angle in the first stack layer is θ_S, the ratio of the two pathlengths is given by

$$\frac{\sec\theta_C}{\sec\theta_S} = \frac{\sec\theta_C}{\sec(\theta_C + \delta\theta_{mcs})} \tag{2.41}$$

$$\approx 1 - \tan\theta_C\,\delta\theta_{mcs}(Z,A)\,, \tag{2.42}$$

where for pathlengths X short enough that slowing down of the incident particle can be neglected, the rms scattering angle $\delta\theta_{mcs}(Z,A)$ can be approximated by (e.g., Kelly, 1980),

$$\delta\theta_{mcs}(Z,A) \approx \frac{1}{\sqrt{3}}\,\frac{20}{\beta^2\gamma m_u c^2}\,\frac{Z}{A}\left[\frac{X}{X_R}\right]^{1/2}, \tag{2.43}$$

where X_R is the radiation length of the material and $m_u = 931.5\ \mathrm{MeV/c^2}$ is the mass per atomic mass unit. The pathlength between the end of the aerogel and the end of layer 1 at $\theta = 30^\circ$ is equivalent to $X = 10.2\ \mathrm{g/cm^2}$ of NaI(Tl) with radiation length $X_R = 9.49\ \mathrm{g/cm^2}$. Thus for an ^{56}Fe nucleus at the aerogel Cerenkov threshold with $\theta = 30^\circ$, the multiple scattering angle is $\delta\theta_{mcs}(Z,A) \approx 0.0030$ radians.

From Equation (2.42), we find that the response ratio $\Omega = C/S$ is more properly given by

$$\Omega \equiv \frac{C}{S} = \frac{N_\mu}{\alpha_S}\,\frac{(\,f(\gamma) + k(\gamma) + b\,)}{s(Z,\gamma)}\,(\,1 - \tan\theta_C\,\delta\theta_{mcs}(Z,A)\,)\,. \tag{2.44}$$

Thus the contribution to velocity resolution from multiple scattering between the

aerogel and layer 1 is

$$\frac{\delta\Delta\gamma_{mcs}}{\Delta\gamma} = \frac{1}{\Delta\gamma}\frac{\partial\gamma}{\partial\Omega}\frac{\partial\Omega}{\partial\delta\theta}\,\delta\theta_{mcs}(Z,A) \tag{2.45}$$

$$= \frac{1}{\Delta\gamma}\,\frac{f(\gamma)+k(\gamma)+b}{f'(\gamma)+k'(\gamma)-\frac{s'(Z,\gamma)}{s(Z,\gamma)}\,[f(\gamma)+k(\gamma)+b]}\,\tan\theta_C\,\delta\theta_{mcs}(Z,A)$$

$$\sim \frac{1}{2}\,\frac{\gamma+1}{\gamma}\,[\gamma^2(n^2-1)-n^2]\,\tan\theta_C\,\delta\theta_{mcs}(Z,A)\,. \tag{2.47}$$

Note that the rms scattering angle is proportional to Z/A, and that therefore the mass uncertainty is proportional to Z. For all possible particle trajectories, this contributes <0.1 amu to the mass uncertainty and is negligible.

2.3.1.5. Index Variation

Fluctuations in the index of refraction of the aerogel blocks on distance scales of centimeters will masquerade as variations in the light-collection efficiency and will be included in the response maps generated from the accelerator calibration. Small-scale fluctuations, however, will not be mapped and will contribute to the variation in the Cerenkov response.

An rms variation δn in the index of refraction of a group of three stacked aerogel blocks generates an uncertainty in $\Delta\gamma$ given by

$$\frac{\delta\Delta\gamma_n}{\Delta\gamma} = \frac{1}{\Delta\gamma}\frac{\partial\gamma}{\partial\Omega}\frac{\partial\Omega}{\partial n}\,\delta n \tag{2.48}$$

$$= \frac{1}{\Delta\gamma}\,\frac{2n/(n^2-1)}{f'(\gamma)+k'(\gamma)-\frac{s'(Z,\gamma)}{s(Z,\gamma)}\,[f(\gamma)+k(\gamma)+b]}\,\delta n \tag{2.49}$$

$$\sim \frac{(\gamma+1)\,n}{\gamma\,(n^2-1)}\,\delta n\,. \tag{2.50}$$

Note that this is only weakly dependent on γ. From the estimated residual variation in index of 4.7×10^{-4} (see §3.6.2), we calculate that the contribution to Cerenkov-Energy

mass resolution is typically ≈ 0.2 amu. This is a significant source of mass error; indeed, near the Cerenkov threshold, this is the largest contribution.

Note also that because the velocity resolution is independent of Z, the mass resolution δA_n is proportional to mass A, and therefore would be significantly smaller for low-mass nuclides.

2.3.1.6. Mapping Errors or Light-Collection Uniformity Variations

Mapping errors, i.e., systematic differences between the observed response and the map value over length scales on the order of centimeters, are a source of velocity uncertainty, as are variations in the light-collection efficiency on small length scales that cannot be corrected in the response maps. Note also that variations in radiator thickness are indistinguishable from efficiency variations, although they are negligible in the aerogel radiator because of the precision of the machining of the blocks. Mapping errors and light-collection variations have the effect of changing the number of photoelectrons expected at a given position and therefore contribute to uncertainty in $\Delta\gamma$ in the following manner,

$$\frac{\delta\Delta\gamma_u}{\Delta\gamma} = \frac{1}{\Delta\gamma}\frac{\partial\gamma}{\partial\Omega}\frac{\partial\Omega}{\partial N_\mu}\delta N_\mu \tag{2.51}$$

$$= \frac{1}{\Delta\gamma}\frac{f(\gamma)+k(\gamma)+b}{f'(\gamma)+k'(\gamma)-\frac{s'(Z,\gamma)}{s(Z,\gamma)}[f(\gamma)+k(\gamma)+b]}\frac{\delta N_\mu}{N_\mu} \tag{2.52}$$

$$\sim \frac{1}{2}\frac{\gamma+1}{\gamma}[\gamma^2(n^2-1)-n^2]\frac{\delta N_\mu}{N_\mu}\,. \tag{2.53}$$

Note that this is also independent of Z and is therefore less significant for low-mass nuclides. The mapping error in the aerogel counter is estimated to be $\sim$1.1% at the time of the accelerator calibration and $\sim$2.3% at the time of the flight (see §3.6.2). The magnitude of this contribution at flight is shown in Figure 2.6. It is clear that the aerogel response maps significantly limit the resolution for Fe.

Small and slowly varying gradients in the response from the radiator would greatly facilitate the mapping. Such gradients would be expected from larger radiators.

2.3.1.7. Aerogel Block Response Normalization

In order to calculate velocities from the response in the aerogel counter, we must normalize the Cerenkov formula to the measured response at a known energy. Uncertainty in the measured response is equivalent to uncertainty in the expected number of photoelectrons N_μ from an aerogel block, and therefore the contribution to velocity resolution has the same functional dependence as the light-collection variations,

$$\frac{\delta\Delta\gamma_{\rm norm}}{\Delta\gamma} = \frac{1}{\Delta\gamma}\frac{\partial\gamma}{\partial\Omega}\frac{\partial\Omega}{\partial N_\mu}\delta N_\mu \,. \tag{2.54}$$

The precision to which the blocks can be normalized with the accelerator calibration data is high since the beam energy is known; however, the normalization was lost as the response of the blocks degraded with time (see §3.6.3). The normalization was re-established for the flight data with high-energy Fe-group events to an estimated accuracy of $\sim$1.5% (§3.6.4), and therefore contributes to the mass resolution with the magnitude depicted in Figure 2.6.

Uncertainty in the block normalization is therefore the third largest contributor to mass uncertainty. This is rather unfortunate, since the accelerator calibration should have established the normalization once and for all.

2.3.1.8. Background Light Level

The background light level, $B \equiv Z^2 N_\mu \sec\theta\, b$, in the aerogel counter must also be properly normalized, and again the precise normalization from the accelerator calibration was lost as the response of the blocks degraded. Fe-group events with velocities below the aerogel Cerenkov threshold were used to re-establish the background normalization, with an estimated precision of $\sim$5%. Because $b \sim 0.04$, the uncertainty is $\delta b \sim 0.002$.

$$\frac{\delta\Delta\gamma_b}{\Delta\gamma} = \frac{1}{\Delta\gamma}\frac{\partial\gamma}{\partial\Omega}\frac{\partial\Omega}{\partial B}\delta B \tag{2.55}$$

$$= \frac{1}{\Delta\gamma} \frac{1}{f'(\gamma) + k'(\gamma) - \frac{s'(Z,\gamma)}{s(Z,\gamma)} [f(\gamma) + k(\gamma) + b]} \delta b \tag{2.56}$$

$$\sim \frac{(n^2-1)(\gamma^2-1)^2}{2\gamma(\gamma-1)} \delta b \, . \tag{2.57}$$

The contribution to mass uncertainty is shown in Figure 2.6 and is relatively small, typically $\sim$0.1 amu.

2.3.1.9. Particle Position Uncertainty in the Aerogel

The positions of Fe events in the aerogel, generated by extrapolation from the measured positions in the NaI(Tl) stack, are estimated to be uncertain by $\hat{\sigma}_x \sim 0.6$ cm (see §3.2.3). We have estimated the effect of the position uncertainty on the calculated values of γ for the final Fe events (selected in §4.4) by allowing their positions in the aerogel to be normally distributed about the extrapolated positions with the estimated resolution. We find

$$\frac{\delta\Delta\gamma_{pos}}{\Delta\gamma} \approx 0.13\% \tag{2.58}$$

or $<$0.1 amu. Thus the position uncertainty in the aerogel has only a small effect on mass resolution.

2.3.2. Contributions to Total Energy Resolution

2.3.2.1. NaI(Tl) Photoelectron Statistical Fluctuations

Statistical fluctuations in the number of photoelectrons collected in the NaI(Tl) stack make a small contribution to the resolution of the total energy measurement. The expected number of photoelectrons can be estimated from the total number of photons generated in the stack and from the collection efficiencies:

$$N_{pe} = \Delta E \frac{dL}{dE} \epsilon_{geom} \epsilon_K \, , \tag{2.59}$$

where the total energy loss in the stack for a typical ^{56}Fe nucleus is ~95 GeV; the average NaI(Tl) scintillation efficiency $<h\nu>$ dL/dE for Fe is ~10%; the scintillation photons have average energy $<h\nu> \sim 3$ eV; the geometric light-collection efficiency ϵ_{geom} from a ray-tracing optical model of a single NaI(Tl) layer (see §3.3 and Buffington *et al.*, 1981) is ~1%; and the photocathode efficiency ϵ_K is typically ~15%. Thus the expected number of photoelectrons collected in the stack is ~5×10^6, which corresponds to a statistical uncertainty in total energy loss of

$$\frac{\delta\Delta E_{pe}}{\Delta E} \sim 0.05\% \tag{2.60}$$

or ~0.03 amu, which is negligibly small.

2.3.2.2. Particle Position Uncertainty in the NaI(Tl)

The uncertainty in particle positions in the stack affects the calculated total energies. As with the calculation of the effect of the position uncertainties in the aerogel, we allowed the positions of the selected Fe events to be normally distributed about the measured positions with their estimated resolution and found

$$\frac{\delta\Delta E_{pos}}{\Delta E} \approx 0.25\% , \tag{2.61}$$

which corresponds to ~0.14 amu in the Cerenkov-Energy technique.

2.3.2.3. Mapping Uncertainty

In §3.3.2 we estimate for the accelerator calibration data that the uncertainty in the measured energy loss in a single NaI(Tl) layer that is not the result of Landau fluctuations, photoelectron statistical fluctuations, or position uncertainty is ~0.45%. We ascribe this residual energy-loss uncertainty to errors in the stack light-collection efficiency maps and in the algorithm used to determine the energy loss (see §3.3), and we assume that the uncertainty is uncorrelated from layer to layer. Thus we estimate that the uncertainty in the total energy deposition resulting from mapping errors is

$$\frac{\delta\Delta E_{map}}{\Delta E} \approx \frac{0.45\%}{\sqrt{N_L}} , \tag{2.62}$$

where N_L is the number of stack layers traversed by the particle. The typical contribution to mass resolution is therefore ~0.08 amu, as shown in Figure 2.6.

2.3.3. Summary of Contributions to Mass Resolution

The total contribution to mass resolution from the total energy measurement in the NaI(Tl), including the instrumental sources discussed in §2.3, is <0.2 amu. This is sufficiently small.

However, the velocity resolution from the aerogel counter is inadequate. This is primarily the result of (1) the degradation of the aerogel response (§3.6.3), which increased the contribution from photoelectron statistical fluctuations by ~40% and created the need for a normalization of the Cerenkov response from the flight data, and (2) the significant stochastic variation in the index of refraction of the aerogel blocks.

Finally, we note that we have attempted to present a comprehensive list of the contributions to velocity resolution, as frequently many of these sources are ignored. In particular, the contributions from index variations, light-collection variations, and Cerenkov response normalization—all of which are independent of charge, and therefore create a mass uncertainty proportional to A—may explain the often-claimed result that the velocity resolution of Cerenkov counters fails to improve linearly with Z.

Chapter 3
Basic Methods and Algorithms

3.1. Bevalac Calibration

The position and energy algorithms discussed below were developed primarily from a calibration of the full HEIST detector system at the Lawrence Berkeley Laboratory Bevalac in November 1982. The beam was ^{55}Mn at a nominal energy of 1752 MeV/amu. In the absence of fragmentation reactions, such ions traversed most of the NaI(Tl) stack, stopping in layer 11 or layer 12. Approximately 900,000 events were recorded over ~95% of the area of the detectors. An auxiliary pair of multiwire proportional chambers, each providing both x and y coordinates with 0.15 cm wire spacing, were placed upstream of the instrument to give particle trajectories. The top plastic scintillator, the aerogel Cerenkov counter, and the first 10 NaI(Tl) stack layers were mapped using positions obtained from these trajectories. The single, brief run with the beam entering the instrument from the rear was statistically insufficient to map the remaining detector elements—the bottom scintillator, the bottom Cerenkov counter, and the final two stack layers. Maps of layers 11 and 12 were generated from a flight data set consisting primarily of particles that penetrated the stack without interacting, allowing the full range of stopping particles to be analyzed. Although a similar technique could be used in the bottom Cerenkov counter and plastic scintillator, these counters have not been mapped.

Additional runs centered in a single stack of three aerogel blocks were made with absorbing materials upstream to degrade the beam energy and generate lower-Z fragments. Table 3.1 lists the run name, the type of absorber, the thickness of the absorber in g/cm^2, the nominal energy of the beam as it exited the absorber in GeV/amu, and the number of events of all charges that exited the absorber. The absorbers employed were lead sheets, each 6% antimony by weight and 0.21 cm (2.3 g/cm^2) thick. The

polyethylene absorber was a single block of unknown purity.

Table 3.1 Bevalac Upstream Material Runs

Run	Absorber	Thickness (g/cm^2)	Energy (MeV/nuc)	Events
	none	0.0	1752	~900000
CH2	polyethylene	4.67	1635	27407
6PB	6 sheets Pb	13.8	1562	5134
12PB	12 sheets Pb	27.6	1371	823

The absorber thickness for the run 12PB was chosen to give an energy below the Cerenkov threshold in the aerogel. These runs were used to study the velocity dependence of the aerogel Cerenkov response and resolution (see §3.7), and to test the algorithms that measure particle mass (see §3.8).

The calibration data suffered from two related systematic effects which complicated their use. Individual photomultiplier gains varied both with event number into each Bevalac beam spill and with time into the beam run. The magnitude of each effect is typically on the order of a few percent. Figures 3.1(a) and 3.1(b) show the "spill-gain" and "run-gain" variations for a particular photomultiplier. Note that we have chosen a photomultiplier with a larger than average variation to make the effect more apparent in the figures.

The source of both variations remains unknown. In particular, high-voltage variations in the photomultiplier bases appear to have been ruled out: The anode and final three dynode voltages were monitored during the calibration and found to be constant to 0.1 volt, which should have assured gains constant to ~0.1% in these 10-stage photomultipliers. Some 9% of the total light yield of NaI(Tl) results from a phosphorescence with a decay time of ~0.15 seconds (McKlveen, 1975); however, this is also not likely to be the source of the variation as the magnitude of the effect differed among the six photomultipliers viewing each crystal. The photomultipliers that view the plastic scintillator—which are identical to those in the NaI(Tl) stack—showed an effect of

similar magnitude, while no variation was seen in the 5-inch photomultipliers of the Cerenkov counters. The spill-gain variation appeared to have a similar shape for all photomultipliers in all runs, and we were able to fit a combination of exponentially damped sinusoidal functions to this variation. Since each photomultiplier showed an effect of different magnitude and in some cases an opposite sign, we assigned each a single multiplicative coefficient, the "spill-gain amplitude." The estimated residual spill-gain variation is $\sim$0.2%.

The run-gain variation was discovered after the detector maps described below were produced, and therefore no correction for this effect was applied. The magnitude of the discontinuities observed in the gains of individual photomultipliers is strongly correlated with the spill-gain amplitude, which suggests that the two effects have a similar origin. The uncorrected run-gain variation may contribute to the energy-loss resolution for the calibration data, as discussed in §3.3.1.

3.2. Position Algorithm

Position information is necessary in the HEIST instrument as a means of correcting for the variation of detector response with position and, in certain circumstances, of correcting for pathlength differences in the detectors with the angle of incidence. Particle positions are measured directly in the NaI(Tl) stack using a technique, first used by Arens (1974), which relies on the principle that the scintillation light is collected unequally among the photomultipliers viewing a detector to a degree that depends on the position at which the light is generated.

The amount of scintillation light collected by a photomultiplier is a function of both the amount of light generated in the scintillator and the position at which it is generated; however, the ratio of responses of photomultipliers viewing the same scintillator depends only on the position. For a large fraction of the area of the HEIST scintillator disks, we have found that the ratio R of the response of opposite photomultipliers varies approximately by a fixed percentage for a unit change in position along the axis bisecting the photomultipliers. Thus the logarithm of the ratio forms a linear relationship with position for that area. Lau (1985) measured the position resolution for muons and accelerator beams of C, Ne, and Mn. He measured the rms deviation about

Figure 3.1(a)

Spill-gain variation for photomultiplier C of NaI(Tl) layer 4. The photomultiplier response is shown as a function of event number in the beam spill. Each point represents a single event, and each spill contains nominally 180 events. We have corrected for this variation with a combination of exponentially damped sinusoids.

Figure 3.1(b)

Run-gain variation for photomultiplier C of NaI(Tl) layer 4. The photomultiplier response is shown as a function of spill number in the beam run. Each point represents a single event. The data file contains only events that stop in the NaI(Tl) without suffering a charge-changing interaction. The spill-gain variation has been corrected for.

Figure 3.1(a)

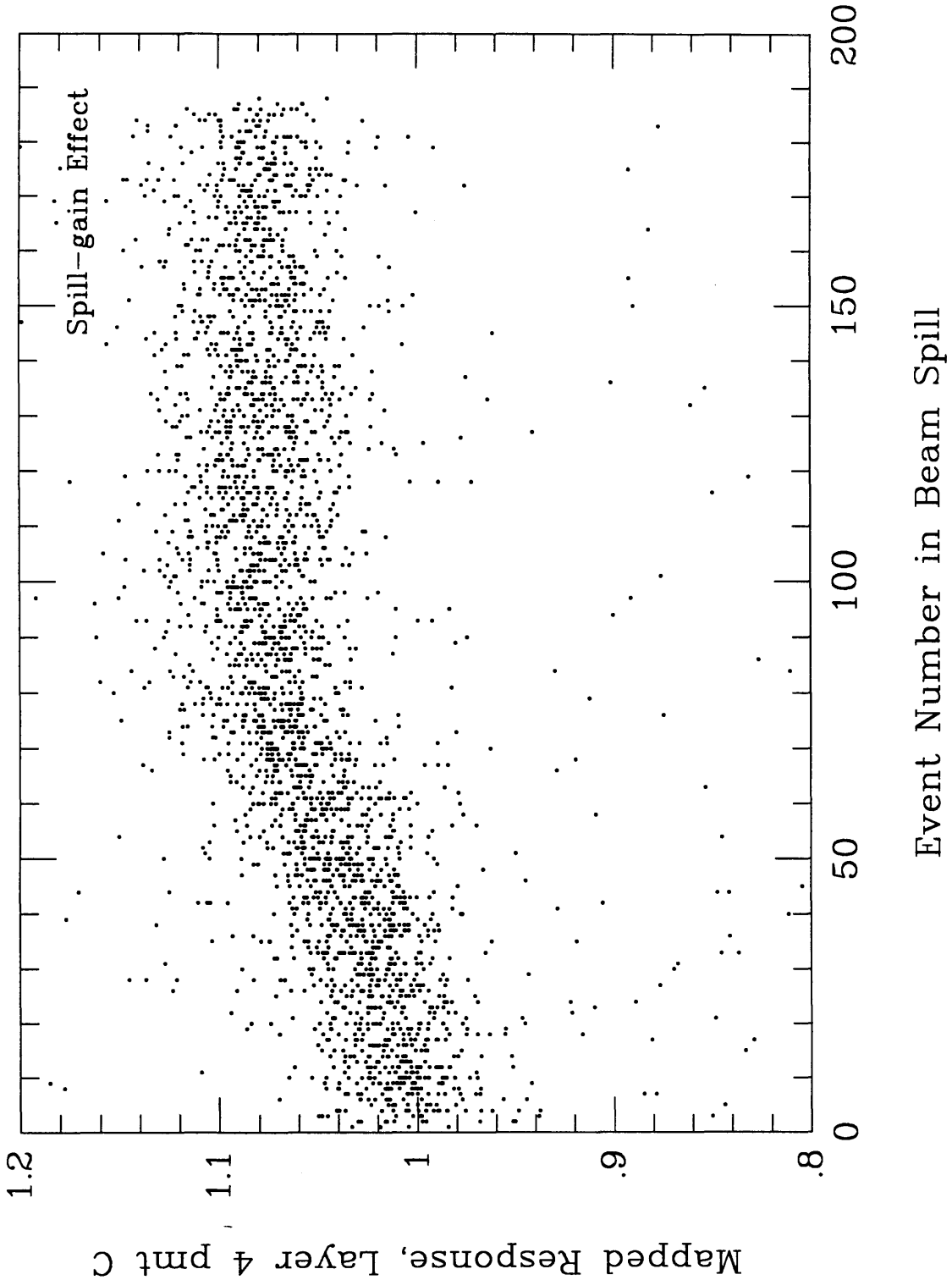
Spill-gain Effect
Mapped Response, Layer 4 pmt C
Event Number in Beam Spill
1.2
1.1
1
.9
.8
0
50
100
150
200

Figure 3.1(b)

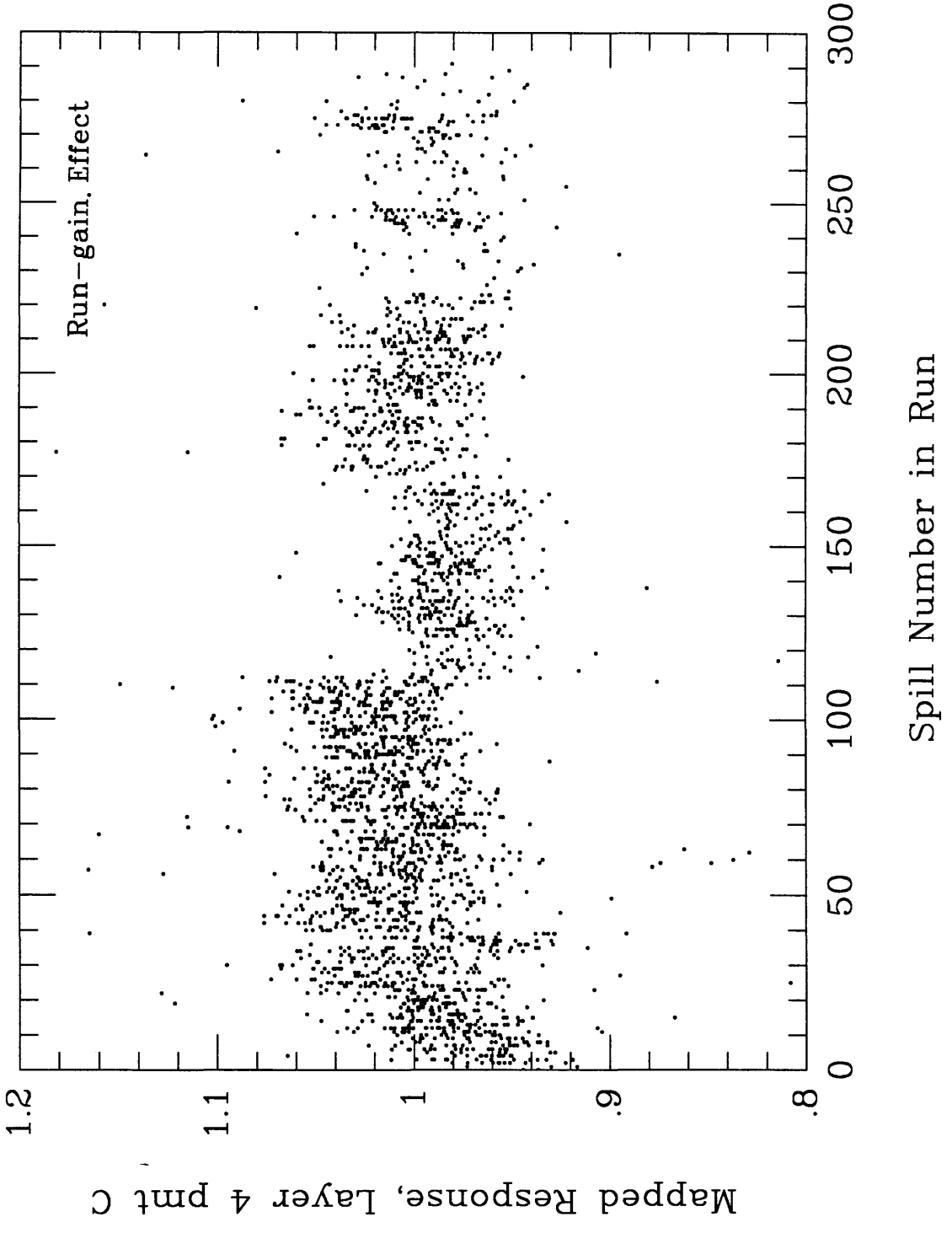
Run-gain Effect
Mapped Response, Layer 4 pmt C
Spill Number in Run
1.2
1.1
1
.9
.8
0
50
100
150
200
250
300

this logarithmic trend for particles near the center of a stack layer and subtracted calculated contributions from the intrinsic wire-chamber resolution and from multiple Coulomb scattering between the wire chambers and the layer. Comparing the results for muons, C, and Ne, he found that the resolution improved linearly with charge Z up to at least $Z = 10$, as one would expect if the resolution were dominated by photoelectron statistics. However, after accounting for the effects of the saturation of the scintillation yield, this scaling broke down for Mn, indicating that systematic effects were beginning to dominate the resolution. He measured a single component of the resolution to be $\sigma_x = 0.17$ cm for Mn over limited regions of the NaI(Tl) disks, before accounting for the wire-chamber and multiple-scattering effects.

Unfortunately, this simple relationship between position and ratio breaks down for the outer third of the area of the disk, and Lau's algorithm fails to provide accurate positions. We have therefore replaced his algorithm with a more general one. Recall that each NaI(Tl) layer is viewed by six photomultipliers. Figure 3.2 shows a contour plot of the map of the logarithm of the ratio of the sum of three adjacent tubes to the sum of the three opposite tubes, where each contour represents a change of 0.15 in the logarithm, or ~15% in the ratio. Both the center region, which is linear in the logarithm of the ratio, and the outer region, where this relation fails, are apparent. Note that one can form three such ratios of sums of adjacent tubes in each layer, and each will have a preferred axis of linearity rotated 60° from the next. It is also apparent that position information is available in the non-linear regions as well: indeed, any region with an appreciable gradient that is smoothly varying will provide useful position information. We have developed an algorithm that employs this fact. We form a quantity d^2 that is a measure of the difference between an observed set of logarithms of ratios and any point on the maps of those logarithms:

$$d^2 = \sum_i (\log R_i - \log M_i)^2 , \tag{3.1}$$

where $\log R_i$ and $\log M_i$ are the observed and mapped values of the logarithm of ratio i of photomultipliers. The position selected is then the one that minimizes the difference. Note that d^2 is minimized when

$$\nabla d^2 = -2 \sum_i (\log R_i - \log M_i) \nabla M_i = 0 , \tag{3.2}$$

where the weighting factor ∇M_i in the sum is the gradient of the mapped logarithm. Thus in calculating positions by minimizing d^2, we are applying a weighting factor to each logarithm equal to its gradient, so that more emphasis is placed on those ratios with steeper gradients, and therefore greater sensitivity to position. A flow chart and detailed description of the minimization procedure appear in Appendix B.

We have found that the position resolution is much improved if, in addition to the sum-of-three versus opposite sum-of-three maps discussed above, we use three maps of the logarithms of the ratios of pairs of photomultipliers that are nearest neighbors, since the sensitive regions of the latter maps complement those of the former. Table 3.2 lists the mapped ratios employed in the top scintillator and the stack, where the letters A through F correspond to the six photomultipliers on a layer. Note that each photomultiplier is used the same total number of times in the ratios, and therefore makes an equal contribution to the position determination. Note also that positions were not calculated in layer 3, because one of the photomultipliers failed shortly after the NaI(Tl) stack was assembled in its hermetic can. Figure 3.3 shows a contour plot of one of the nearest-neighbor maps in layer 1, with the contours spaced at intervals of 0.30 in the logarithm.

Table 3.2: Photomultiplier Ratios for Position Algorithm

Layer	Ratios
S_1, L_1–L_{10} excluding L_3	(A+B+C)/(D+E+F) (B+C+D)/(E+F+A) (C+D+E)/(F+A+B) A/B, C/D, E/F

Because the ratios B/C, D/E, and F/A have not been used, there does exist some bias in the representation of certain areas of the NaI(Tl) layers: The regions between these photomultipliers are not treated in the same way as the regions between the other

Figure 3.2

Contour plot of the logarithm of the ratio of the sum of three adjacent photomultipliers to the sum of the opposite three photomultipliers, log[(A+B+C)/(D+E+F)]. Contours are spaced at 0.15 in the logarithm. The filled diamonds mark the contour with a ratio of unity. Elsewhere, the contours cycle through the following three symbols: open circle, filled circle, and plus sign. The use of three symbols allows the unambiguous interpretation of the slope.

Figure 3.2

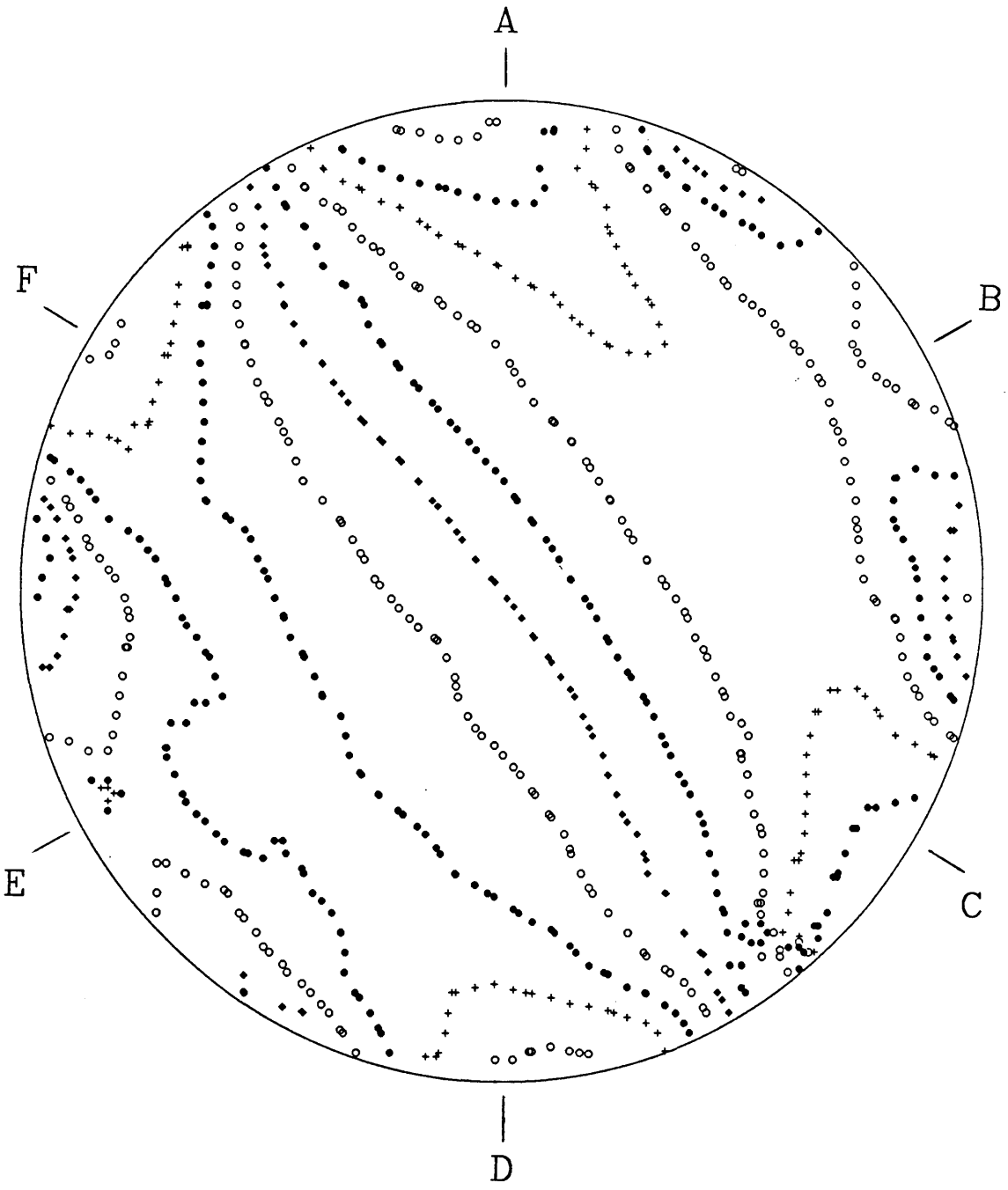

Figure 3.3

Contour plot of the logarithm of a ratio of adjacent photomultipliers, log[F/A]. Contours are spaced at 0.30 in the logarithm. The filled diamonds mark the contour with a ratio of unity. Elsewhere, the contours cycle through the following three symbols: open circle, filled circle, and plus sign. The use of three symbols allows the unambiguous interpretation of the slope.

Figure 3.3

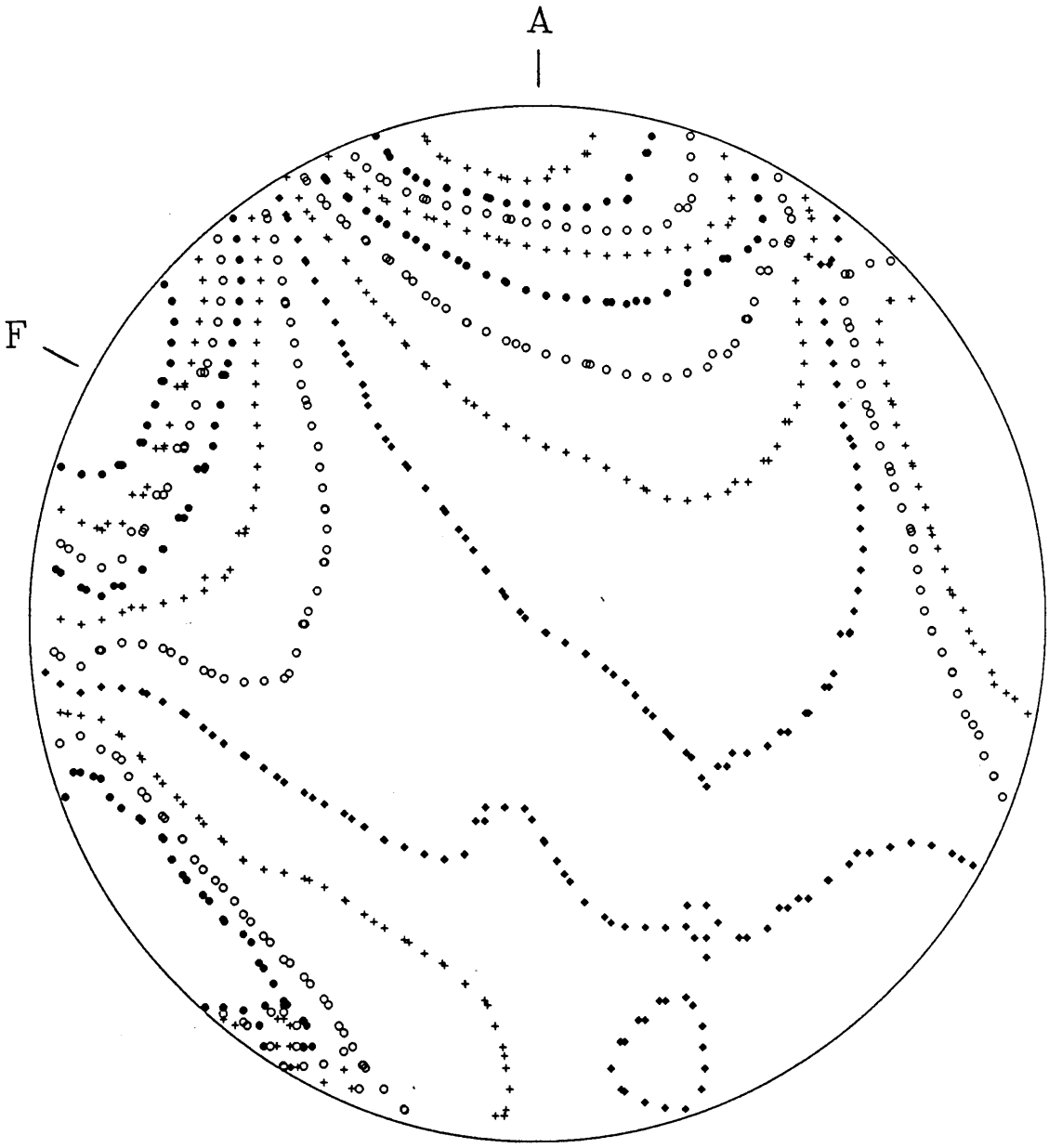

pairs of adjacent tubes. No attempt was made to rectify this problem, because the position algorithm provided sufficiently accurate positions when it was applied to the calibration data.

We have mapped the logarithms of ratios listed in Table 3.2 in the top plastic scintillator and the first 10 layers of the NaI(Tl) stack using the Bevalac data. We chose not to map the final two layers with the Bevalac data, because the variation in response increases near the end of range because of range straggling and the finite energy dispersion of the beam. Although our use of the ratio of photomultiplier responses does indeed remove the dependence on the charge of the beam particle, we chose to map with only non-interacting Mn to remove any bias in the distribution of pulse heights among the photomultipliers which might be caused by the daughters which accompany interacting particles. Mn events in a given layer were selected by windowing on the response in the following layer, and were assigned to 1 cm^2 bins according to the trajectories provided by the external wire chambers. Each bin of a map contains the average of the logarithm for all events in that bin. Holes in the maps resulting from poor coverage of the NaI(Tl) disks by the Bevalac data were filled by interpolating or extrapolating from averages of neighboring bins. Approximately 5% of the area of the disks had to be filled in this manner.

3.2.1. Bevalac Position Resolution

Figure 3.4 shows a histogram of the difference between a single wire-chamber coordinate and the measured position for Mn in layer 1 in the Bevalac data. The rms resolution in the single coordinate is $\sigma_x \sim 0.17$ cm, which is identical to the value obtained by Lau (1985). The data were selected from a time period showing relatively small run-gain variations. Although the data are from a limited region of a single layer, they are indicative of the resolution obtainable throughout the NaI(Tl) in such time periods. No evidence of degradation of the resolution is observed to a radius of 20 cm.

The position uncertainty in layer 1 that is due to multiple Coulomb scattering estimated from Equation (2.40) is negligible. The uncertainty in extrapolating from the pair of wire-chamber positions is ~0.07 cm. We therefore conclude that the position resolution in a single coordinate achievable with this algorithm for Mn in the Bevalac

data is ~0.15 cm.

Without wire chambers to provide absolute positions, the resolution during the flight is not as straightforward to measure, and we will defer the measurement until we have calculated trajectories.

3.2.2. Trajectory Algorithm

The measured positions in the top scintillator and the first 10 stack layers were combined to determine the particle trajectory through the instrument. We determined the trajectory by making an unweighted linear least-squares fit to the measured positions in the top scintillator and the first 10 stack layers, excluding from the fit those layers with a mapped response, calculated at the measured position, less than 70% of the response in layer 1. This cut was intended to eliminate layers after the incident particle had stopped or undergone a significant nuclear interaction in the stack. The factor of 70% unfortunately was high enough that the stopping layer was usually rejected when it need not have been, but the cut was effective in eliminating layers containing only fragments, which in many cases had measured positions that were obviously incorrect. After a first trial fit was made, those layers with measured positions more than 2σ from the trajectory were rejected, and a second fit was made. This procedure was repeated until no layers were rejected. Note that this algorithm on occasion rejected all but one layer. When this occurred, the trajectory was generated from the top scintillator and the first two stack layers by default. Such events usually showed evidence of substantial charge-changing interactions above or at the top of the stack. Note that we have assumed that multiple scattering is negligible or, at the very least, makes an equal contribution in each layer.

3.2.3. Flight Position Resolution

Because the wire chambers are not available in flight to provide reference positions, we must attempt to measure the position resolution from the difference between the positions determined by the algorithm of §3.2 and the positions calculated from the trajectories of §3.2.2.

Figure 3.4

Histogram of the difference between a single coordinate of the wire chamber position and the position measured from the NaI(Tl) for ^{55}Mn from the calibration data in the first stack layer. The position resolution is $\sigma_x = 0.17$ cm.

Figure 3.4

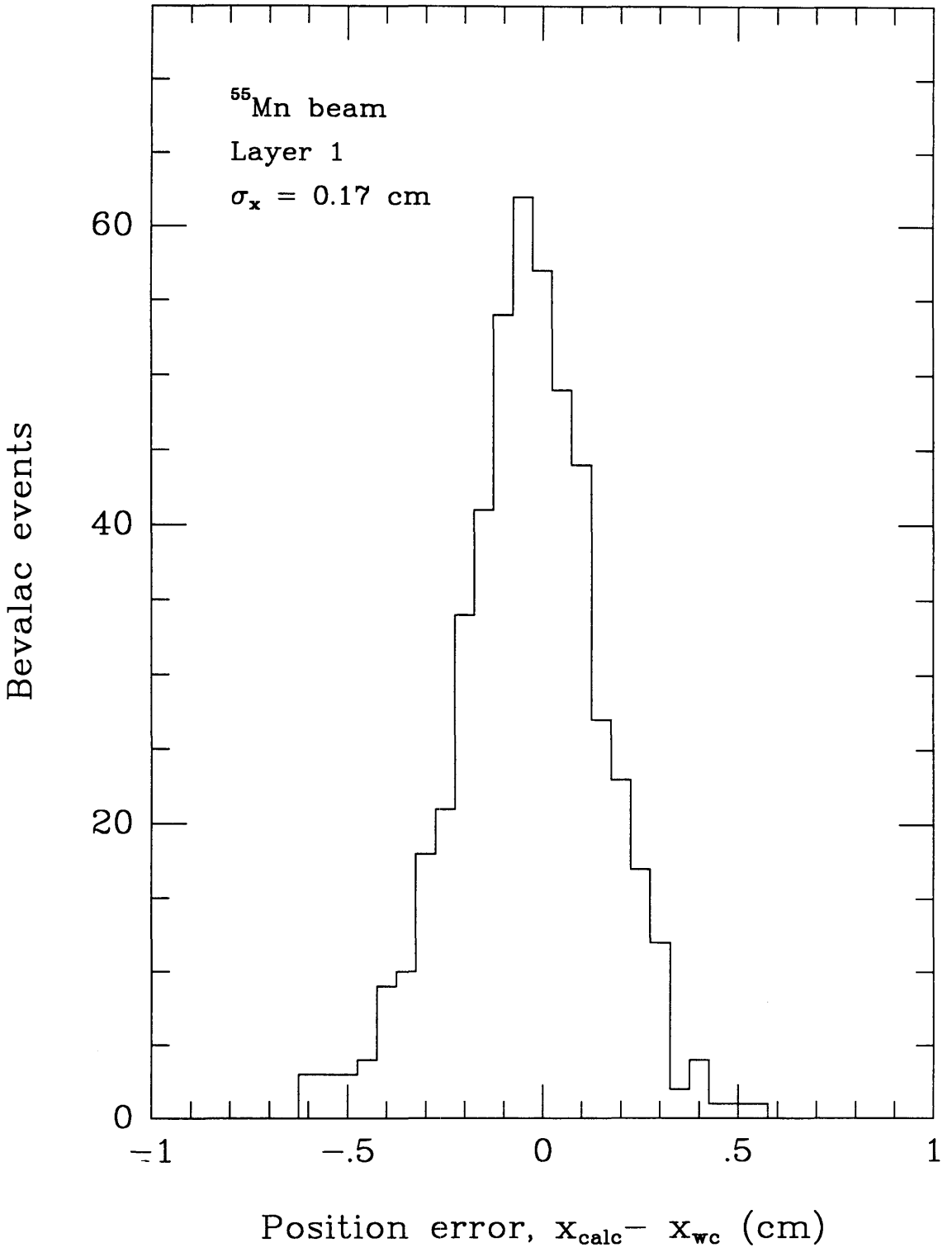
^{55}Mn beam
Layer 1
σ_x = 0.17 cm
Bevalac events
60
40
20
0
−1
−.5
0
.5
1
Position error, $x_{calc} - x_{wc}$ (cm)

We assume that the trajectory gives the true position and that the resolution is identical in each layer. If the position errors are Gaussian and uncorrelated from layer to layer, the sum of the residuals should follow a χ^2 distribution with the number of degrees of freedom equal to the number of coordinates calculated (two per layer) minus the number of parameters in the trajectory fit (four, the two components of the slope and the two coordinates of the offset):

$$\sigma_x^2 \chi^2(\nu) = \sum_i (\vec{r}_i^{\,calc} - \vec{r}_i^{\,traj})^2 , \tag{3.3}$$

where σ_x is a single component of the position resolution, $\vec{r}_i^{\,calc}$ is the position in layer i calculated by the algorithm of §3.2, and $\vec{r}_i^{\,traj}$ is the position in layer i given by the trajectory. The number of degrees of freedom ν is $9\times2-4=14$, because the trajectories used in the figure are formed from the calculated positions in nine layers.

Figure 3.5 shows the distribution of residuals for the Fe events from the flight that penetrate the NaI(Tl) stack without suffering charge-changing interactions. The smooth curve is $\sigma_x^2 \chi^2(14)$ with the position resolution $\sigma_x = 0.47$ cm. This is approximately a factor of three larger than that obtained from the Bevalac data.

Several factors may contribute to the worsening of the resolution for the flight data. For example, small changes in the position dependence of the scintillation yield may have developed between the time of the calibration and the flight. Second, particles collected during the flight are not vertically incident and therefore sample a finite region as they traverse the scintillator, perhaps modifying the distribution of light among the photomultipliers. Finally, statistical and systematic errors in photomultiplier gain corrections (§4.1.1) can result in a bias in the measured response ratios, creating an error in the calculated positions.

If we assume negligible multiple scattering and position resolution σ_x identical in each layer, we can show that the expected trajectory resolution is

$$\sigma_{\sec\theta} = \sqrt{2} \sin\theta \frac{\sigma_x}{\sqrt{\sum z_i^2}} , \tag{3.4}$$

where the z_i are the separations of the layers used in the trajectory measured from the

midpoint of the path through the NaI(Tl). For a typical Fe event (1500 MeV/nucleon, $\theta = 30^\circ$), the trajectory resolution is therefore $\sigma_{\sec\theta} \sim 0.02$, or $\sigma_\theta \sim 0.8^\circ$.

The uncertainty in the position derived from the trajectory at a point in the instrument that is a vertical distance z_p from the midpoint of the path through the stack is given by the error hyperbola (e.g., Yost, 1984),

$$\hat{\sigma}_x(z_p) = \sigma_x \left[\frac{1}{n} + \frac{z_p}{\sum z_i^2} \right]^{1/2}, \tag{3.5}$$

where n is the number of NaI(Tl) layers used in the trajectory. For example, in the aerogel, which has $z_p \approx 20$ cm for typical Fe, the position uncertainty is $\hat{\sigma}_x(\text{aero}) \sim 0.6$ cm. The effect on mass resolution is discussed in §2.3.1.9 and §2.3.2.2.

3.3. Energy Loss Algorithm

The Bevalac calibration also allowed the construction of two-dimensional light-collection efficiency maps of the top plastic scintillator and the first 10 layers of the stack. As in §3.2, we chose not to map the light-collection efficiency in the final two layers with the Bevalac data; however, in this case, these layers were subsequently mapped with flight data. Bevalac events were selected by windowing on Mn in the following layer and assigned to 1 cm^2 bins according to the trajectories provided by the external wire chambers, and the mean pulse height was calculated in each bin separately for each photomultiplier of each layer. Again, approximately 5% of the area of the maps had to be filled in by interpolation or extrapolation from the averages in neighboring bins.

The center plug of the hermetic can cover caused an additional ~100 MeV/amu energy loss above the NaI(Tl) stack, so that the events that passed through the plug stopped ~0.8 layers before the typical beam particles. Because these two classes of events had different ranges in the NaI(Tl), the disparity in energy loss in the layers of the bottom half of the stack was substantial. To correct for this difference, we found the scale factor which, when applied to the sum of the six raw photomultiplier pulse heights for the center plug events for each layer, made the summed signal continuous across the edge of the center plug. The shadow of the center plug was then removed

Figure 3.5

Flight Fe position resolution. The histogram shows the distribution of residuals $\sum (\vec{r}_i^{calc} - \vec{r}_i^{traj})^2$, where $\vec{r}_i^{calc}$ is the position in layer i calculated by the algorithm of §3.2, and $\vec{r}_i^{traj}$ is the position in layer i given by the trajectory, for the Fe events from the flight that penetrate the NaI(Tl) stack without suffering charge-changing interactions. The smooth curve is $\sigma_x^2 \chi^2(14)$ with position resolution $\sigma_x = 0.47$ cm.

Figure 3.5

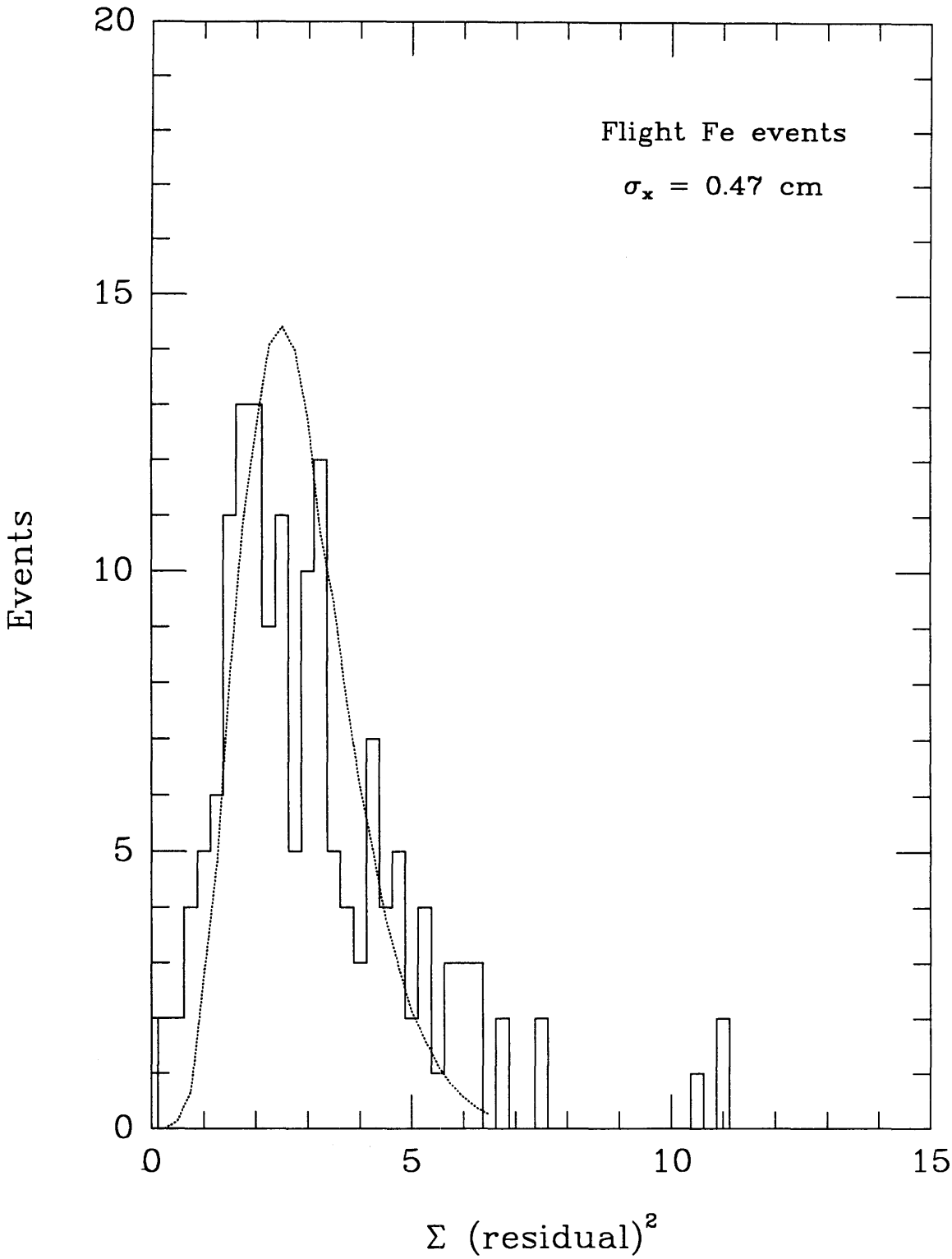
Flight Fe events
σ_x = 0.47 cm
Events
Σ (residual)^2
0
5
10
15
20

from the maps for single photomultipliers by scaling the appropriate bins by this factor.

Figure 3.6(a) shows a contour plot of the map for photomultiplier A of layer 1. The position of the photomultiplier is indicated. Each contour represents a change in light collection of 20% of the value at the center of the disk. We see that the map value varies by a factor of ~7 from its twin minima approximately $\pm 60^\circ$ from the tube around the circumference of the disk to its maximum value directly in front of the tube face. The average single photomultiplier response gradient is ~2.8% cm^{-1}. The relatively flat regions near the response minima we have termed the "blind regions," because a simple ray-tracing optical model of the system of scintillator, light-pipe, and photomultiplier tube face (Buffington *et al.*, 1981) showed a decrease in the number of valid non-attenuated light paths from these areas because of trapping by total internal reflection. The zones of increased efficiency located almost directly across from the tube are the result of reflections off the opposite scintillator-light-pipe interface and are predicted by the optical model. The left-right asymmetry is not well understood but is presumably the result of subtle asymmetries in the optical coupling at the material interfaces. Figure 3.6(b) shows an isometric view of the map of the same photomultiplier. The reflection regions and the blind regions are apparent.

Figure 3.6(c) shows an isometric view of the map of the sum of six photomultipliers. The minimum value of the summed response is ~70% of the value at the center of the disk, and the gradient is less than ~1% cm^{-1} over ~40% of the area of the disk.

To calculate the mapped response ΔL in a layer—which is the estimate of the scintillation light yield—we interpolated from each photomultiplier map at the position given by the calculated trajectory, using the six-point method (Abramowitz and Stegun, 1964, Relation 25.2.67), and applied the interpolated values M_i in the following weighted sum:

$$\Delta L = \sum_i \frac{P_i}{M_i} w_i , \tag{3.6}$$

where

$$w_i = \frac{(P_i/\nabla M_i)}{\sum_k (P_k/\nabla M_k)} . \qquad (3.7)$$

The sums run over all six photomultipliers. P_i is the gain-balanced response of photomultiplier i—that is, the raw ADC output minus its pedestal value and divided by its gain; M_i and ∇M_i are the interpolated map value and map gradient for photomultiplier i. The gradient is calculated directly from differences in adjacent map values. The response/gradient weighting factor w_i emphasizes those regions of the map with large response and small gradient, where interpolation is least susceptible to position errors. This weighting factor was found to give the smallest rms variation in mapped response among several weighting methods tried, including an inverse-gradient weighting.

3.3.1. Bevalac Energy Resolution

Figure 3.7 shows a histogram of the mapped response for Mn from Bevalac data in the first stack layer. Although the data plotted are from a limited region of layer 1 only, they are typical of the full area of the 10 layers mapped using the Bevalac data. The rms resolution calculated from a Gaussian fit to the distribution is $\sigma_{\Delta L}/\Delta L = 1.1\%$. We should compare this result with known contributions to energy resolution.

The ionization energy loss of charged particles is a statistical process because the collisions responsible for this loss are each independent. Thus particles of given energy do not lose the same amount of energy in traversing an absorber of given thickness. For high-Z particles in the thick NaI(Tl) layers, the distribution of energy losses is approximately Gaussian; however, for low-Z particles and thin absorbers, the distribution of energy losses is asymmetric, with a tail corresponding to large energy loss, which is described by the theory of Landau (1944). Note that it is traditional to use the term "Landau fluctuations" primarily in reference to Landau's asymmetric distribution of energy losses; however, we will adopt this term also for the Gaussian distributions. Under the assumption that the slowing-down of the Mn beam is negligible in a single stack layer—which is an appropriate assumption in the first few layers—one can show

Figure 3.6(a)

Contour plot of the response of photomultiplier A of layer 1. The position of the photomultiplier is indicated. Each contour represents a change in light collection of 20% of the value at the center of the disk. The response varies by a factor of ~7 over the disk. The filled diamonds mark the contour with response equal to twice that at the center. Elsewhere, the contours cycle through the following three symbols: open circle, filled circle, and plus sign. The use of three symbols allows the unambiguous interpretation of the slope.

Figure 3.6(b)

Oblique view of the response map for photomultiplier A of layer 1. The vertical scale is linear. The reflection zones across the disk from the photomultiplier are apparent.

Figure 3.6(c)

Oblique view of the response map for the sum of the six photomultipliers viewing layer 1. The vertical scale is linear. The minimum value is ~70% of the value at the center.

Figure 3.6(a)

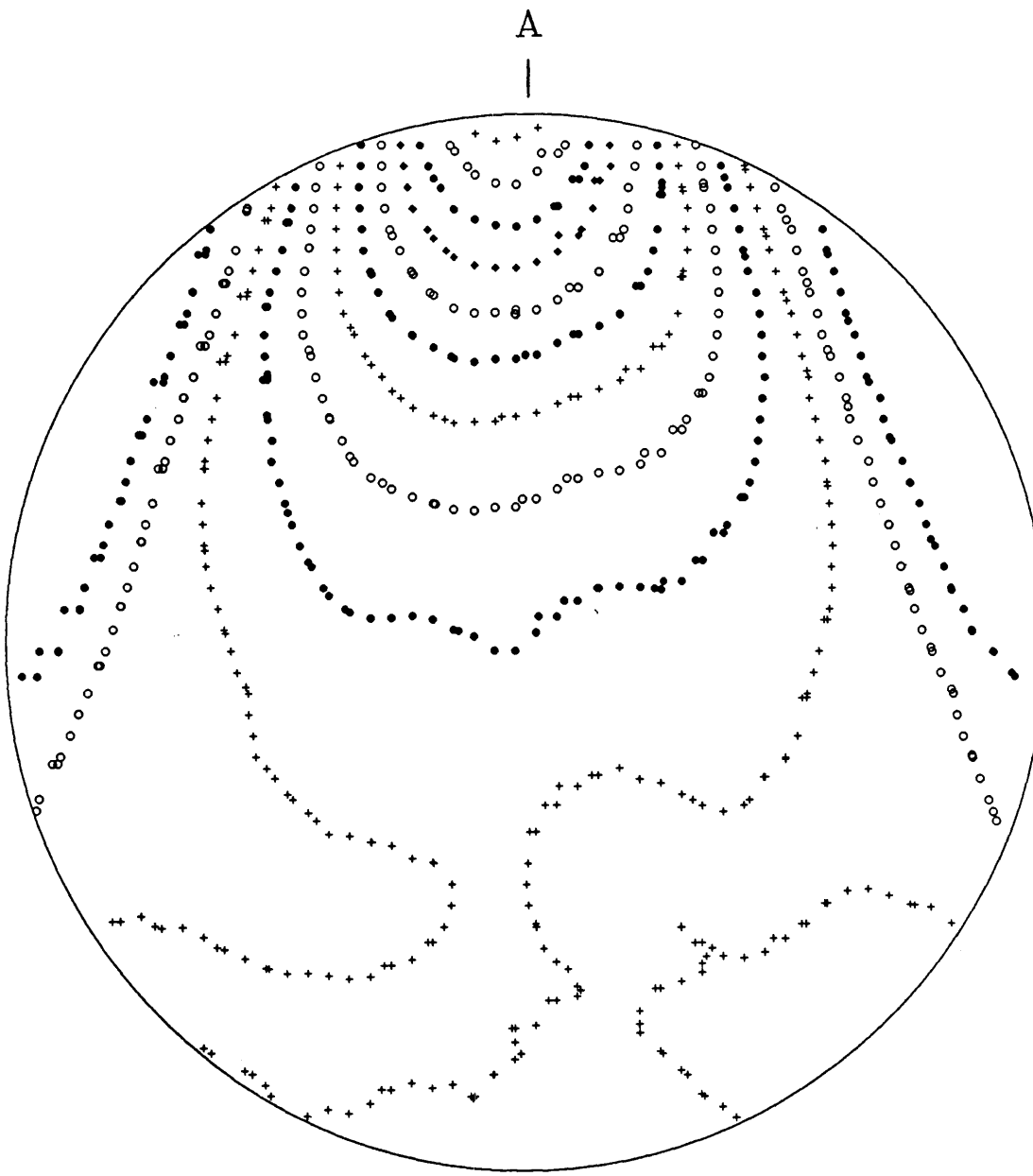

Figure 3.6(b)

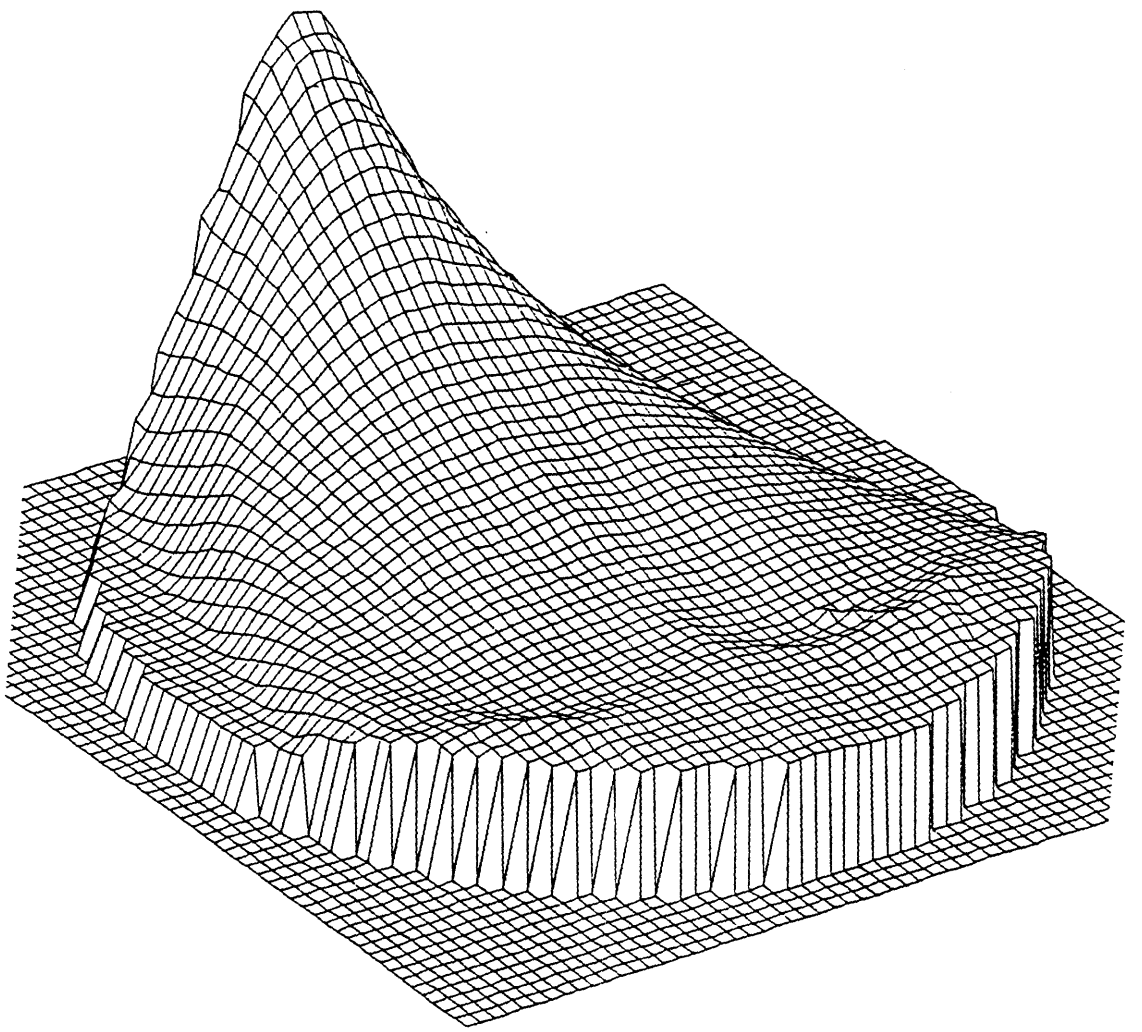

Figure 3.6(c)

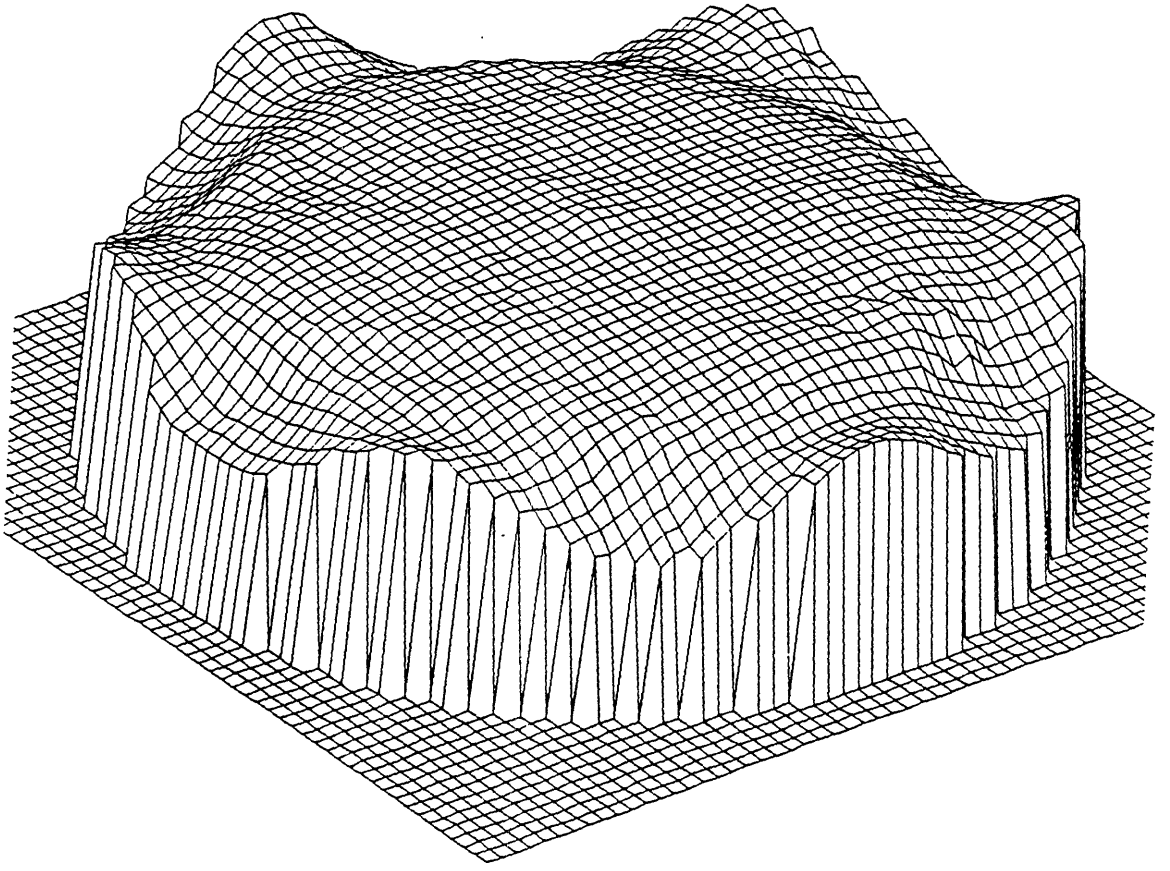

Figure 3.7

Energy loss resolution. The histogram shows the distribution of scintillation yields in layer 1 for the ^{55}Mn beam. The standard deviation, which is a measure of the energy loss resolution, is $\sigma_{\Delta L}/\Delta L = 1.1\%$.

Figure 3.7

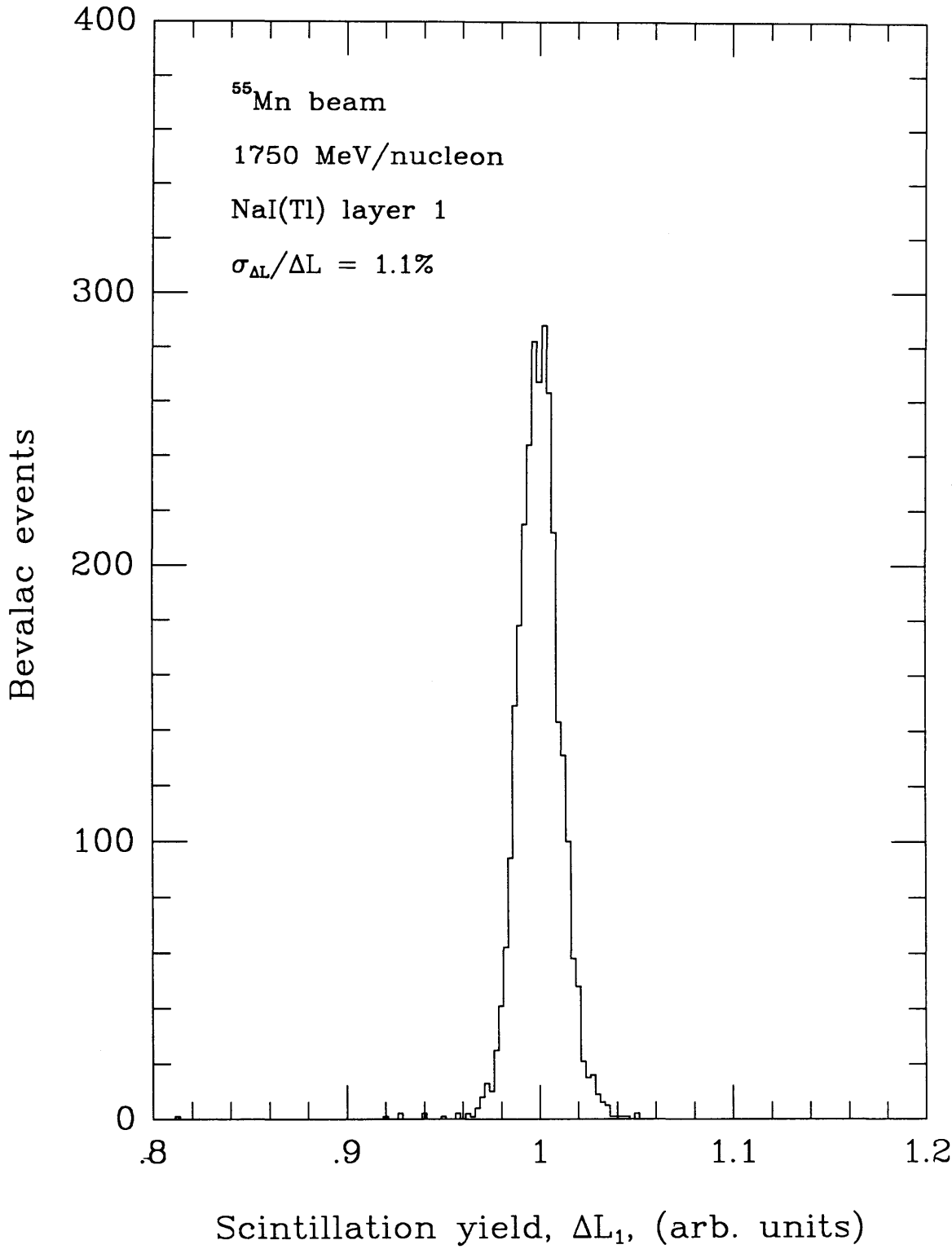
400
300
200
100
0
Bevalac events
^{55}Mn beam
1750 MeV/nucleon
NaI(Tl) layer 1
$\sigma_{\Delta L}/\Delta L$ = 1.1%
.8
.9
1
1.1
1.2
Scintillation yield, ΔL_1, (arb. units)

(Rossi, 1952) that for a beam with charge Z and velocity β, the square of the Landau fluctuation σ_L in energy loss is

$$\sigma_L^2 \approx 0.301\ Z^2\ m_e c^2\ \frac{Z_T}{A_T}\ (\frac{1}{\beta^2} - \frac{1}{2})\ \Delta x\ E'_{max}\ , \tag{3.8}$$

where $E'_{max} = 2m_e c^2 \beta^2 \gamma^2$ is the maximum energy that can be imparted to a knock-on electron, and Z_T and A_T are the charge and mass number of the target material of thickness Δx g/cm^2. From this formula we calculate an rms response variation in layer 1 because of Landau fluctuations of ~0.6%.

Statistical fluctuations in the number of photoelectrons collected in the six photomultipliers viewing each layer also contribute to the observed width. The expected number of photoelectrons can be estimated from the number of photons generated in a NaI(Tl) layer and from the collection efficiencies:

$$N_{pe} = \Delta E\ \frac{dL}{dE}\ \epsilon_{geom}\ \epsilon_K\ , \tag{3.9}$$

where the average energy loss for ^{55}Mn in layer 1 is ~6.1 GeV; the average scintillation efficiency $<h\nu>\ dL/dE$ for ^{55}Mn is ~10%; the scintillation photons have average energy $<h\nu> \sim 3$ eV; the geometric light collection efficiency ϵ_{geom} from the optical model discussed above is ~1%; and the photocathode efficiency ϵ_K is typically ~15%. Thus we expect to collect ~3x10^5 photoelectrons in layer 1, which corresponds to a statistical uncertainty of ~0.2%.

Uncertainty in the wire-chamber positions and multiple scattering contribute to the uncertainty in energy loss through the interpolation from the maps. Following the procedure in §3.2.1, we estimate the position error in layer 1 at the Bevalac from these sources to be ~0.07 cm. To estimate the uncertainty in the mapped scintillation response caused by this position uncertainty, we recalculated ΔL for a set of Bevalac events, fluctuating the positions in a normal distribution about the wire chamber values with an rms deviation of 0.07 cm, and we measured the change in the interpolated map value. The resulting change in mapped response has an rms variation of ~0.1%.

Subtracting the contributions from Landau fluctuations, photoelectron statistics, wire-chamber position uncertainty, and multiple scattering, we find a residual energy

resolution of $\sigma \sim 0.9\%$. A significant fraction of this error can be traced to the spill-gain and file-gain effects. The stack and scintillator maps were made with the functional correction to the spill-gain effect (§3.1), which left an estimated residual spill-gain variation in the mapped responses in a single layer $\sim$0.2%; however, no correction was applied for the run-gain variation, which is estimated to be $\geq$0.6%, leaving an error of as much as $\sim$0.6% unaccounted for.

3.3.2. Flight Energy Resolution

A measurement of the energy resolution during the flight is not as straightforward since a monoenergetic beam of particles at a constant angle of incidence is not available. However, we can estimate the energy resolution from the ratio of mapped responses in adjacent layers under the assumption that the resolution in each layer is equal and that the errors are uncorrelated. The rms variation of the ratio is therefore $\sqrt{2}$ times the resolution in a single layer: $\sigma_{\Delta L_1/\Delta L_2} \approx \sqrt{2}\,\sigma_{\Delta L}$. Figure 3.8 shows a histogram of the ratio of the mapped response in layer 2 to that in layer 1 for a set of Fe-group events selected according to the procedure described in §4.3. The layer-to-layer normalization is a free parameter. The distribution has an rms width of 1.6%, which implies under the above assumption, that the rms energy resolution in layer 1 for elements in the Fe group is $\sim$1.1%, which is unchanged from the calibration results. This agreement is somewhat surprising, as the spill-gain and file-gain variations are presumably not present in the flight data. Apparently the increased position uncertainty in the flight data compensates for their absence. To estimate the contribution to the energy resolution from the position uncertainty in the flight data, we allowed the positions of the selected Fe events to be normally distributed about the measured positions in the stack with the estimated position resolution of $\sigma_x = 0.47$ cm. The change in the interpolated map value had an rms variation of $\sim$0.78%. Subtracting the estimated contributions from Landau fluctuations and photoelectron statistical fluctuations (§3.3.1), we conclude that the residual energy resolution that is unaccounted for in a single layer for the flight Fe data is $\sim$0.45%. We will attribute this residual variation to mapping errors that arise from small changes in the position dependence of the scintillation yield that may have developed between the time of the calibration and the flight.

Figure 3.8

Flight energy loss resolution. The ratio of the mapped response in layers 2 to that in layer 1 is shown for stopping Fe events from the flight. The deduced energy loss resolution is $\sigma_{\Delta L}/\Delta L = 1.1\%$.

Figure 3.8

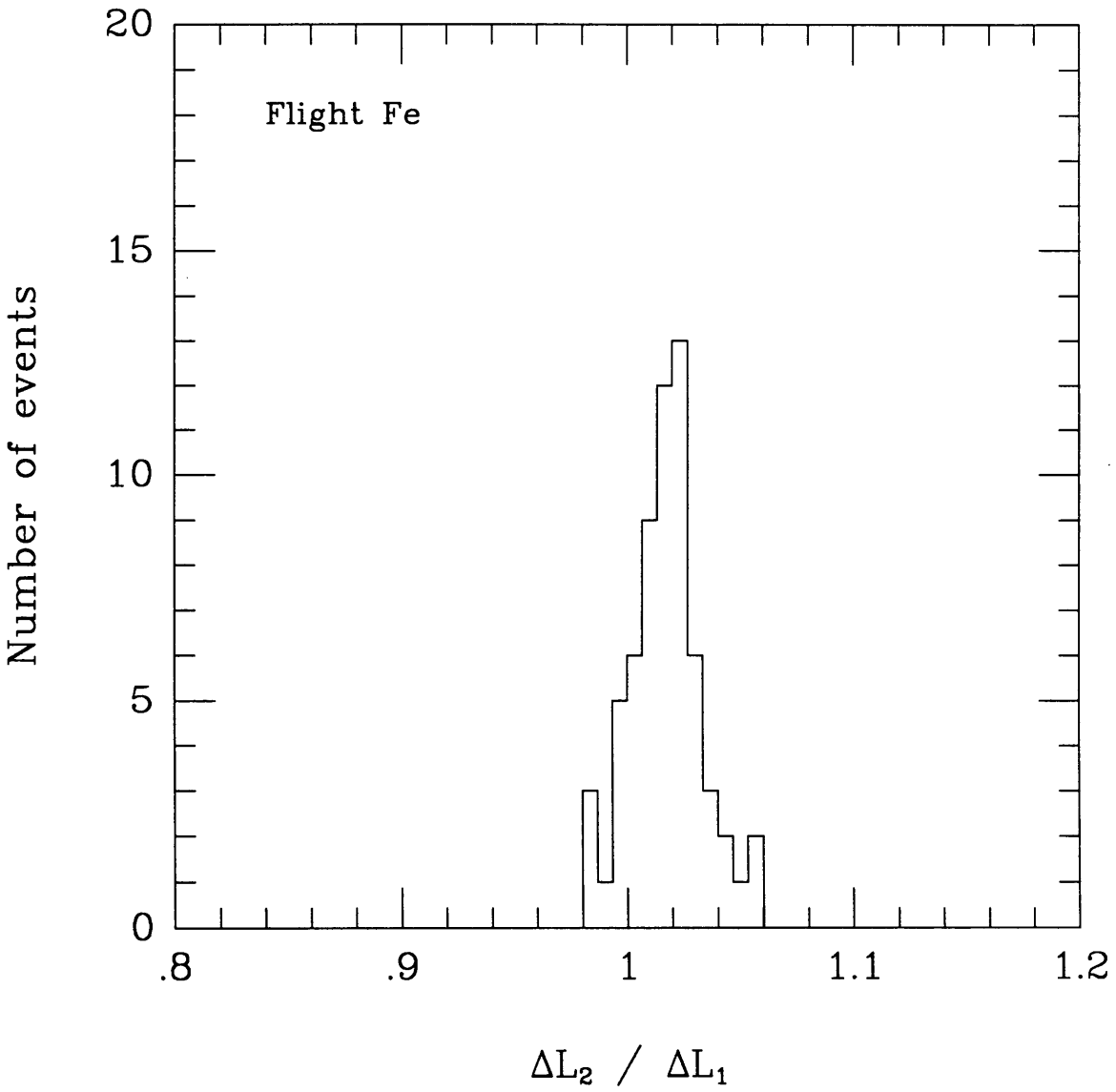

A discussion of combining the mapped responses in the individual layers to measure the total energy loss will be deferred to §3.5.

3.4. Determination of Scintillation Efficiency

The average scintillation efficiency $<dL/dE>$ and correction factors for the energy loss in the Cerenkov radiator and in the light shields that separate the NaI(Tl) stack layers will be used in the calculation of total energy loss described in §3.5. We have chosen to calculate both quantities from model particle trajectories derived by fitting calculated responses to the observed ratio of scintillation yields in the final two layers of a particle's range in the NaI(Tl).

We have developed a kinematics program to simulate the slowing down and stopping of heavy charged particles in the HEIST detector system, using the dE/dx algorithm of Newport, Klarmann, and Waddington described in §2.2.2. The instrument is divided into slabs of thickness $\delta x = 0.05$ g/cm^2. We model each stopping Bevalac event by a ^{55}Mn nucleus and flight event by an ^{56}Fe nucleus at the measured angle of incidence, varying the energy at the top of the instrument until the ratio of the calculated scintillation light yield in the last two layers of the model trajectory equals the observed ratio to sufficient precision. The model light yield in a given layer is

$$\Delta L_{model} = \sum_s \left(\frac{dL}{dE}\right)_s \left(\frac{dE}{dx}\right)_s \delta x_s \,, \tag{3.10}$$

where the sum is over range steps s in the layer. The choice of stepsize $\delta x = 0.05$ g/cm^2 is small enough that we can assume negligible deceleration inside each step.

The average scintillation efficiency for the model particle, therefore, is the mean of the efficiencies calculated in each slab.

This procedure does create a small bias toward ^{55}Mn and ^{56}Fe. To estimate its magnitude, we repeated the fitting under the assumption that each event was ^{54}Fe and found that the average saturation correction decreased by 0.18%. Thus an ^{54}Fe event modeled as ^{56}Fe is assigned a total energy that is ~0.18% too large (see Equation (3.11)), and therefore shows a mass ~0.1 amu too high. This magnitude of bias is

acceptable, given the mass resolution of ~0.65 amu.

3.5. Total Energy Algorithm

Because of the saturation of the NaI(Tl) scintillation light yield, the total energy deposition in the stack is not the sum of the layer responses. To be employed in the mass algorithm, the total energy must contain the total energy deposition in the stack, the energy deposition in the material between the point at which the velocity measurement is made in the aerogel counter and the top of the first stack layer, and the energy deposition in the light shields separating the stack layers. We have used the algorithm described in §3.4 above to make the corrections for scintillation efficiency and the energy loss in the other materials.

We estimate the total energy loss ΔE_{tot} from the following relation,

$$\Delta E_{tot} = \left[\sum_{i=1}^{stop} \Delta L_i \left(1 + \frac{\Delta E_{m(i)}}{\Delta E_i}\right) \right] \frac{\left(1 + \frac{\Delta E_{above}}{\Delta E_{stack}}\right)}{<\frac{dL}{dE}>}, \qquad (3.11)$$

where ΔL_i is the mapped response in layer i (§3.3), ΔE_i is the calculated energy loss in layer i for the model particle, and $\Delta E_{m(i)}$ is the calculated energy loss in the material separating scintillator i from scintillator i-1. In the case of layer 1, $\Delta E_{m(1)} = 0$, since the energy loss in the bottom half of the aerogel, the Cerenkov counter cover, and the hermetic can cover is accounted for in the factor $\Delta E_{above}/\Delta E_{stack}$, where the numerator is the calculated energy loss in the material above the NaI(Tl) stack, and the denominator is that in the NaI(Tl) itself. Thus we have corrected for the other materials by scaling the observed layer responses with the ratio of model energy losses in the scintillator and the other material.

Note that we have applied the saturation correction as an average over the entire range rather than on a layer-by-layer basis. Had we applied the saturation correction to each layer individually, we would have propagated the observed Landau fluctuations from each layer into the total energy measurement. By treating the NaI(Tl) stack as a single unit, we have allowed the fluctuations to enter only through the correction for the material above layer 1 and through the very small correction for the light shields.

3.5.1. Bevalac Total Energy Resolution

Figure 3.9 shows a histogram of total energies calculated by the above procedure for a subset of the ^{55}Mn data collected at the Bevalac. The data were selected from a period with relatively small run-gain variations. The total energy resolution is $\sigma_E/E = 0.73\%$, which corresponds to a contribution to a mass resolution of 0.40 amu for ^{55}Mn. The tail of low energy losses evident in the histogram is the result of neutron-stripping interactions in the instrument. The number of such interactions is consistent with the predicted value (§5.3).

The expected contribution to mass resolution from the total energy measurement can be calculated from the contributions listed in §2.3.2—statistical fluctuations in the number of photoelectrons collected in the NaI(Tl) stack, uncertainty in the particle positions in the stack, and residual mapping errors. Note that the contribution from position uncertainty for the Bevalac data is significantly smaller than the value estimated in §2.3.2.2, because the positions have been calculated from the wire chamber data. Note also that the contribution from mapping errors was evaluated in §2.3.2.3 assuming that the errors were uncorrelated from layer to layer. This assumption may not be valid for the vertically incident Bevalac particles because they sample the same region of the maps in each layer. Neglecting this complication, from §2.3.2 we estimate a lower limit on the resolution of the total energy measurement of $\sim$0.27%, or $\sim$0.15 amu. We presume that correlated mapping errors and residual spill-gain and run-gain variations in the selected data account for the significantly larger value of the observed resolution.

3.6. Velocity Algorithm

Particle velocities are calculated in the aerogel Cerenkov counter by the method discussed in §3.6.1 below. The bottom Cerenkov counter was not employed in this analysis.

The aerogel blocks were produced by the University of Lund, Sweden (Henning and Svensson, 1981) with an index $n = 1.05$ for use in the AFS experiment at the

CERN Intersecting Storage Ring (Henning *et al.*, 1981). They were subsequently recycled and provided to us by I. L. Rasmussen of the Danish Space Research Institute. The index was increased to 1.1 by sintering the blocks at 950 ° C for 80-85 minutes. Some details of the processing and selection of blocks can be found in Rasmussen *et al.* (1983). The average index of refraction can be calculated directly from the density with the following relation (e.g., Poelz, 1986):

$$n - 1 = (0.210 \pm 0.002)\,\rho \tag{3.12}$$

at a wavelength $\lambda = 632.8$ nm with density ρ measured in g/cm^3. This relation appears to hold for indices ranging from 1.01 to 1.25 (Rasmussen, 1989). The average effective index of a particular group of three blocks was measured with the Bevalac data to be $n = 1.0945 \pm 0.001$ (see §3.6.2), in excellent agreement with the average value of 1.0949 ± 0.0010 obtained from the densities of the blocks and Equation (3.12). The uncertainty in the density index is set by the systematic uncertainty in the coefficient in Equation (3.12). This agreement indicates that the effective index of refraction for the Cerenkov emission, which peaks in the near-uv or blue, is equivalent to the index in the orange-red band. Before the blocks were machined, the index was measured near a 90 ° corner of each block by the deflection of a He-Ne laser beam (Rasmussen *et al.*, 1983). The index thus determined is systematically lower than the density index by approximately $\Delta n = 0.005$, as shown in Figure 3.10. Because of the large amount of light scattering, this method unfortunately could not be employed elsewhere in the blocks. Although a few millimeters of the edge material is removed in the final machining, it is possible that some low-index material remains.

3.6.1. Calculation of Lorentz Factor

The response of the each group of three aerogel blocks as a function of position was mapped using the Bevalac data. A fit to the following high-order polynomial was generated for the summed response of twelve photomultipliers,

$$\begin{aligned} M(x,y) = {} & a_0 + a_1x + a_2y + a_3x^2 + a_4y^2 + a_5xy + a_6x^3 + a_7y^3 + a_8x^4 + \\ & + a_9y^4 + a_{10}x^2y^2 + a_{11}x^5 + a_{12}y^5 + a_{13}x^3y^3 + a_{14}x^4y^4 + a_{15}x^5y^5 \end{aligned} \tag{3.13}$$

Figure 3.9

The total energy resolution for the ^{55}Mn beam at 1750 MeV/nucleon is $\sigma_E/E = 0.73\%$, which corresponds to a contribution to a mass resolution of 0.40 amu for the calibration data. The tail of low energy losses is the result of neutron-stripping interactions in the instrument.

Figure 3.9

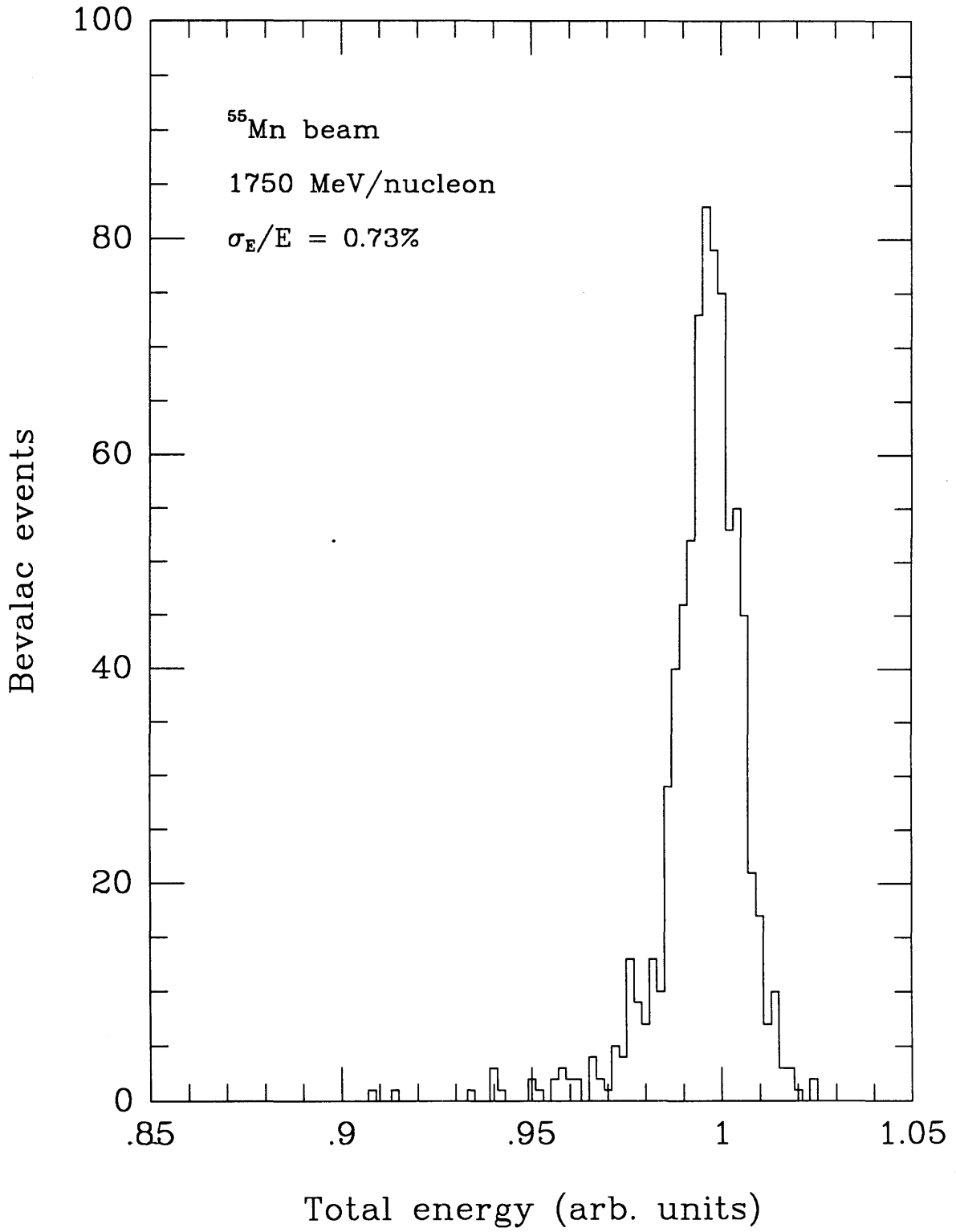
100
80
60
40
20
0
.85
.9
.95
1
1.05
^{55}Mn beam
1750 MeV/nucleon
σ_E/E = 0.73%
Bevalac events
Total energy (arb. units)

Figure 3.10

Scatter plot of the index of refraction of the aerogel blocks as determined by the density of each block and by the deflection of a laser beam as it passed through a 90° corner of each block. The latter measurement is systematically lower by approximately $\Delta n = 0.005$.

Figure 3.10

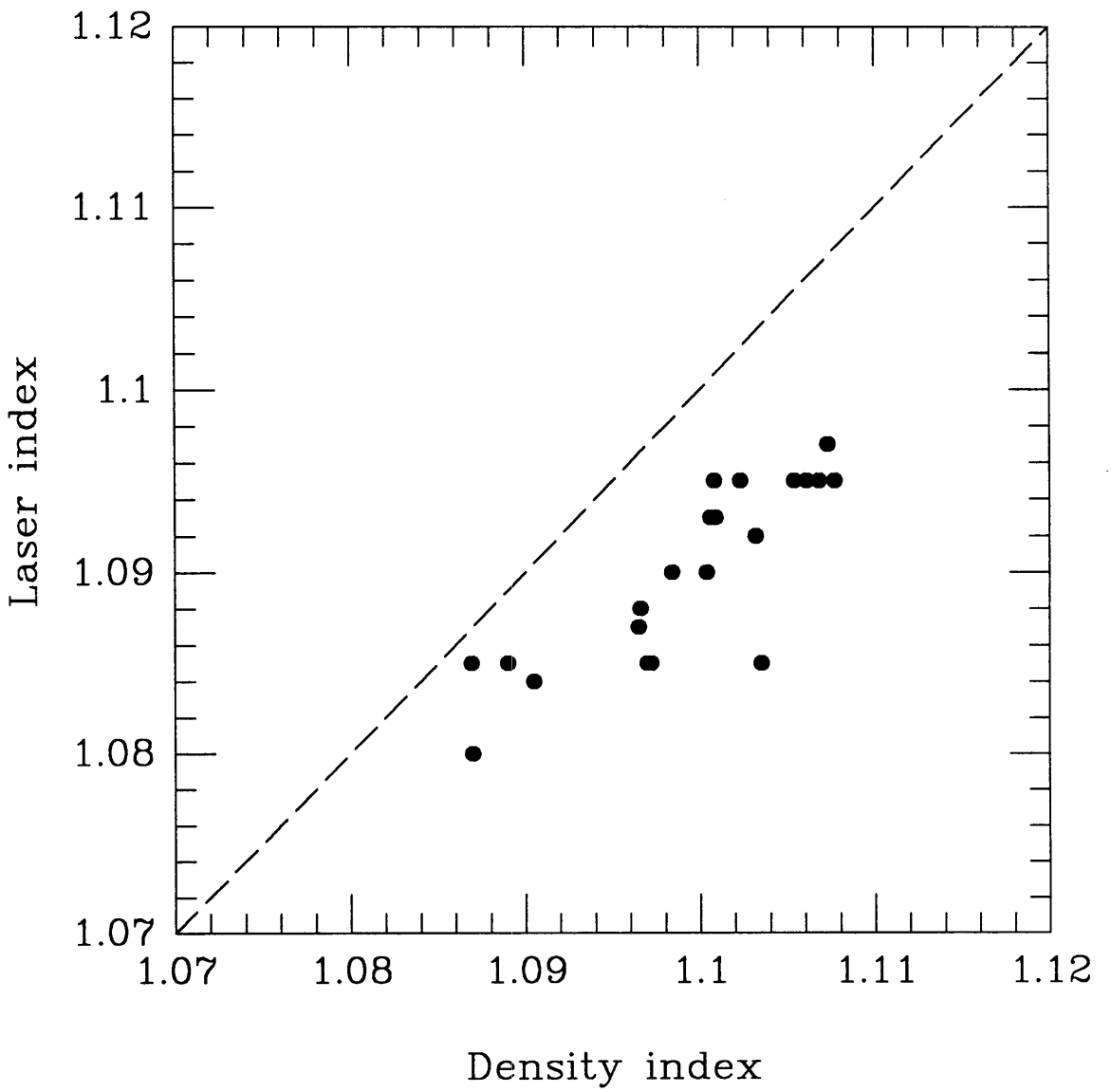
1.12
1.11
1.1
1.09
1.08
1.07
Laser index
1.07
1.08
1.09
1.1
1.11
1.12
Density index

Extensive trials of a variety of polynomials were held, and this polynomial was found to give an adequate fit in all blocks.

Figure 3.11 shows a contour plot of the polynomial map of aerogel group 7. Each contour labels a 1% decrease in response from the maximum value. The gradient of the response is $<2\%$ cm^{-1} for more than 75% of the area of the mosaic. Aerogel group 7 shows particularly large gradients, with only $\sim$50% of the area having gradients $<2\%$ cm^{-1}.

Recall that we concluded in §2.3 that the total mass resolution would be improved if the velocity were calculated from the ratio of responses in the aerogel counter and the first stack layer. The Lorentz factor for an incident particle is calculated by solving the following relation for γ,

$$\Omega_{obs} = \frac{N_\mu}{\alpha_s} \frac{f(n,\gamma) + k(\gamma) + b}{s(Z,\gamma)} , \tag{3.14}$$

where Ω_{obs} is the observed ratio of responses, $f(n,\gamma)$ is the fraction of relativistic light (Equation (2.6)), $k(\gamma)$ is the average Cerenkov component produced by knock-on electrons (Equation (2.4)), b is the additional background light in the aerogel counter (§2.2.1 and below), and $s(Z,\gamma)$ contains the velocity dependence of the ionization energy loss dE/dx and the scintillation efficiency dL/dE (Equation (2.9)). Note that the proper normalization N_μ/α_s must be established between the model and the observed values, and that the magnitude of the background signal b must be determined (see §3.6.2). To reduce the probability that fluctuations in the Cerenkov signal would cause a subthreshold event to be interpreted as having an energy above threshold, events with $f(n,\gamma) < 2\%$ are not considered.

Because the three aerogel blocks in each group have distinct refractive indices, we have used the following effective index in Equation (3.14). Above the Cerenkov threshold in all three blocks, the total Cerenkov signal from a primary particle is the sum of the contributions from each block,

$$Z^2 N_\mu f(n_{eff},\gamma_{eff}) \equiv \sum_i Z^2 N_i \frac{n_i^2(\gamma_i^2-1) - \gamma_i^2}{(\gamma_i^2-1)(n_i^2-1)} . \tag{3.15}$$

If we assume that the Lorentz factor γ_i and the relativistic yield N_i are identical in each

block, we find that the square of the effective index n_{eff} is given by

$$n_{eff}^2 = \frac{\sum \frac{n_i^2}{n_i^2-1}}{\sum \frac{1}{n_i^2-1}} . \tag{3.16}$$

Simulations of the slowing-down of Fe nuclei in the aerogel mosaic indicate that this assumption of an effective index of refraction and a single, average velocity for a group of three blocks results in a bias in the mass of <0.07 amu in all cases and a contribution to mass resolution of ~ 0.02 amu. Note that this contribution was ignored in the discussion of §2.3.

Equation (3.14) is solved for γ by the Newton-Raphson method (e.g., Press *et al.*, 1986), which requires the evaluation of both a function g(x) and its derivative $g'(x)$ at arbitrary points x. In this case, $g(x) = \Omega_{obs} - \Omega_{model}$, where Ω_{model} is just the right-hand side of Equation (3.14). In the neighborhood of a root, a function can be approximated by a first-order Taylor expansion

$$g(x+\delta) \approx g(x) + g'(x)\,\delta . \tag{3.17}$$

At a root, $g(x+\delta) = 0$; thus the distance from the current point x to the root is simply

$$\delta = -\frac{g(x)}{g'(x)} . \tag{3.18}$$

The Newton-Raphson method applies this technique iteratively, beginning at a guess x_{guess} and repeatedly calculating the distance to the root and setting the next guess equal to $x_{guess} + \delta$. The functions of Equation (3.14) are sufficiently well-behaved that no local extrema—which can break the search—and only one root exist in the region for which the functions are valid.

3.6.2. Bevalac Cerenkov Resolution

Calibration data were accumulated at four different energies (§3.1) in a single aerogel group of blocks, which is designated as group 7. With these data we were able to verify that the effective index of refraction of the three blocks in the group corresponds

Figure 3.11

Contour plot of the polynomial map of the response of aerogel group 7 to the ^{55}Mn beam at 1750 MeV/nucleon. Each contour marks a decrease of 1% from the maximum value.

Figure 3.11

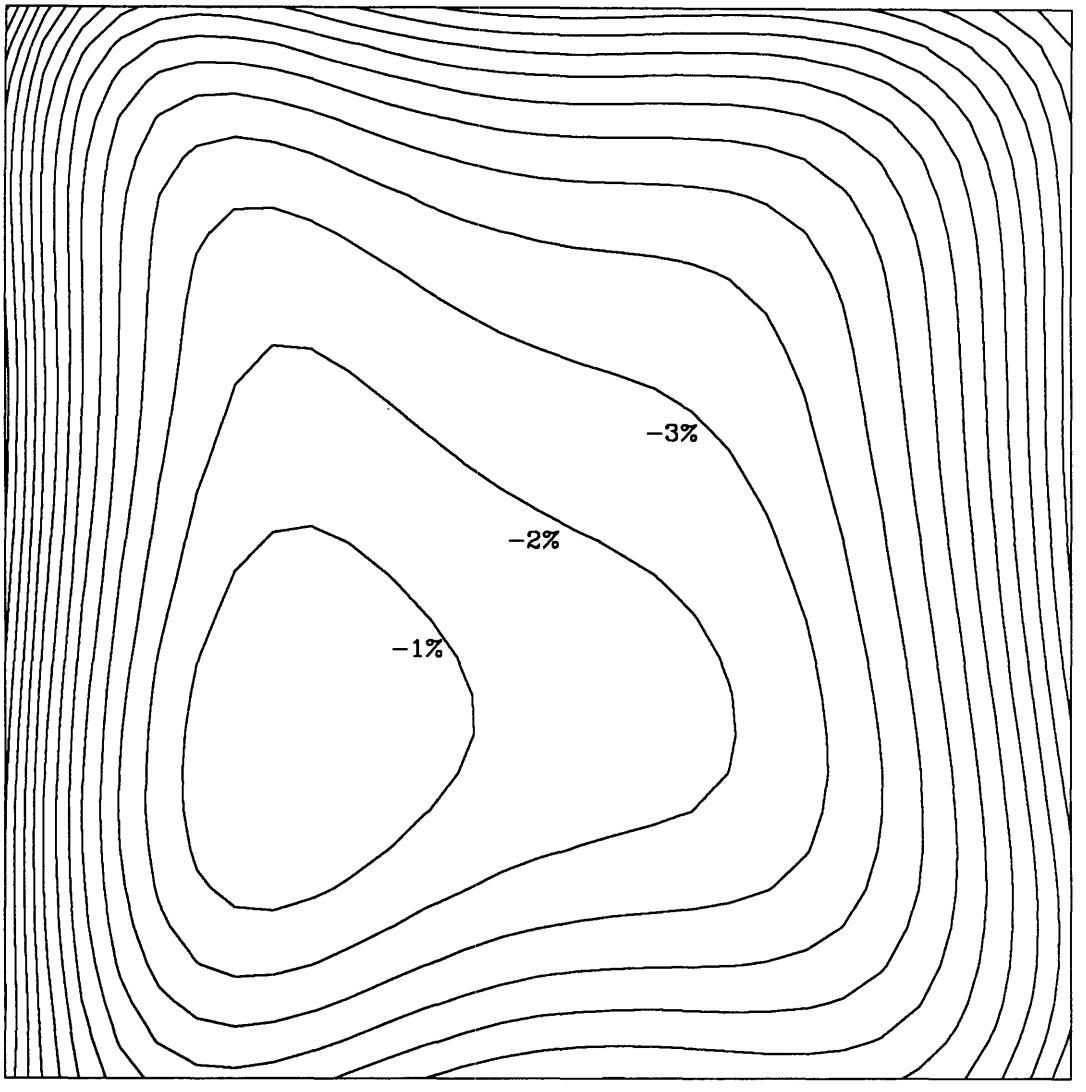

Aerogel group 7
1% contour spacing

to that calculated from the density and to measure the number of photoelectrons Z^2N_μ and the stochastic variation in index σ_n in the group.

Aerogel group 7 contains the three blocks with the largest dispersion of index as calculated from the density (see Figure 2.3 and §2.1). The intent in selecting the energies of the Bevalac data was to provide a single data point below the Cerenkov threshold of all blocks in a group; however, because of a misunderstanding of the value of the density index of the blocks in group 7, the choice of beam energy for the lowest-energy point was, in fact, above the threshold of the uppermost block. The observed Cerenkov response is plotted as a function of β^{-2} in Figure 3.12. The uncertainty in the mean response at each energy is smaller than the point size. The systematic uncertainty in the beam energy is comparable to the point size. The solid curve is the calculated total Cerenkov signal normalized at the highest energy point, with the assumption that the yield of each block is identical at velocity $\beta = 1$. The discontinuities in the slope correspond to the threshold energies of the three blocks. The constant background contribution $b = 0.017$ is estimated by subtracting the calculated knock-on contribution (Appendix A) and the Cerenkov yield in the single block. Because the Cerenkov response is proportional to $1 - n^{-2}\beta^{-2}$, the observed response should depend roughly linearly on β^{-2} and, in particular, the intercept of the linear relation above the threshold of the three blocks with the sum of the knock-on electron component, and the constant background level should correspond to the Cerenkov threshold velocity $\beta_{th} = 1/n$. The effective index is thus determined to be $n = 1.0945 \pm 0.001$, in excellent agreement with the value determined from the density, $n = 1.0949 \pm 0.0010$.

The Cerenkov resolution can be used to estimate the number of photoelectrons Z^2N_μ and the magnitude of the stochastic variation σ_n in the index of refraction. The contributions to the Cerenkov resolution include (1) statistical fluctuations in the number of photoelectrons collected in the photomultipliers; (2) stochastic variations in the index of refraction of the aerogel blocks in the group; (3) fluctuations in the Cerenkov response from knock-on electrons; (4) residual variations in the light-collection efficiency not accounted for in the maps of the aerogel response; and (5) momentum divergence of the Bevalac beam. The first four contributions are discussed in detail in §2.3. The other contributions listed in §2.3 are expected to be negligible in the Bevalac

data and have not been considered here.

The fractional contribution to the Cerenkov resolution in all cases is calculated from

$$\frac{\sigma_C}{C} = \frac{1}{C}\frac{\partial C}{\partial \xi}\sigma_\xi , \tag{3.19}$$

where the parameter ξ signifies any of the five contributions. For example, the contribution from index variations is given by

$$\frac{\sigma_C}{C} = \frac{1}{C}\frac{\partial C}{\partial n}\sigma_n \tag{3.20}$$

$$= \frac{\partial f}{\partial n}(n,\gamma)\,\frac{1}{f(n,\gamma) + k(\gamma) + b}\,\sigma_n \tag{3.21}$$

$$\sim \frac{2n/(n^2-1)}{\gamma^2(n^2-1) - n^2}\,\sigma_n , \tag{3.22}$$

where, following the method of §2.3, the final expression is an approximation neglecting the secondary Cerenkov sources ($k(\gamma) \equiv 0$, $b \equiv 0$). Of course, this is a poor approximation near the Cerenkov threshold, and it has been derived merely to show the dependence on n and γ to leading order. The complete form, Equation (3.21), should be used to calculate the contribution.

Figure 3.13 shows the result of a least-squares fit to the measured Cerenkov resolution σ_C/C for the four Bevalac runs in aerogel group 7. The curves represent the five contributions to the resolution list above, with the total shown by the solid curve. The breaks occur at the threshold energies of the three blocks, where the energy shown is the energy in the center of the middle block. Free parameters of the fit were the number of photoelectrons N_μ and the index variation σ_n. The fluctuations in the Cerenkov response from knock-on electrons were given by the model in Appendix A. The residual variations in the light-collection efficiency were measured to be 0.75% in group 7, following the procedure outlined in §3.6.3 below. We have used the measured momentum divergence $\sigma_p/p \approx 0.1\%$ of a beam of Au at 960 MeV/nucleon (H. J. Crawford, 1988, personal communication). The fit shows $\chi^2_{red} = 2.7$ for two degrees of freedom. The least-squares estimates of N_μ and σ_n for the group of three blocks (6 cm of

Figure 3.12

Measurement of index of refraction of aerogel group 7. The solid circles give the mean Cerenkov response for the four Bevalac beam energies. The points are plotted at the velocity at the center of the stack of three blocks in the group. The uncertainty in the mean response is smaller than the point size. The systematic uncertainty in the beam energies is comparable to the point size. The discontinuities in the slope of the total response appear at the threshold energies of the three blocks. The average index of refraction of the blocks is given by the intersection of the extension of the total Cerenkov response (the dotted line) with the curve representing the summed secondary light sources (the short-dash, long-dash curve). The index is 1.0945 ± 0.001, which is in excellent agreement with the value determined from the density, $n = 1.0949 \pm 0.0010$.

Figure 3.12

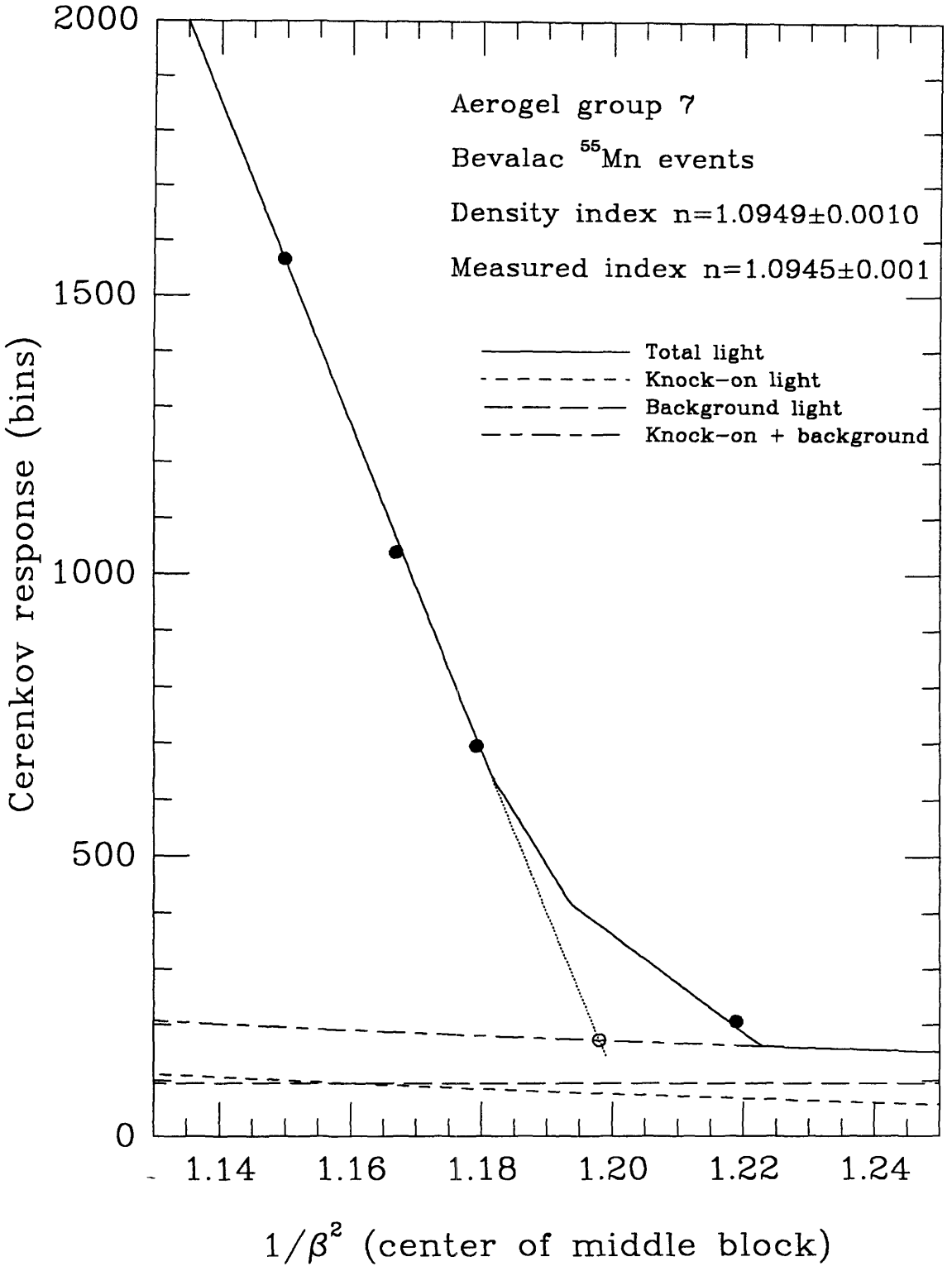
Aerogel group 7
Bevalac ^{55}Mn events
Density index n=1.0949±0.0010
Measured index n=1.0945±0.001
Total light
Knock-on light
Background light
Knock-on + background
Cerenkov response (bins)
2000
1500
1000
500
0
1.14
1.16
1.18
1.20
1.22
1.24
$1/\beta^2$ (center of middle block)

Figure 3.13

Cerenkov resolution for the calibration data. The observed fractional Cerenkov resolution σ_C/C is modeled as the sum of contributions from photoelectron statistical fluctuations, stochastic index of refraction variations, fluctuations in the Cerenkov yield of knock-on electrons, divergence of the accelerator beam momentum, and residual variations in the light-collection efficiency, or mapping errors. The energy shown is the kinetic energy in the center of the middle aerogel block. The least-squares estimate of the number of photoelectrons from a $Z=1$ particle with velocity $\beta=1$ is $N_\mu=18.4^{+2.6}_{-2.0}$, and the estimate of the standard deviation of the index is $\sigma_n=(4.7\pm0.4)\times10^{-4}$ for the group of three blocks (6 cm of aerogel with $n=1.1$).

Figure 3.13

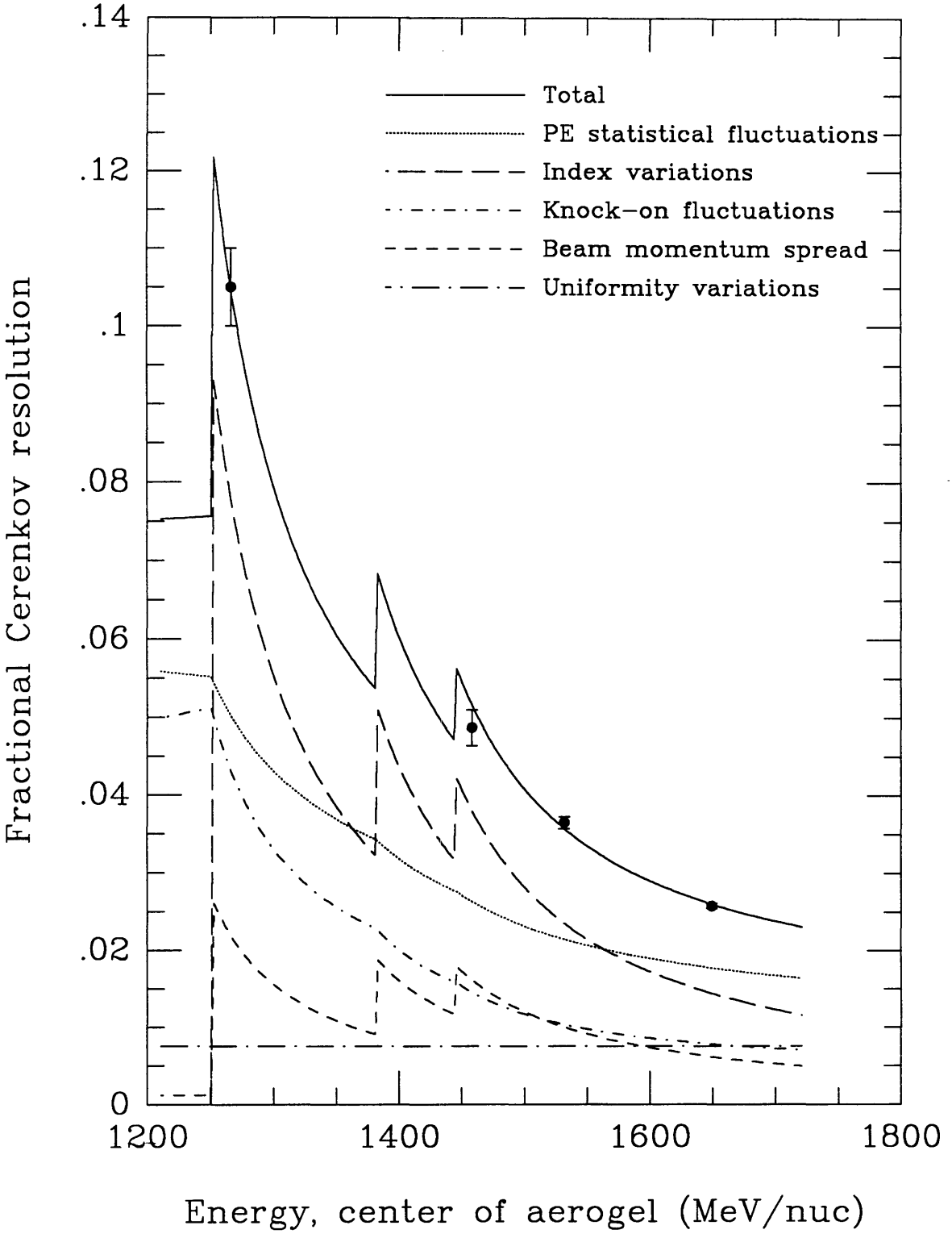
.14
.12
.1
.08
.06
.04
.02
0
1200
1400
1600
1800
Fractional Cerenkov resolution
Energy, center of aerogel (MeV/nuc)
Total
PE statistical fluctuations
Index variations
Knock-on fluctuations
Beam momentum spread
Uniformity variations

aerogel) are given in Table 3.3.

Table 3.3 Bevalac Aerogel Parameters

Parameter	Meaning	Value
N_μ	number of photoelectrons	$18.4^{+2.6}_{-2.0}$
σ_n	stochastic index variation	$(4.7\pm0.4)\times10^{-4}$

The number of photoelectrons from a relativistic particle with charge $Z=1$ can also be estimated from the width of the Cerenkov signal from sea-level, cosmic-ray muons. Note that because the contribution from index variations is independent of the charge of the particle and $\sigma_{pe}/C \propto Z^{-1}$, the index contribution is negligible for muons. Data collected in November 1982 give a lower limit of $\sim$15 photoelectrons, consistent with the value in Table 3.3.

The stochastic index variation reported in Table 3.3 represents the variation in the stack of three blocks; thus a single block should show an rms variation that is larger by a factor of $\sqrt{3}$, or $\sigma_n=(8.1\pm0.6)\times10^{-4}$. The magnitude of the variation is quite high: Indeed the index variation is the dominant source of Cerenkov uncertainty below 1550 MeV/nucleon in this group. A similar fit has been performed on calibration data collected with a single aerogel block—a spare for the mosaic—in a small test chamber. The statistics of the measurement are poor, but they indicate a value of $\sigma_n=(8\pm2)\times10^{-4}$, in excellent agreement with the above value. Note that in both cases the quoted uncertainties in the value of σ_n are statistical only and that the magnitude of σ_n depends particularly on the assumed contributions from the fluctuations in the knock-on signal and the momentum spread of the Bevalac beam, since these contributions have a similar dependence on the beam energy. However, because the contributions are added in quadrature, substantial increases in these other two contributions would be required to reduce the contribution from index variations by a significant amount. For example, doubling the estimated momentum divergence to $\sigma_p/p=0.2\%$

would drop the index variation in the group of three blocks to 3.3×10^{-4}.

3.6.3. Degradation of Aerogel Cerenkov Yield

Figure 3.14 shows the response of the aerogel counter to sea-level, cosmic-ray muons. These data were routinely collected, and only a fraction is shown in the figure. By the time of the flight in May 1984, the amplitude of the signal had decreased to $\sim$55% of its value at the time of the Bevalac calibration in November 1982. The average decrease was $\sim$2% per month. The width of the muon signal in April 1984 gives a lower limit of $\sim$8 photoelectrons, consistent with a decrease of a factor of $\sim$2. However, these effects were not noticed until after the flight. In addition, when the Cerenkov counter was opened in late 1985, we observed that the aerogel blocks had assumed a yellow-brown color.

The high-voltage system for the aerogel photomultipliers was changed immediately after the calibration, and the dashed line on the figure indicates that muon data for the November 1982 time period are not available. Following the installation of the new high-voltage system, the anode voltage remained constant to $<0.1\%$, and therefore cannot account for the observed decrease in response.

Recall that each photomultiplier has an associated preamplifier to bring the signal to a reasonable level in the ADCs in the muon mode (§2.2.1). The gains of the preamplifiers were monitored periodically and showed drifts of $\sim$1% over the entire time interval; thus they cannot be the source of the decrease in response.

The muon response of the bottom Cerenkov counter, which was painted with $BaSO_4$ at the same time as the aerogel counter and which contained photomultipliers of the same type and age, showed no evidence for a change of $>1\%$ over the same time period. Thus any aging of the paint and the photomultipliers is negligible.

We conclude that the decrease is due to a degradation of the optical properties of the aerogels, and therefore the number of photoelectrons at the time of the flight was $N_\mu \approx 9$. Other investigators have observed a decrease in Cerenkov yield in aerogel counters, although of a smaller magnitude.

Fernandez *et al.* (1984) constructed a modular aerogel counter for the European Hybrid Spectrometer at CERN containing a mosaic of blocks with total thickness

Figure 3.14

Degradation of Cerenkov yield of aerogel. The signal in the aerogel counter from sea-level, cosmic-ray muons shows a decrease of a factor of $\sim$2 from the time of the accelerator calibration in November 1982 to the flight in May 1984. The break in the slope of the degradation coincides with the start of a dry-N_2 flush intended to drive off any accumulated moisture in the aerogels. Before the break, the degradation averaged $\sim$2% per month.

Figure 3.14

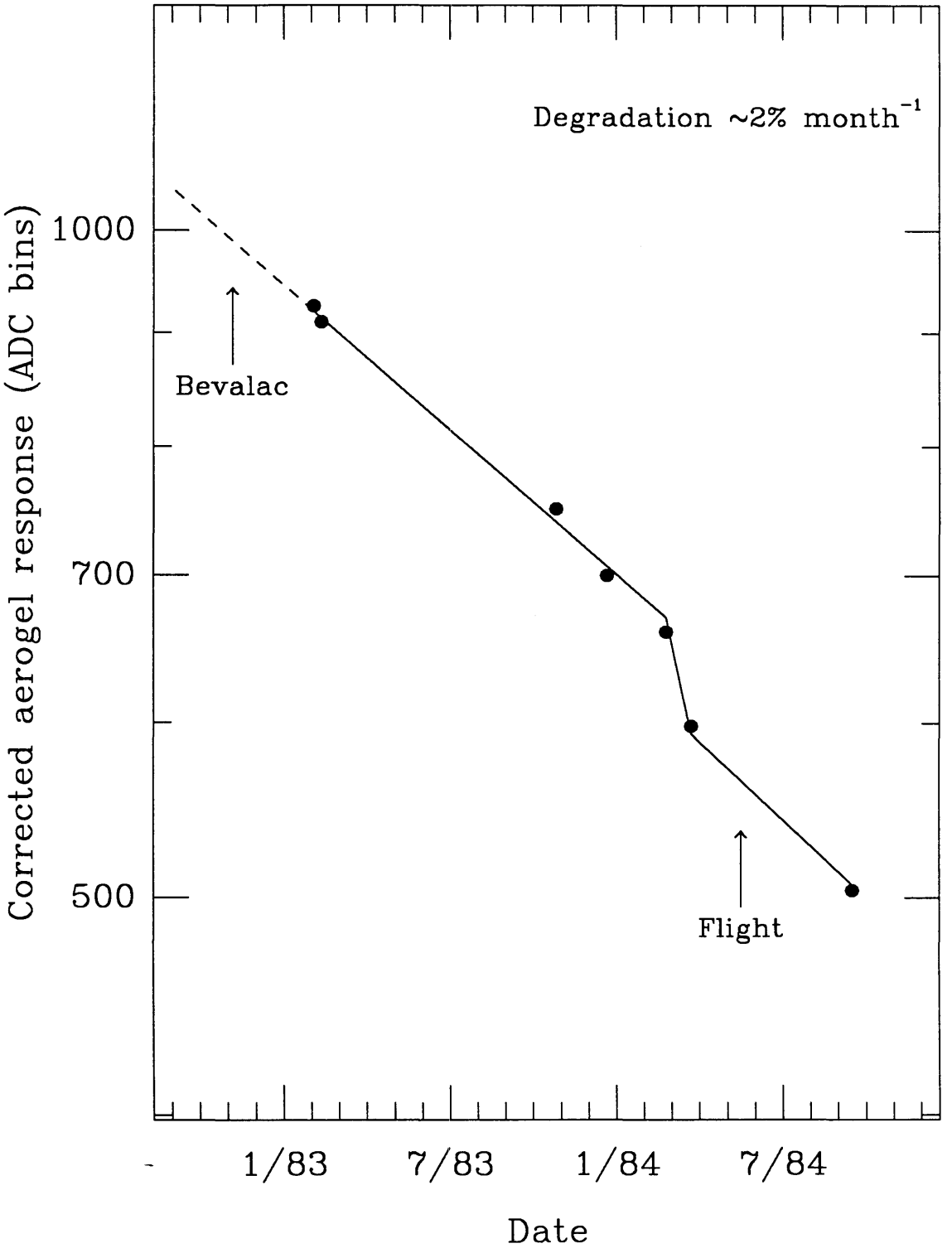
Degradation ~2% month^{-1}
Corrected aerogel response (ADC bins)
1000
700
500
Bevalac
Flight
1/83
7/83
1/84
7/84
Date

between 13 and 15 cm, with an index of 1.031. The reflective surfaces of the light-collection system were made from aluminized mylar. They observed a decrease in light yield of 30% in the first three years of operation, or ~1% per month, which they attributed to the absorption of water by the aerogel. This explanation seems unlikely, however, as the attenuation length for Cerenkov photons in water is ~60 m (Dye, 1989).

The large counter constructed by the TASSO collaboration at DESY (Burkhardt *et al.*, 1981) contained 1700 liters of aerogel 14.4 cm thick with indices of 1.024 and 1.021. The surfaces of the counter were lined with Millipore paper. They observed a decrease in light yield of 50% in five years, of which they attributed ~15% to degradation of the Millipore and ~35%, or ~0.7% per month, to absorption by the aerogel of "organic vapours from paints and from double sticky tapes" (Poelz, 1986). The blocks were observed to have become brownish in color, and their transmission lengths at 436 nm were reduced by 15% to 25% (Poelz, 1986).

The French-Danish aerogel counter aboard *HEAO 3* contained a radiator of thickness 5.6 cm and index 1.053 (Cantin *et al.*, 1981). The diffusion box was lined with Millipore paper, and the counter was open to the vacuum of space. They observed a decrease in yield of 2% after three months and 4% after nine months. However, because the ratio of signals from upward and downward traveling particles remained unchanged, and the Cerenkov light from downward particles passed through one more thickness of aerogel on the average than the light from upward particles, they concluded that the cause of the decrease was not the aerogel but most likely an electronic drift. In any case, the decrease of $<0.5\%$ per month is significantly smaller than the decrease we observed.

Note the break in the slope of the decrease in aerogel response in Figure 3.14. This coincides with the start of a dry-N_2 flush of the counter intended to drive off any accumulated moisture in the aerogels before the flight. Presumably the water driven from the aerogels had been acting as an efficient Cerenkov radiator. We can estimate the thickness of water required. Attributing the difference in muon response entirely to Cerenkov emission from water, we find from the figure that the water had to have provided ~1/12 of the Cerenkov yield of the aerogel. Since the Cerenkov yield of a

radiator of index n is proportional to $1-n^{-2}$ for particles with $\beta=1$ (see Equation (2.2)), water ($n=1.33$) produces $\sim$2.5 times more light per unit length than does aerogel ($n=1.1$). Assuming equal absorption lengths for Cerenkov photons for the water and the aerogel, the thickness of water required to generate the extra Cerenkov radiation is $\sim$3% of the aerogel, or $\sim$0.2 cm. This pathlength seems rather large.

Although the average Cerenkov yield of the aerogel blocks decreased by $\sim$50%, the yield as a function of location in the groups remained remarkably constant, and therefore the maps created from the Bevalac data remained useful. Figure 3.15 summarizes the small changes that occurred in group 10. To test the constancy of the maps, we divided each group into an array of bins 2 cm on a side. In each bin, we calculated the mean of the mapped response for ^{55}Mn data from the Bevalac and of the mapped response for relativistic B through Si data from the flight. If the maps were perfect representations of the Bevalac data, any deviations of the binned means of the Bevalac data from unity would be statistical, and if the radiator yield as a function of position had changed significantly by the time of the flight, systematic differences between the flight data averages and the map values would be apparent. In Figure 3.15, the open circles represent the mean Bevalac response in each bin, and the crosses represent the mean flight response. The uncertainties in the Bevalac data are smaller than the point size. The points are plotted such that their abscissas correspond to the placement of bin centers, and the deviations of their ordinates from the dashed lines correspond to the deviations from the map value. The scale of the ordinate is such that a deviation of 10% would place the point on the dashed line corresponding to null deviation for the neighboring bin. The rms variation of the Bevalac means from the map values for all groups is $\sim$1.1% and of the means of the flight data is $\sim$2.3%. These quantities are a measure of the mapping errors for both data sets. Systematic deviations for the Bevalac data in group 10 are apparent in the figure and presumably arise from an inadequate choice of polynomial terms in the mapping procedure. Although the deviations of the flight data are slightly smaller than average in group 10, we chose this group for the figure because the coverage of the data was particularly good and the statistical errors were particularly small. If the deviations of the flight means from the map values are statistical, they should be distributed as a χ^2. The reduced $\chi^2_{48}=1.27$, which corresponds to a probability of 10% for 48 degrees of

Figure 3.15

Deviations of measured calibration and flight responses from the aerogel map for group 10. The open circles represent the mean mapped response from the ^{55}Mn beam in each of 49 bins 2 cm on a side. The statistical uncertainties are smaller than the point size. The crosses represent the mean mapped response for relativistic B through Si from the flight. The points are plotted such that their abscissas correspond to the placement of bin centers, and the deviations of their ordinates from the dashed lines correspond to the deviations from the map value. The scale of the ordinate is such that a deviation of 10% would place the point on the dashed line corresponding to null deviation for the neighbor bin. Systematic differences are apparent between the mean values and the map values, indicating that mapping errors are present for both data sets.

Figure 3.15

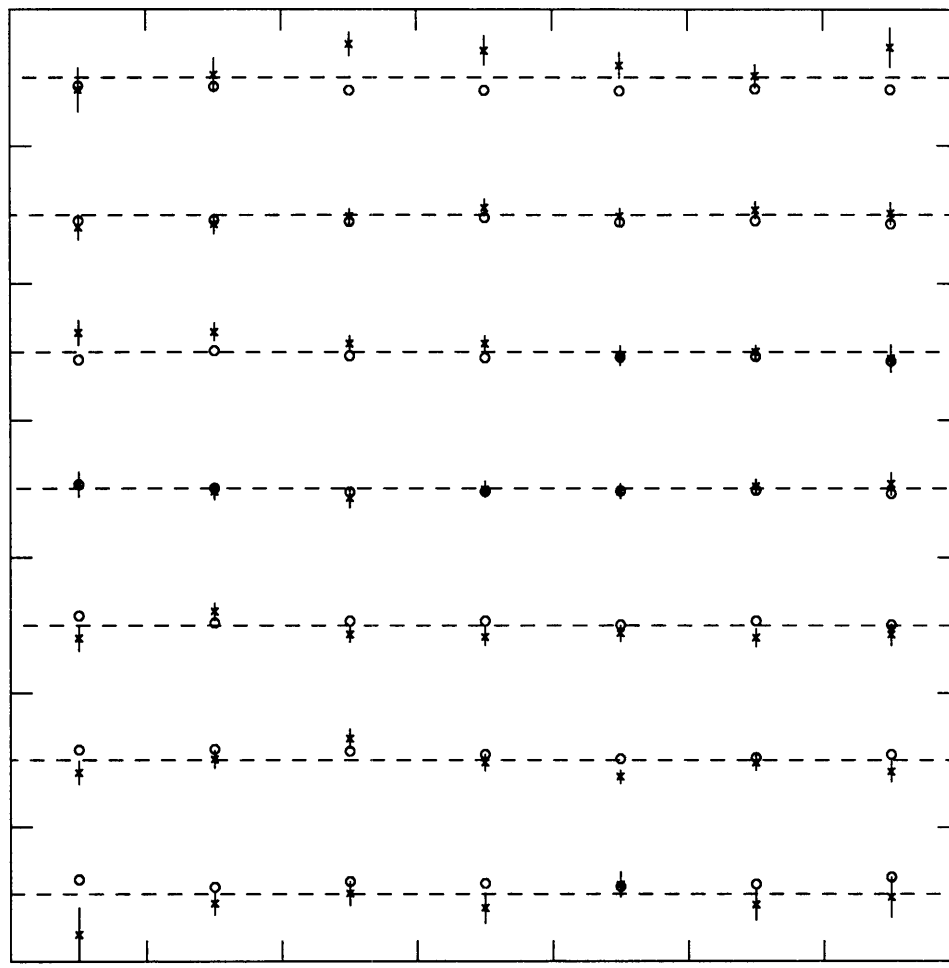

freedom, indicates that statistical fluctuations alone can account for the deviations. We have concluded that this probability is sufficiently high that the maps are adequate.

It is important to consider whether the index of refraction has changed as a result of the apparent contamination of the blocks. We have measured the index of several aerogel groups with the flight data, following a procedure similar to that used to measure the index in group 7 from the Bevalac data (§3.6.2 and Figure 3.12). In all cases, the measured index is consistent with the index derived from the density (Equation (3.12)), within the measurement uncertainty of $\Delta n = \pm 0.005$, and we conclude that there is no evidence for a change in index larger than this value. For example, Figure 3.16 shows the observed C/S response ratio for the four ^{56}Fe flight events in group 10. Iron events were selected according to the procedure described in 3. Four of the five events in group 10 showed a most-probable mass number of $A = 56$. In the figure, the events have been assigned velocities for the best-fit model ^{56}Fe particles described in §3.4. The C/S normalization is given by the procedure in §3.6.4 below, from the many events with subthreshold energy. Uncertainties in the velocities are derived from uncertainties in the measured angle of incidence, and these dominate the uncertainty in the index measured from the flight data. The index is measured to be $n = 1.093 \pm 0.005$, which is consistent with the index calculated from the density, $n = 1.0964 \pm 0.0010$. We did not measure the index of group 7 with the flight data, because only two events showed a most-probable mass of $A = 56$.

3.6.4. Aerogel Block Response Normalization

In order to calculate velocity from the observed Cerenkov response, the correspondence between signal and velocity must be established in each aerogel group. While this normalization was easily established from the Bevalac data, it was lost because of the degradation of the aerogel which, as shown below, occurred with differing magnitude among the groups of the mosaic.

The normalization has been re-established from a data set consisting of all events in the Fe peak in the top scintillator and layer 1. Because the events are allowed to undergo interactions deeper in the NaI(Tl), their trajectories may not be of the highest quality; however, the statistics rapidly become inadequate if charge restrictions are

applied deeper in the stack. Figure 3.17 shows the Fe track in aerogel block 11 formed by plotting the the pathlength-corrected response $\Delta L_1/\sec\theta$ in layer 1 against the observed C/S ratio. The events with energies below the Cerenkov threshold make an apparent vertical band because the C/S ratio remains approximately constant, while $\Delta L_1/\sec\theta$ increases as the energy decreases. The track turns vertical also as the particle energy enters the region of the relativistic rise in energy loss, where again C/S remains approximately constant, while $\Delta L_1/\sec\theta$ increases. By selecting events in these two energy intervals and choosing a suitable model of the response of both counters, we can renormalize the aerogel response. The dashed boxes in Figure 3.17 enclose the selected events.

The C/S ratio has the following form (see Equation 3.14),

$$\Omega \equiv \frac{C}{S} = \frac{N_\mu}{\alpha_s} \frac{f(n,\gamma)+k(\gamma)+b}{s(Z,\gamma)}, \tag{3.23}$$

where the relativistic yield N_μ/α_s and the background contribution b in the aerogel counter are free parameters. Over a velocity interval $\Delta\gamma_i$, the model predicts an average ratio of

$$<\Omega_i> = \frac{N_\mu}{\alpha_s} \frac{\int_{\Delta\gamma_i} \frac{dN}{d\gamma} \frac{f(n,\gamma)+k(\gamma)}{s(Z,\gamma)} d\gamma}{\int_{\Delta\gamma_i} \frac{dN}{d\gamma} d\gamma} + b \frac{N_\mu}{\alpha_s} \frac{\int_{\Delta\gamma_i} \frac{dN}{d\gamma} \frac{1}{s(Z,\gamma)} d\gamma}{\int_{\Delta\gamma_i} \frac{dN}{d\gamma} d\gamma} \tag{3.24}$$

$$\equiv A I_{c,i} + B I_{b,i}, \tag{3.25}$$

where $A = N_\mu/\alpha_s$ and $B = bA$, and where we have assumed a cosmic-ray differential energy spectrum $dN/d\gamma \propto \gamma^{-2.5}$. The integrals can be evaluated numerically in the subthreshold and high-energy regions, giving two equations in two unknowns,

$$<\Omega_{low}> = A I_{c,low} + B I_{b,low} \tag{3.26}$$

$$<\Omega_{high}> = A I_{c,high} + B I_{b,high}, \tag{3.27}$$

Figure 3.16

Index of refraction of aerogel group 10 measured with ^{56}Fe from the flight data set. The ratio of the Cerenkov signal to the scintillation signal for the four ^{56}Fe events in group 10 is plotted at the velocity derived from the model particle (§3.4). The C/S ratio removes the angular dependence and, to the extent that the scintillation signal is constant, preserves the property that the intersection of the C/S curve and the total signal from secondary sources corresponds to the Cerenkov threshold velocity. The index of refraction thus derived is $n = 1.093 \pm 0.005$, which agrees with the value measured from the density, $n = 1.0964 \pm 0.0010$. There is no evidence for a change in index of refraction of the aerogel greater than $\Delta n = \pm 0.005$ from the time of the calibration to the time of the flight.

Figure 3.16

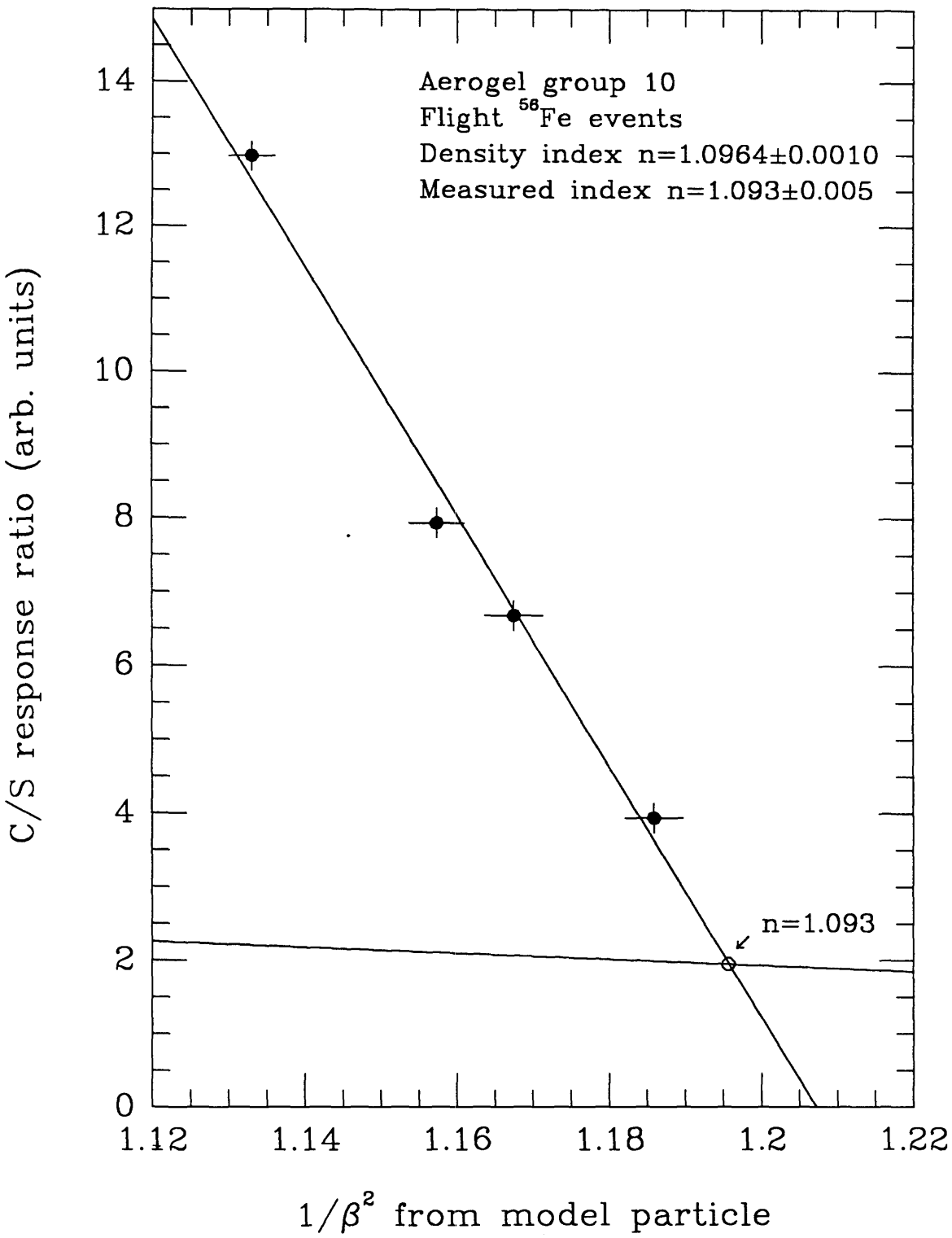
Aerogel group 10
Flight ^{56}Fe events
Density index n=1.0964±0.0010
Measured index n=1.093±0.005
n=1.093
C/S response ratio (arb. units)
$1/\beta^2$ from model particle
0
2
4
6
8
10
12
14
1.12
1.14
1.16
1.18
1.2
1.22

Figure 3.17

Cerenkov response model and group normalization in aerogel group 7. The track of events from the Fe peak in the top plastic scintillator and the first NaI(Tl) layer makes a vertical band for particle energies below the Cerenkov threshold, where C/S remains approximately constant while $\Delta L_1/\sec\theta$ increases as the energy decreases. The track also turns vertical as the particle energy enters the region of the relativistic rise in energy loss, where the Cerenkov response C saturates. The dashed boxes enclose the events selected for the normalization of the response model. The normalized model track is shown as a solid line.

Figure 3.17

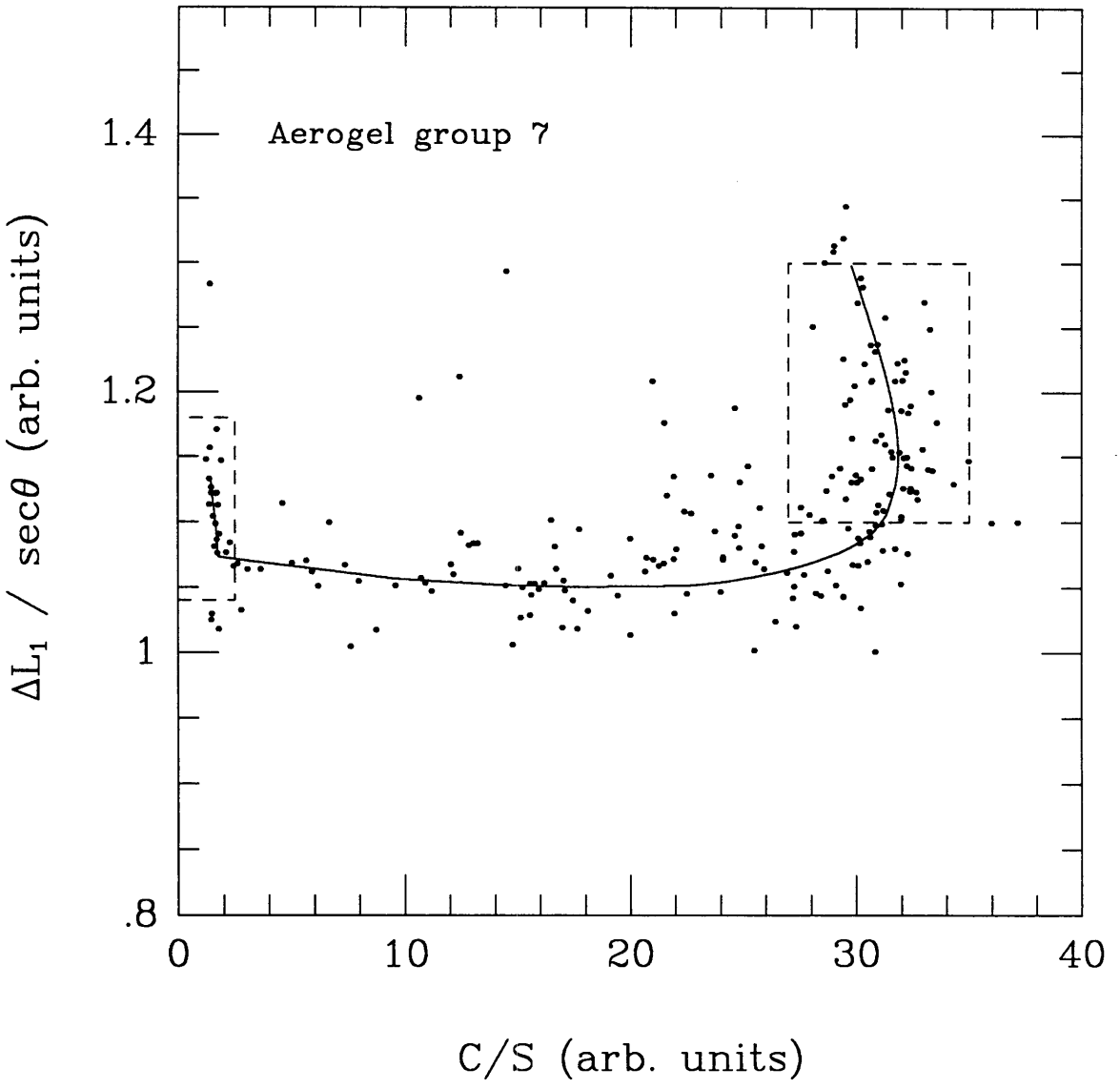
Aerogel group 7
1.4
1.2
1
.8
0
10
20
30
40
ΔL_1 / secθ (arb. units)
C/S (arb. units)

Figure 3.18

Comparison of aerogel response normalization factors for the calibration and the flight data. The solid circles show the normalization factors for the four center groups, while the open circles show the normalization factors for the eight outer square groups. All groups suffered a similar degradation in Cerenkov yield: Deviations from the factor of $\sim$2 average decrease were less than $\sim$6%.

Figure 3.18

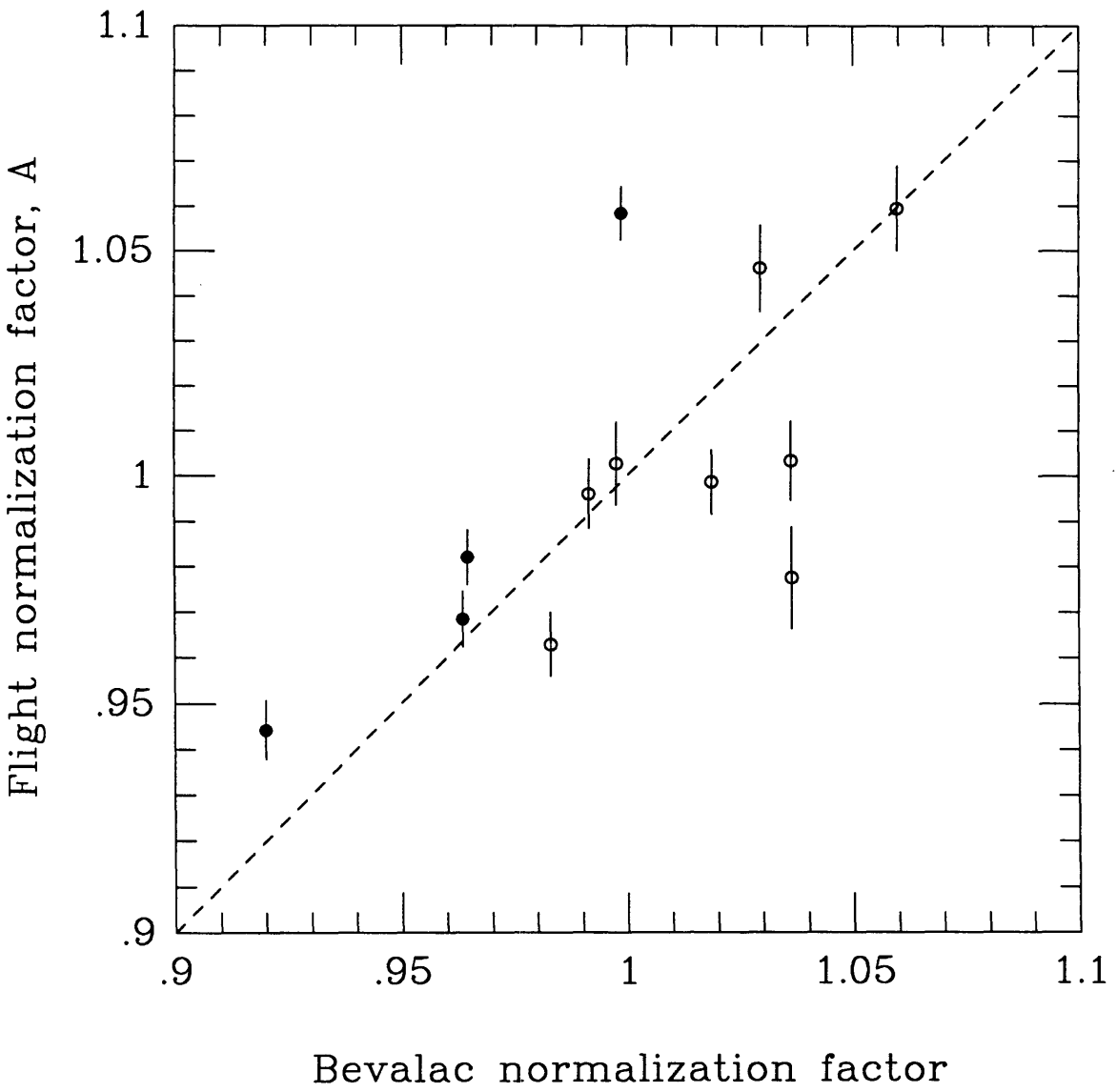
1.1
1.05
1
.95
.9
Flight normalization factor, A
.9
.95
1
1.05
1.1
Bevalac normalization factor

where $<\Omega_{low}>$ and $<\Omega_{high}>$ are the observed mean values of C/S in the subthreshold and high-energy regions, respectively. We know that the background contribution b is on the order of a few percent, so the free parameters A and B should differ by that factor.

The uncertainty in the determination of A and B is the result of both the error in the observed means of the ratios in the two intervals and of the error in choosing the endpoints of the integration. We estimate that the uncertainty in choosing the endpoints results in an uncertainty in $I_{c,high}$ of $\sim$0.7%. The observed rms variation of the mean $<\Omega_{high}>$ ranges from 0.6% to 1.1%, with the average in the four center blocks $\sim$0.6%, while the rms variation of the mean $<\Omega_{low}>$ is typically $\sim$5%. Propagation of errors shows that the uncertainties in the two free parameters are $\sigma_A/A \sim 1-1.5\%$ and $\sigma_B/B \sim 5\%$. In the calculation of the expected mass resolution in §2.3, we assumed $\sigma_A/A = 1.5\%$.

In Figure 3.18, the values of A for the twelve square groups are plotted against the normalizations calculated from the Bevalac data. Both normalizations have been rescaled such that their average values are unity. The four groups that occupy the center of the mosaic are shown as filled circles, while the outer eight square groups are shown as open circles. The four triangular groups were not renormalized with the flight data. It is apparent that all groups suffered a similar though not identical degradation in yield: Deviations from the average decrease of a factor of $\sim$2 were less than $\sim$6%. The normalization should be related to the light-collection efficiency of the position of the group in the counter as well as the absorption characteristics of the blocks in the group. Evidently, the center groups, which should show similar light-collection efficiencies, must have differing absorption characteristics.

The ratio of parameters B/A is $\sim$0.04, indicating that at the time of the flight, the extra background contribution b amounted to 4% of the relativistic primary Cerenkov signal. This is an increase of slightly more than a factor of two over the Bevalac value of $b = 0.017$ (§3.6.2), which is consistent with our assumption that this extra light is generated outside the radiator, insofar as the light collection is not dominated by paths through the radiator.

Chapter 4
Flight Data and Mass Analysis

4.1. Flight Summary

The HEIST instrument was launched from Palestine, Texas, at 0018 GMT on 14 May 1984 and spent approximately $35^h\ 32^m$ at a mean float altitude of 6.03 g/cm^2 of residual atmosphere. A fault in the ballast system caused the altitude to drop to ~8.5 g/cm^2 for a period of about seven hours during the second night of the flight (see Figure 4.1). The instrument was sealed in a pressurized and insulated aluminum shell 1.01 g/cm^2 thick, and the evaporative cooler maintained the NaI(Tl) stack at 24.5±0.6 ° C. The flight path ranged in vertical geomagnetic cutoff rigidity from ~4.1 GV to ~5.4 GV (see Figure 4.1), for an average of 4.60 GV, as interpolated from the 5 ° × 5 ° International Geomagnetic Reference Field for Epoch 1980.0 (Shea and Smart, 1983). The flight was terminated at 1703 GMT on 15 May and the payload recovered approximately 85 km southwest of San Antonio, Texas. 431,187 events were recorded on board. No serious problems with the instrument were encountered during the flight, and all electronic systems associated with the detectors and the data handling performed as expected.

4.1.1. Photomultiplier Gain Stability

The photomultiplier tubes showed excellent gain stability throughout the flight. To establish a relative gain for each photomultiplier in the plastic and NaI(Tl) scintillators for the entire flight, we required that the ratio of the mapped response of each tube to the total light yield in a layer (ΔL from §3.3) be identical when summed over a data set consisting primarily of particles that penetrated the NaI(Tl) stack without interacting. This data set was generated by requiring 15% agreement in the ratio of raw summed response from layer to layer, and was dominated by C, N, and O events. The

Figure 4.1

Residual atmosphere and vertical geomagnetic cutoff rigidity during the flight of the HEIST instrument from Palestine, Texas. An atmospheric depth of 6 g/cm^2 corresponds to an altitude of ~115,000 feet. A fault in the ballast system caused the altitude to drop to ~8.5 g/cm^2 for a period of about seven hours during the second night of the flight.

Figure 4.1

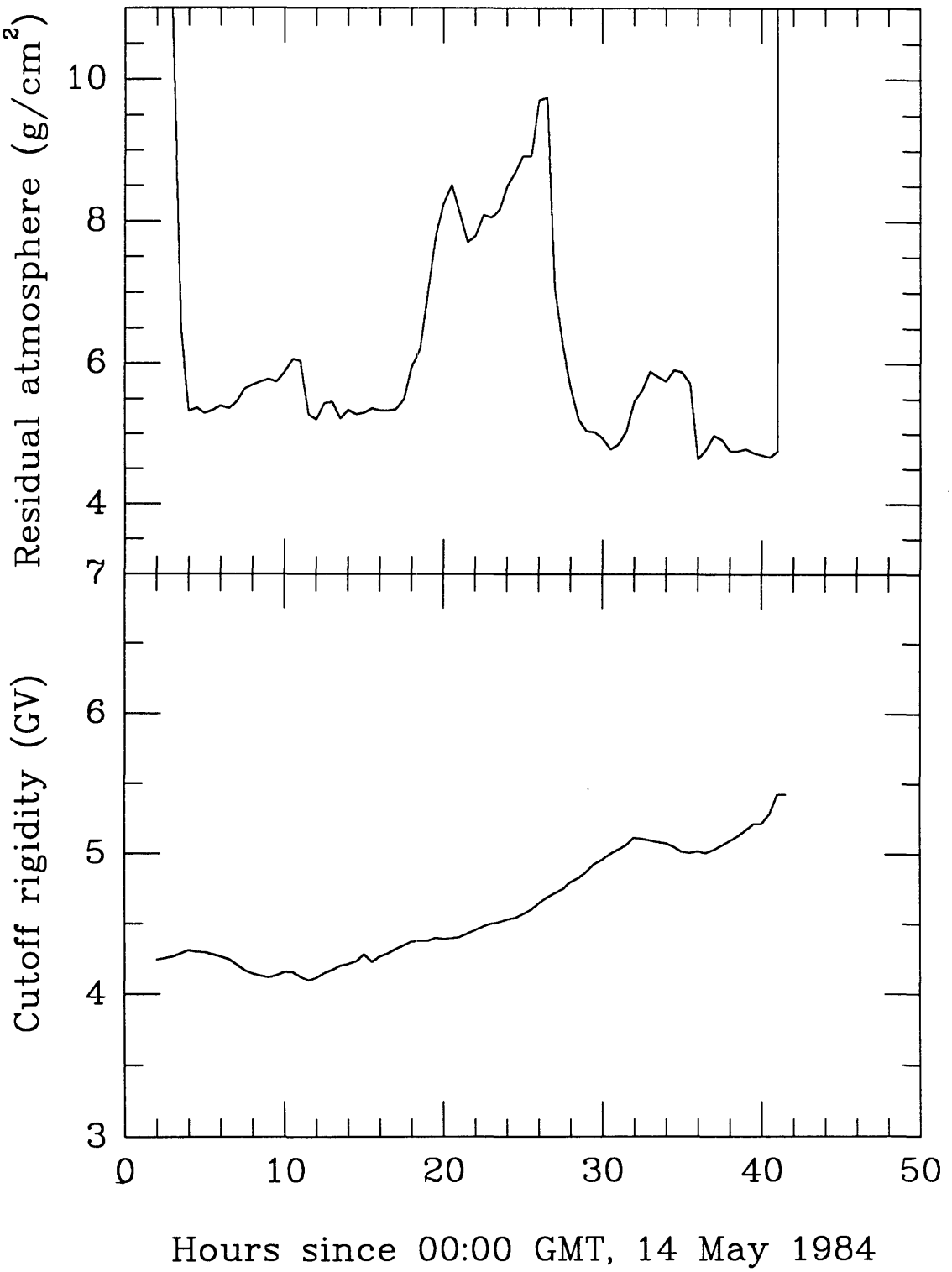
Residual atmosphere (g/cm^2)
10
8
6
4
7
Cutoff rigidity (GV)
6
5
4
3
0
10
20
30
40
50
Hours since 00:00 GMT, 14 May 1984

aerogel Cerenkov photomultipliers were balanced by requiring equal response summed over penetrating events passing within a radius of 5 cm of the center of the counter. To check for gain drifts, we divided the penetrating data into eight time periods and repeated the gain-balancing procedure in each period. Only a single tube, photomultiplier F on layer 9, varied in gain by more than 1.5%, and we were able to correct for this drift with a simple scale factor linear in the event number. The ADC pedestal values taken from EXTERNAL TRIGGER events (see §2.1.1) showed no drifts greater than 0.25 ADC bins and were taken to be constant.

Because a particle's total energy is measured by summing the responses in each of the NaI(Tl) layers, the layers must be normalized among themselves. This layer-to-layer balancing was accomplished with the Fe-group events from the data set of penetrating, non-interacting particles. The Fe group was selected by windowing on the mapped response ΔL in layers 1, 6, and 10, and the balancing factors were chosen to make each layer contribute to the sum of the layers an amount proportional to its thickness. The statistical uncertainty in the balancing factor for each layer is $\sim$0.4%. This precision is adequate, because all events must pass through at least five layers to trigger the system, which reduces the error in total energy from improper layer-to-layer balancing to $<$0.2%.

4.2. Monte Carlo Simulation

We have developed a detailed Monte Carlo simulation of the instrument in flight to estimate the expected number of Fe events and to aid in understanding the data selection procedure described in §4.3. The simulation follows a number of Fe cosmic rays from the top of the atmosphere down through the instrument, allowing them to undergo nuclear interactions as they progress, and includes the temporal variations of the atmospheric depth, livetime fraction, and vertical cutoff.

The incident Fe differential energy spectrum at the top of the atmosphere used in the simulation is our parameterization above 1000 MeV/nucleon of the French-Danish HEAO-3 Fe spectrum (Engelmann *et al.*, 1985),

$$\frac{dJ}{dE} = 1.90\,(E + m_u + 300\ \mathrm{MeV/nuc})^{-2.5}\quad \mathrm{m^{-2}sr^{-1}s^{-1}(MeV/nuc)^{-1}}\,, \qquad (4.1)$$

where E is the kinetic energy per nucleon in MeV/nucleon and $m_u = 931.5$ MeV is the mass per atomic mass unit. The HEAO data were taken from November 1979 to June 1980, when the Mt. Washington neutron monitor averaged 2190. This is reasonably close to the 26-day average of 2136 for our flight time period, so we conclude that the spectrum for our flight should show similar solar modulation. In any case, the effect of solar modulation on the Fe spectrum at energies above the Cerenkov threshold in the aerogel counter (~1300 MeV/nucleon) is relatively small (see §5.4).

Nuclear interaction lengths are calculated from the fit to the Bradt-Peters charge-changing cross sections with overlap given in Westfall *et al.* (1979):

$$\sigma_{\Delta Z \geq 1} = \pi r_0^2 (A_T^{1/3} + A_i^{1/3} - b)^2 , \qquad (4.2)$$

where A_i is the mass number of the incident nucleus and A_T the mass number of the target, and where $r_0 = 1.35 \pm 0.02$ fm and $b = 0.83 \pm 0.12$ for target species other than hydrogen. These parameters give a charge-changing interaction length for ^{56}Fe in NaI(Tl) of 44.2 g/cm^2. Thus Fe nuclei at typical angles (~30°) and typical energies (~1500 MeV/nucleon) stopping in the instrument must traverse ~1.5 interaction lengths of NaI(Tl) alone, and the simulation shows that ~92% of cosmic-ray Fe nuclei that trigger the instrument suffer charge-changing interactions before they stop: some 40% interact in the atmosphere, and the remainder interact in the instrument. Atmospheric depth data were supplied by the National Scientific Balloon Facility. Livetime fractions were calculated from the observed event rate and the known behavior of the trigger-logic subsystem. Estimated effective cutoff rigidities at arbitrary zenith and azimuth angles were generated by scaling from the tables of Shea and Smart (1975).

To verify that the simulation accurately mimicked the performance of the instrument, we modeled a single hour from the flight and compared the predicted number of Fe and O entering layers 1 and 2 without having interacted with the number actually observed. We created a flight data set of all events that triggered the system for the hour beginning 1100 GMT on 14 May 1984, and ran the simulation with the appropriate atmospheric depth, livetime fraction, and geomagnetic cutoff rigidity. From the data, we selected all events in the O peak in the pathlength-corrected mapped response, $\Delta L/\sec\theta$, in layer 2 and subtracted the estimated number of N and F nuclei

contaminating that peak. We selected those Fe events that had pathlength-corrected mapped responses in layers 1 and 2 that were within 5% of each other. We counted ~875 O and ~70 Fe, while repeated runs of the simulation gave 922±30 O and 60±8 Fe. The agreement is satisfactory, and we conclude that the simulation is sufficiently accurate.

For the entire flight the simulation predicted that 180±14 Fe should have stopped in the NaI(Tl) stack without interacting. Approximately 50% of these had energies below the Cerenkov threshold or a fraction of relativistic light $f(n,\gamma) < 2\%$ (see §4.3.8), and ~34% of the remaining events had trajectories that passed within 3 mm of an aerogel block edge. Approximately 6% of those events that survived these cuts were within 3 mm of the edge of the hermetic can center plug or a NaI(Tl) layer. Note that the predicted fraction below threshold is strongly dependent on the model we have chosen for the cutoff rigidity at arbitrary angles and the value of the vertical cutoff, and therefore may not be a realistic prediction. Finally, we have rejected all simulated events passing through the triangular aerogel groups, amounting to ~5% of the remainder. The simulation thus predicted for the entire flight 54±8 Fe events with energies above Cerenkov threshold and stopping in the NaI(Tl) stack having undergone no charge-changing interactions.

4.3. Data Selection

As discussed in §2.2.5, we have chosen to analyze only the Fe-group nuclei, which stop in the NaI(Tl) stack. Since such events comprise only ~0.01% of the events recorded during the flight, we must be cautious in rejecting data. Figure 4.2 presents a flow chart for the data selection and mass analysis. Ovals mark points at which the data or the maps enter the procedure; diamonds mark selection decisions; rectangular boxes mark steps in the linear progression of the algorithm; and octagons mark stopping points. Sections 4.3.1 to 4.3.12 following summarize each step in the algorithm.

4.3.1. Translate Tapes

The data tapes recorded in the on-board VCRs are first translated to 75 ips magnetic tape. Two cuts on data quality are applied in the translation. First, the video playback circuit passes only those events that begin with the proper 16-bit sync word, thereby ensuring that each event translated to magnetic tape begins in the proper phase. Second, the translation software requires that the first and second copies of the event in a video frame be identical. This cut removes events that have a high tape noise level, those that drift out of sync somewhere in the video frame, and those with other recording problems. Note that the checksum, which was present in each copy, was not used to verify the data quality, since the consistency check between the first and second copies proved adequate to reject the poorly recorded events. Approximately 98.5% of the 431,187 events recorded on VCR tape met these criteria and were successfully translated to magnetic tape. This success rate is typical of the results of preflight tests of the video recording and playback systems.

4.3.2. Select Events Not Flagged

Events marked by a HAZARD or EXTERNAL TRIGGER flag are removed at this time. The HAZARD flag is set whenever an event is preceded within 256 μs by a T1T2 coincidence. The EXTERNAL TRIGGER flag labels events that are generated periodically by the trigger logic and do not correspond to heavy ion events. These EXTERNAL TRIGGER events were used to verify the value and stability of the ADC pedestals during the flight. See §2.1.1 for a more complete discussion of these flags. As indicated by the real-time housekeeping data printouts, the T1T2 coincidence rate averaged $\sim$500 s^{-1} during the flight, which implies by Poisson statistics that $\sim$12% of the events should have been flagged as HAZARD events. In addition, from the average trigger rate throughout the flight of $\sim$3 s^{-1}, we expect that $\sim$4800 EXTERNAL TRIGGERs should have been generated by the 1.5-second timeout triggers (see §2.1.1) during the flight, comprising $\sim$1% of the total data set. We observed that approximately 14% of the events that reached this step had one or both flags set and were rejected, leaving $\sim$365,000 events. This is good agreement.

Figure 4.2

Flow chart of the data selection and mass analysis. Ovals mark points at which the data or the maps enter the procedure; diamonds mark selection decisions; rectangular boxes mark steps in the linear progression of the procedure; and octagons mark stopping points.

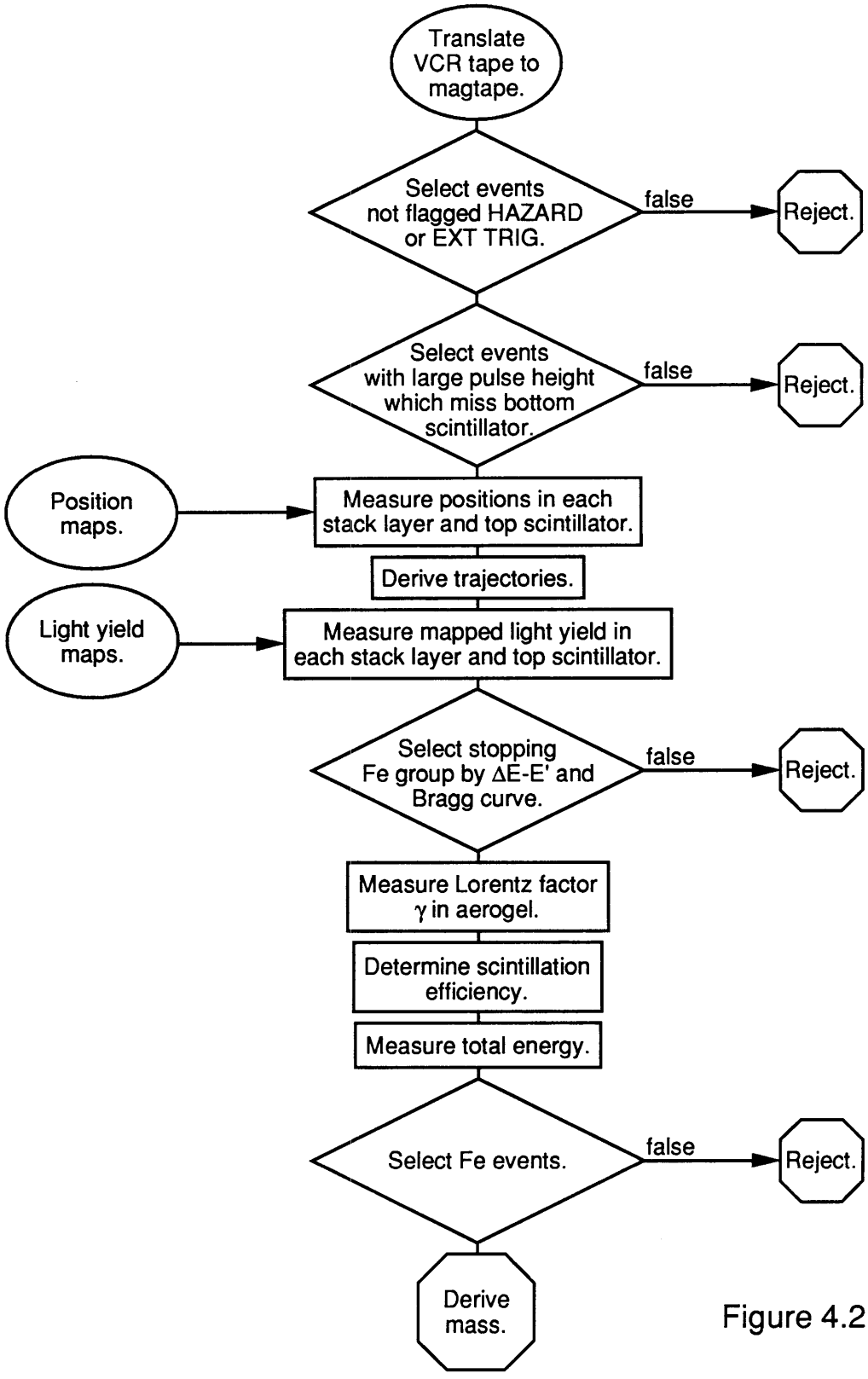
Translate VCR tape to magtape.
Select events not flagged HAZARD or EXT TRIG.
false
Reject.
Select events with large pulse height which miss bottom scintillator.
false
Reject.
Position maps.
Measure positions in each stack layer and top scintillator.
Derive trajectories.
Light yield maps.
Measure mapped light yield in each stack layer and top scintillator.
Select stopping Fe group by ΔE-E' and Bragg curve.
false
Reject.
Measure Lorentz factor γ in aerogel.
Determine scintillation efficiency.
Measure total energy.
Select Fe events.
false
Reject.
Derive mass.

Figure 4.2

4.3.3. Select Large Pulse Height in Layer 1, Miss Bottom Scintillator

The data selected to this point are dominated by elements of the CNO group and wide-angle He that manage to trigger the system. A selection criterion that removes these events but safely passes the Fe events would significantly reduce the computational burden for the remainder of the data selection and analysis. Such a criterion would be one that accepts only events with large responses in the first NaI(Tl) stack layer.

The data set of penetrating particles discussed in §4.1 indicates that typical Fe events near the center of the first NaI(Tl) layer have total pulse heights in the sum of the six photomultipliers of ~2000 ADC bins. It also shows that the minimum value of this raw sum is ~1000 bins. We chose conservatively to accept only those events generating 500 bins or more in the raw sum of six photomultipliers in layer 1.

Events that show no response in the bottom plastic scintillator have either stopped in the NaI(Tl) stack, escaped out the side of the stack, or interacted in the stack in such a way that all daughters have either stopped or escaped. In contrast, penetrating events and most interacting events show a significant signal in the bottom scintillator. Since ~75% of the Fe nuclei are expected to suffer charge-changing nuclear interactions in the NaI(Tl), a cut that passes only those events with a reasonably small signal in the bottom scintillator should remove a large fraction of the remaining unwanted data.

We cannot put the cut at the value of the sum of the six ADC pedestals because those pedestals are not strictly constant. A histogram of the scintillator pedestal noise distribution made just prior to flight indicates that the summed pedestals have an rms variation of 1.7 bins. Thus the cut must be at least several bins above the nominal pedestal sum to pass all the good events, but it should not be so high as to pass a significant fraction of the interaction products. We can use sea-level muons to estimate the response for relativistic protons at typical angles during flight, or we can scale from typical relativistic Fe from the flight if we correct for the difference in scintillation efficiencies (Salamon and Ahlen, 1981, and §2.2.3). Both methods give ~5 bins in the sum of six photomultipliers for minimum-ionizing particles in the NaI(Tl) and ~8 bins

in the plastic scintillators. We have conservatively placed the cut between relativistic H and He, 18 bins more than the pedestal in the bottom scintillator.

Only 9261 events survive these cuts.

4.3.4. Measure Positions

Next we measure positions in the top scintillator and the first 10 layers of the stack for the 9261 remaining events. Recall that detailed maps of the last two layers could not be generated at the Bevalac. The position algorithm is described in detail in §3.2 and Appendix B. No events were rejected.

4.3.5. Derive Trajectory

From the measured positions in the stack and top scintillator we derive a linear trajectory for each particle through the instrument. This algorithm is described in detail in §3.2.2. Briefly, we perform a linear least-squares fit to the measured positions, rejecting positions from layers having one or more of the following characteristics: positions that deviate from the fit by more than two sigma, default positions assigned when the position algorithm fails, or mapped responses that are $<70\%$ of the response in the first stack layer. The last cut eliminates layers after a particle stops in the NaI(Tl). The algorithm is implemented such that it will never fail to provide a trajectory, and no events are rejected.

4.3.6. Measure Responses

For the 9261 events, we measure the mapped response ΔL in each of the 12 stack layers and the top scintillator, correcting for the spatial variation of the light-collection efficiency as described in §3.3. For bookkeeping purposes, we assign a known large response to those layers with positions from the trajectory that lie off the NaI(Tl) disk. Layers assigned this known response will not be considered in the total energy calculation to follow (§4.3.10).

4.3.7. Select Stopping Fe Group

We select stopping Fe-group nuclei with a two-step process. First, we require that the events lie on or near the Fe track formed by plotting the pathlength-corrected mapped response $\Delta L_1/\sec\theta$ in layer 1 against the total energy deposited in the stack. Neglecting scintillation efficiency, the pathlength-corrected mapped response in a single layer is proportional to the specific ionization energy loss dE/dx and therefore to Z^2. Thus the elements should form tracks separated approximately by the ratio of the square of their charges, which is $\sim$8% in the case of Fe and Mn. This scatter plot appears in Figure 4.3, where to approximate the total energy, we have simply summed the mapped responses of all 12 layers, rejecting layers with trajectories that lie off the disk. The layers were normalized one to another with the data set of penetrating, non-interacting Fe from the flight according to the procedure described in §4.1. The trapezoid marks the window about the Fe track, and has a half-width of about 8% in $\Delta L_1/\sec\theta$. Note that Fe events with measured $\sec\theta$ in error by more than $\sim$8% would be rejected by this cut. In §3.2.3, we saw that the trajectory resolution was $\sigma_{\sec\theta} \sim 0.02$, or $\sim$2% for typical Fe events. Thus, if the trajectory errors are normally distributed, events with errors as large as 8% should be extremely rare. The smearing of the tracks is the result of the $\sim$1% energy resolution, the mass differences among the isotopes, and the crude event selection criteria to this point that pass most interacting events. Much of the background is due to events that do not stop in the NaI(Tl), but instead escape out the side of the stack without hitting the bottom scintillator. We find that 358 events satisfy the cut about the Fe track.

Second, we plot the Bragg curve for each event that lies in the window about the Fe track—that is, we plot the average dE/dx in each layer, which we approximate as the mapped response multiplied by the layer-to-layer balancing factor and divided by the layer thickness. We select by hand those events with smooth Bragg curves and no evidence of interaction daughters in the layers following the stopping layer. Examples of a particle with a smooth Bragg curve and a particle that interacts and has accompanying daughters appear in Figure 4.4. Neutron-stripping interactions and interactions in the stopping layer that do not produce obvious long-ranged daughters cannot be detected by the procedure. Indeed proton-stripping interactions may be difficult to

detect since the proton generates a signal that is only ~5 bins in the sum of six photomultipliers on each layer (§4.3.3), or ~1/400 of the Fe response. We have tried to be lenient in selecting events, so that those events with questionable Bragg curves are allowed to pass, to be rejected later if necessary. Of the events in the window about the Fe track, 197 events appear to have good Bragg curves and are candidates for stopping Fe. Recall that the Monte Carlo simulation predicted 180±14 stopping Fe.

4.3.8. Measure Lorentz Factor

We measure the Lorentz factor γ from the C/S ratio, as described in detail in §3.7. We reject all events with trajectories that pass within 3 mm of any aerogel block edge. Because we could not derive sufficiently accurate normalizations for the triangular corner groups of the aerogel mosaic, we also reject all events that pass through these groups. We find that these cuts remove ~36% of the Fe-group events, in good agreement with the simulation, which predicted ~39% for these two cuts (see §4.2). In addition, to reduce the possibility that fluctuations in the light yield might cause events are below threshold to appear to be above threshold, we reject all events with an apparent fraction of relativistic light f(γ) below 2%. We find that ~56% of the remaining Fe-group events are thus rejected, which is somewhat larger than the ~50% predicted by the simulation. Since the fraction below threshold depends strongly on the incident spectrum and the filtering by the geomagnetic field, the magnitude of the discrepancy between the observation and the prediction is perhaps not unreasonable. The simulation rejected an additional ~6% for passing near the edges of the hermetic can center plug or the NaI(Tl) disks, although none of the flight events were so rejected. We find that 55 Fe-group events survive. Recall that the simulation predicted 54 surviving Fe alone.

4.3.9. Determine Scintillation Efficiency

We calculate the average scintillation efficiency and the energy loss above the stack for model particles using the algorithm described in §3.5. None of the 55 events passed through the hermetic-can center plug, so no corresponding correction to the energy loss was necessary. The calculated scintillation efficiencies for the model ^{56}Fe

Figure 4.3

Selection of stopping Fe-group events. The trapezoid encloses the events selected as members of the Fe group ($24 \leq Z \leq 28$) that stop in the NaI(Tl) stack. To reduce the clutter, only 10% of the data with $\Delta L_1/\sec\theta < 0.4$ have been plotted. The smearing of the track is the result of the $\sim$1% energy resolution, the mass differences among the isotopes, and the crude event selection criteria to this point that pass most interacting events. Much of the background is due to events that do not stop in the stack, but instead escape out the side of the stack without striking the bottom scintillator.

Figure 4.3

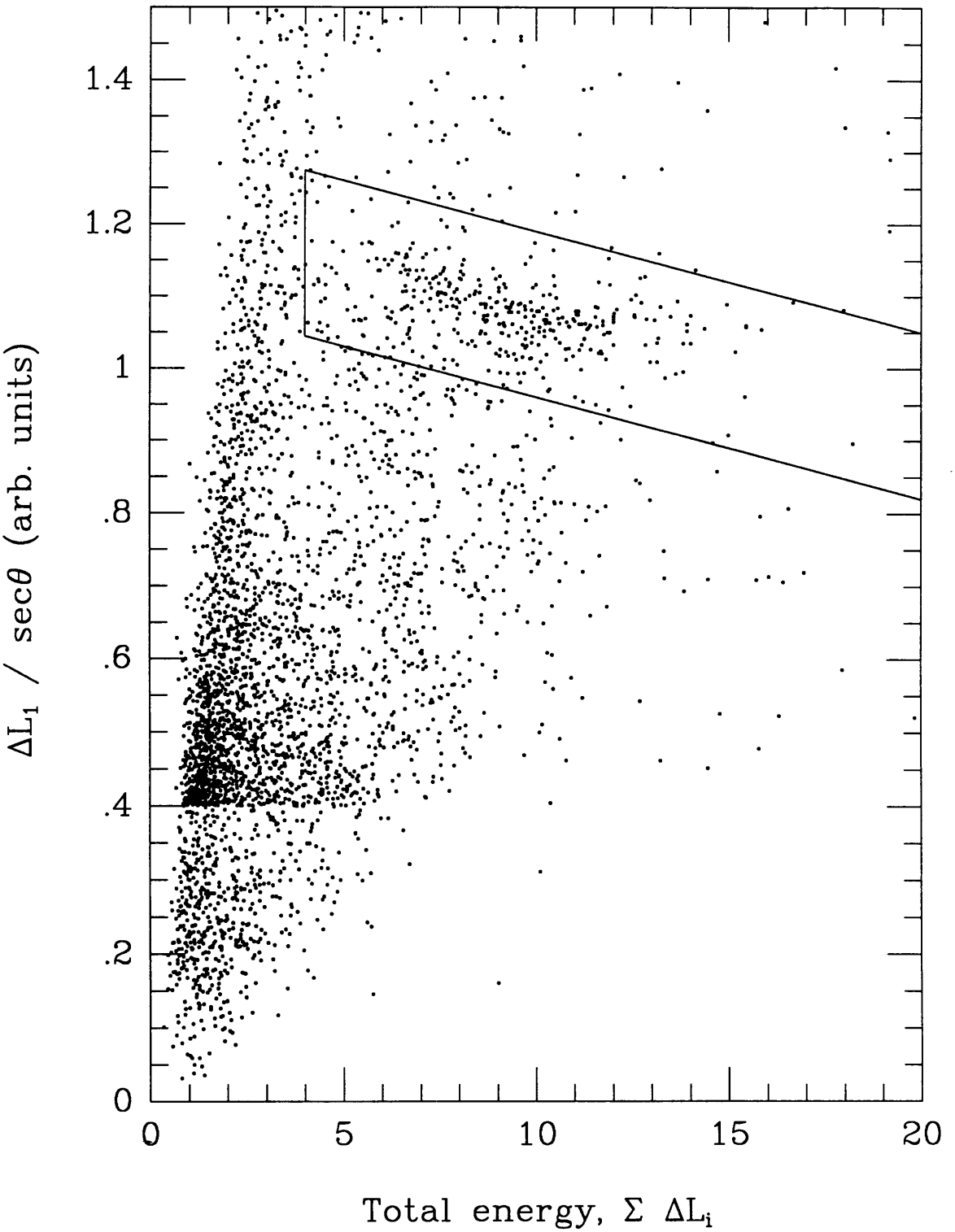
1.4
1.2
1
.8
.6
.4
.2
0
0
5
10
15
20
ΔL_1 / secθ (arb. units)
Total energy, Σ ΔL_i

Figure 4.4

Examples of Fe-group nuclei that stop in the NaI(Tl) without interacting and that suffer charge-changing interactions in the NaI(Tl).

Figure 4.4

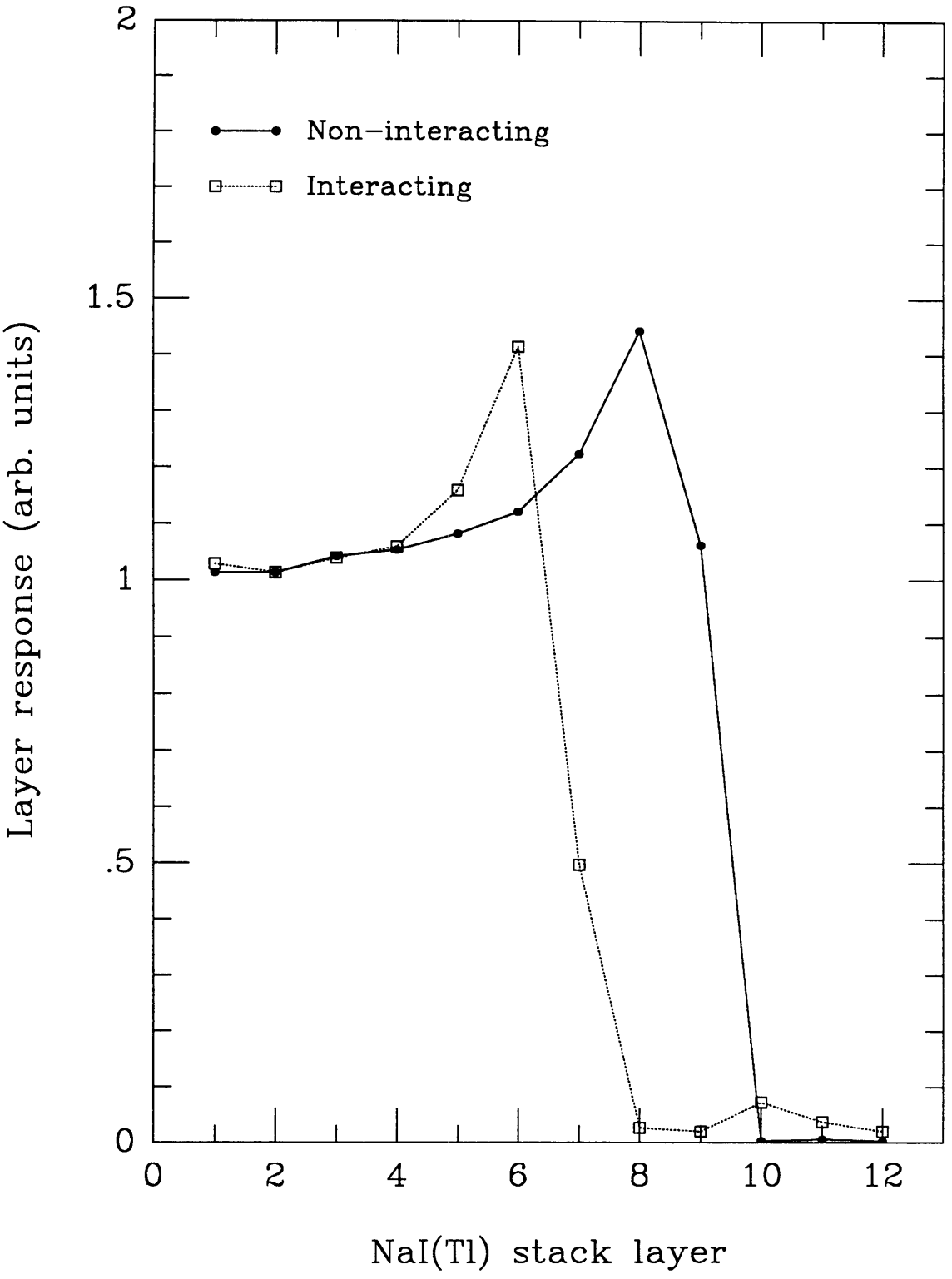
Non-interacting
Interacting
Layer response (arb. units)
NaI(Tl) stack layer
0
.5
1
1.5
2
0
2
4
6
8
10
12

trajectories will be used in the total energy algorithm (§4.3.10) and in the final selection of Fe events (§4.3.11).

4.3.10. Measure Total Energy

Total energies are measured as in §3.6. The total energy is derived from the measured scintillation light yield in the NaI(Tl) stack, the calculated energy loss in the material between the center of the aerogel and the first stack layer, and the average scintillation efficiency. Again, none of the 55 events passed through the hermetic-can center plug, so no corresponding energy correction was necessary.

4.3.11. Select Fe Events

We perform the final selection of Fe from among the surviving Fe-group events by measuring the charge at three places in the instrument: in layers 1 and 2 of the NaI(Tl) stack, in the last four layers of each particle's range, and in the last two layers of each particle's range. The algorithms used to measure charge are discussed below. From the three charge measurements, we form a "charge quality" parameter that quantifies the difference from Fe in terms of the charge resolution, and select only those events with good charge quality and the correct charge number.

Charges are measured in the first two stack layers by comparing the measured scintillation responses ΔL_1 and ΔL_2 with the calculated light yields ΔL_{c1} and ΔL_{c2} for the best-fit model ^{56}Fe particles generated in §4.3.9. The charge in the top scintillator is, therefore, given by

$$Z_L = 26 \left\{ \frac{1}{2} \left[\frac{\Delta L_1}{\Delta L_{c1}} + \frac{\Delta L_2}{\Delta L_{c2}} \right] \right\}^{1/2} . \tag{4.3}$$

The square root accounts for the fact that the energy loss in the NaI(Tl) is proportional to Z^2. Note, however, that the charge scale is compressed by the saturation of the scintillation response: if we substitute the calculated light yield of a model ^{55}Mn nucleus of the same range for the observed light yields, we find an apparent charge $Z_L = 25.3$. We chose to average the responses in two layers to reduce the charge uncertainty, which is dominated by the uncertainty in the observed light yields. It averages $\sigma_L \sim 0.33$ charge

units for the surviving 55 Fe-group events.

Near the end of range, a variation of the dE/dx-E technique for determining mass discussed by Stone (1974) can be used to measure the charge. We can approximate the range-energy relation for a particle of charge Z, mass $M = Am_u$, and kinetic energy E as a power law,

$$R = k \frac{A}{Z^2} \left(\frac{E}{M}\right)^{\alpha}, \tag{4.5}$$

and we can write a similar relation for the residual range $R' = R - T$ for the particle after it has traversed a pathlength $T = T_0 \sec\theta$,

$$R' \equiv R - T = k' \frac{A}{Z^2} \left(\frac{E'}{M}\right)^{\alpha'}, \tag{4.6}$$

where E' is the residual kinetic energy. Following Lau (1985), we note that with only two equations in three unknowns—R, Z, and A—the solution will not be unique. However, we know that the mass is approximately twice the nuclear charge, so we can define a mass difference ΔA such that

$$A \equiv 2Z + \Delta A \tag{4.7}$$

and solve for A and Z simultaneously. Because of the large energy loss in the thick NaI(Tl) layers, a single power law for both R(E) and $R'(E')$ is inadequate. Extending Lau's treatment to the case of two distinct power laws, we find

$$\hat{Z} = \left[\frac{k}{T_0 \sec\theta \, 2^{\alpha-1} m_u^{\alpha}} \right]^{\frac{1}{\alpha+1}} \left(E^{\alpha} - \frac{k'}{k} m_u^{\alpha-\alpha'} A^{\alpha-\alpha'} E'^{\alpha'}\right)^{\frac{1}{\alpha+1}}, \tag{4.8}$$

where

$$\hat{Z} \equiv Z \left[1 + \frac{\Delta A}{2Z}\right]^{\frac{\alpha-1}{\alpha+1}} \approx Z + \frac{\alpha-1}{\alpha+1} \frac{\Delta A}{2}. \tag{4.9}$$

The kinematics program discussed in §3.5 was used to simulate the slowing-down and stopping of the model ^{56}Fe particles in a thick slab of NaI(Tl). Best estimates of the power-law index α and coefficient k were obtained from fits to the calculated ranges

for a variety of energy intervals and are presented in Table 4.1. Deviations of the fits from the calculated ranges are $<0.1\%$ for the three highest energy intervals, but rise as high as $\sim 0.5\%$ for the lowest three intervals.

Table 4.1: Range-Energy Relations in NaI(Tl)

$$R = k \frac{A}{Z^2}(\gamma - 1)^{\alpha}$$

Energy (MeV/nucleon)	k (g/cm^2)	Index α
100-400	522.7	1.590
300-700	486.7	1.515
600-1000	465.5	1.411
1150-1400	470.3	1.290
1400-1650	478.2	1.250
1650-2150	492.3	1.201

We use Equation (4.8) to identify the charge of each of the 55 selected events near the particle's end of range in the following two independent ways: (1) we take the residual energy measurement E' from the stopping layer and the energy loss ΔE from the previous layer, and (2) we take E' from the final two layers of the range and ΔE from the two previous layers. In both cases we calculate E' and ΔE from the measured light yield and the estimated average scintillation efficiency $<dL/dE>$ in the appropriate NaI(Tl) layers for the best-fit model ^{56}Fe particles of §4.3.9:

$$E' = \frac{L'}{<dL/dE>'} \qquad \Delta E = \frac{\Delta L}{<dL/dE>_{\Delta}} . \tag{4.10}$$

We denote the charge determined from the stopping layer and the previous layer as $\hat{Z}_1$. Fe-group particles enter the stopping layer with energies ranging from ~ 0 to ~ 350 MeV/nucleon and enter the previous layer with energies from ~ 300 to ~ 700 MeV/nucleon. Because the calculation of E' depends strongly on the precise energy-dependence of the scintillation efficiency, we have not measured the charge of those

events that enter their stopping layer with residual range $R' < 1$ g/cm^2, or $E' < 90$ MeV/nucleon. Instead, we have labeled those events as ^{56}Fe for $\hat{Z}_1$. Only four of the 55 remaining events are so affected. Note that the common isotopes of Fe have $A > 2Z$: thus equation (4.8) and the values from Table 4.1 imply that ^{56}Fe nuclei should have an effective charge $\hat{Z}_1 = 26.4$. The estimated charge resolution from the uncertainty in E', ΔE, and $\sec\theta$ is $\sigma_1 \sim 0.33$ charge units, averaged over the 55 surviving Fe-group events.

Similarly, we denote the charge determined from the final two layers and the two previous layers as $\hat{Z}_2$. Fe-group particles have $300 < E' < 700$ MeV/nucleon and $600 < \Delta E < 1000$ MeV/nucleon. In this case, ^{56}Fe nuclei should have an effective charge $\hat{Z}_2 = 26.2$ and an average charge resolution $\sigma_2 \sim 0.25$ charge units.

From the three measured charges for each event, we form the following quantity, the "charge quality" ς^2, which is a measure of the deviation of measured charge from the effective charge for ^{56}Fe,

$$\varsigma^2 = \sum_i \left[\frac{Z_i - <Z_i>}{\sigma_i} \right]^2, \qquad (4.11)$$

where the sum runs over the three measurements of the charge, where $<\hat{Z}_1> \equiv 26.4$, $<\hat{Z}_2> \equiv 26.2$, and $<Z_L> \equiv 26$, and where the compression of the Z_L charge scale has been accounted for. The charge quality should be distributed as χ^2 for three degrees of freedom. An error of a single charge unit in any one of the three charges corresponds to ~9-16 units of charge quality.

The charge quality is plotted against the weighted average of the three charge measurements in Figure 4.5 for the remaining 55 Fe-group events. It is apparent that the value of ς^2 rises rapidly as the measured charge deviates from 26. Also indicated on the figure are the expected locations of Mn ($Z = 25$) and Cr ($Z = 24$) events. The window placed on the Fe-group track (§4.3.7) is expected to pass some Mn as well as, perhaps, some Cr and Ni ($Z = 28$). We accept all events with charge 26 ± 0.5 and charge quality $\varsigma^2 < 8$, equivalent to a probability of not exceeding $\chi^2(3)$ of 95%, and close to the value of ς^2 expected for an error of a single charge unit in one of the three charges.

Figure 4.5

Final selection of stopping Fe. The charge quality is a measure of the deviation of the observed charge from the expected charge for ^{56}Fe and is distributed as χ^2 with three degrees of freedom. The dotted lines indicate the probability of not exceeding $\chi^2(3)$. The dashed box encloses the 32 selected events.

Figure 4.5

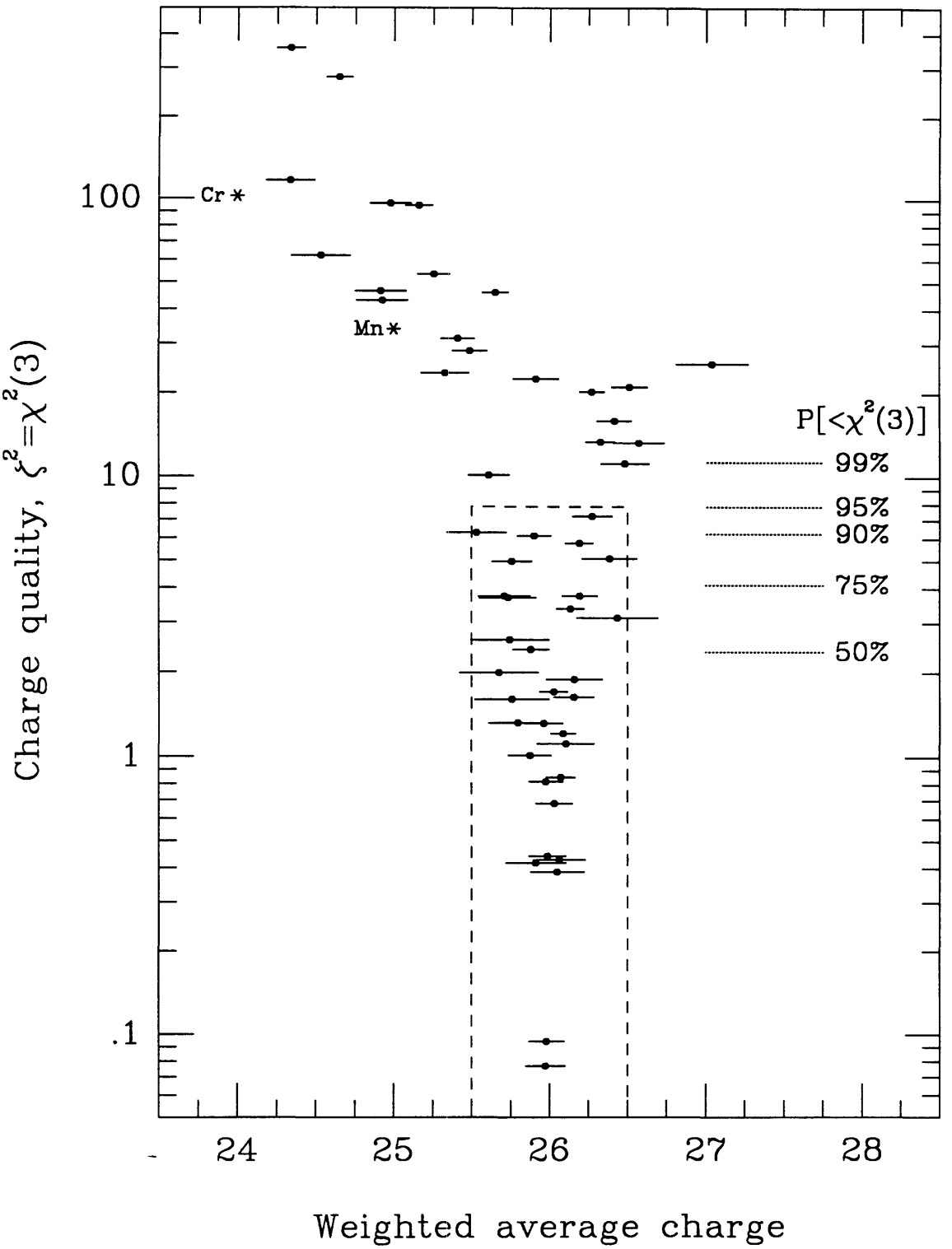
Charge quality, $\zeta^2=\chi^2(3)$
100
10
1
.1
Cr*
Mn*
$P[<\chi^2(3)]$
99%
95%
90%
75%
50%
24
25
26
27
28
Weighted average charge

Figure 4.6

Histogram of calculated masses for the 32 Fe events. The mass scale is arbitrary and has been chosen to place the mass peak near 56 amu.

Figure 4.6

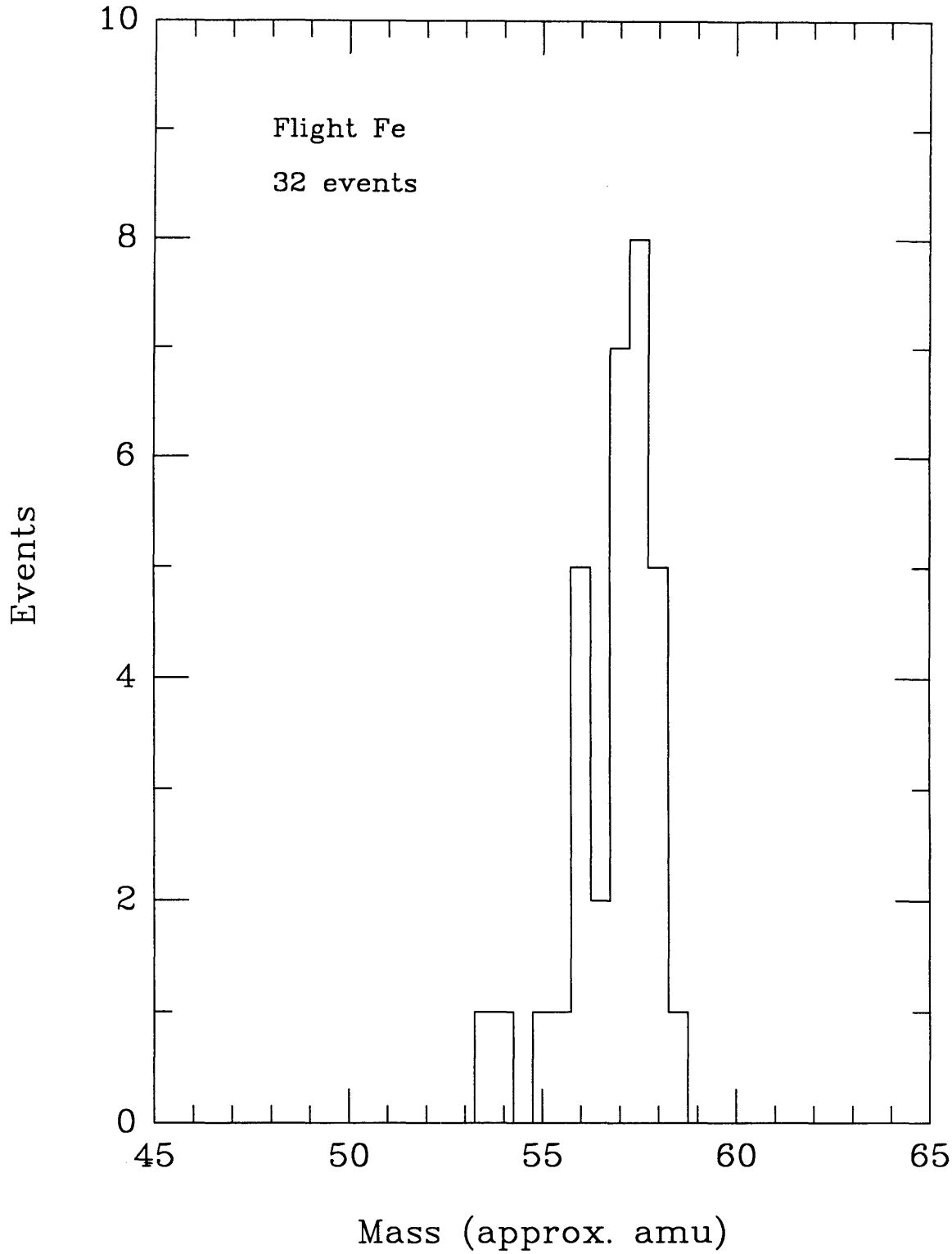
Flight Fe
32 events
Events
Mass (approx. amu)
0
2
4
6
8
10
45
50
55
60
65

The 32 surviving events form our final Fe data set. This number is significantly smaller than the predicted number of 54±8 from the Monte Carlo simulation. It is unlikely that the difference is entirely statistical, as the cumulative Poisson probability of observing 32 or fewer events, when 54 were expected, is much less than 1%. We must conclude that systematic effects in the stack that are not modeled in the simulation cause some events to be rejected as having poor charge quality. Any process in which the incident particles lose energy that is never converted to scintillation photons would have this effect. The true source of the discrepancy remains unknown.

4.3.12. Derive Mass

The mass derived from the Cerenkov-Energy technique is

$$A_{CE} = \kappa \frac{\Delta E_m}{(\gamma_m - 1)}, \tag{4.12}$$

where ΔE_m is the measured total energy loss from §4.3.10, and γ_m, the measured Lorentz factor from §4.3.8. The proportionality constant κ is necessary because the total-energy algorithm does not provide an absolute energy scale.

4.4. Final Fe Mass Histogram

The final mass histogram for the 32 selected Fe events is shown in Figure 4.6. The mass scale has been chosen to place the mass peak near 56 amu. The interpretation of this histogram is deferred to §5.3, where a maximum-likelihood technique will be used to extract the $^{54}Fe/^{56}Fe$ and $^{58}Fe/^{56}Fe$ abundance ratios, the mass resolution, and the mass scale factor required to move ^{56}Fe to 56 amu.

Chapter 5
Interpretation of Measurements

5.1. Cross Sections for Nuclear Interactions

The composition of cosmic rays observed at Earth is modified from that at the galactic cosmic ray source (GCRS) by propagation through ~5-8 g/cm^2 of the interstellar medium (ISM), consisting of ~90% H and ~10% He by number (e.g, Meyer, 1987). Because such a pathlength is significantly longer than the mean-free-path for mass-changing interactions for Fe in H (~2 g/cm^2), the vast majority of primary cosmic rays in the Fe group will undergo nuclear interactions before being collected. Proper interpretation of the observed isotopic abundances therefore requires an accurate knowledge of the appropriate interaction cross sections.

Extrapolations of the previous observations of the isotopic composition of Fe back to the GCRS (Tarlé *et al.*, 1979; Mewaldt *et al.*, 1980; Webber, 1981; and Young *et al.*, 1981) have relied on the semiempirical relations of Silberberg and Tsao (1973a, 1973b, 1977; and Tsao and Silberberg, 1979), which have an estimated accuracy of ~30%. Since the late 1970s and the availability of beams of relativistic heavy nuclei at the Bevalac, significant progress has been made in measuring the cross sections relevant to cosmic-ray propagation calculations. In particular, the recent measurements (e.g., Webber, 1983) of the fragmentation of heavy nuclei, including ^{56}Fe, at a variety of energies up to ~2000 MeV/nucleon have permitted Webber (1987) to develop a formula that predicts the observed cross sections in H to an accuracy of ~10% or better.

The important relevant changes in the cross sections are summarized in Figure 5.1, which shows the neutron-stripping cross sections for ^{56}Fe at 1000 MeV/nucleon as calculated by the original formalism of Silberberg and Tsao (1973a) and by the formalism of Webber (1987). Note the decrease of the Webber values relative to the Silberberg and Tsao values by a factor of ~2 in the cross section for ^{56}Fe into ^{54}Fe and by a

Figure 5.1

Neutron-stripping cross section of ^{56}Fe on hydrogen at 1000 MeV/nucleon as calculated by Webber (1987) and Silberberg and Tsao (1973a). The two-neutron-stripping cross section of Webber is a factor of $\sim$2 lower than that of Silberberg and Tsao, and the three-neutron-stripping cross section is a factor of $\sim$10 lower.

Figure 5.1

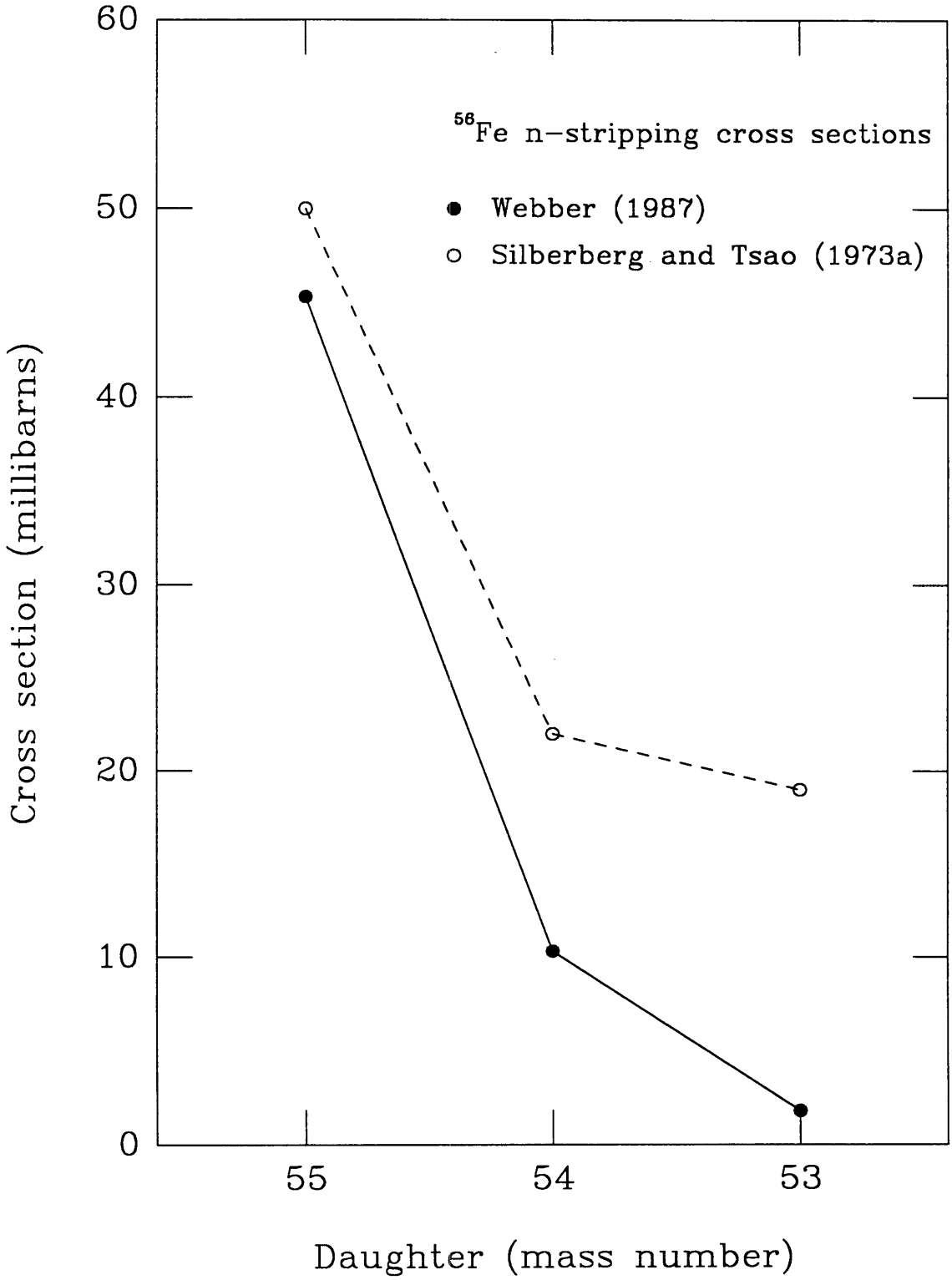
60
50
40
30
20
10
0
Cross section (millibarns)
^{56}Fe n-stripping cross sections
Webber (1987)
Silberberg and Tsao (1973a)
55
54
53
Daughter (mass number)

factor of ~10 in the cross section for ^{56}Fe into ^{53}Fe. The former has a substantial effect on the interpretation of the ^{54}Fe/^{56}Fe ratio observed at Earth. For example, assuming a solar-system abundance ratio at the GCRS, Webber's cross sections predict ~15% less ^{54}Fe at Earth at ~1500 MeV/nucleon than do the original Silberberg and Tsao cross sections.

The energy-dependence of sample total and partial cross sections for neutron-stripping according to Webber (1987) is shown in Figure 5.2. It is apparent that the total cross sections have only a small dependence on energy, varying by ~15% from 200 MeV/nucleon to 2000 MeV/nucleon, while the partial cross sections are ~50% larger at several hundred MeV/nucleon than at 1000 MeV/nucleon. The energy dependence of the cross sections has been included in the propagation calculations (§5.2 and §5.4) and has a small effect on the interpretation of the observed mass histograms.

The cross sections for Fe on H at 1000 MeV/nucleon calculated by the formulation of Webber (1987) are listed in Table 5.1 below. The total cross sections are for all mass-changing interactions. The values in parentheses are calculated according to Silberberg and Tsao (updates to 1979). Isotopes ^{53}Fe and ^{52}Fe decay by β^+ emission with half-lives of 8.5 minutes and 8.3 hours, respectively. Because the half-lives are so short, the cross sections into these two isotopes are added instead to those of their respective stable daughters, ^{53}Mn and ^{52}Cr, for the galactic propagation described in §5.4. The undecayed cross sections given in the table for these isotopes are appropriate for calculations of propagation in the atmosphere and in the instrument (§5.2).

Table 5.1: Cross Sections for Iron on Hydrogen
1000 MeV/nucleon, Values in millibarns

		daughter						
		total	^{57}Fe	^{56}Fe	^{55}Fe	^{54}Fe	^{53}Fe	^{52}Fe
parent	^{58}Fe	778	67.0	14.8	3.6	0.2	(1.4)	(0.32)
	^{57}Fe	769	0	57.8	12.6	3.0	(2.4)	(0.56)
	^{56}Fe	760	0	0	45.3	10.3	1.8	(0.98)
	^{55}Fe	751	0	0	0	34.2	(6.8)	(3.0)
	^{54}Fe	742	0	0	0	0	(34.7)	(3.7)
	^{53}Fe	733	0	0	0	0	0	(30.3)
	^{52}Fe	724	0	0	0	0	0	0

Table 5.2 contains a similar set of cross sections for Mn, and will be used in §5.3 to interpret the Bevalac mass histogram. Again, values are from Webber (1987), except for those in parentheses, which are from Silberberg and Tsao (updates to 1979).

Table 5.2: Cross Sections for Manganese on Hydrogen
1000 MeV/nucleon, Values in millibarns

		daughter					
		total	^{54}Mn	^{53}Mn	^{52}Mn	^{51}Mn	^{50}Mn
parent	^{55}Mn	751	61.7	14.7	(9.4)	(3.5)	(0.5)
	^{54}Mn	742	0	48.9	(11.6)	(5.0)	(0.9)
	^{53}Mn	732	0	0	(37.8)	(6.2)	(2.6)
	^{52}Mn	722	0	0	0	(32.8)	(3.3)
	^{51}Mn	712	0	0	0	0	(28.4)
	^{50}Mn	702	0	0	0	0	0

Figure 5.2

The energy dependence of the total cross section for mass-changing interactions and the partial cross sections for single and double neutron-stripping for ^{56}Fe on hydrogen, calculated according to Webber (1987).

Figure 5.2

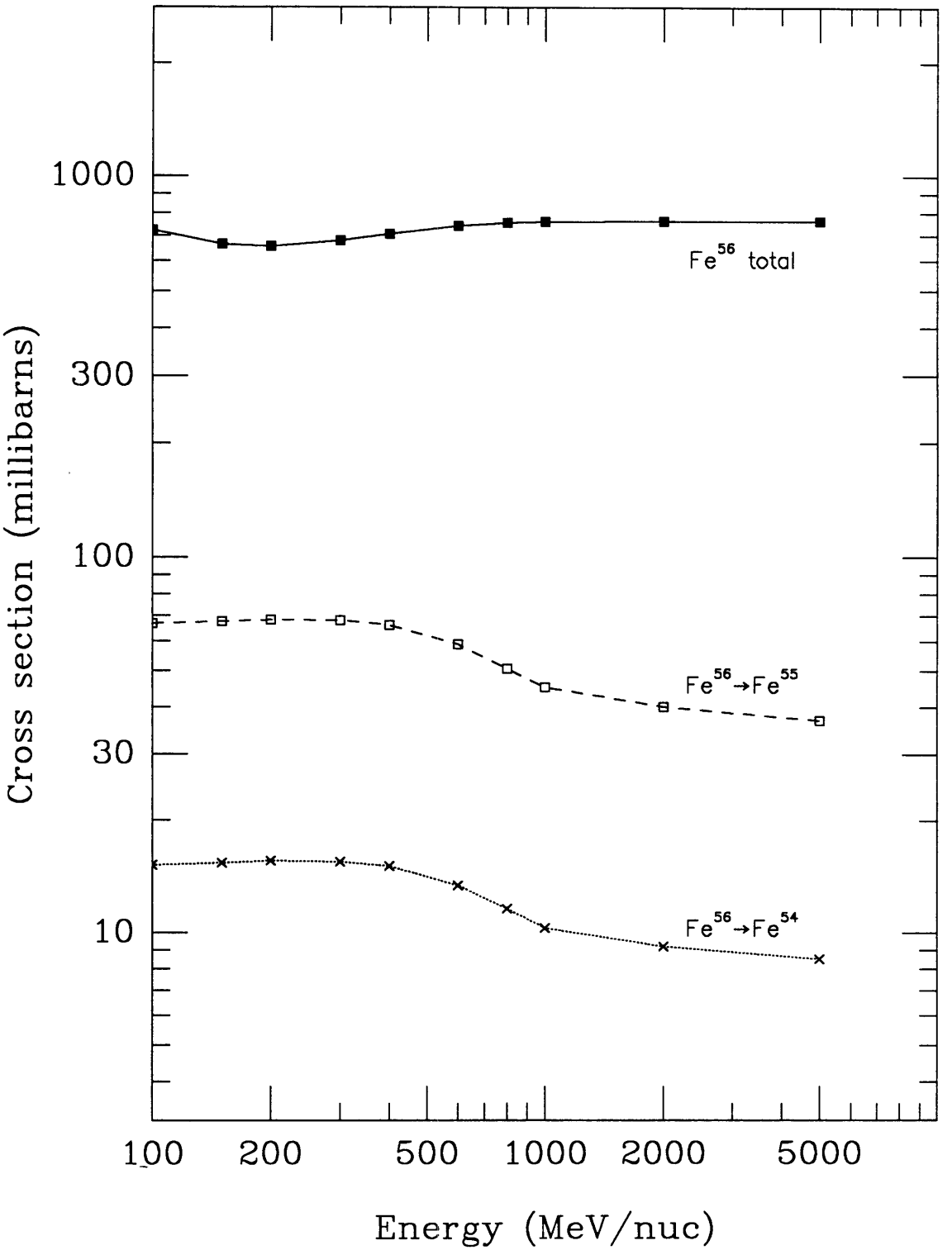
1000
300
100
30
10
Cross section (millibarns)
Fe56 total
Fe56→Fe55
Fe56→Fe54
100
200
500
1000
2000
5000
Energy (MeV/nuc)

Total mass-changing cross sections on the high-Z materials of the HEIST instrument are calculated from the Bradt-Peters formula with overlap, given in Westfall *et al.* (1979):

$$\sigma_{p,t}(\Delta A \geq 1) = \pi r_0^2 (A_p^{1/3} + A_t^{1/3} - b)^2 , \tag{5.1}$$

where A_p and A_t are the mass numbers of the incident and target nuclei, respectively, and where $r_0 = 1.47 \pm 0.04$ fm and $b = 1.12 \pm 0.16$. Neutron-stripping cross sections in the high-Z materials of the HEIST instrument are calculated by scaling from the cross sections on H,

$$\sigma_{ps,t} = \sigma_{ps,H} \frac{\sigma_{p,t}(\Delta A \geq 1)}{\sigma_{p,H}(\Delta A \geq 1)} \tag{5.2}$$

for parent species p going to daughter species s, where $\sigma_{ps,H}$ and $\sigma_{p,H}(\Delta A \geq 1)$ are given in Tables 5.1 and 5.2. In §5.4 we show that these cross sections give good agreement with the observed amount of neutron stripping as measured at the Bevalac, and therefore that this extrapolation of partial cross sections is reasonable. Total and partial mean-free-paths in compounds are related to the cross sections in the individual materials by

$$\lambda_s = \frac{\sum_t m_t}{\sum_t \sigma_{s,t}} , \tag{5.3}$$

where the m_t are the masses of the elements in one molecule of the target compound, and the $\sigma_{s,t}$ are the appropriate cross sections.

5.2. Atmospheric and Instrumental Propagation

The isotopic composition of Fe measured in the HEIST instrument is modified from that at the top of the atmosphere by nuclear interactions in the atmosphere and in the detectors. Indeed a non-negligible number of neutron-stripping interactions will occur in the NaI(Tl) stack, leading to a low-mass tail for a beam of a single isotopic

species. We have developed a maximum-likelihood algorithm that fits the observed masses in the instrument with calculated mass distributions that account for these neutron-stripping interactions in the atmosphere and instrument. The algorithm thus yields abundances at the top of the atmosphere. The calculated mass distributions are described below, and the maximum-likelihood algorithm is described in §5.3.

We use a slab model to propagate the Fe isotopes from the top of the atmosphere to the top of the NaI(Tl) stack, and a Monte Carlo calculation in the NaI(Tl) stack to account for the more subtle effect of neutron-stripping interactions in the NaI(Tl) on the measured mass.

With a slab model, the change in the abundance of any isotopic species as a function of depth is governed by the continuity equation, which can be expressed in finite-difference form as follows, if the step size δx is small enough that secondary interactions can be ignored,

$$N_s(x_0 + \delta x) = N_s(x_0) \left[1 - \frac{\delta x}{\lambda_s} \right] + \sum_{p>s} N_p(x_0) \frac{\delta x}{\lambda_{ps}}, \qquad (5.4)$$

where $N_s(x)$ is the abundance of isotopic species s at depth x, λ_s is the total mean-free-path for mass-changing interactions, and λ_{ps} is the partial mean-free-path for the spallation of parent species p into species s. Note that we make the assumption that if a particle undergoes a mass-changing interaction, its velocity remains unchanged—that is, it maintains the same kinetic energy per mass unit.

If a particle suffers a neutron-stripping interaction in the NaI(Tl) stack, the total energy deposited in the scintillator through ionization energy-loss decreases, and the calculated mass (Equation (2.18)) decreases by the corresponding amount. This leads to a low-mass tail for a beam of incident nuclei. We have developed a Monte Carlo program that propagates trial particles through the NaI(Tl) in steps, allowing them to interact stochastically according to the appropriate cross sections, and rejecting those that suffer charge-changing interactions. Non-interacting and neutron-stripping particles are tallied, with the apparent mass of a neutron-stripping particle given by the weighted average of its mass at each step in its range through the NaI(Tl):

$$\overline{A} = \frac{\sum A_s \Delta E_s}{\sum \Delta E_s} , \tag{5.5}$$

where the sums are over the range steps into which the stack has been divided, and the weighting factor ΔE_s is the calculated energy loss in step s.

We apply the atmospheric and instrumental propagation algorithm separately for each isotopic species. The algorithm propagates a large number of trial particles of a given species from the top of the atmosphere, through the top scintillator and the aerogel counter, to the top of the NaI(Tl) at the measured angle and range of each of the 32 selected Fe events. It modifies the composition of the beam at each $\delta x = 0.05$ g/cm^2 step according to Equation (5.4). From the top of the stack, the Monte Carlo program propagates the trial particles as described above to their end of range in the NaI(Tl), calculating masses according to Equation (5.5). The mass of each of these trial particles is accumulated to form an apparent-mass distribution for each species, which represents the expected amount of neutron-stripping averaged over the 32 selected Fe events.

A histogram of the apparent mass of a beam of ^{56}Fe is presented in Figure 5.3. The abundance spikes at integral mass values are comprised of trial particles that interact above the NaI(Tl), while the continuum of non-integral masses is comprised of trial particles that interact in the NaI(Tl).

5.3. Abundance Fits

We assume that the mass resolution function is a Gaussian with variance σ^2, which we convolve with the apparent-mass distributions for pure beams of the five Fe isotopes present at the top of the atmosphere—^{58}Fe, ^{57}Fe, ^{56}Fe, ^{55}Fe, and ^{54}Fe. We then fit the observed masses for the 32 selected events with the convolved apparent-mass distributions by the maximum-likelihood technique—making certain assumptions about the abundances of the rare isotopes ^{57}Fe and ^{55}Fe—to give the estimated ^{54}Fe/^{56}Fe and ^{58}Fe/^{56}Fe abundance ratios at the top of the atmosphere.

We approximate the convolution by a discrete sum over the bins of the histogram of the apparent-mass distribution (Figure 5.3); thus, for example, the convolved

apparent-mass distribution for ^{56}Fe is

$$\frac{dN^c_{56}}{dA}(A,\sigma) = \sum_b \frac{dN_{56}}{dA}(b) \frac{1}{\sigma\sqrt{2\pi}} \exp\left[\frac{-(A-A_b)^2}{2\sigma^2}\right], \tag{5.6}$$

where the sum is over the bins of the histogram of Figure 5.3, and $dN_{56}(b)/dA$ and A_b are the fraction of the parent beam surviving in bin b and the fractional mass to which bin b corresponds.

We have made no attempt to fit the abundances of ^{57}Fe and ^{55}Fe: instead we have assumed a solar-system abundance of these isotopes at the GCRS and propagated them to the top of the atmosphere with the algorithm described in §5.4. Note that the solar-system abundance of ^{55}Fe is negligible, and thus its abundance at the top of the atmosphere is equal to the amount produced by the galactic propagation. Free parameters of the fit are the ^{54}Fe/^{56}Fe abundance ratio α_{54} at the top of the atmosphere, the ^{58}Fe/^{56}Fe ratio α_{58} at the top of the atmosphere, the average mass resolution σ, and the mass scale factor μ. The scale factor is used as a multiplicative factor to correct the measured masses (Figure 4.6) so that ^{56}Fe has $\mu A_{meas} = 56$. The best fit is calculated by the maximum-likelihood technique, with the logarithm of the likelihood function given by

$$\log L = \sum_{evt} \log\left\{\sum_s \left[\frac{\alpha_s}{1.0686+\alpha_{58}+\alpha_{54}} \frac{dN^c_s}{dA}(\mu A_{evt},\sigma)\right]\right\}, \tag{5.7}$$

where the first sum is over the 32 Fe events, and the second sum is over the isotopes of Fe, and the convolved apparent-mass distributions dN^c_s/dA have the form given in Equation (5.6). The factor of 1.0686 is the sum of the assumed abundance ratios of the isotopes other than ^{54}Fe and ^{58}Fe at ~1600 MeV/nucleon: $\alpha_{55}+\alpha_{56}+\alpha_{57} = 1.0686$.

5.3.1. Bevalac Mass Histogram

To test whether the instrumental propagation model adequately describes the neutron stripping, we fit the apparent-mass distribution for ^{55}Mn to a mass histogram of Bevalac data, as shown in Figure 5.4. The data were selected from a period with relatively small run-gain variations and are identical to those shown in Figure 3.9. We

Figure 5.3

The apparent-mass distribution of an ^{56}Fe beam. The abundance spikes at integral mass values are comprised of trial particles that interact above the NaI(Tl) stack, while the continuum of non-integral masses is comprised of those trial particles that interact in the NaI(Tl).

Figure 5.3

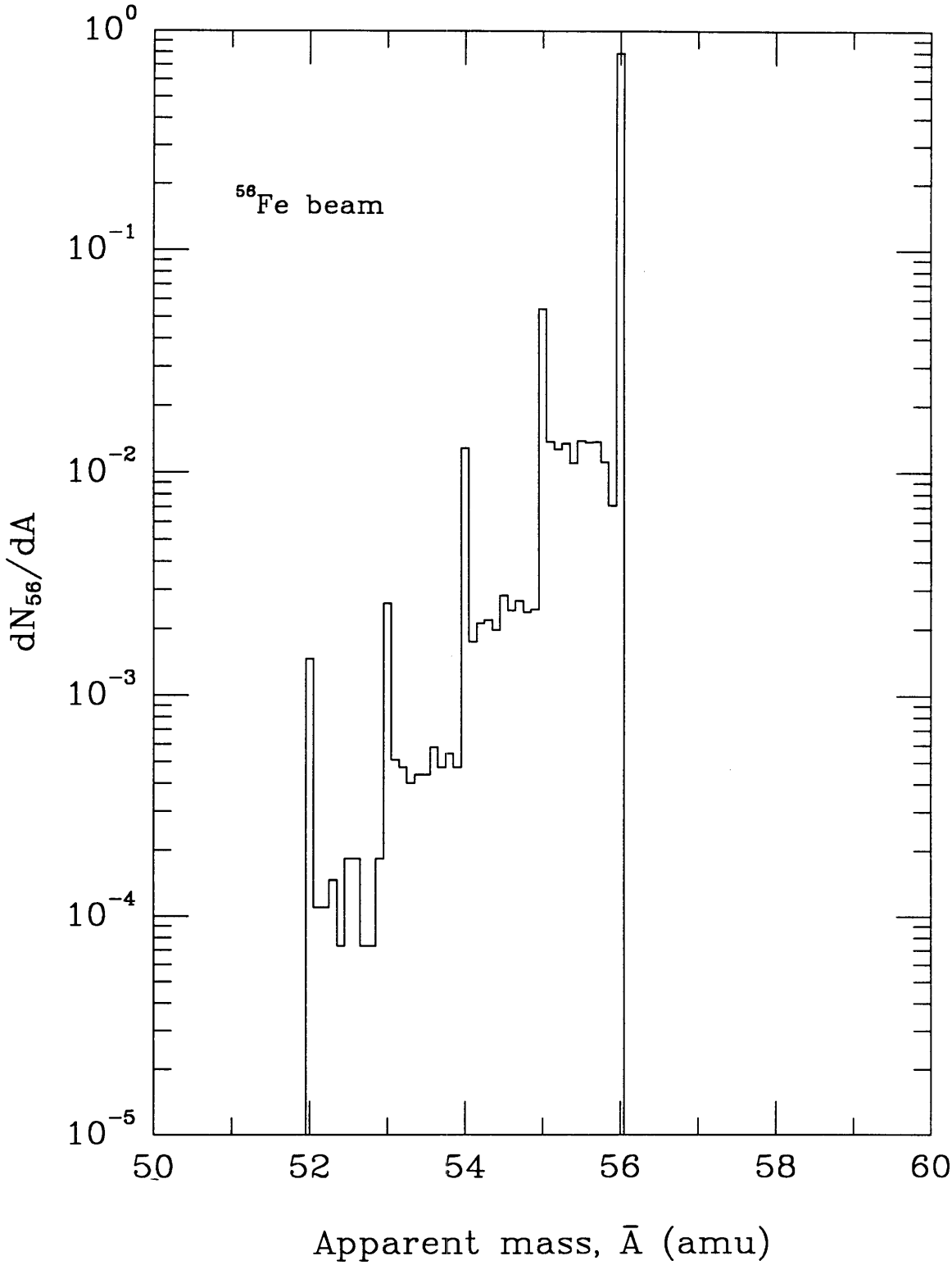
10^0
10^{-1}
10^{-2}
10^{-3}
10^{-4}
10^{-5}
^{56}Fe beam
dN_{56}/dA
50
52
54
56
58
60
Apparent mass, $\bar{A}$ (amu)

Figure 5.4

Mass histogram of ^{55}Mn at 1750 MeV/nucleon. The smooth curve is the convolved apparent-mass distribution. The fit gives a mass resolution of 0.52±0.01 amu.

Figure 5.4

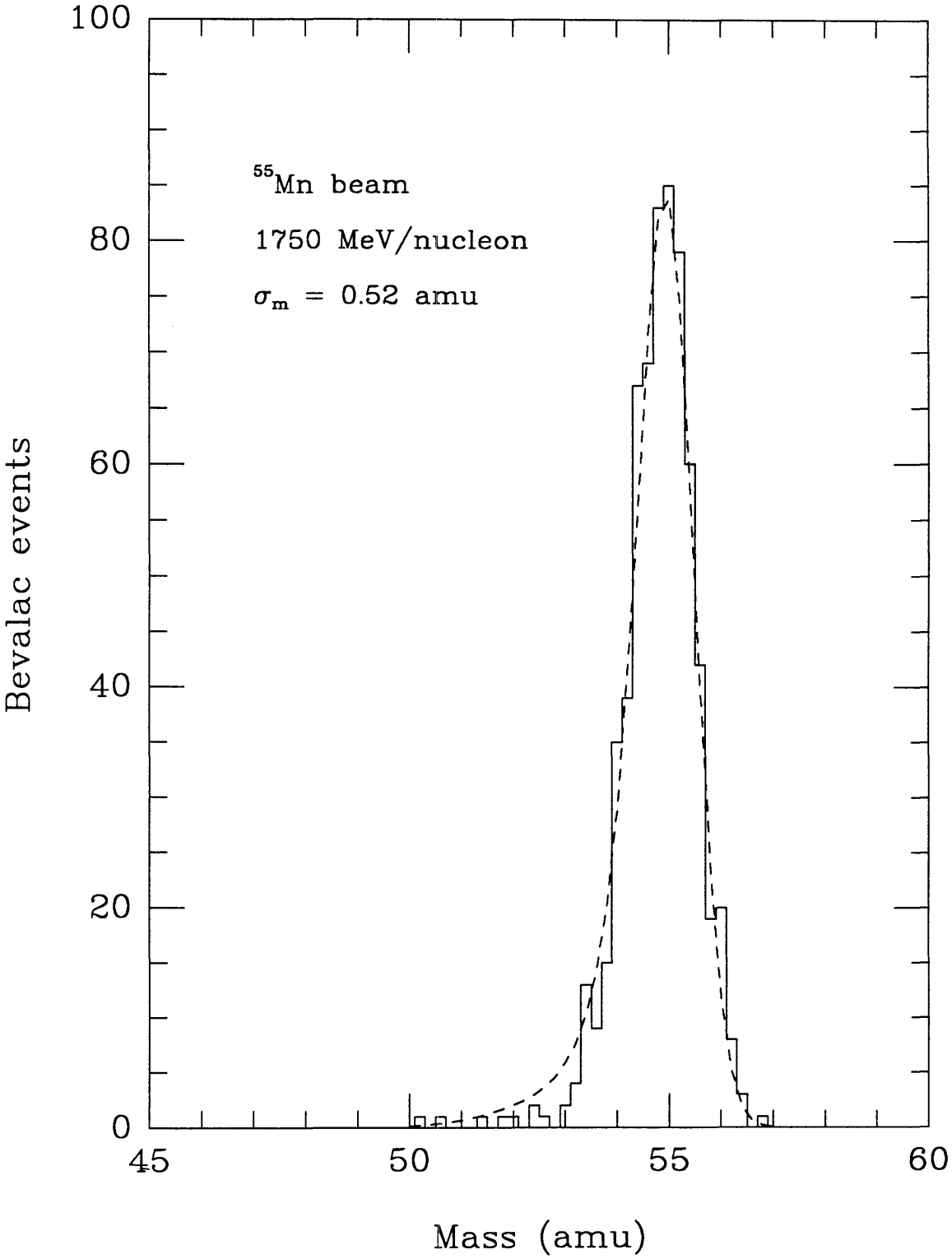
100
80
60
40
20
0
45
50
55
60
Bevalac events
Mass (amu)
^{55}Mn beam
1750 MeV/nucleon
σ_m = 0.52 amu

assumed a beam of pure ^{55}Mn at the exit of the Bevalac beam pipe, which we propagated to its end of range in the NaI(Tl) stack using the cross sections listed in Table 5.2. Free parameters in this fit were the mass resolution and the mass scale factor. The figure shows adequate agreement between the model and the observations, although there is some evidence for an overestimation of two-neutron-stripping interactions in the model. The propagation model, using the cross sections from Webber and from Silberberg and Tsao, is sufficiently accurate. The extrapolation of partial cross sections of Fe on high-Z materials from those of Fe on H (Equation (5.2)) is also demonstrated to be satisfactory.

The fit gives a mass resolution of 0.52±0.01 amu. From the Cerenkov resolution measured in §3.6.2, we calculate a contribution to mass resolution from the aerogel counter of 0.38 amu, which is dominated by contributions from photoelectron statistical fluctuations and stochastic variations in the index of refraction (Figure 3.14). The measured total energy resolution corresponds to 0.40 amu (§3.5.1) and is apparently dominated by residual spill-gain and run-gain variations. The sum in quadrature of the Cerenkov and total energy uncertainties is 0.54 amu; thus the observed total mass resolution is consistent with only a very small correlation between Cerenkov and total energy errors, which is to be expected, given the dominant sources in each measurement.

5.3.2. Maximum-Likelihood Estimators and Uncertainties

The likelihood function is maximized by Powell's direction-set method (e.g., Press, 1986), which relies on successive maximization along a set of conjugate, or non-interfering, directions. Direction $\vec{u}$ is said to be conjugate to $\vec{v}$ if $\vec{u}$ is orthogonal to the change in the gradient in direction $\vec{v}$ of the function to be maximized. This condition insures that once the function has been maximized in direction $\vec{v}$, the subsequent maximizations in the conjugate directions will not spoil the first.

The maximum-likelihood errors are estimated numerically. Near the maximum of the likelihood function, we imagine a transformation to a new set of parameters $\vec{u}$ such that $L(\vec{u})$ is a multivariate Gaussian. Note that such a transformation may not strictly exist. However, the central-limit theorem implies that it must exist asymptotically

(Yost, 1984); therefore there probably exists some transformation to a set of parameters which is nearly multivariate normal. Then the probability that the true value of the transformed parameter u_i lies in the interval $[u_i^{max} - \sigma_i , u_i^{max} + \sigma_i]$ is 68%, provided that the other parameters of $\vec{u}$ remain fixed at their maximum-likelihood values. The value of logL at the limits of this confidence interval is given by

$$\log L(u_i^{max} \pm \sigma_i) = \log L_{max} - \tfrac{1}{2} . \tag{5.8}$$

Although the transformation is likely to be such that the principal axes of the surface defined by Equation (5.8) are not aligned with the model parameters $\vec{m}$, we never need to know the transformation from the $\vec{m}$ to $\vec{u}$: the 68% confidence interval on the model parameter m_i is given by the extreme values of m_i which satisfy (Yost, 1984)

$$\log L(m_i) = \log L_{max} - \tfrac{1}{2} . \tag{5.9}$$

We found the extrema by evaluating logL in a grid of points about their likely locations and subsequently interpolating from the grid to increase the accuracy.

As one would expect, Powell's method finds two local minima in the likelihood function, one corresponding to an Fe composition dominated by ^{56}Fe ($^{58}Fe/^{56}Fe$ is small) and the other corresponding to a composition dominated by ^{58}Fe ($^{58}Fe/^{56}Fe$ is large). The minima are equally likely. However, the measurement of Mewaldt *et al.* (1980) clearly established that ^{56}Fe is the dominant isotope, so we have assumed that this condition would hold in our data and have discarded the latter minimum.

The maximum-likelihood estimate for the $^{58}Fe/^{56}Fe$ ratio is vanishingly small, and the contour defined by Equation (5.9) extends to $^{58}Fe/^{56}Fe = 0.042$. This should correspond to the 84% confidence upper limit; however, we note that the Poisson 84% confidence limit when no events are observed is $-\ln(1-0.84) = 1.83$ events. Because we have observed 32 Fe events and the maximum-likelihood estimate of the $^{54}Fe/^{56}Fe$ ratio is $\alpha_{54} = 0.14$, and because we have assumed $\alpha_{55} + \alpha_{57} = 0.0686$, this corresponds to an $^{58}Fe/^{56}Fe$ ratio of 0.07. We will use this higher value for the 84% confidence upper limit.

The maximum-likelihood estimates and errors for the four free parameters are listed in Table 5.3. Note that the estimates for the $^{54}Fe/^{56}Fe$ and $^{58}Fe/^{56}Fe$ abundance

ratios apply at the top of the atmosphere. The average mass resolution for the 32 selected Fe events predicted from the contributions listed in §2.3 is ~0.65 amu, which is in excellent agreement with the maximum-likelihood estimate of $\sigma = 0.67^{+0.17}_{-0.17}$ amu.

Table 5.3: Maximum-likelihood estimates
Top of the atmosphere, ~1550-2200 MeV/nucleon

parameter	quantity	estimate
α_{54}	$^{54}Fe/^{56}Fe$	$0.14^{+0.18}_{-0.11}$
α_{58}	$^{58}Fe/^{56}Fe$	≤ 0.07
σ	mass resolution (amu)	$0.67^{+0.17}_{-0.17}$
μ	mass scale factor	$0.978^{+0.004}_{-0.005}$

The mass histogram of the 32 selected Fe events is repeated in Figure 5.5, renormalized by the maximum-likelihood mass scale factor. The smooth curves are the convolved apparent-mass distributions for the isotopes of Fe. Although ^{58}Fe was used in the fit, its convolved apparent-mass distribution is not shown, because its abundance is small.

Figures 5.6(a-f) show slices through the surface defined by Equation (5.9) onto the six planes defined by the maximum-likelihood estimates of the model parameters α_{54}, α_{58}, σ, and μ. Some correlation among the parameters does exist that is not apparent from the two-dimensional slices. The deviation of the contours from elliptical shape gives a sense of the deviation from normal errors.

5.4. Galactic Propagation

We propagate trial Fe isotopic abundances at the GCRS to the top of the atmosphere using a recent version of the Comstock code (1969). This program employs a simple Leaky Box model, a steady-state and homogeneous model of cosmic-ray propagation in which the galaxy is represented by a containment volume in which the cosmic rays bounce around with a small probability of escape at each encounter with the

boundary. The cosmic rays are continuously decelerated by ionization of the ISM, which is assumed to be purely hydrogen, and their composition is modified through nuclear interactions with that medium. Unstable species are allowed to undergo radioactive decay. The interstellar intensity $J_s(E)$ of nuclear species s at kinetic energy E is obtained from the following form of the transport equation (e.g., Protheroe *et al.*, 1981),

$$\frac{J_s(E)}{\lambda_s^{esc}(R)} + \frac{J_s(E)}{\lambda_s^{spl}(E)} + \frac{J_s(E)}{\lambda_s^{dec}(E)} + \frac{\partial}{\partial E}\left[\frac{dE_s}{dx} J_s(E)\right] = \tag{5.10}$$

$$Q_s(R) + \sum_{p>s} \frac{J_p(E)}{\lambda_{ps}^{spl}(E)} + \sum_{p \neq s} \frac{J_p(E)}{\lambda_{ps}^{dec}(E)} ,$$

where the loss terms have been collected on the left-hand side, and creation terms on the right. $\lambda_s^{esc}(R)$ is the rigidity-dependent mean pathlength for escape from the containment volume; $\lambda_s^{spl}(E)$ is the mean pathlength for mass-changing nuclear interactions; and $\lambda_s^{dec}(E)$ is the mean pathlength for the radioactive decay of species s, if applicable. dE/dx is the specific ionization energy loss in hydrogen. $Q_s(R)$ accounts for the production of cosmic rays at the GCRS, assumed to be uniformly distributed throughout the containment volume. $\lambda_{ps}^{spl}(E)$ and $\lambda_{ps}^{dec}(E)$ are the pathlengths for spallation and radioactive decay of parent species p into species s.

The measured abundance at Earth of cosmic-ray species thought to be absent, or present in small amounts, at the GCRS can be used to determine the mean pathlength for escape $\lambda_s^{esc}(R)$ as a function of magnetic rigidity. Using the parameters of Engelmann *et al.* (1985), i.e., a source term that is a power law in rigidity, $Q_s(R) \propto R^{-2.41}$, and a mean escape length given by

$$\lambda_s^{esc}(R) = \begin{cases} 22\, R^{-0.60}\ g/cm^2 & \text{for } R \geq 5.5\ GV \\ 7.9\ g/cm^2 & \text{for } R < 5.5\ GV \end{cases} \tag{5.11}$$

and assuming a mean mass density of 0.3 amu/cm^3 in the propagation volume, we find a good fit with the propagation code to the secondary-to-primary ratio (Sc+Ti+Cr)/Fe observed by Engelmann *et al.* (1983) and by Dwyer and Meyer (1985). The mean escape length and interstellar mass density correspond to a mean containment time in

Figure 5.5

Mass histogram of 32 Fe events, renormalized by the maximum-likelihood mass scale factor. The smooth curves are the convolved apparent-mass distributions for the isotopes of Fe. The mass resolution is $0.67^{+0.17}_{-0.17}$ amu. The $^{54}Fe/^{56}Fe$ abundance ratio at the top of the atmosphere is $0.14^{+0.18}_{-0.11}$, and the 84% confidence upper limit on $^{58}Fe/^{56}Fe$ is 0.07.

Figure 5.5

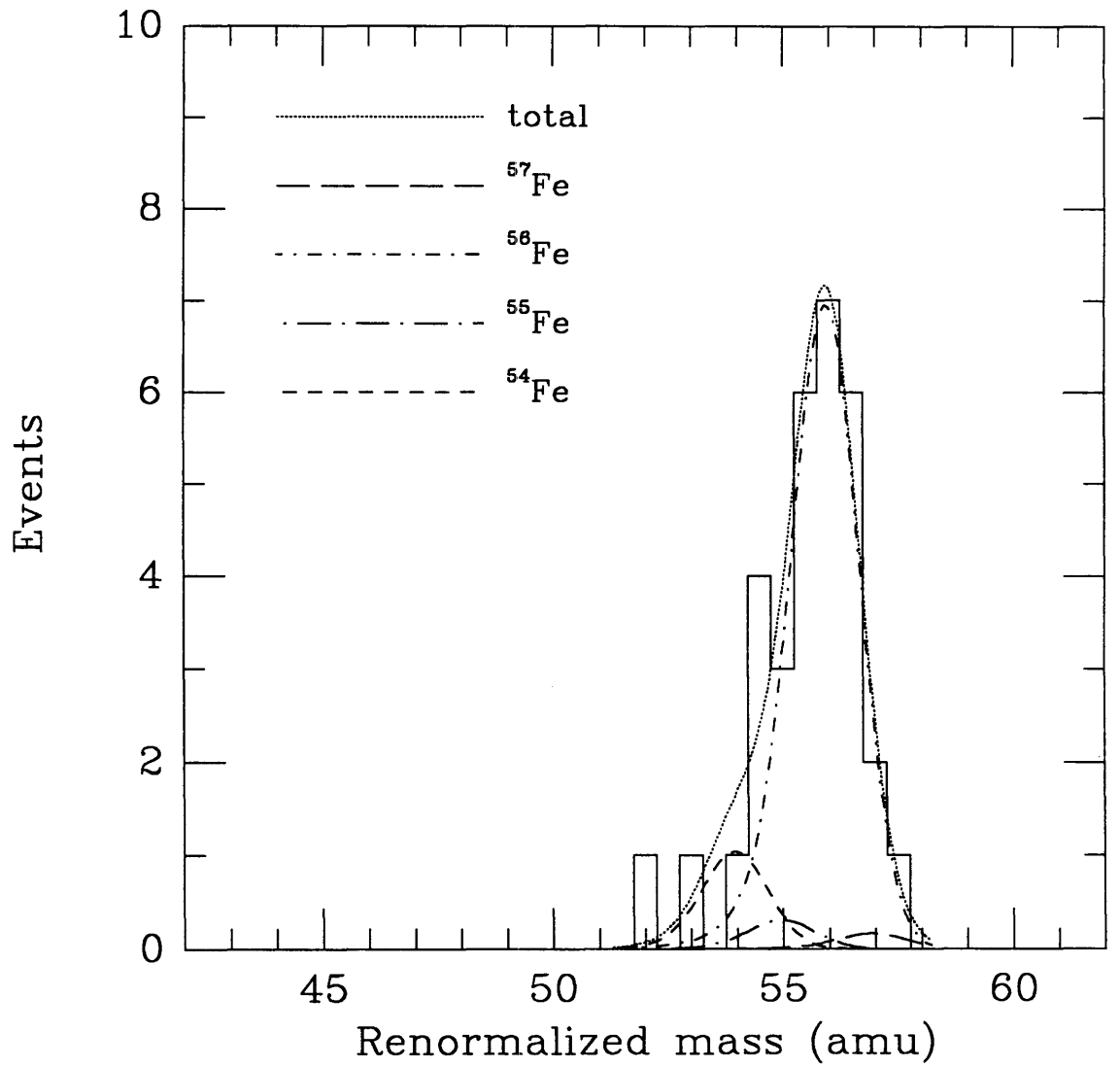
10
8
6
4
2
0
Events
total
^{57}Fe
^{56}Fe
^{55}Fe
^{54}Fe
45
50
55
60
Renormalized mass (amu)

Figure 5.6(a)

Contour plot of $\log L_{max} - ½$ with mass scale factor $\mu = 0.978$ and $^{58}Fe/^{56}Fe = 0$.

Figure 5.6(b)

Contour plot of $\log L_{max} - ½$ with mass resolution $\sigma = 0.67$ and $^{58}Fe/^{56}Fe = 0$.

Figure 5.6(c)

Contour plot of $\log L_{max} - ½$ with $^{54}Fe/^{56}Fe = 0.14$ and $^{58}Fe/^{56}Fe = 0$.

Figure 5.6(d)

Contour plot of $\log L_{max} - ½$ with mass resolution $\sigma = 0.67$ and $^{54}Fe/^{56}Fe = 0.14$.

Figure 5.6(e)

Contour plot of $\log L_{max} - ½$ with mass scale factor $\mu = 0.978$ and $^{54}Fe/^{56}Fe = 0.14$.

Figure 5.6(f)

Contour plot of $\log L_{max} - ½$ with mass resolution $\sigma = 0.67$ and mass scale factor $\mu = 0.978$.

Figure 5.6(a)

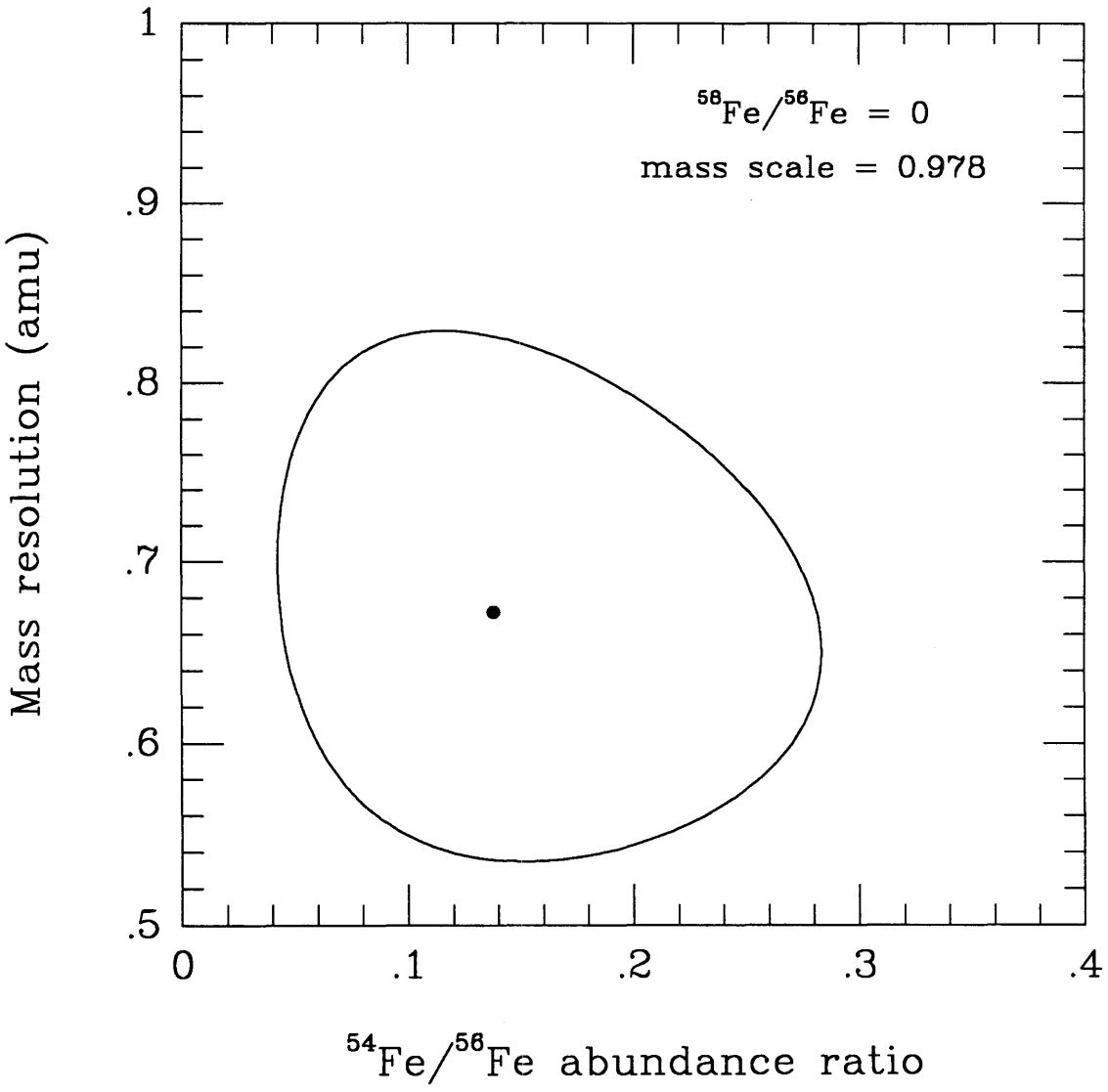
$^{58}Fe/^{56}Fe$ = 0
mass scale = 0.978
1
.9
.8
.7
.6
.5
0
.1
.2
.3
.4
Mass resolution (amu)
$^{54}Fe/^{56}Fe$ abundance ratio

Figure 5.6(b)

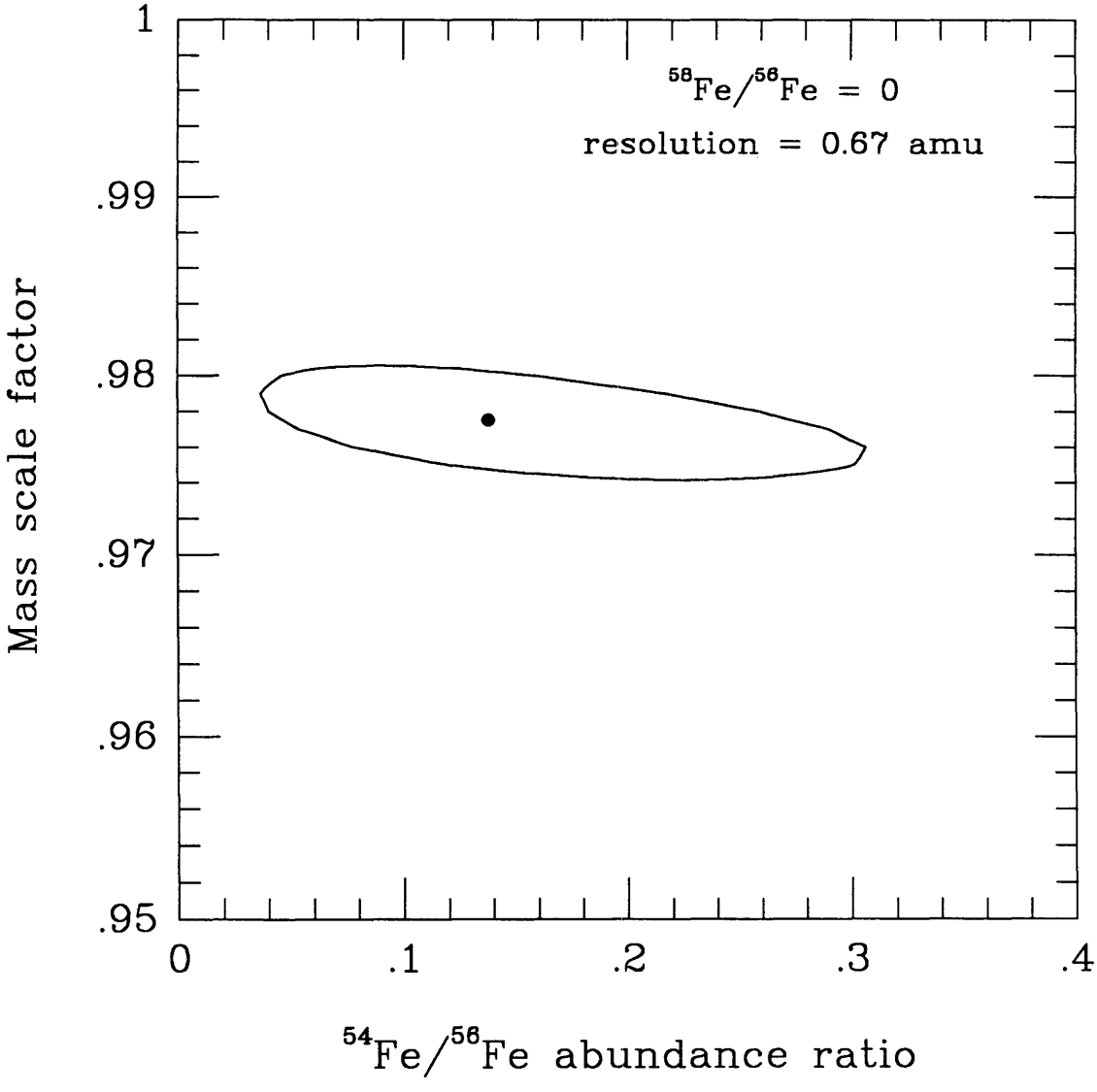
1
.99
.98
.97
.96
.95
0
.1
.2
.3
.4
$^{58}Fe/^{56}Fe$ = 0
resolution = 0.67 amu
Mass scale factor
$^{54}Fe/^{56}Fe$ abundance ratio

Figure 5.6(c)

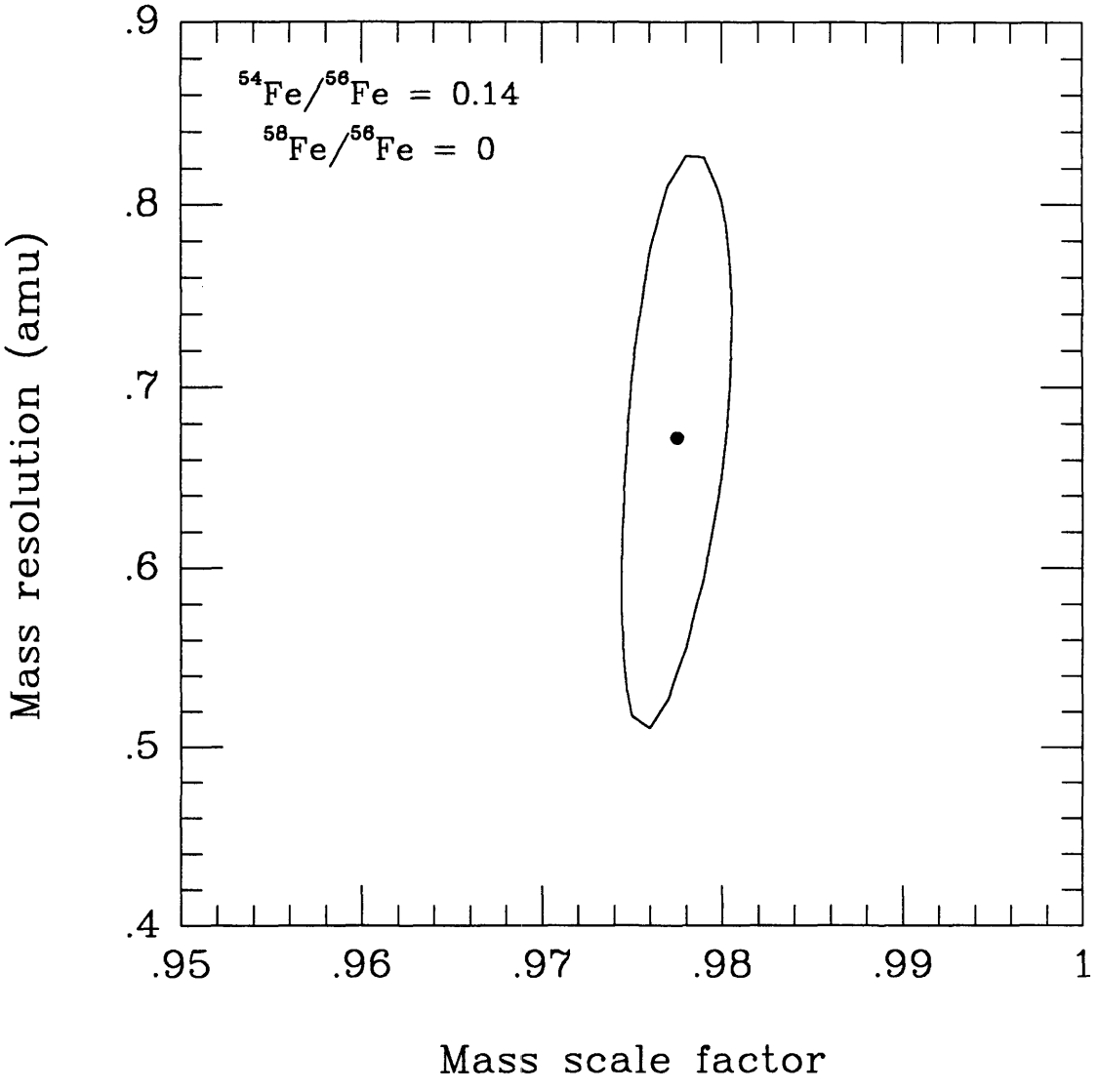
$^{54}Fe/^{56}Fe$ = 0.14
$^{58}Fe/^{56}Fe$ = 0
.9
.8
.7
.6
.5
.4
.95
.96
.97
.98
.99
1
Mass resolution (amu)
Mass scale factor

Figure 5.6(d)

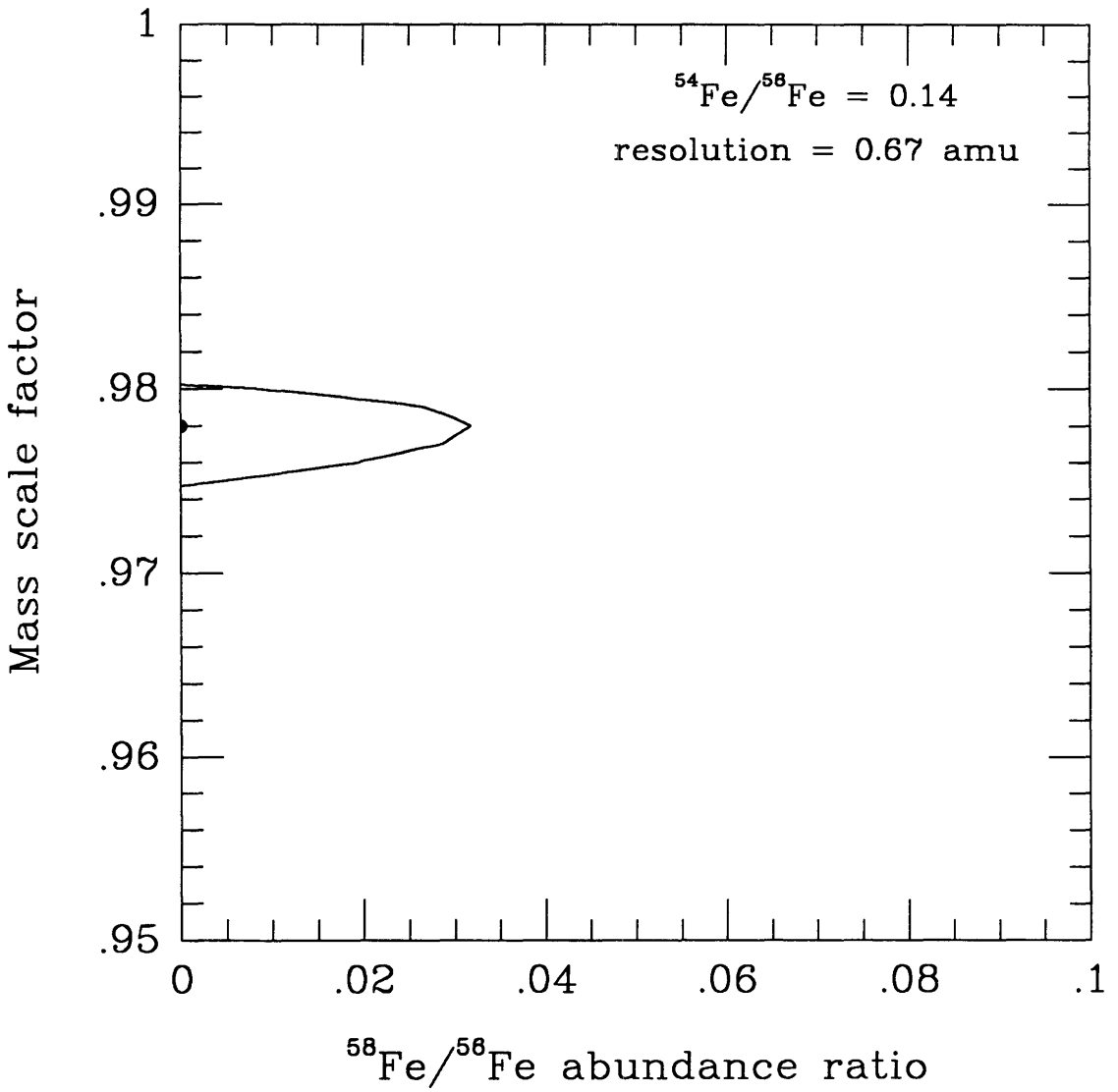
1
.99
.98
.97
.96
.95
Mass scale factor
$^{54}Fe/^{56}Fe$ = 0.14
resolution = 0.67 amu
0
.02
.04
.06
.08
.1
$^{58}Fe/^{56}Fe$ abundance ratio

Figure 5.6(e)

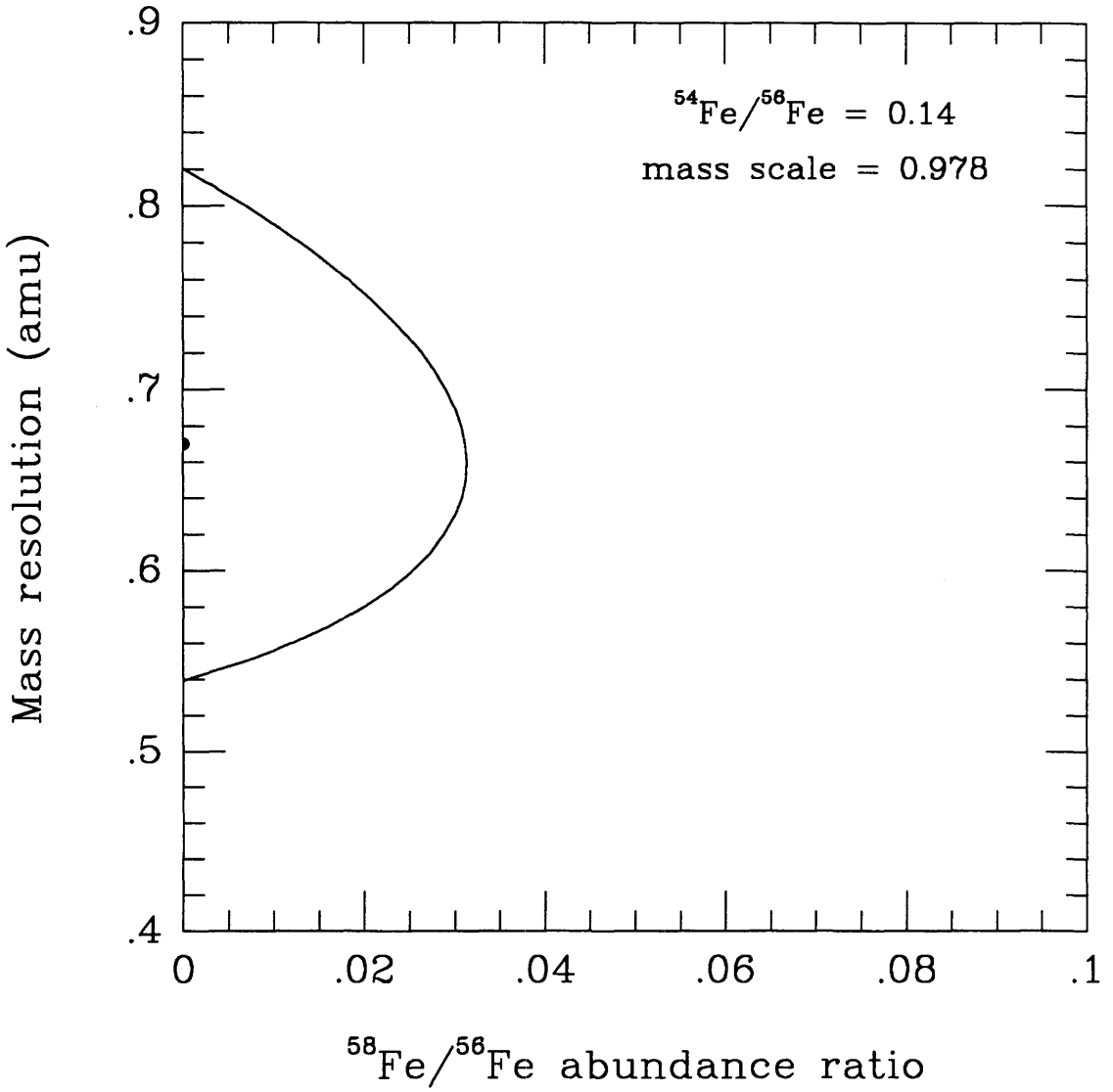
.9
.8
.7
.6
.5
.4
0
.02
.04
.06
.08
.1
$^{54}Fe/^{56}Fe$ = 0.14
mass scale = 0.978
Mass resolution (amu)
$^{58}Fe/^{56}Fe$ abundance ratio

Figure 5.6(f)

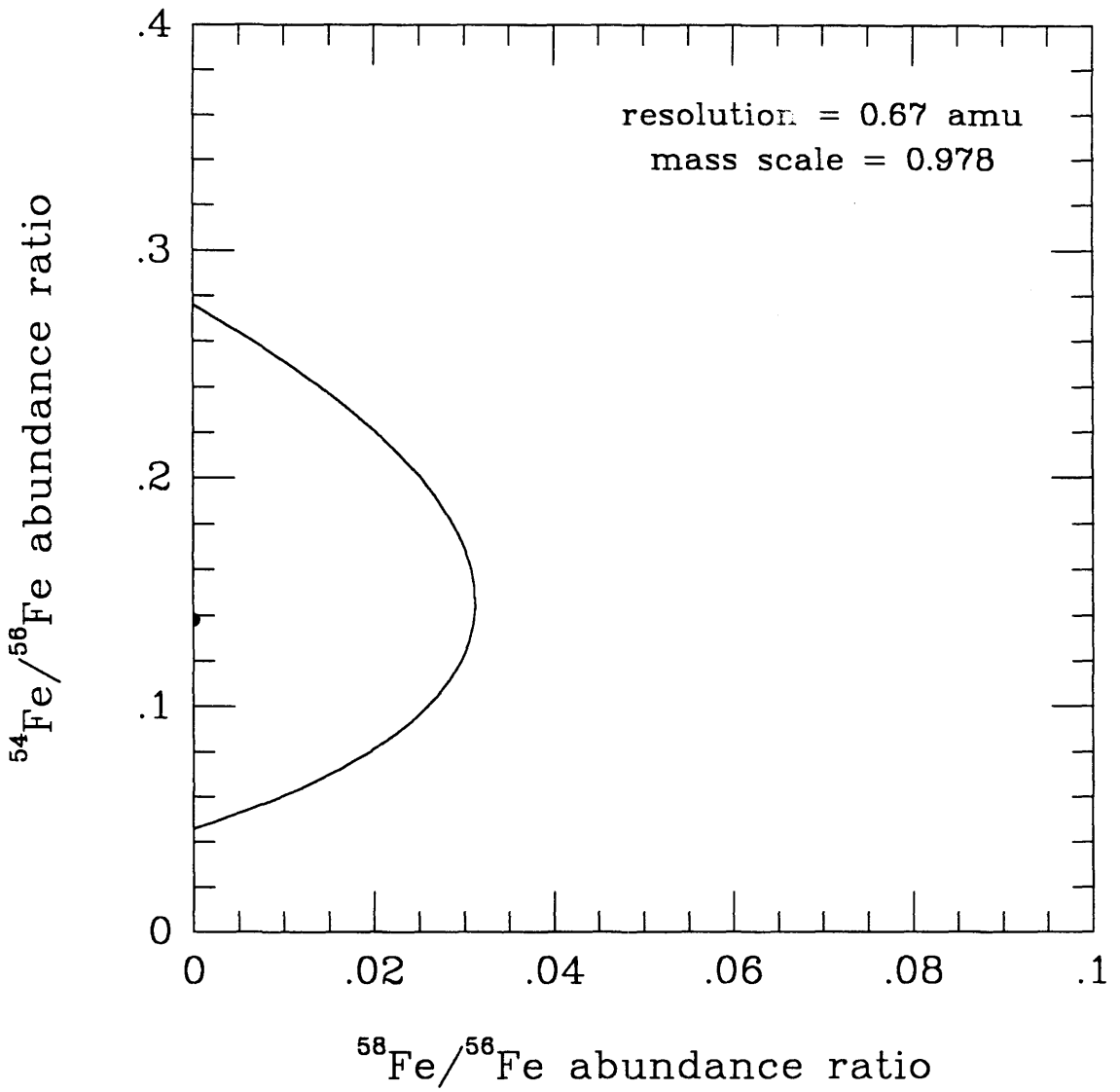
resolution = 0.67 amu
mass scale = 0.978
.4
.3
.2
.1
0
0
.02
.04
.06
.08
.1
$^{54}Fe/^{56}Fe$ abundance ratio
$^{58}Fe/^{56}Fe$ abundance ratio

the Leaky Box of $\sim 1.8 \times 10^7$ years for R $<$ 5.5 GV.

At energies below a few GeV per nucleon, the intensity and spectral shape of the cosmic rays arriving at the orbit of Earth have been substantially modified by the expanding solar wind and the frozen-in interplanetary magnetic field it carries. We have included the effects of this solar modulation on the observed composition by using the force-field approximation of Gleeson and Axford (1968). The modulated flux of species s at kinetic energy per nucleon E (measured in MeV/nucleon) is obtained from the interstellar flux by

$$J_s^{mod}(E) = \frac{E^2 + 2000\,E}{(E+\Phi)^2 + 2000\,(E+\Phi)} J_s(E+\Phi)\,, \qquad (5.12)$$

where $\Phi = Ze\phi/A$ is the mean energy loss experienced by the particles in traveling from the heliospheric boundary to 1 AU. Given the similarity in the magnitude of solar activity at the time of the HEIST flight and during the period of the HEAO-3 data collection (see §4.2), we have taken the deceleration parameter $\phi = 600$ MV in accordance with that assumed by Engelmann *et al.* (1985). We note also that because of the small difference in the charge-to-mass ratio, the propagated $^{54}Fe/^{56}Fe$ and $^{58}Fe/^{56}Fe$ ratios are rather insensitive to the magnitude of the modulation: we find that dropping the deceleration parameter to $\phi = 200$ MV results in a change of less than 2% in either ratio. A single choice of modulation level is therefore sufficient for the interpretation of the HEIST measurements along with the previous $^{54}Fe/^{56}Fe$ and $^{58}Fe/^{56}Fe$ measurements.

The species followed include all the stable isotopes between ^{4}He and ^{62}Ni, as well as the long-lived β-decay and electron-capture isotopes ^{10}Be, ^{26}Al, ^{36}Cl, and ^{54}Mn. Of course, the species with charge Z $<$ 25 do not influence the composition of Fe.

Note that ^{54}Mn may decay by β^- emission to ^{54}Fe during propagation. Unfortunately, the time constant for this decay is not well known, as it is usually masked in the laboratory by electron capture. Cassé (1973) has estimated a half-life of $\tau_{1/2} \sim 1.5\text{–}2 \times 10^6$ years, while the calculation of Wilson (1978) indicates that this value is between 6×10^4 and 1×10^7 years. Since the half-life appears to be on the order of the containment time for cosmic rays, this decay can have a significant effect on the interpretation of the $^{54}Fe/^{56}Fe$ ratio observed at Earth (R. A. Mewaldt and B. T.

Hayes, 1989, private communication). From the energy dependence of the observed Mn/Fe ratio in the HEAO-3 data set, Koch *et al.* (1981) have derived a half-life of 1-2 million years, in good agreement with Cassé. We have taken $\tau_{½} = 2 \times 10^6$ years. Note that if we assume a solar-system abundance ratio at the GCRS (i.e., ^{54}Mn absent and ^{54}Fe/^{56}Fe = 6.32%), this half-life increases the observed ^{54}Fe/^{56}Fe ratio at 1750 MeV/nucleon by ~15% with respect to the ratio derived assuming that the weak decay does not occur.

As stated above, the electron-capture species ^{55}Fe is assumed to be absent in the GCRS and is created by spallation during the propagation. Since the parent nuclei are completely stripped of orbital electrons, the ^{55}Fe nuclei are formed completely stripped, and therefore cannot decay unless they attach electrons from the ISM. The two important points to address are (1) whether the mean time for stripping an attached electron is long enough so that decay can occur, and if so, (2) whether the fraction of ^{55}Fe which attaches an electron is significant. The single-electron attachment cross section for Fe in H, calculated according to the formalism given in Crawford (1979), is $\sigma_a \approx 20$ mb at 1750 MeV/nucleon. The probability that a nucleus will attach an electron in traversing δx g/cm^2 of interstellar H is

$$p_a \approx 1 - \exp\left[-\frac{\sigma_a \delta x}{m_H}\right], \tag{5.13}$$

where m_H is the mass of a hydrogen atom. Also from Crawford (1979), the cross section for stripping the single electron is calculated to be $\sigma_s \approx 160$ barns, and the mean time for stripping is therefore

$$\tau_s \approx \frac{\gamma}{\sigma_s n_H \beta c}, \tag{5.14}$$

where $n_H \sim 0.3$ cm^{-3} is the number density of H in the propagation volume, and where βc and γ are the velocity and Lorentz factor of the ^{55}Fe nucleus. Since the mean time for stripping ($\tau_s \sim 6{\times}10^4$ years) is much longer than the half-life against electron capture with a single electron attached ($\tau_{½} \sim 5$ years), all ^{55}Fe nuclei that attach electrons will decay. Noting that ^{55}Fe is a secondary species, we take 2 g/cm^2 as an estimate of its pathlength in the ISM. Thus the probability of attachment is ~2%. Because the

propagated abundance of ^{55}Fe is only ~5% of ^{56}Fe (see Table 5.5), we have ignored this small correction and have assumed that ^{55}Fe is stable.

Our assumption of negligible abundance of ^{55}Fe at the GCRS will not be valid if the time delay between nucleosynthesis and acceleration is less than the lifetime of ^{55}Fe against electron capture ($\tau_{1/2} \sim 2.7$ years). Cassé and Soutoul (1975) proposed that the relative abundances of the electron capture isotopes of Fe, Co, and Ni could be used to measure this time delay. Soutoul *et al.* (1978) and Koch-Miramond *et al.* (1981) have used the observed *elemental* abundance ratios Ni/Fe and Co/Fe, and have concluded that the data are inconsistent with a delay of less than about one year. We have concluded that this is sufficient evidence to neglect ^{55}Fe at the source.

The recent measurement of charge-changing cross sections for ^{56}Fe on ^{4}He by Ferrando *et al.* (1988) allows the inclusion of interstellar He in propagation calculations of elemental abundances. The appropriate mass-changing cross sections have not as yet been published; however, Webber (1989, private communication) indicates that only small relative differences in mass-changing cross sections for ^{56}Fe are observed. We note that in any case it is unlikely that a proper accounting of spallation on He would have a significant effect on the propagated ^{54}Fe/^{56}Fe ratio: the small He/H ratio in the ISM (~10%) and the finite source abundance of ^{54}Fe substantially dilute any difference in ^{54}Fe production. We have ignored any such effects.

For comparison with solar-system abundances, we have adopted the isotopic abundance standard for Fe from Anders and Ebihara (1982) as shown in Table 5.4. This standard is essentially identical to that of Cameron (1973), to which the previous measurements of cosmic-ray Fe isotopic abundances were compared.

Table 5.4: Solar-system Fe isotopic composition Anders and Ebihara (1982)		
isotope	% of all Fe	% of ^{56}Fe
^{54}Fe	5.80	6.32
^{55}Fe	0.0	0.0
^{56}Fe	91.76	100.0
^{57}Fe	2.15	2.34
^{58}Fe	0.29	0.32

As an example of the effect of the galactic propagation on the composition of Fe observed at the orbit of the Earth, Table 5.5 shows the propagated composition at ~1750 MeV/nucleon if the composition at the GCRS is assumed to be equivalent to that of the solar system. The abundances of ^{54}Fe and ^{55}Fe, respectively, are enhanced by ~2% and ~4.4% of ^{56}Fe. Note that the relative abundances of ^{56}Fe and ^{57}Fe are only slightly modified by propagation because of the lack of abundant species beyond the Fe peak.

Table 5.5: Sample propagated Fe isotopic composition Solar-system composition assumed at GCRS, 1750 MeV/nucleon		
isotope	% of all Fe	% of ^{56}Fe
^{54}Fe	7.26	8.39
^{55}Fe	3.77	4.36
^{56}Fe	86.50	100.0
^{57}Fe	2.11	2.44
^{58}Fe	0.36	0.42

5.4.1. Propagation of Observations

The galactic propagation model described above was repeated, assuming a variety of $^{54}Fe/^{56}Fe$ and $^{58}Fe/^{56}Fe$ abundance ratios at the GCRS, generating a table of expected ratios at the top of the atmosphere corresponding to ratios at the GCRS. Our estimates of the $^{54}Fe/^{56}Fe$ and $^{58}Fe/^{56}Fe$ ratios at the GCRS were then derived by cubic-spline interpolation (e.g., Press *et al.*, 1986) from the table. Table 5.6 below summarizes our observations. Note the large lower error bar for the $^{54}Fe/^{56}Fe$ ratio. Uncertainties in the propagation correction are large enough that our estimate of the $^{54}Fe/^{56}Fe$ ratio at the GCRS may be considered to be an upper limit.

Table 5.6: Fe abundance ratios
~1550-2200 MeV/nucleon

Ratio	Top of Atmosphere	GCRS
$^{54}Fe/^{56}Fe$	$0.14^{+0.18}_{-0.11}$	$0.12^{+0.18}_{-0.11}$
$^{58}Fe/^{56}Fe$	≤ 0.07	≤ 0.07

5.5. Comparison with Previous Observations

The mass histograms from the four previous measurements of Fe isotopic composition are shown in Figures 5.7(a-d).

The observations of Tarlé *et al.* (1979) (Figure 5.7(a)) were made with a balloon-borne Cerenkov-Range telescope. The range measurement was made with a passive stack of Lexan polycarbonate track detectors, and the Pilot-425 Cerenkov radiator ($n = 1.5$) set the sensitive energy interval to 320-500 MeV/nucleon at the detector, or ~600-900 MeV/nucleon at the top of the atmosphere. The observed resolution was 0.65 amu, and 260 Fe events were collected. Although they lacked an absolute mass scale and sufficient resolution to resolve adjacent isotopes, their results were in clear contradiction to the early measurements of Webber *et al.* (1973) and Simpson *et al.*

(1977), which showed $^{58}Fe/^{56}Fe \sim 0.3$. Table 5.7 repeats their reported abundance ratios, given as upper limits. Whether the results should be taken to be propagated to the top of the atmosphere or back to the GCRS is not clear from the paper. We have assumed that they are values at the top of the atmosphere.

Table 5.7: Summary of Tarlé et al., 1979
Fe composition, ~600-900 MeV/nucleon

Isotope Ratio	Top of Atmosphere (%)
$^{54}Fe/(^{55}Fe+^{56}Fe+^{57}Fe)$	≤ 10
$^{58}Fe/(^{55}Fe+^{56}Fe+^{57}Fe)$	≤ 10

The observations of Mewaldt *et al.* (1980) (Figure 5.7(b)) were made with an array of solid-state detectors on board the *ISEE 3* spacecraft in the energy interval from 83-284 MeV/nucleon at the orbit of the Earth. The instrument showed excellent mass resolution ($\sigma = 0.37 \pm 0.05$ amu), and because the total thickness of the instrument was only ~0.1 interaction lengths (compared to >1.5 for HEIST), no correction was required for neutron-stripping. An accelerator calibration provided an absolute mass scale. Although the measurement suffered from low statistics (30 Fe events), it established that ^{56}Fe is the dominant species in the cosmic rays. Their results are repeated in Table 5.8 below as a percentage of total Fe, with 68% confidence intervals or 84% confidence limits. They have assumed that ^{55}Fe does not decay following acceleration.

Figure 5.7(a)

Mass histogram of Fe for ~600-900 MeV/nucleon from Tarlé *et al.* (1979).

Figure 5.7(b)

Mass histogram of Fe for 83-284 MeV/nucleon from Mewaldt *et al.* (1980).

Figure 5.7(c)

Mass histogram of Fe for ~600-900 MeV/nucleon from Young *et al.* (1981).

Figure 5.7(d)

Mass histogram of Fe for ~600-900 MeV/nucleon from Webber (1981).

Figure 5.7(a,b)

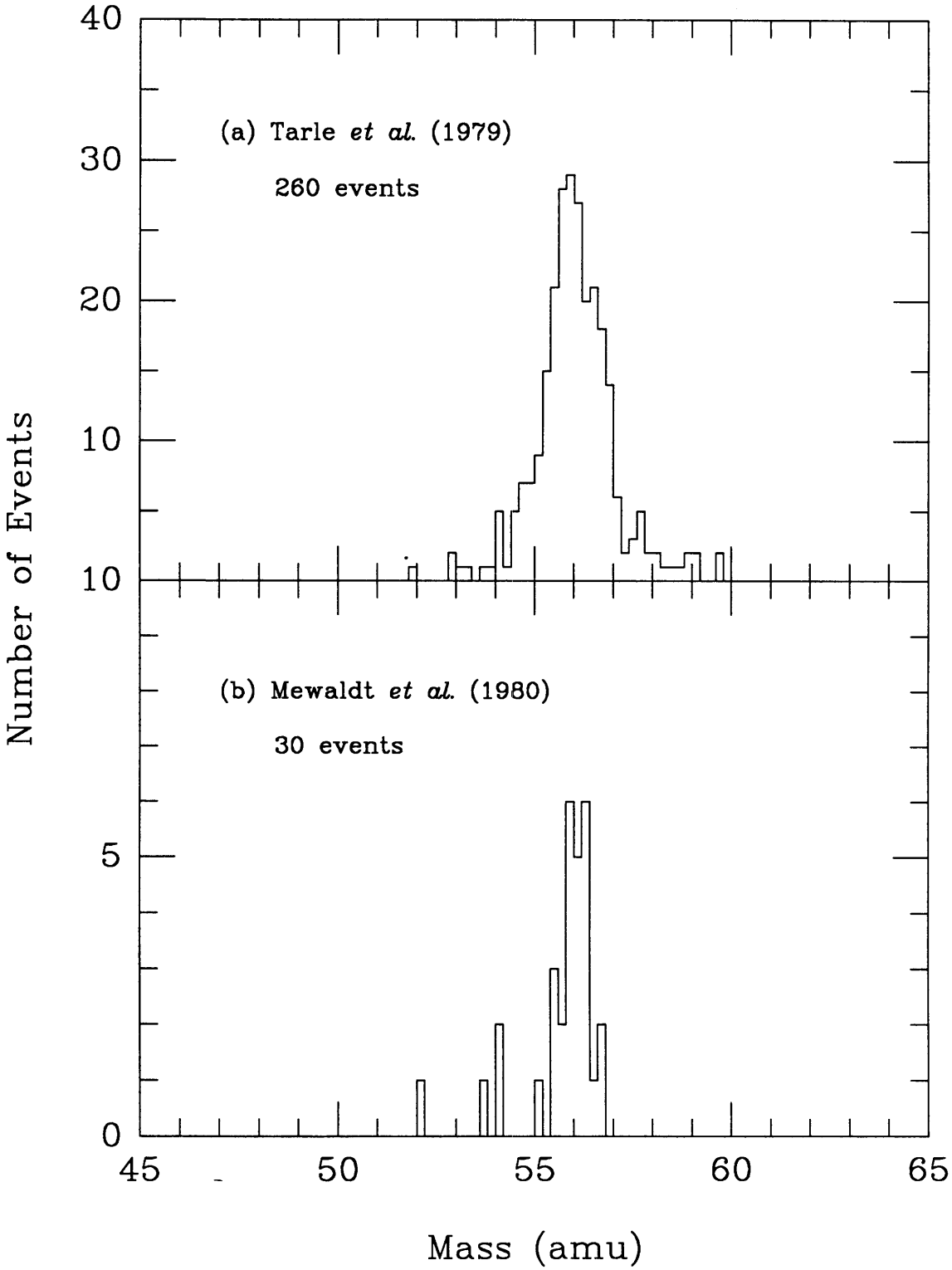
(a) Tarle *et al.* (1979)
260 events
(b) Mewaldt *et al.* (1980)
30 events
Number of Events
Mass (amu)
40
30
20
10
10
5
0
45
50
55
60
65

Figure 5.7(c,d)

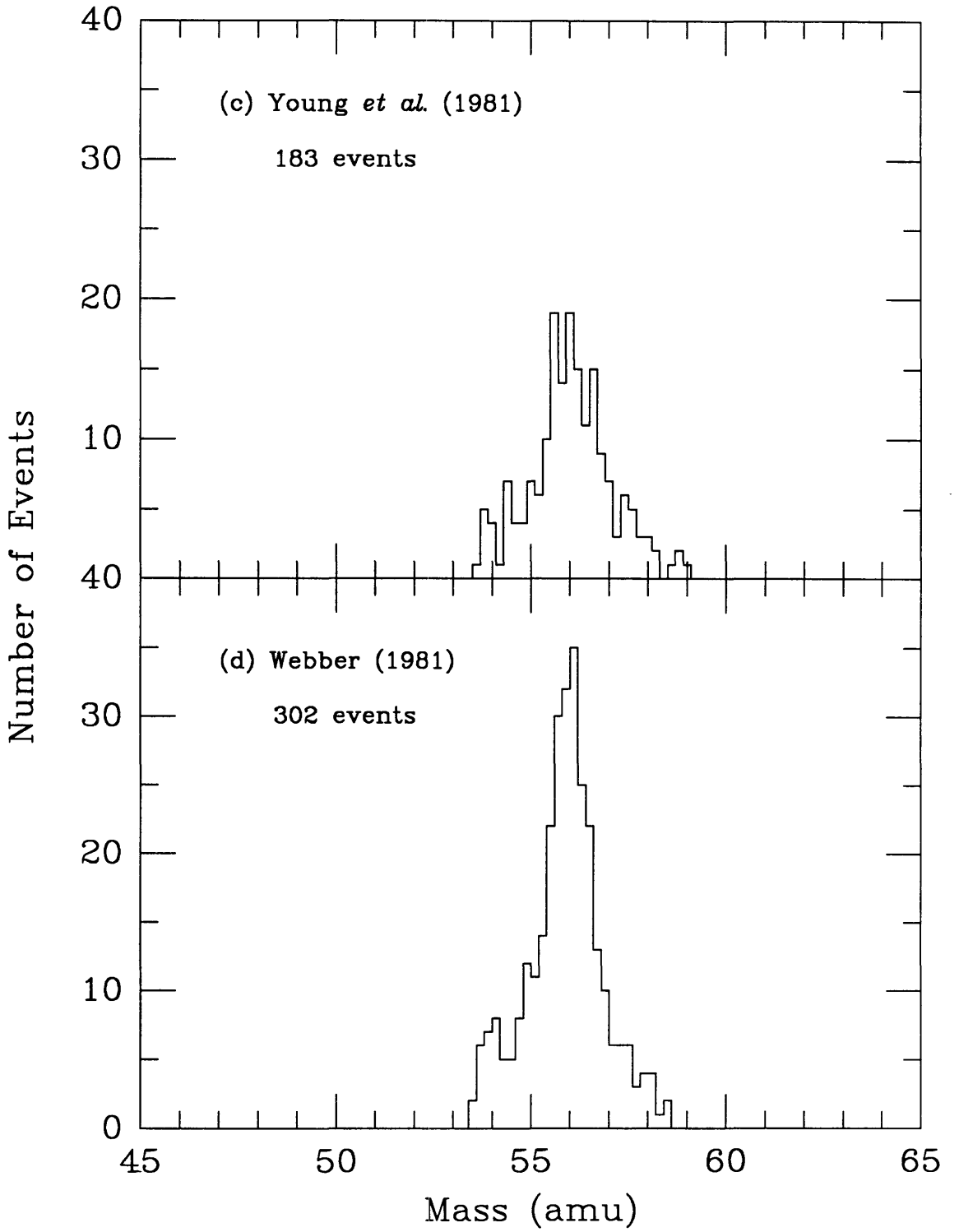
(c) Young *et al.* (1981)
183 events
(d) Webber (1981)
302 events
Number of Events
Mass (amu)
0
10
20
30
40
45
50
55
60
65

Table 5.8: Summary of Mewaldt et al., 1980 Fe composition, 83-284 MeV/nucleon		
Isotope	Observed (%)	GCRS (%)
^{54}Fe	10^{+8}_{-4}	9^{+8}_{-5}
^{55}Fe	≤ 10	≤ 7
^{56}Fe	90^{+0}_{-15}	91^{+5}_{-11}
^{57}Fe	≤ 8	≤ 8
^{58}Fe	≤ 6	≤ 6

The observations of Young *et al.* (1981) (Figure 5.7(c)) were made with a balloon-borne Cerenkov-Range telescope, with the range measurement provided by a nuclear emulsion stack and the velocity measurement by a Pilot Cerenkov radiator (n = 1.5). The sensitive energy interval at the top of the atmosphere was calculated to be 607-911 MeV/nucleon for ^{56}Fe. The observed resolution was estimated to be 0.55 amu, and 183 events were collected. Although the instrument could not resolve adjacent isotopes of Fe, the authors chose to fit their data with the abundance of each of the five species of Fe present at the top of the atmosphere—^{58}Fe, ^{57}Fe, ^{56}Fe, ^{55}Fe, and ^{54}Fe—as free parameters. The validity of such a procedure is questionable, as it could tend to overestimate the abundance of the presumably rare isotopes ^{55}Fe and ^{57}Fe, which lie in the tails of ^{56}Fe, at the expense of that more abundant isotope. Indeed, because the individual isotopes are not resolved, the deconvolution of the mass distribution depends on a precise knowledge of the resolution function. We conclude that the uncertainties reported by Young *et al.* are statistical only, and that the systematic errors arising from the method of deconvolution are likely to be much larger. Table 5.9 repeats the isotopic composition reported by Young *et al.*, given as percentages of all Fe.

Table 5.9: Summary of Young et al., 1981
Fe composition, ~600-900 MeV/nucleon

Isotope	Observed (%)	Top of Atmosphere (%)	GCRS (%)
^{54}Fe	10.8±3.1	6.6±1.9	4.8
^{55}Fe	8.8±3.6	4.2±1.7	0
^{56}Fe	59.4±7.6	65.7±8.4	69.9
^{57}Fe	13.3±4.3	14.5±4.7	≤20
^{58}Fe	7.6±3.4	9.0±4.0	≤15

The observations of Webber (1981) (Figure 5.7(d)) were made during two balloon flights of a Cerenkov-Energy telescope employing a UVT Lucite radiator (n = 1.5). The sensitive energy interval at the top of the atmosphere was calculated to be 646-900 MeV/nucleon for ^{56}Fe. The observed mass resolution was 0.40 amu, and ~300 events were collected. Table 5.10 shows the composition reported by Webber, given as numbers of events. From the figure it is apparent that Webber's measurement shows good resolution and the best statistics of all Fe isotope measurements.

Table 5.10: Summary of Webber, 1981
Fe composition, ~600-900 MeV/nucleon

Isotope	Events Observed	Top of Atmosphere
^{54}Fe	25±11	95±40
^{55}Fe+^{56}Fe+^{57}Fe	272	1281±82
^{58}Fe	≤8	≤40

Table 5.11 summarizes our measurement of the ^{54}Fe/^{56}Fe ratio corrected to the top of the atmosphere and back to the GCRS, along with our calculations from the four previous measurements. The weighted average of our measurement with that of

Mewaldt *et al.* and of Webber is given in the last row. The average, which is dominated by the Webber's measurement, is consistent with the upper limit of Tarlé *et al.*. The data of Young *et al.* have not been used because the true errors are unknown. Figure 5.8(a) shows the results from all five experiments propagated back to the GCRS. The data are plotted approximately at the average of their energy intervals at the top of the atmosphere (or the orbit of Earth). The dashed line marks the solar-system ratio.

Table 5.11: Summary of $^{54}Fe/^{56}Fe$

Author	Energy (MeV/nuc)	Top of Atmosphere	GCRS
Tarlé *et al.*	~600-900	≤ 0.11	≤ 0.084
Mewaldt *et al.*	84-284	$0.11^{+0.091}_{-0.048}$	$0.085^{+0.096}_{-0.051}$
Young *et al.*	~600-900	0.10 ± 0.032	0.077 ± 0.032
Webber	~600-900	0.079 ± 0.034	0.056 ± 0.035
This work	~1550-2200	$0.14^{+0.18}_{-0.11}$	$0.12^{+0.18}_{-0.11}$
Average			$0.064^{+0.032}_{-0.027}$

Table 5.12 gives a similar summary of the observations of $^{58}Fe/^{56}Fe$. The last row gives an estimate of the 84% confidence upper limit, which we have derived by summing our data with those of Mewaldt *et al.*. To give a conservative estimate, we assumed that one ^{58}Fe event had been observed—the event with highest mass from our mass histogram—out of 26.5 ^{56}Fe from our data set and 27 ^{56}Fe from the Mewaldt *et al.* data set. The Poisson 84% confidence upper limit of the expected number of events when fewer than two are observed is 3.3 events, from which we derive a ratio of $^{58}Fe/^{56}Fe = 0.062$. We have not used the data of Webber to derive this limit because of the difficulty of properly subtracting the contributions from ^{57}Fe and the tail of ^{56}Fe. Figure 5.8(b) shows the $^{58}Fe/^{56}Fe$ ratio propagated back to the GCRS. Again the data are plotted approximately at the average of their energy intervals, and the dashed line

Figure 5.8(a)

Calculated $^{54}Fe/^{56}Fe$ abundance ratios at the cosmic-ray source. The data are plotted approximately at the average of their energy intervals at the top of the atmosphere or the orbit of Earth. The dashed line marks the solar-system ratio. Open circle, Mewaldt *et al.*, (1980); filled square, Tarlé *et al.*, (1979); cross, Webber (1981); open square, Young *et al.*, (1981); filled circle, this work.

Figure 5.8(b)

Calculated $^{58}Fe/^{56}Fe$ upper limits at the cosmic-ray source. The data are plotted approximately at the average of their energy intervals at the top of the atmosphere or the orbit of Earth. The dashed line marks the solar-system ratio. Open circle, Mewaldt *et al.*, (1980); filled square, Tarlé *et al.*, (1979); cross, Webber (1981); open square, Young *et al.*, (1981); filled circle, this work.

Figure 5.8(a)

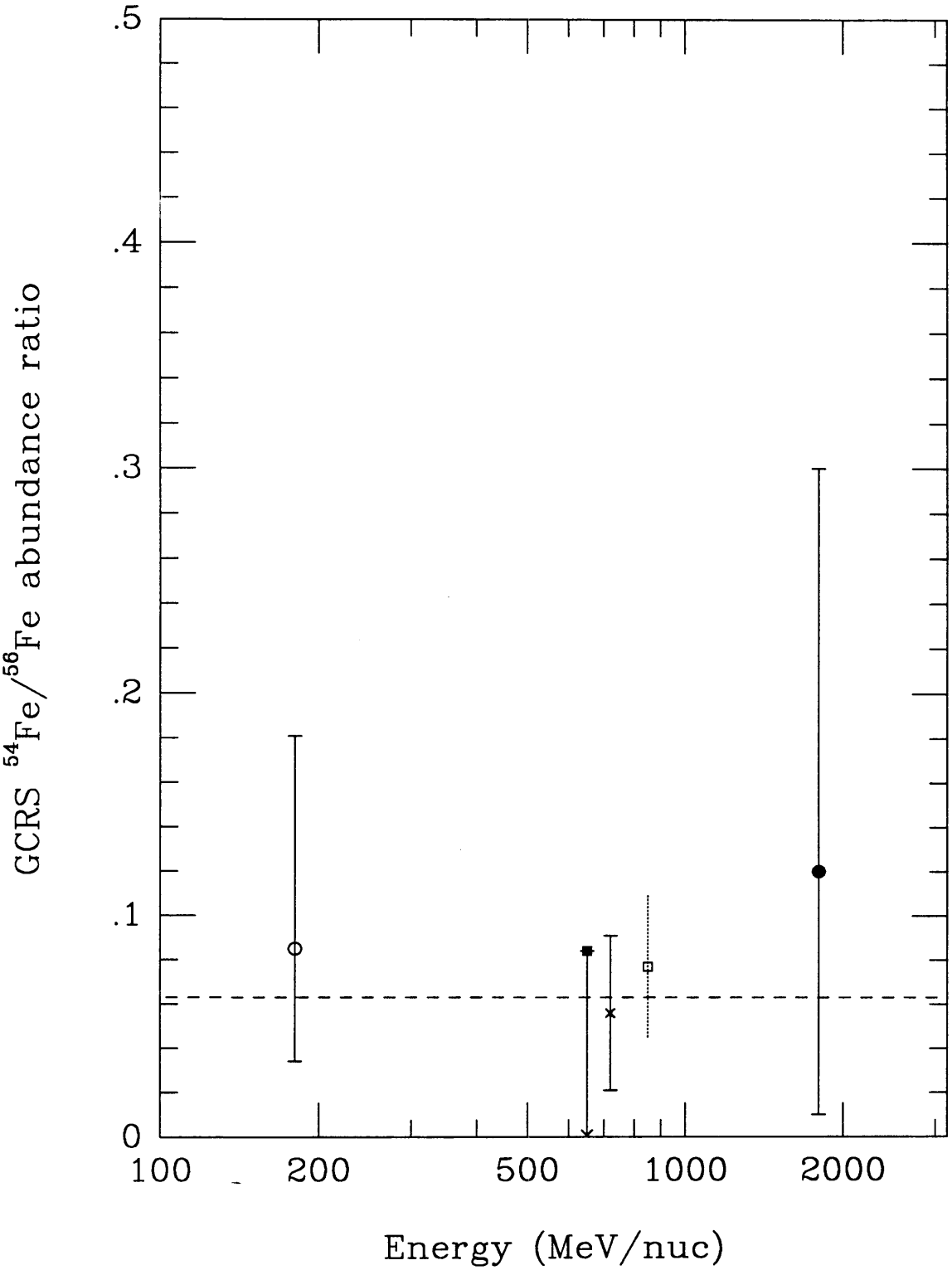
.5
.4
.3
.2
.1
0
100
200
500
1000
2000
GCRS $^{54}Fe/^{56}Fe$ abundance ratio
Energy (MeV/nuc)

Figure 5.8(b)

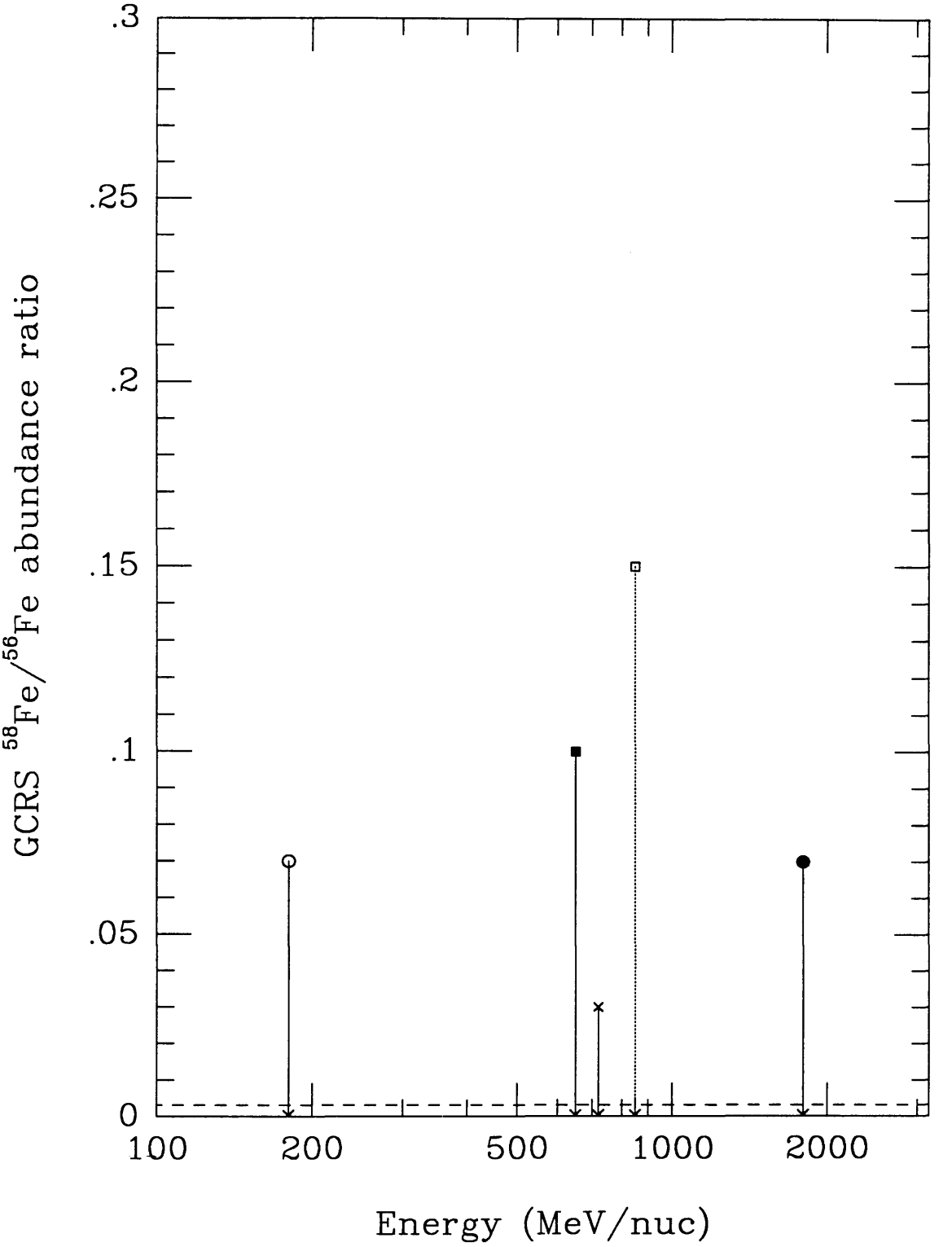
.3
.25
.2
.15
.1
.05
0
100
200
500
1000
2000
GCRS $^{58}Fe/^{56}Fe$ abundance ratio
Energy (MeV/nuc)

marks the solar-system ratio.

Table 5.12: Summary of $^{58}Fe/^{56}Fe$

Author	Energy (MeV/nuc)	Top of Atmosphere	GCRS
Tarlé *et al.*	~600-900	$\leq$0.10	$\leq$0.10
Mewaldt *et al.*	84-284	$\leq$0.07	$\leq$0.07
Young *et al.*	~600-900	$\leq$0.15	$\leq$0.15
Webber	~600-900	$\leq$0.03	$\leq$0.03
This work	~1550-2200	$\leq$0.07	$\leq$0.07
Average			$\leq$0.062

To reduce any discrepancy that might arise from differences in assumed cross sections, the results of the previous measurements have been derived by propagating the abundance ratio reported at the top of the atmosphere back to the GCRS by the procedure described in §5.4. The three mid-energy balloon measurements are made in thick instruments, and the extrapolation to the top of the atmosphere requires a correction for interactions in the detectors. Although this could result in a bias that depends on the cross sections used by the various authors, we have not modified the authors' instrumental and atmospheric corrections in any way.

We have made additional modifications to the reported results of the previous measurements. Webber reports abundances of ^{54}Fe, $^{55}Fe + ^{56}Fe + ^{57}Fe$, and ^{58}Fe. We have corrected for his summing of abundances by subtracting the amount of ^{55}Fe and ^{57}Fe expected at the top of the atmosphere, assuming solar-system abundances at the GCRS. Tarlé *et al.* report only an upper limit on the $^{54}Fe/(^{55}Fe + ^{56}Fe + ^{57}Fe)$ and $^{58}Fe/(^{55}Fe + ^{56}Fe + ^{57}Fe)$ abundance ratios at the GCRS. We have corrected for this difference in the same way. The uncertainties given by Young *et al.* are shown dotted in Figures 5.8(a) and 5.8(b), as the true uncertainties are certainly larger than reported.

The combined data are in agreement with a solar-system composition at the GCRS, although the uncertainties include the possibility of an enhancement as large as a factor of 1.6 in the $^{54}Fe/^{56}Fe$ ratio, and as large as a factor of 20 in the $^{58}Fe/^{56}Fe$ ratio. Our data permit an enhancement of a factor of $\sim$4.4 in $^{54}Fe/^{56}Fe$. The implications for the nucleosynthesis of cosmic-ray Fe are discussed below.

5.6. Nucleosynthesis of Iron

The nucleosynthesis of the Fe-group elements occurs deep within stellar interiors under conditions of extreme temperature ($T > 10^9$ °K) and density ($\rho > 10^7$ g/cm^3). Because ^{56}Fe has the highest binding energy per nucleon of all stable nuclides, its synthesis represents the end of the exothermic nucleosynthetic chain from which the lighter nuclei are formed. It is now generally accepted that the Fe-group elements are created in zones of supernovae that undergo silicon burning either just preceding or during explosive ejection (Burbidge *et al.*, 1957; Fowler and Hoyle, 1964; Bodansky *et al.*, 1968). The burning proceeds rapidly to a state of nuclear statistical equilibrium ("NSE", or "*e*-process"), in which the rates of all nuclear reactions other than β-decays are equal to their inverse reactions.

The final composition of the Fe-group depends on the temperature and density attained, the time scale for nucleosynthesis and ejection of the material, and the neutron excess of the stellar core. The neutron excess is defined to be the fractional mass excess of bound and unbound neutrons in the material. The time scale is important because it determines the degree to which β-decays can increase the neutron excess. The calculations of Woosley *et al.* (1973) show that for temperatures $T > 4\times10^9$ °K and densities $\rho > 10^7$ g/cm^3, the composition becomes nearly independent of T, ρ, and the time scale, and sensitive primarily to neutron excess.

Because of their high binding energies, the isotopes of Fe will contain most of the extra neutrons during NSE, and therefore the dependence of the final composition on the neutron excess is quite strong. The neutron excess is given by

$$\eta = \sum \frac{N_i - Z_i}{A_i} X_i , \qquad (5.15)$$

where the sum runs over all nuclear species, $N_i = A_i - Z_i$ is the neutron number of species i, and X_i is its mass fraction. The abundance of a given isotope of Fe will be maximized at the value of η equal to the neutron excess of that isotope. Figure 5.9 shows the mass fraction of several Fe-group species as a function of η in NSE at $T = 5\times10^9$ °K and $\rho = 5\times10^7$ g/cm^3 as calculated by Hainebach *et al.* (1974). With a neutron excess of 0.07, ^{56}Fe is synthesized directly only in zones with high η; in zones with $\eta < 0.036$, it is synthesized primarily as ^{56}Ni, which has no neutron excess and subsequently decays to ^{56}Fe. For intermediate values of neutron excess ($0.02 \leq \eta \leq 0.05$), ^{54}Fe is the dominant species. Note that in no zone is ^{55}Fe or ^{57}Fe dominant.

Figure 5.10 shows the ratios of mass fractions of isotopes of Fe relative to ^{56}Fe. The figure is taken from Woosley (1976) and is based on the calculations of Hainebach *et al.* (1974). The solar-system values of ^{54}Fe/^{56}Fe and ^{58}Fe/^{56}Fe are indicated with arrows. Hainebach *et al.* concluded that the solar-system composition of Cr, Fe, and Ni could be explained by assuming that the source of solar-system material was characterized by at least two zones with differing values of η. The dominant zone showed a low neutron excess ($\eta \approx 0.003$) and was responsible for the production of at least 85% of the Fe-group species. As can be deduced from Figure 5.9, this zone is the source of ^{54}Fe, ^{56}Fe, and ^{57}Fe, where the latter two are formed as ^{56}Ni and ^{57}Ni. The remainder of the Fe-group was synthesized in a zone of high η ($0.065 \leq \eta \leq 0.080$), with a negligible contribution from intermediate zones.

The average ^{54}Fe/^{56}Fe and ^{58}Fe/^{56}Fe abundance ratios from the five experiments are also indicated in Figure 5.10. Because the ^{54}Fe/^{56}Fe ratio is double-value, the measured ratio does not determine uniquely the neutron excess. Following the analysis of Tarlé *et al.* (1979), Mewaldt *et al.* (1980), and Young *et al.* (1981), we have indicated in the upper panel the regions of η that are consistent with the observed abundance ratios. We conclude that the composition of Fe in the cosmic rays is consistent with a source with either high neutron-excess ($\eta \approx 0.07$) or low neutron-excess ($0.002 \leq \eta \leq 0.005$), or indeed some combination of the two.

5.6.1. Sources of Cosmic Ray Iron

The extreme conditions under which NSE is reached are met in both Type I and Type II supernovae. The standard model of Type I supernovae (SN I) and the results of their nucleosynthesis are discussed below; however, we note that such supernovae are not preferentially located in the arms of spiral galaxies (Maza and van den Bergh, 1976). Ormes and Freier (1978) estimate that the diffusion distance of cosmic rays is $\sim$1 kpc. If this is indeed the case, SN I will presumably make a substantial contribution to the composition of the cosmic rays only if the cosmic rays are a sample of older material stored in the ISM.

Type II supernovae (SN II), on the other hand, are located in regions of active star formation in the arms of spiral galaxies. We discuss below the Supermetallicity model of Woosley and Weaver (1981), which was proposed to account for the observed enhancements of the neutron-rich isotopes of Ne, Mg, and Si. We will see that a small enhancement in the $^{54}Fe/^{56}Fe$ ratio is expected.

Finally, we will discuss briefly the nucleosynthesis in Wolf-Rayet stars. Such stars were proposed by Cassé and Paul (1982) to be the source of these neutron-rich enhancements. The isotopic composition of Fe in these stars is modified by neutron capture, which leads to a small expected enhancement in $^{57}Fe/^{56}Fe$ and $^{58}Fe/^{56}Fe$.

5.6.1.1. Type I Supernovae

Type I supernovae are generally considered to be the dominant source of Fe-group elements in the galaxy (Woosley, 1986). This follows from the observation that SN I and Type II supernovae occur with approximately equal frequency in our galaxy (roughly one per 40 years; Tammann, 1982), while SN I produce typically two to six times more ^{56}Fe than do SN II (Woosley, 1986). Note, however, that because of the substantial uncertainties in the average supernova rates and the magnitude of the production of Fe, this conclusion is not universally accepted (e.g., Arnett *et al.*, 1989). SN I are characterized by a lack of hydrogen lines in their spectra near maximum light (see the review by Wheeler, 1982). In the current "standard model," SN I are the result of the deflagration of accreting carbon-oxygen white dwarfs in binary systems. When the mass of such a star reaches 1.4 $M_{\odot}$, the core ignites, and a subsonic wave of nuclear

Figure 5.9

Mass fraction of the isotopes of Fe and their radioactive progenitors as a function of neutron excess η under nuclear statistical equilibrium as calculated by Hainebach *et al.* (1974). The figure is taken from Hainebach *et al.*. The mass fraction of a given species peaks at a value of η equal to the neutron excess of that isotope.

Figure 5.9

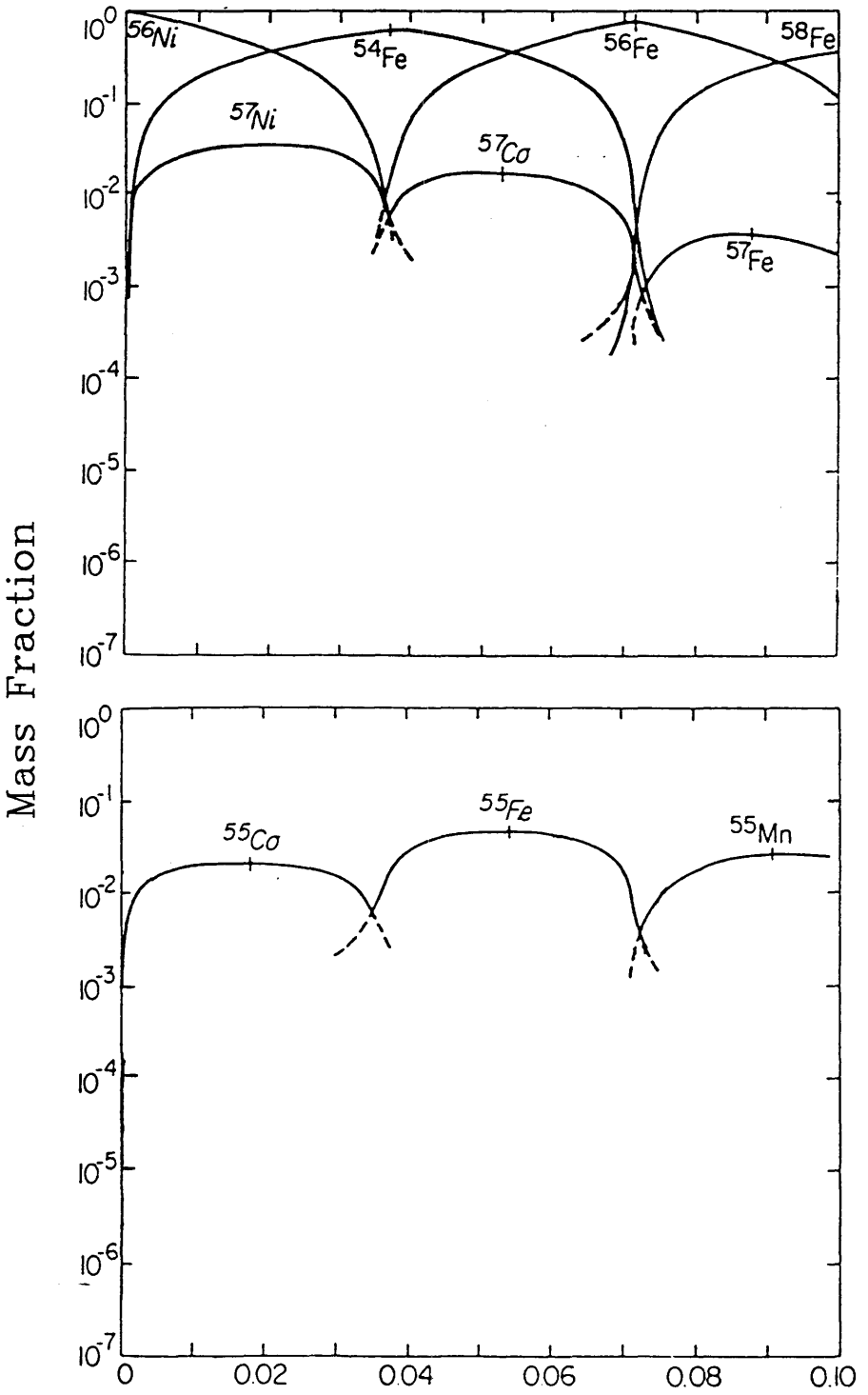
Mass Fraction
10^{0}
10^{-1}
10^{-2}
10^{-3}
10^{-4}
10^{-5}
10^{-6}
10^{-7}
^{56}Ni
^{54}Fe
^{56}Fe
^{58}Fe
^{57}Ni
^{57}Co
^{57}Fe
^{55}Co
^{55}Fe
^{55}Mn
0
0.02
0.04
0.06
0.08
0.10
Neutron Excess, η

Figure 5.10

Ratios of mass fractions of the isotopes of Fe as a function of neutron excess η. The figure is based on the calculations of Hainebach *et al.* (1974) and is adapted from Mewaldt *et al.* (1980). The abundance of each isotope includes the abundances of all radioactive progenitors that decay to the given species. The arrows mark the solar-system ratios. The solid points mark the average $^{54}Fe/^{56}Fe$ and $^{58}Fe/^{56}Fe$ abundance ratios in the cosmic rays. The upper panel indicates the regions of η that are consistent with the calculated abundance ratios.

Figure 5.10

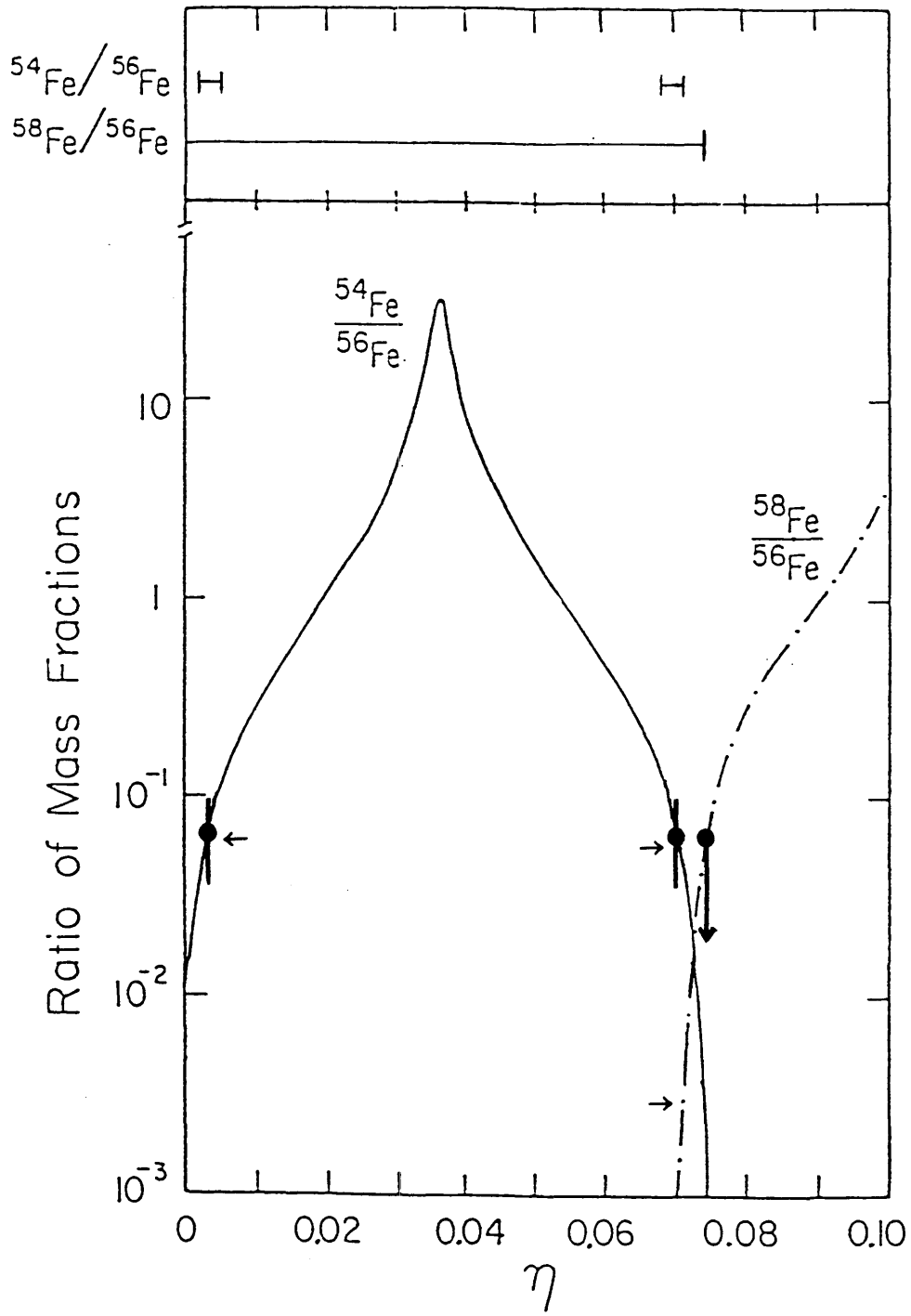
$^{54}Fe/^{56}Fe$
$^{58}Fe/^{56}Fe$
$\frac{^{54}Fe}{^{56}Fe}$
$\frac{^{58}Fe}{^{56}Fe}$
Ratio of Mass Fractions
10
1
10^{-1}
10^{-2}
10^{-3}
0
0.02
0.04
0.06
0.08
0.10
η

burning propagates outward. The burning proceeds to NSE, producing the Fe-group elements. Because the wave is subsonic, a portion of the white dwarf is able to expand rapidly enough that it is ejected unburned, along with material that has experienced intermediate temperatures and pressures. SN I are therefore efficient producers of intermediate-mass elements (Si-Ca) as well: the models of Nomoto *et al.* (1984) and Woosley and Weaver (1986) show the production of roughly half of the solar-system abundance ratio of these elements with respect to ^{56}Fe. In the core, burning proceeds to NSE, producing typically $\sim$0.9 $M_{\odot}$ of Fe-group elements, of which $\sim$0.6 $M_{\odot}$ is ^{56}Ni. No condensed remnant is expected. The amount of ^{56}Ni produced is sufficient to account for the observed light curves of SN I, and the production of intermediate-mass elements is consistent with the observed absorption spectra from SN I.

Deflagration models are not, however, without their difficulties. The recent models of Thielemann *et al.* (1986) produce an abundance ratio of ^{54}Fe/^{56}Fe that is $\sim$2.5 times the solar-system value and ^{58}Ni/^{56}Fe that is $\sim$5 times the solar-system value. The overabundance of these neutron-rich species is due to an increase in the neutron-excess of the core from the rapid electron-capture in the high-density core (Woosley and Weaver, 1986). Measurements of the Ni/Fe elemental ratio in the cosmic rays (e.g., Binns *et al.*, 1988) are consistent with or comparable to the solar-system value of 5.5% (Anders and Ebihara, 1982) and would appear to rule out any such enhancement in the abundance of Ni, if the cosmic rays are a sample of freshly synthesized material. Woosley and Weaver (1986) suggest that a more complete understanding of the flame propagation may resolve this difficulty. Indeed, by limiting the initial velocity of the burning front, they are able to produce ^{54}Fe and ^{58}Ni in solar-system proportions, while overproducing ^{58}Fe by a factor of about three. Models of the flame propagation are currently in a state of rapid evolution. Until a consensus is reached, reliable estimates of the expected composition of the Fe-group elements produced by SN I will not be available, and their contribution to cosmic-ray composition will remain uncertain.

5.6.1.2. Supermetallicity Model

The Supermetallicity model of Woosley and Weaver (1981) suggests that a significant fraction of the cosmic rays are synthesized in SN II that are metal-rich by a

factor of about two relative to the solar system. SN II occur in massive young stars at the end of their stable burning lifetimes. In a typical SN II, the core of a star with mass $\sim$25 $M_\odot$ burns to the Fe-group elements via NSE. The $\sim$1 $M_\odot$ core then collapses and rebounds, ejecting $\sim$0.1-0.3 $M_\odot$ of ^{56}Ni as well as the overlying material. In particular, from the light curve of the recent Type II supernova SN1987a in the Large Magellanic Cloud, Woosley (1988) calculated that $\sim$0.075 $M_\odot$ of ^{56}Ni was ejected.

The neutron excess of the presupernova star is related to its initial metallicity. The metallicity Z is defined as the mass fraction of nuclei heavier than He; the Sun has $Z_\odot = 0.020$ (Anders and Ebihara, 1982). The isotopes of C, N, and O account for essentially all of the initial metallicity and are converted to ^{14}N at the end of hydrogen burning (e.g. Clayton, 1968). The neutron-rich species ^{18}O and ^{22}Ne are created from ^{14}N during the subsequent helium burning by the following sequence,

$$^{14}\mathrm{N}\,(\alpha,\gamma)\,^{18}\mathrm{F}\,(\mathrm{e}^{+}\nu)\,^{18}\mathrm{O}\,(\alpha,\gamma)\,^{22}\mathrm{Ne}\ . \tag{5.16}$$

The mass fraction of ^{22}Ne at this stage is therefore $\mathrm{X}(^{22}\mathrm{Ne}) \approx 0.02\,(Z/Z_\odot)$, and consequently the neutron excess is $\eta \approx 0.002\,(Z/Z_\odot)$ (Woosley and Weaver, 1981).

The Supermetallicity model centers on the observation that the production of ^{22}Ne is proportional to the initial metallicity. At the conclusion of helium burning, some ^{22}Ne is destroyed through the $^{22}\mathrm{Ne}\,(\alpha,\mathrm{n})\,^{25}\mathrm{Mg}\,(\alpha,\gamma)\,^{29}\mathrm{Si}$ and $^{22}\mathrm{Ne}\,(\alpha,\gamma)\,^{26}\mathrm{Mg}\,(\alpha,\gamma)\,^{30}\mathrm{Si}$ reactions, leading to enhancements of these neutron-rich species as well.

Table 5.13 lists the expected enhancements of certain isotopes, assuming a source with metallicity $Z = 1.8 Z_\odot$ or neutron excess $\eta \approx 0.0036$. The enhancement factors in the table are scaled from the factors given by Woosley and Weaver (1981), who assumed a metallicity of $Z = 2.5 Z_\odot$. The increase in metallicity is a free parameter and has been chosen to give a good fit to the observed excess for Mg and Si. It is clear that the model requires an additional source of ^{22}Ne in the cosmic rays. In their paper, Woosley and Weaver estimated an enhancement in the ^{54}Fe/^{56}Fe ratio of about two for $Z = 2.5 Z_\odot$, with a warning that electron captures during silicon burning can mask the effect of the increased metallicity. Woosley has subsequently stated that, given this uncertainty, he would not give a prediction for ^{54}Fe/^{56}Fe if he were to write the paper again (personal communication with R. A. Mewaldt, 1987). Recall that the calculations

of Hainebach *et al.* (1974) indicate that most solar-system Fe was synthesized in a zone with $\eta \approx 0.003$; thus in the absence of extensive electron captures in the core, an enhancement of only $\sim$1.2 is expected in the $^{54}Fe/^{56}Fe$ ratio for $Z = 1.8 Z_{\odot}$. Even if electron captures increase the neutron excess and consequently the production of ^{54}Fe, the possible significant contribution of Fe of unknown composition from SN I may dilute any enhancement from SN II in the cosmic rays. For these reasons, we have placed a question mark in the table following the expected enhancement factor. Note that no enhancement is expected for ^{58}Fe, as the calculations of Hainebach *et al.* indicate for zones with $\eta < 0.07$.

Table 5.13: Supermetallicity Isotopic Enhancements
$Z = 1.8 Z_{\odot}$, after Woosley and Weaver (1981)

Isotope Ratio	GCRS/SS
$^{22}Ne/^{20}Ne$	1.8
$^{25}Mg/^{24}Mg$	1.7
$^{26}Mg/^{24}Mg$	1.5
$^{29}Si/^{28}Si$	1.5
$^{30}Si/^{28}Si$	1.6
$^{54}Fe/^{56}Fe$	$\sim$1.2 ?
$^{58}Fe/^{56}Fe$	1

5.6.1.3. Wolf-Rayet Model

Wolf-Rayet stars are the exposed helium-burning cores of massive stars ($M_{ZAMS} \sim 50\, M_{\odot}$) undergoing rapid mass-loss ($\dot{M} > 10^{-5}\, M_{\odot}\, yr^{-1}$) to a high-speed stellar wind ($v_{WR} \sim 2000$ km s^{-1} $\sim 5\, v_{solar\ wind}$) (e.g., de Loore and Willis, 1982). A subclass of these stars, the WC stars, have spectra dominated by emission lines of He, C, and O, indicating that the freshly processed nuclear material is available at the stellar surface (e.g., Willis and Wilson, 1978). Cassé and Paul (1982) have proposed that the ^{22}Ne

formed by the helium-burning of ^{14}N (Equation (5.15)) should therefore be enhanced at the surface of WC stars to a value $^{22}Ne_{WR}/^{22}Ne_{\odot} = (CNO)_{\odot}/^{22}Ne_{\odot} \sim 120$, when the initial metallicity is assumed to be solar. The abundance of ^{20}Ne is preserved in helium-burning zones. Again, at the end of helium burning, some ^{22}Ne is destroyed by the (α,n) and (α,γ) reactions leading to ^{25}Mg and ^{26}Mg; however, the temperature does not reach a sufficiently high level that the Coulomb barrier for α-capture on ^{25}Mg and ^{26}Mg is overcome, indicating that ^{29}Si and ^{30}Si are not produced in excess. Neutrons from $^{22}Ne(\alpha,n)^{25}Mg$ can drive some s-process nucleosynthesis, leading in particular to an enhancement of ^{57}Fe and ^{58}Fe.

Table 5.14 shows the isotopic enhancements in the stellar wind of a WC star with Zero-Age Main-Sequence Mass $M_{ZAMS} \sim 80M_{\odot}$, adapted from Prantzos (1984). The expected enhancements in the cosmic rays are given in the third column, based on the assumptions that WC stars comprise 60% of all Wolf-Rayet stars and that one out of 25 cosmic ray particles of the dominant species listed in the table is produced in a Wolf-Rayet star. The remaining cosmic ray particles are assumed to have solar-system isotopic composition. The dilution factor of 25 is a free parameter which was chosen to fit the observed $^{22}Ne/^{20}Ne$ enhancement, and it may not apply to the composition of Fe. It is clear from the table that the observed isotopic anomalies of Ne and Mg can be explained quite readily, while an additional source of neutron-rich Si in the cosmic rays must be found.

Table 5.14: WC Isotopic Enhancements
$M_{ZAMS} \sim 80 M_{\odot}$, Prantzos (1984)

Isotope Ratio	WC/SS	GCRS/SS
$^{22}Ne/^{20}Ne$	120	~3.9
$^{25}Mg/^{24}Mg$	35	~1.5
$^{26}Mg/^{24}Mg$	40	~1.5
$^{29}Si/^{28}Si$	3	~1
$^{30}Si/^{28}Si$	5	~1
$^{57}Fe/^{56}Fe$	15	~1.2
$^{58}Fe/^{56}Fe$	40	~1.6

Note that small enhancements in ^{57}Fe and ^{58}Fe are predicted; however, both are rather difficult to observe because of the small solar-system abundance ratios (Tables 5.4 and 5.5). Clearly, the measurements to date are unable to test the predictions of this model for Fe, and, in fact, significant increases in exposure time will be necessary. Such measurements will be at the limit of the statistical accuracy of isotope spectrometers aboard the *CRRES*, *Ulysses*, and *WIND* spacecraft to be launched in the early 1990s (R. A. Mewaldt, 1989, personal communication).

Chapter 6
Conclusions and Prospects for the Future

6.1. Isotopic Composition of Cosmic Ray Iron

We have reported an $^{54}Fe/^{56}Fe$ abundance ratio of $0.14^{+0.18}_{-0.11}$ and an 84% confidence upper limit of $^{58}Fe/^{56}Fe \leq 0.07$ in the energy interval ~1550-2200 MeV/nucleon at the top of the atmosphere. Using a propagation model that assumes that ^{54}Mn decays to ^{54}Fe with a half-life of 2×10^6 years and that ^{55}Fe is absent at the GCRS, the measurements correspond to abundance ratios of $^{54}Fe/^{56}Fe = 0.12^{+0.18}_{-0.11}$ and $^{58}Fe/^{54}Fe \leq 0.07$ at the source. Both are consistent with a solar-system abundance at the GCRS; however, they permit significant enhancements of ^{54}Fe and ^{58}Fe.

Combining our data with those of Tarlé *et al.* (1979), Mewaldt *et al.* (1980), Webber (1981), and Young *et al.* (1981), we derive $^{54}Fe/^{56}Fe = 0.064^{+0.032}_{-0.027}$ and $^{58}Fe/^{56}Fe \leq 0.062$ at the GCRS. These values are consistent with the solar-system composition, for which $^{54}Fe_\odot/^{56}Fe_\odot = 0.0632$ and $^{58}Fe_\odot/^{56}Fe_\odot = 0.0032$ (Anders and Ebihara, 1982). From the calculations of Hainebach *et al.* (1974), we conclude that these abundance ratios are consistent with the nucleosynthesis of cosmic-ray Fe having occurred via nuclear statistical equilibrium in a single zone or combination of zones with low neutron excess ($0.002 \leq \eta \leq 0.005$) or high neutron excess ($\eta \approx 0.07$).

6.2. Limitations of Aerogels

Because aerogel is a solid material with an index of refraction that corresponds to an energy range that is readily available from a Shuttle orbit or the proposed Space Station, aerogel Cerenkov radiators hold a promise for future high-resolution, cosmic-ray mass spectrometers; however, several limitations of the material have become apparent and should be addressed.

(1) Aerogels suffer from relatively low light yield. The design goal of a Cerenkov detector is maximum light yield—i.e., maximum resolution—with a minimum number of nuclear interactions and minimum ionization energy loss. Because the Cerenkov yield from a particle with velocity $\beta = 1$ is proportional to $1 - n^{-2}$ (see Equation (2.2)), radiators with low refractive indices—high Cerenkov thresholds—produce inherently less Cerenkov radiation than do radiators with high indices and low thresholds. To compensate for this decreased light output, low-index radiators tend to be thicker, resulting in a larger number of nuclear interactions. R. A. Mewaldt (1985) has studied the Cerenkov yields of counters containing a variety of radiators reported in the literature. There is, of course, considerable uncertainty in accounting for systematic differences among counters, such as differences in photocathode efficiency and light-collection efficiency. After accounting for difference in yield for $\beta = 1$ particles, we conclude that the relative yield per interaction length of Fe for aerogels is somewhat smaller than, but not less than half, that of conventional radiators such as lucite and fused silica.

Using a variation of the p-terphenyl (PTP) wavelength-shifter employed by the New Hampshire group (Webber and Kish, 1983), we have succeeded in doubling the yield of Teflon and fused silica radiators. In a first attempt to use wavelength-shifters with aerogels, we wrapped spare aerogel blocks in 0.002" Teflon sheets coated with PTP. We found that the Cerenkov yield from an ^{56}Fe beam at the Bevalac increased by $\sim$15% with respect to unwrapped blocks. Wavelength-shifting techniques warrant further investigation.

(2) The Cerenkov yield from aerogels degrades with time. The 2%-per-month decrease which we observed is higher than that observed by other groups (§3.6.3), and the question of whether this might be due to the exposure to the $BaSO_4$ paint or perhaps due to the sintering deserves to be addressed. Because of their porous nature, aerogels have extremely large effective surface area, and are therefore highly susceptible to contamination. Care must be taken to ensure that aerogels are stored in a clean, dry environment. Indeed, we have stored aerogel blocks that were intended as spares for the mosaic in dessicator jars, and these blocks have not visibly yellowed in the six years

since they were delivered. While we have not removed blocks from the mosaic to make a systematic comparison of light yield with those kept in the clean environment, we suspect that the spares would not show the severe degradation.

(3) Aerogels appear to suffer from stochastic variations in index of refraction over length scales <1 cm (§3.6.2) that significantly affect their velocity resolution. The level of stochastic variation observed in the HEIST aerogel blocks ($\sigma_n = 4.7\times10^{-4}$ for 6 cm of aerogel) results in a significant contribution to the velocity resolution of the counter (§2.3.1.5 and §3.6.2). The magnitude of this variation should be confirmed in aerogels from a different manufacturing lot, and the dependence on the average index of refraction should be studied.

(3) Aerogels are currently manufactured only in small sizes. The limits on the size of blocks that can be produced currently are set by the size of ovens available for the sintering process. Large sizes are needed to reduce the number of block edges in large-area counters, and larger blocks may have more uniform absorption and transmission characteristics. Efforts are under way to produce blocks 60 cm on a side (Rasmussen, 1989).

6.3. Enhancements in the HEIST Detector System

The HEIST instrument has been extensively modified since the May 1984 flight. One of its advantages is that it is readily tunable to a wide range of energy intervals. Having flown the instrument for high energies, we have elected to decrease the energy and increase the statistical accuracy. At low energies, particles stop in the NaI(Tl) stack; thus the Cerenkov-Energy technique is used rather than the Cerenkov-ΔE-Cerenkov technique. Thus the bottom Cerenkov counter has been removed, and the top aerogel counter replaced with two counters: the upper counter contains a Teflon radiator ($n = 1.33$) 3.4 g/cm^2 thick, and the lower counter contains a Pilot-425 radiator ($n = 1.5$) 1.7 g/cm^2 thick (Christian *et al.*, 1987). The Cerenkov yield from both radiators is significantly greater than that from the aerogel: the number of photoelectrons collected in the Teflon counter is $N_\mu = 60$, and in the Pilot-425 counter, $N_\mu = 85$.

The new configuration, with its lower energy threshold, should produce measurements with improved statistics and higher resolution.

More events of all charges will be collected. (1) Because the flux of cosmic rays falls off approximately as a power law in total energy, $dN/dW \propto W^{-2.5}$, the flux is greater in the lower energy interval. (2) Particles at lower energies will have shorter ranges in the NaI(Tl) stack and therefore will suffer fewer nuclear interactions. (3) Because the particles will have shorter ranges in the stack, the instrument will have a larger effective acceptance angle and geometry factor. (4) Single-piece Cerenkov radiators will eliminate the loss of ~33% of the data from the position uncertainty near the aerogel block edges. (5) Finally, because of the lower threshold energy, significant numbers of particles with charge $Z<26$ will stop in the stack. In the HEIST I instrument, events with $Z<26$ that were above the aerogel Cerenkov threshold penetrated the stack.

The resolution is improved. (1) Both Cerenkov counters have significantly higher photoelectron yields than the aerogel counter had, reducing the contribution from photoelectron statistical fluctuations (§2.3.1.1). (2) Because both radiator materials are more uniform than aerogel, we expect that the magnitude of stochastic index variations should be reduced (§2.3.1.5). Calibration data taken at the Bevalac in November 1987 should allow this to be measured. (3) Gradients in the Cerenkov response have been measured to be $<0.2\%$ cm^{-1} over $>90\%$ of the Pilot radiator, and $<2\%$ cm^{-1} over 90% of the Teflon radiator. The smaller gradients should reduce the contribution from mapping errors, as the maps will be easier to construct (§2.3.1.6). The contribution from position uncertainty should be correspondingly reduced as well (§2.3.1.9). (4) The contributions from Cerenkov response normalization should be dramatically reduced (§2.3.1.7), as flight data should not be necessary for the normalization. (5) At energies above the Cerenkov threshold in the Pilot-425 counter, the two Cerenkov counters give independent velocity measurements. (6) The NaI(Tl) stack is being remapped currently from the 1982 calibration data using new, more detailed corrections for the spill-gain and run-gain effects. This remapping should improve both the position and energy loss resolution.

The instrument was readied for flight from Ainsworth, Nebraska, in August 1986; however, the balloon failed on ascent and no data were gathered. The instrument

suffered minor damage, was repaired, and was subsequently flown from Prince Albert, Saskatchewan, during 25-27 August 1988. The instrument spent $\sim$34 hours at float altitude. We estimate that $>$300 non-interacting Fe events with mass resolution $\leq$0.4 amu were gathered, along with $>$1500 each of Ne, Mg, and Si, and $>$5000 each of C and O.

Appendix A
Contribution to Cerenkov Signal from Knock-on Electrons

A.1 Introduction

It is well known that the knock-on electrons generated above and within a Cerenkov radiator by the passage of a high-energy charged particle will produce Cerenkov radiation amounting to a few percent of the Cerenkov radiation from a relativistic primary particle. Lezniak (1976) gives a numerical algorithm for calculating the average Cerenkov component that is due to knock-on electrons. We have developed an improved algorithm based on Lezniak's which more accurately calculates the mean and also yields the standard error in the mean knock-on electron component from fluctuations in the number and energies of the electrons. The results are presented below. The contribution to mass resolution of HEIST from the knock-on electron fluctuations is discussed in §2.3.1.3.

We have modeled the HEIST aerogel Cerenkov detector with material upstream from the radiator appropriate for both the Bevalac calibration and the flight, and have made simple functional fits to the result. We have found that for a primary particle of charge Z, the knock-on electrons contribute typically $\sim$2% of the relativistic light Z^2N_μ, with a standard error of the mean of typically $\sim 5Z^{-1}\%$ of Z^2N_μ, where N_μ is the number of photoelectrons generated in the entire thickness of the radiator by a vertically incident relativistic particle with Z=1.

Section A.2 below outlines the development of the algorithm, Section A.3 the numerical techniques, and Section A.4 the results of the numerical algorithm. A simple Monte Carlo simulation of the production of knock-on electrons is discussed in §A.5. The results are applied to the interpretation of the Bevalac data in §3.6.2.

A.2 The Algorithm

Lezniak presents the development of his algorithm in detail, and the important steps are repeated below for completeness. We examine the effect of his approximation for the energy loss of electrons, and our enhancements to his algorithm are emphasized. The additional steps required to calculate the standard error of the knock-on electron component follow the discussion from Lezniak. As an example, Lezniak modeled a Cerenkov counter with a lucite radiator (n = 1.49) 2.25 g/cm^2 thick with a variable thickness of overlying material. We will use his results as a point of reference for our changes in the algorithm.

First, the number of photoelectrons produced per g/cm^2 of radiator by a particle of charge Z and kinetic energy per nucleon E and collected in the viewing system of a Cerenkov counter can be expressed as follows,

$$\frac{dC}{dx}(Z,E) = \frac{Z^2 N_\mu \sec\theta}{t \sec\theta} \frac{1 - \frac{1}{n^2\beta^2}}{1 - \frac{1}{n^2}} \qquad \beta > n^{-1}, \tag{A.1}$$

where N_μ is the number of photoelectrons collected from a vertically incident primary particle of charge Z=1 and velocity β=1, β is the particle velocity, and n is the index of refraction of the radiator. The thickness of the radiator is t g/cm^2, and the angle of incidence of the particle is θ. Note that the angular dependence cancels.

From the first Born approximation, one can derive the the number of knock-on electrons having energies between E′ and E′ + dE′ produced per g/cm^2 of target material by the passage of a particle of charge Z at velocity β and Lorentz factor γ (e.g., Rossi, 1952),

$$\phi_{mat}(Z,E,E')\, dE'\, dx' = \frac{\alpha_{mat} Z^2}{\beta^2} \frac{1}{E'^2} \left[1 - \beta^2 \frac{E'}{E_{max}} \right] dE'\, dx' \qquad 0 \le E' \le E_{max} \tag{A.2}$$

where $E_{max} = 2m_e c^2(\gamma^2 - 1)$ is the maximum energy that can be imparted to a knock-on electron, and $\alpha_{mat} = 0.30058\ m_e c^2\ Z_t/A_t$ MeVcm^2/g, where Z_t and A_t are the charge and mass numbers of the target material.

The knock-on electrons are produced at an angle ψ about the trajectory of the primary particle, which is determined by the kinematics of the interaction and given by

$$\cos\psi(E,E') \approx \frac{1}{\beta}\left[\frac{\gamma'-1}{\gamma'+1}\right]^{\frac{1}{2}}, \qquad (A.3)$$

where γ' is the Lorentz factor of the knock-on electron. Note that this implies, as one would expect, that the high-energy knock-on electrons, which would tend to penetrate the radiator, are produced at small angles, and that low-energy knock-on electrons, which would tend to stop, are produced at larger angles. Therefore the inclusion of the production angle should have only a small effect on the calculated knock-on electron component of the total Cerenkov emission, and indeed we find that including the production angle increases this component by $\sim$1% or less. Therefore an assumption of constant production angle (e.g., $\psi = 0°$) would be adequate and would simplify the numerical methods; however, we have chosen not to make this approximation.

The model detector system is shown in Figure A.1, which was taken from Lezniak. The overlying material of thickness δ g/cm^2 occupies the interval from 0 to δ, and the radiator of thickness t the interval from δ to $\delta+t$. The point x$'$ represents the point along the path of the primary particle at which a knock-on electron is produced with energy E$'$ at an angle ψ with respect to the angle of incidence θ of the primary. We take the detector elements to be infinite in lateral extent. Knock-on electrons are produced in the overlying material and in the radiator and are allowed to propagate through the detector system, losing energy as they travel. They generate Cerenkov light whenever they are in the radiator and have $\beta' > n^{-1}$.

Lezniak neglected the deceleration of the primary particle as it traversed the detector elements. This approximation is certainly valid for primary particles with ranges much longer than the detector thickness, although one can imagine detector configurations for which the residual range for primary particles in the Cerenkov radiator is comparable to the radiator thickness. Such conditions have arisen in our accelerator calibrations of Cerenkov radiators. For completeness, we have accounted for the energy loss of the primary particle, using the power-law range-energy relation for heavy charged particles in NaI(Tl) (Equation (4.5)) evaluated, using the parameters

from Table 4.1. In our model of the aerogel counter, inclusion of the energy loss of the primary particle causes a negligible increase in the Cerenkov signal generated by the knock-on electrons. At the much lower energies appropriate for Lezniak's lucite counter with 2.0 g/cm^2 of overlying material, the increase in the contribution from knock-on electrons is still small, $<1\%$. We conclude that for typical Cerenkov detector configurations, with radiator and overlying material thicknesses each a few g/cm^2, the effect of the slowing of the primary particle is negligible.

To account for the energy loss of the knock-on electrons in the overlying material and the radiator, we have adopted the extrapolated range relation for electrons, also known as the "practical" range relation, modified from that given by Kobetich and Katz (1968) for aluminum,

$$R(E) = h(Z_t,A_t)\,A\,E\left[1 - \frac{B}{1+D\,E}\right], \tag{A.4}$$

where $A = 0.537\ g\,cm^{-2}MeV^{-1}$, $B = 0.9815$, and $D = 3.1230\ MeV^{-1}$ for electrons with energies between 0.3 keV and 20 MeV. We have added the multiplicative correction factor $h(Z_t,A_t)$ to account for the dependence on the target material. From the tabulation of calculated electron ranges of Berger and Seltzer (1964), we have deduced the following approximate scaling relation for materials free of hydrogen:

$$h(Z_t,A_t) = 0.911 + 2.41\left(1 - \frac{2Z_t}{A_t}\right), \tag{A.5}$$

where Z_t and A_t are the average charge and mass number of the target material. Hydrogenic compounds do not obey the above relation; however, from Berger and Seltzer we can deduce that the correction factors for lucite and polyethylene, for example, are 0.813 and 0.753, respectively. At high electron energies, when bremsstrahlung becomes important, the scale factor $h(Z_t,A_t)$ fails to account for differences among materials. Evans (1955) gives the following heuristic for estimating the ratio of radiative to ionization energy losses for electrons:

$$\frac{(dE/dx)_{rad}}{(dE/dx)_{ion}} \sim \frac{Z_t E}{700}, \tag{A.6}$$

Figure A.1

Schematic representation of the production of knock-on electrons in a Cerenkov counter with a radiator of thickness t and overlying material of thickness δ. The primary particle has an angle of incidence θ. The knock-on electron is produced at depth x' along the path of the primary particle and at an angle ψ with respect to the trajectory of the particle. The left-hand diagram corresponds to knock-on electrons produced in the material above the radiator, where $0 < x' < \delta \sec\theta$. The right-hand diagram corresponds to electrons produced within the radiator, where $\delta \sec\theta < x' < (\delta + t)\sec\theta$.

The figure is adapted from Lezniak (1976).

Figure A.1

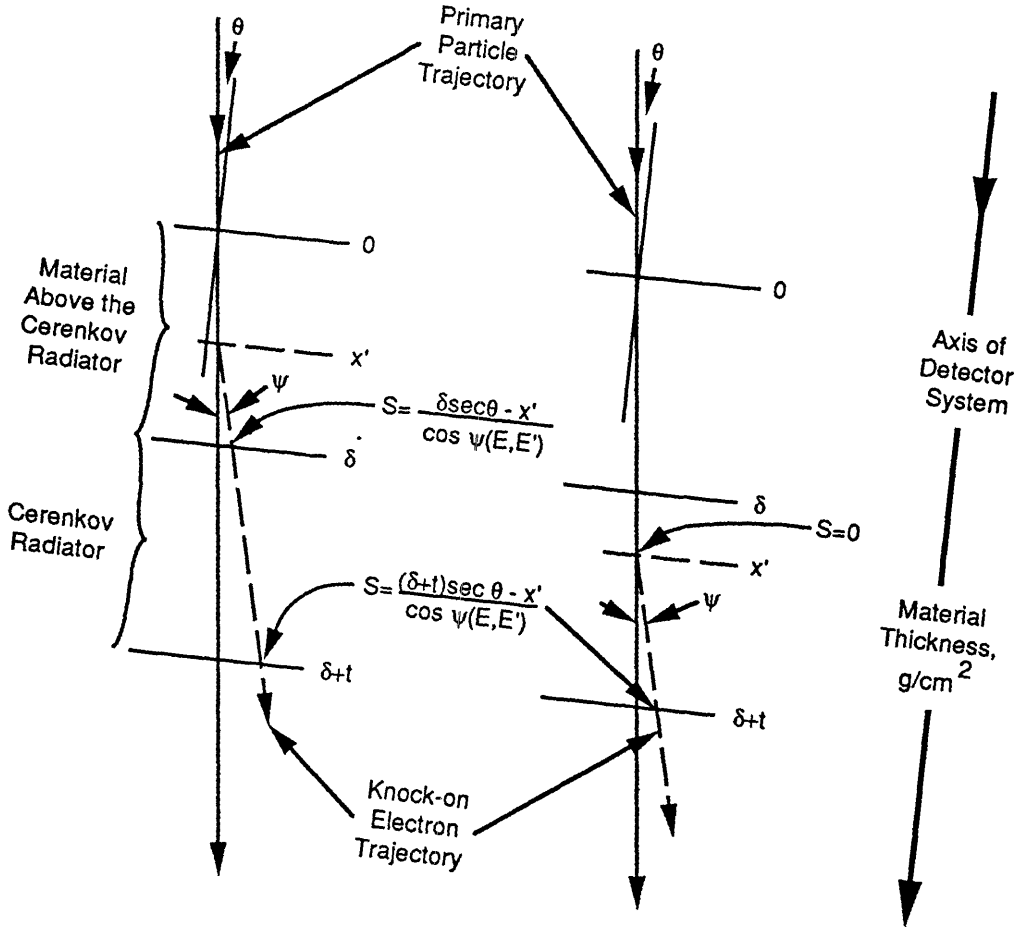

Diagram for Knock-on Electrons Produced above the Cerenkov Radiator

Diagram for Knock-on Electrons Produced within the Cerenkov Radiator

where the kinetic energy E is measured in MeV and Z_t is the average charge of the target material. Radiative losses in aerogel (SiO_2) should therefore be similar to those in aluminum, and therefore Equation (A.4) should be appropriate up to 20 MeV.

The inverse relation, energy as a function of electron range, can be shown to be

$$\epsilon(R) = \frac{1}{2hAD}\left[DR - hA(1-B) + \left\{4hADR + (DR - hA(1-B))^2\right\}^{1/2}\right] \quad (A.7)$$

and we can differentiate Equation (A.4) to give the effective energy loss

$$\frac{dE}{dx} = \frac{1}{hA}\left[\frac{(1+DE)^2}{(1+DE)^2 - B}\right]. \quad (A.8)$$

In modeling his sample lucite counter, Lezniak used a constant $dE/dx = 2\ MeV\,cm^2/g$, which is ~50% too low for electrons with energies at the Cerenkov threshold (~180 keV). Since the range for such electrons is less than the value Lezniak deduces, they drop below the threshold energy more quickly and the knock-on electron contribution decreases. We find that inclusion of the improved range-energy relation results in a decrease of ~30% in the knock-on electron Cerenkov contribution relative to Lezniak's calculated value. For counters with higher thresholds, such as the HEIST aerogel counter, Lezniak's approximation is more appropriate, since inspection of Equation (A.4) shows that at energies above 1 MeV, dE/dx is within ~5% of its asymptotic value, $1.86/h(Z_t,A_t)\ MeV\,cm^2/g$. Thus any difference between the prediction of Lezniak's algorithm and our algorithm for the aerogel counter will be dominated by the difference in magnitude of the approximately constant dE/dx.

The extrapolated range is calculated from the measured transmission probability of monoenergetic beams of electrons through absorbers of known thickness, and it therefore includes the effects of electron scattering as an average over many beam particles. We have assumed that the extrapolated range is an adequate estimate of both the pathlength and the average range of electrons in the detector materials.

The Cerenkov signal $Y(E,\theta,E',x')$ generated by a single knock-on electron of kinetic energy E' produced at position x' by a primary particle of energy E can be calculated by integrating the Cerenkov formula (Equation (A.1)) along the trajectory of

the knock-on in the radiator, or equivalently, by integrating over the electron energy along the path through the radiator. Thus we write

$$Y(E,\theta,E',x') = \int_{E_l}^{E_u} \frac{dC}{dx}(Z=1,E'') \frac{dx}{dE}(E'') \, dE'' , \tag{A.9}$$

where the limits of integration ensure that only those knock-on electrons with energies above the Cerenkov threshold energy in the radiator are counted. For knock-on electrons produced in the radiator, for which $\delta \sec\theta < x' < (\delta + t)\sec\theta$, the limits are given by

$$E_u = \max\left\{ \epsilon\left[R(E') - \frac{(\delta+t)\sec\theta - x'}{\cos\psi(E,E')} \right], E_{th} \right\} \tag{A.10}$$

$$E_l = E' , \tag{A.11}$$

where E' is the energy at which the knock-on electron is created, and E_{th} is the threshold energy for generation of Cerenkov radiation by electrons,

$$E_{th} = \left[\frac{1}{(1 - n^{-2})^{1/2}} - 1 \right] m_e c^2 . \tag{A.12}$$

The integral is therefore evaluated from the initial electron energy down to the greater of (1) the threshold energy, or (2) the energy of the electron at the point at which it escapes from the radiator. For knock-on electrons produced in the overlying material, for which $0 < x' < \delta \sec\theta$, the limits of integration are given by

$$E_u = \max\left\{ \epsilon\left[R(E') - \frac{(\delta+t)\sec\theta - x'}{\cos\psi(E,E')} \right], E_{th} \right\} \tag{A.13}$$

$$E_l = \epsilon\left[R(E') - \frac{\delta\sec\theta - x'}{\cos\psi(E,E')} \right], \tag{A.14}$$

Thus the upper limit is unchanged from the previous case, but the lower limit is now the remaining energy at the point at which the electron enters the radiator.

The average number of photoelectrons $K(Z,E,\theta)$ collected from the Cerenkov radiation generated by all knock-on electrons produced by a primary particle is the

expectation value of the light yield $Y(E,\theta,E',x')$ per knock-on electron weighted by the probability of generation $\phi_{mat}(Z,E,E')$ in both the overlying material and the radiator, multiplied by the number of knock-on electrons $N_{mat}(Z,E,\theta)$ that generate Cerenkov radiation. This has the form

$$K(Z,E,\theta) \equiv N_{over}(Z,E,\theta) \langle Y(E,\theta,E',x') \rangle_{over} + N_{rad}(Z,E,\theta) \langle Y(E,\theta,E',x') \rangle_{rad} \quad (A.15)$$

$$= \int_{x'=0}^{x'=\delta \sec\theta} \int_{E'=E_{low}}^{E'=E_{max}} \phi_{over}(Z,E,E')\, Y(E,\theta,E',x')\, dE'\, dx' + \quad (A.16)$$

$$\int_{x'=\delta \sec\theta}^{x'=(\delta+t)\sec\theta} \int_{E'=E_{th}}^{E'=E_{max}} \phi_{rad}(Z,E,E')\, Y(E,\theta,E',x')\, dE'\, dx' ,$$

where the lower limit of energy integration $E' = E_{low}$ for the overlying material is

$$E_{low} = \min \left\{ \epsilon \left[R(E_{th}) + \frac{\delta \sec\theta - x'}{\cos\psi(E,E')} \right], E_{max} \right\}, \quad (A.17)$$

which corresponds to the lesser of (1) the energy required to reach the radiator with a residual energy greater than the Cerenkov threshold energy, and (2) the maximum energy that can be imparted to a knock-on electron, $E_{max} = 2m_e c^2(\gamma^2-1)$. Note that evaluating the $E' = E_{low}$ limit requires solving a transcendental equation, since the cosine of the production angle is a function of the initial electron energy E', which is the integration variable.

The number of knock-on electrons with energies above the Cerenkov threshold produced in either the overlying material or the radiator is

$$N_{mat}(Z,E,\theta) = \int\int \phi_{mat}(Z,E,E')\, dE'\, dx' \quad (A.18)$$

$$= \Delta x_{mat} \frac{\alpha_{mat} Z^2}{\beta^2} \left[\frac{1}{E_-} - \frac{1}{E_+} - \frac{\beta^2}{E_+} \ln\left(\frac{E_+}{E_-}\right) \right], \quad (A.19)$$

where Δx_{mat} is $\delta \sec\theta$ in the overlying material and $t \sec\theta$ in the radiator, where for each material the lower and upper limits E_- and E_+ of the integral over energy are the same as the appropriate limits for $K(Z,E,\theta)$ above (Equation (A.16)).

Note that all of the Z dependence of $K(Z,E,\theta)$ is contained in $\phi_{mat}(Z,E,E')$, so that the average contribution from the knock-on electrons is proportional to Z^2. Note also that the number of knock-on electrons produced is proportional to the pathlength of the primary particle, and therefore that $K(Z,E,\theta)$ is proportional to $\sec\theta$ to leading order. This dependence is not strictly true, however, since the Cerenkov yield $Y(E,\theta,E',x')$ per knock-on electron is a function of the radiator thickness through the limit of integration given in Equation (A.10). In §A.4 we will find that the deviation from proportionality is small.

Having calculated the mean knock-on component, we proceed beyond Lezniak's algorithm to calculate the standard error. We assume that the variation in the average Cerenkov yield from all knock-on electrons produced by a primary particle is normally distributed, with rms $\sigma_K(Z,E,\theta)$. This is likely to be a reasonable assumption for heavy primary particles, such as those in the Fe group ($24 \leq Z \leq 28$), since the average number of knock-on electrons that generate Cerenkov light is large (see §A.4), particularly for radiators having high refractive indices, and therefore low threshold energies. In §A.5 we discuss a Monte Carlo simulation of the production and propagation of the knock-on electrons that confirms that this is an adequate assumption.

The variation in the knock-on electron contribution to the Cerenkov signal results from fluctuations in both the number of electrons produced and the energies at which they are produced. Propagation of errors in Equation (A.15) for $K(Z,E,\theta)$ shows that the square of the standard error of the mean number of photoelectrons collected from knock-on electrons produced in either the radiator or the overlying material is

$$\sigma^2_{mat}(Z,E,\theta) = N^2_{mat}(Z,E,\theta)\,\sigma^2_{<Y>} + <Y(E,\theta,E',x')>^2_{mat}\,\sigma^2_N , \qquad (A.20)$$

where the variance of the mean number of knock-on electrons produced is $\sigma^2_N = N_{mat}(Z,E,\theta)$, and the variance of the mean light yield per knock-on electron is

$$\sigma^2_{<Y>} = \frac{1}{N_{mat}(Z,E,\theta)}\left[<Y^2(E,\theta,E',x')>_{mat} - <Y(E,\theta,E'\,x')>^2_{mat}\right], \qquad (A.21)$$

and therefore Equation (A.18) simplifies to

$$\sigma^2_{mat}(Z,E,\theta) \;=\; N_{mat}(Z,E,\theta) <Y^2(E,\theta,E',x')>_{mat} \,. \tag{A.22}$$

Knock-on electrons are produced independently in the overlying material and the radiator, so their fluctuations are added in quadrature. Thus the standard error of the mean number of photoelectrons collected is

$$\sigma_K(Z,E,\theta) \;=\; (\sigma^2_{over} + \sigma^2_{rad})^{1/2} \,. \tag{A.23}$$

Because $N_{mat}(Z,E,\theta)$ is proportional to the pathlength of the primary particle in the material, the standard error is to leading order proportional to $\sec^{1/2}\theta$. However, there is a significant correction term in the mean-square Cerenkov yield per knock-on electron arising from the increase in the apparent thickness of the radiator. In §A.4 we give an approximate dependence on the angle of incidence for the HEIST aerogel counter.

A.3 Integration Techniques

The integral for the Cerenkov yield $Y(E,\theta,E',x')$ per knock-on electron, Equation (A.9), can be evaluated analytically. Defining $m \equiv m_e c^2$ for the sake of brevity, we find

$$\begin{aligned} Y(E,\theta,E',x') \;=\; h(Z_t,A_t)\,A\,\frac{N_\mu}{t}\,\frac{n^2}{n^2-1}\Bigg\{ & \frac{n^2-1}{n^2}\,(E_u - E_l) \\ & - \frac{m}{2n^2}\,(1-B)\,\log\left[\frac{E_u}{E_l}\right] \\ & + \frac{m}{2n^2}\left[1 - \frac{B}{(2Dm-1)^2}\right]\log\left[\frac{E_u+2m}{E_l+2m}\right] \\ & - \frac{2m}{n^2}\,(Dm-1)\,\frac{BDm}{(2Dm-1)^2}\,\log\left[\frac{1+CE_u}{1+CE_l}\right] \\ & + \frac{m}{n^2}\,\frac{B}{Dm}\left[n^2 - 1 + \frac{D^2m^2}{2Dm-1}\right]\left[\frac{1}{1+CE_u} - \frac{1}{1+CE_l}\right]\Bigg\}, \end{aligned} \tag{A.24}$$

where the upper and lower limits of integration, E_u and E_l, respectively, are given by Equations (A.10) and (A.11) or (A.13) and (A.14) for the appropriate material. The

Cerenkov yield in the limit where dE/dx is constant can be obtained by setting B = 0.

The triple integrals of Equations (A.16) and (A.23) have therefore been reduced to double. In addition, we have replaced the distance integral by a discrete sum to reduce the problem to a single integral. The remaining energy integral was evaluated by the method of Romberg, which is both fast and robust (e.g., Press *et al.*, 1986). Each of the two terms of Equations (A.16) and (A.23) thus has the form

$$K_{mat}(Z,E,\theta) = \frac{t_{mat}}{S_{max}} \sum_{s=1}^{S_{max}} \int_{E_{low}}^{E_{max}} \phi_{mat}(Z,E,E') \, Y(E,\theta,E',x'(s)) \, dE' \qquad (A.25)$$

or

$$\sigma^2_{mat}(Z,E,\theta) = \frac{t_{mat}}{S_{max}} \sum_{s=1}^{S_{max}} \int_{E_{low}}^{E_{max}} \phi_{mat}(Z,E,E') \, Y^2(E,\theta,E',x'(s)) \, dE' \ , \qquad (A.26)$$

where S_{max} is the number of distance slabs into which the material has been divided.

A.4 Results

With the electron energy loss held constant, we are able to reproduce Lezniak's results for his sample lucite counter to the precision with which they can be read from his paper. Using the energy loss given by Equation (A.8), we find a decrease in the average knock-on component near the threshold of ~30%, with the decrease lessening to a few percent at energies above a few thousand MeV/nucleon.

We have modeled the HEIST aerogel Cerenkov detector with overlying materials and thicknesses appropriate for both the Bevalac calibration and the May 1984 flight. We have neglected knock-on electrons produced in the atmosphere above the gondola in flight, as the air is so tenuous that the electrons are produced at large distances above the instrument and scatter out of the acceptance angle of the Cerenkov detector. The mean knock-on electron contribution K(Z=25,E,θ=0) is plotted in Figure A.2 along with the primary Cerenkov light in the counter for the Bevalac conditions. We have assumed an index of refraction n = 1.10. The dashed line indicates the contribution from knock-on electrons produced in the radiator only, and the solid circles are the results of a Monte Carlo calculation (§A.5). Note that the knock-on electrons

Figure A.2

The Cerenkov yield of a ^{55}Mn nucleus at $\theta = 0^\circ$ and its associated knock-on electrons in the aerogel counter as a function of the energy of the primary particle. The index of refraction of the aerogel is taken to be $n = 1.1$. The curve labeled "$C_{primary}$" is the Cerenkov yield of the primary particle, expressed as a fraction of its yield at velocity $\beta = 1$, Z^2N_μ. The mean knock-on electron contribution $K(Z=25,E,\theta=0)$ and the standard error in the mean $\sigma_K(Z=25,E,\theta=0)$ are given by the solid lines so labeled. The dashed lines represent the contribution from electrons produced in the radiator only, and the solid circles are the results of the Monte Carlo calculation.

Figure A.2

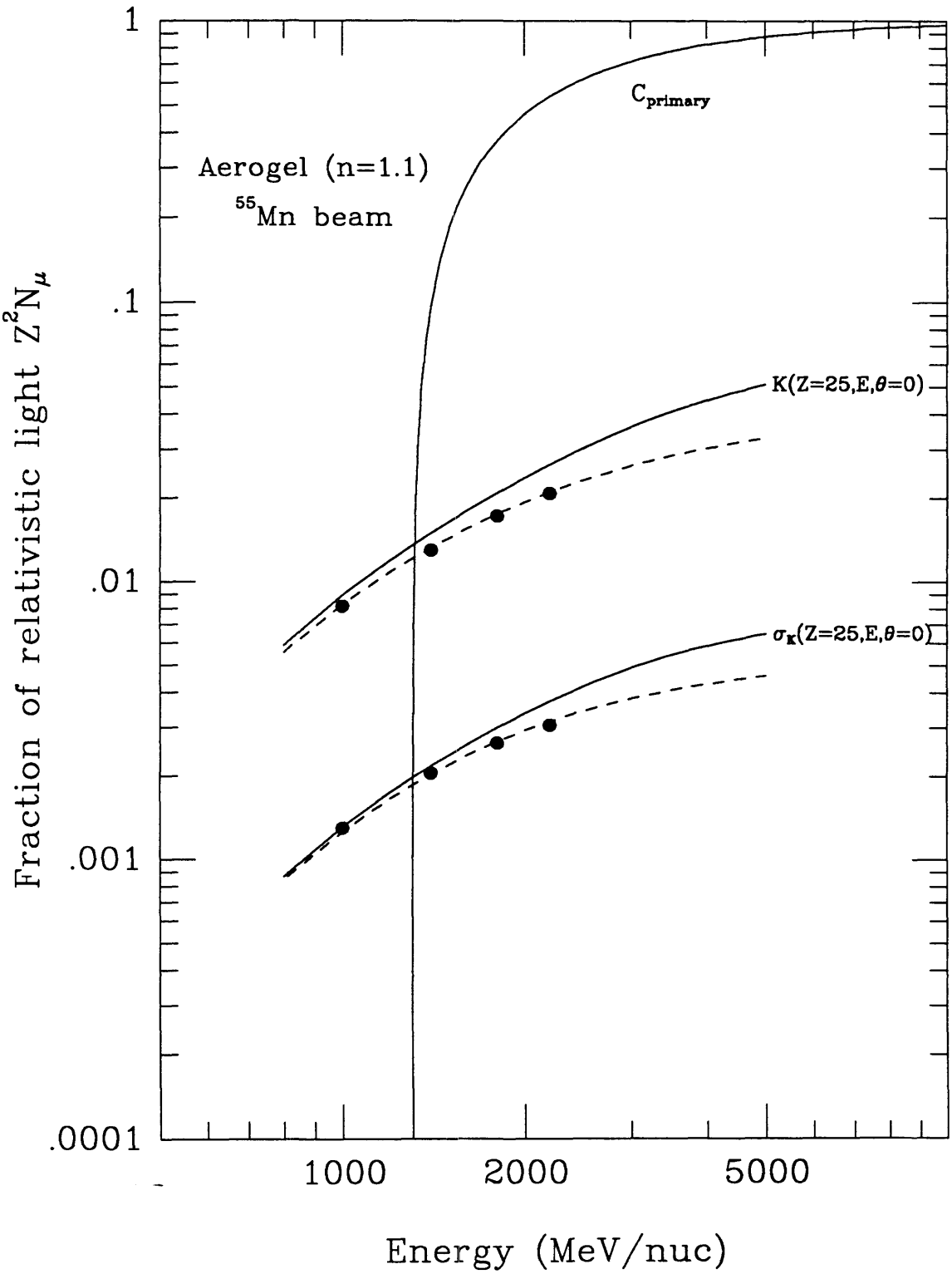
1
.1
.01
.001
.0001
Fraction of relativistic light Z^2N_μ
Aerogel (n=1.1)
^{55}Mn beam
$C_{primary}$
K(Z=25,E,θ=0)
σ_K(Z=25,E,θ=0)
1000
2000
5000
Energy (MeV/nuc)

contribute typically ~2% of the relativistic Cerenkov yield $Z^2N_\mu \sec\theta$, and therefore that the ratio of the knock-on electron Cerenkov yield to the Cerenkov signal from the primary particle is charge-independent. The total signal from knock-on electrons is dominated by those produced in the radiator. Approximately 85% of the added Cerenkov signal in the aerogel counter is generated by knock-on electrons produced in the radiator, with the remainder generated by electrons produced in the overlying material.

To reduce the possibility that fluctuations in the light yield might cause primary Fe particles with subthreshold energies to appear to be above threshold, we have analyzed only those events in the flight data set with a fraction $f(n,\gamma) > 2\%$ of relativistic primary light (§3.6.1 and §4.3.8). Thus in the useful energy interval of the aerogel counter (~1300 MeV/nucleon to ~2000 MeV/nucleon), the Cerenkov signal from knock-on electrons ranges from ~50% to ~4% of that from the primary particle.

The standard error of the mean Cerenkov yield from knock-on electrons $\sigma_K(Z=25,E,\theta=0)$ for ^{55}Mn in the counter for the Bevalac conditions is also shown in Figure A.2. The dashed line represents the contribution from knock-on electrons produced only in the radiator, and the solid circles indicate the results of a Monte Carlo calculation (§A.5). Recall that we have shown that the standard error is proportional to Z. The ratio of the standard error to the total Cerenkov light is therefore proportional to 1/Z, and the fluctuations are more important for lower Z primary particles, as one would expect from a Poisson process. From the figure we see that for ^{55}Mn the fluctuation is typically ~0.2% of Z^2N_μ, or, in general, ~(5/Z)% of Z^2N_μ.

The square of the fractional standard error can be written as

$$\frac{\sigma_K^2(Z,E,\theta)}{K^2(Z,E,\theta)} = \frac{\sigma_Y^2}{<Y(E,\theta,E',x'>^2 N_{mat}(Z,E,\theta)} + \frac{1}{N_{mat}(Z,E,\theta)}, \qquad (A.27)$$

where the first term on the right-hand side represents the contribution from variations in the energies of the knock-on electrons, and the second term represents the contribution from fluctuations in the number of electrons produced with energies above the Cerenkov threshold. Throughout the useful energy range of the aerogel counter (~1300 MeV/nucleon to ~2000 MeV/nucleon), the average number of knock-on electrons above the threshold energy produced by a vertically incident primary particle is $\sim 0.23\, Z^2$, or

$\sim$150 for Mn or Fe, which corresponds to a statistical fluctuation of $\sim$8%. From the figure, we see that the standard error is $\sim$15% of the knock-on electron light in the useful energy range for a ^{55}Mn beam, which implies that the fractional contribution to the standard error from fluctuations in the light yield per electron is $\sim$13%. We conclude, therefore, that knock-on electrons from the tail of the differential energy spectrum $\phi(Z,E,E')$ produce a sufficiently large amount of Cerenkov light that the standard error is dominated by fluctuations in the light yield per knock-on electron. We also note the interesting property that the relative contributions to the standard error from fluctuations in the energies and in the number of electrons produced is independent of the charge of the primary particle, since both contributions are proportional to $N_{mat}^{\frac{1}{2}}(Z,E,\theta)$. Thus the fractional standard error is larger for lower charges, but the fluctuations in the light yield, which are the result of fluctuations in the energies of the knock-on electrons, still dominate.

Lezniak defines an equilibrium distribution of knock-on electrons as that distribution obtained whenever the range of the maximum energy electron is equal to or less than the total thickness of the detector system. In this case, the production of knock-on electrons is balanced by their loss by deceleration. In the aerogel counter, the maximum energy for knock-on electrons from a primary particle at the highest energy for which mass analysis is possible ($\sim$2000 MeV/nucleon) is $\sim$9 MeV. Such electrons have a range of $\sim$4.5 g/cm^2, which is somewhat smaller than the thickness of the aerogel and the detector elements above it ($\sim$6.3 g/cm^2). We conclude that the equilibrium condition applies.

We have investigated the dependence of $K(Z,E,\theta)$ and $\sigma_K(Z,E,\theta)$ for the aerogel counter on the energy and angle of incidence of the primary particle by repeating the integration at several values of E and θ. We find that the mean knock-on component is almost precisely proportional to $\sec\theta$, which is to be expected since the number of knock-on electrons produced is proportional to the thickness of the combined materials. The increased yield per electron produced in the radiator—which results from the greater effective thickness of the radiator—is offset by the decreased yield from electrons produced in the overlying material—which results from such electrons' having lost more energy before entering the radiator. The resulting deviation from proportionality

is $<1\%$. If the thickness of the overlying material were sufficiently great that the distribution of electrons reached equilibrium in that material, the Cerenkov contribution from those electrons would have been independent of θ, and the total knock-on electron signal would have increased.

We find that the standard error of the mean knock-on electron light $\sigma_K(Z,E,\theta)$ in the aerogel counter follows the approximate relation $\sigma_K(Z,E,\theta) \propto \sec^{1/2}\theta\,(\sec\theta)^{(0.077+0.098(\gamma-\gamma_{th}))}$, where $\gamma_{th}=2.40$ is the Lorentz factor corresponding to the Cerenkov threshold energy. A dependence of $\sec^{1/2}\theta$ is expected from the increase in the number of radiating knock-on electrons produced. The extra factor arises from the increased effective thickness of the radiator, which allows high-energy electrons to radiate over a longer pathlength. In this case, the decrease in the contribution from electrons produced in the overlying material has only a small effect on the total because the contribution is added in quadrature (Equation (A.21)).

When the trajectory of the primary particle is not normal to the surface of the radiator, the remaining thickness of radiator along the initial trajectory of a knock-on electron can become a strong function of the production angle. We have ignored this complicating factor, because a proper treatment of this effect would require an algorithm that accounts for the significant amount of electron scattering which occurs as the electrons travel through the radiator.

For some purposes, such as the calculation of the contribution to velocity resolution of the counter from knock-on electrons, analytic expressions for $K(Z,E,\theta)$ and $\sigma_K(Z,E,\theta)$ are useful. Simple analytic fits to the results of the numerical algorithm are given below. The fits deviate from the results for $\sec\theta=1.0$ by $<5\%$ over the velocity ranges listed and by $<10\%$ over $1.0<\sec\theta\leq 2.25$. Note that the fit applies equally well to both the Bevalac and flight data, since the total knock-on light is dominated by that from knock-on electrons produced in the aerogel and the amount of overlying material in the two configurations differs by only $\sim 30\%$.

Aerogel:

Deviation of fit from calculation $<5\%$ at $\sec\theta=1.0$.

Deviation of fit $<10\%$ for $1.0 < \sec\theta < 2.25$.

Valid for velocity in radiator $2.0 \leq \gamma \leq 3.5$.

$$K(Z,\gamma,\theta) \equiv Z^2 N_\mu \sec\theta\, k(\gamma) = Z^2 N_\mu \sec\theta \left[0.01356\,(\gamma-1) - 0.00547 \right] \quad (A.28)$$

$$\sigma_K(Z,\gamma,\theta) = Z N_\mu (\sec\theta)^{(1+a(\gamma))/2} \left[0.0469\,(\gamma-1) - 0.0165 \right] \quad (A.29)$$

$$a(\gamma) = 0.153 + 0.196\,(\gamma - \gamma_{th}) \quad (A.30)$$

A.5 Monte Carlo Simulation

We have developed a simple Monte Carlo simulation of the production of knock-on electrons in the radiator to confirm that the assumption of Gaussian errors is reasonable. The simulation creates a number of knock-on electrons at random depths uniformly distributed in the radiator, varying the average number created (Equation (A.18)) according to Poisson statistics. Electron energies are assigned by solving the following equation for E′,

$$r\, N_{rad}(Z,E,\theta) = \frac{\alpha_{rad} Z^2}{\beta^2} \frac{1}{E'^2} \left[1 - \beta^2 \frac{E'}{E_{max}} \right], \quad (A.31)$$

where r is uniformly distributed between 0 and 1. The Cerenkov light yield $Y(E,E',x')$ for each knock-on electron is calculated from Equation (A.24), and the average number of knock-on electrons $N_{rad}(Z,E,\theta)$ produced in the radiator with energies above the Cerenkov threshold is calculated from Equation (A.18). The mean and standard error of the knock-on electron Cerenkov yields from the simulation are plotted for several energies in Figure A.2. The results of the simulation are in excellent agreement with those of the numerical algorithm.

Figure A.3 shows a histogram for 1000 trials of the total Cerenkov yield of all knock-on electrons produced by a primary particle at 1400 MeV/nucleon. The dashed curve is a Gaussian distribution with mean and standard error equal to the result from the numerical algorithm for the radiator only. The two distributions have equal area.

Figure A.3

Comparison of results of Monte Carlo and numerical algorithm. The histogram shows the Cerenkov yield of knock-on electrons produced in the aerogel from a ^{55}Mn beam at 1400 MeV/nucleon expressed as a fraction of the relativistic light Z^2N_μ at vertical incidence. The dotted smooth curve is a Gaussian distribution with mean and standard deviation given by the numerical algorithm. The mean of the Gaussian is $\sim$2% higher than the mean of the Monte Carlo data and $\sim$6% higher than the mode. While the Monte Carlo distribution does show a tail of large light yields, the deviation from Gaussian shape is evidently not large.

Figure A.3

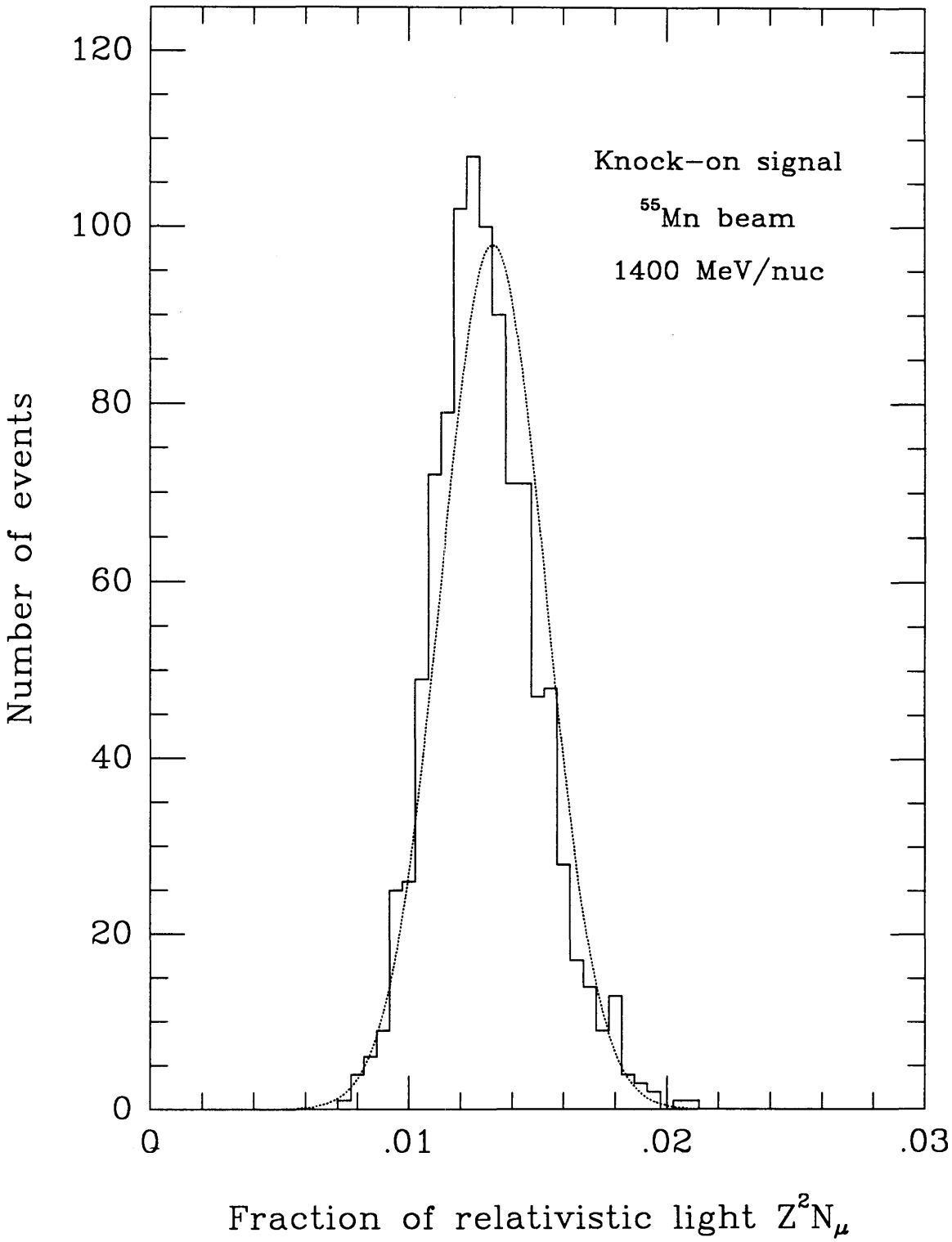
120
100
80
60
40
20
0
0
.01
.02
.03
Number of events
Fraction of relativistic light Z^2N_μ
Knock-on signal
^{55}Mn beam
1400 MeV/nuc

The mean of the numerical result is ~2% higher than the mean of the distribution from the simulation, and ~6% higher than the mode. It is apparent from the figure that the number of knock-on electrons produced in the radiator by a primary ^{55}Mn particle is sufficiently large to produce a distribution of Cerenkov yields which is approximately Gaussian. Radiators with larger refractive indices, and therefore lower Cerenkov threshold energies, are sensitive to a larger average number of knock-on electrons, and therefore should show distributions of secondary contributions that are more Gaussian. Similar agreement between the simulation and the numerical algorithm is obtained in Lezniak's lucite counter. We conclude that our numerical algorithm, which is much faster than the Monte Carlo simulation, yields adequate results for high-Z primary particles for a broad range of Cerenkov radiators.

Appendix B
Position Algorithm

The positions of particles traversing the HEIST instrument are calculated by comparing ratios of responses of photomultipliers in the NaI(Tl) stack layers and in the top plastic scintillator (§3.2). Figure B.1 shows a flow chart of the algorithm we have used to determine particle positions. The discussion below details the steps of the algorithm, with each heading in boldface corresponding to a numbered step in the flow chart. This procedure is followed separately in each layer of the NaI(Tl) stack and in the top scintillator; subsequently a least-squares linear fit to all measured positions is taken to be the particle trajectory through the instrument (§3.2.2).

B.1 Outline of position algorithm

1. Read in maps of ratios. The program reads in the six maps of the logarithms of ratios of photomultiplier responses in the selected layer. With the photomultipliers lettered in sequence about the layer, the ratios taken are (A+B+C)/(D+E+F), (B+C+D)/(E+F+A), (C+D+E)/(F+A+B), B/C, D/E, and F/A, (§3.2 and Figure 3.2). We use the notation "Σ_3" to denote any of the first three maps, which are the ratios of sums of three adjacent photomultipliers. The map of a particular ratio is a 60×60 array of 1 cm^2 bins containing the average value of the logarithm of the ratio calculated from the calibration data. Note that this square array of 3600 bins covers an area larger than the area of the NaI(Tl) disks, which have a radius of 26.5 cm. The bins of the maps of the top plastic scintillator, which has a radius of 39.5 cm, are 1.5 cm on a side.

2. Fit triangular planes to maps. We assign the value associated with each bin of each map to the center of that bin, and group the bin centers into threes, forming an array of 7200 isosceles right-angle triangles for each map. Figure B.2 depicts the relationship between the triangles and the square bins. We have found that the

Figure B.1

Flow chart of the algorithm used to determine particle positions in the NaI(Tl) and the plastic scintillators.

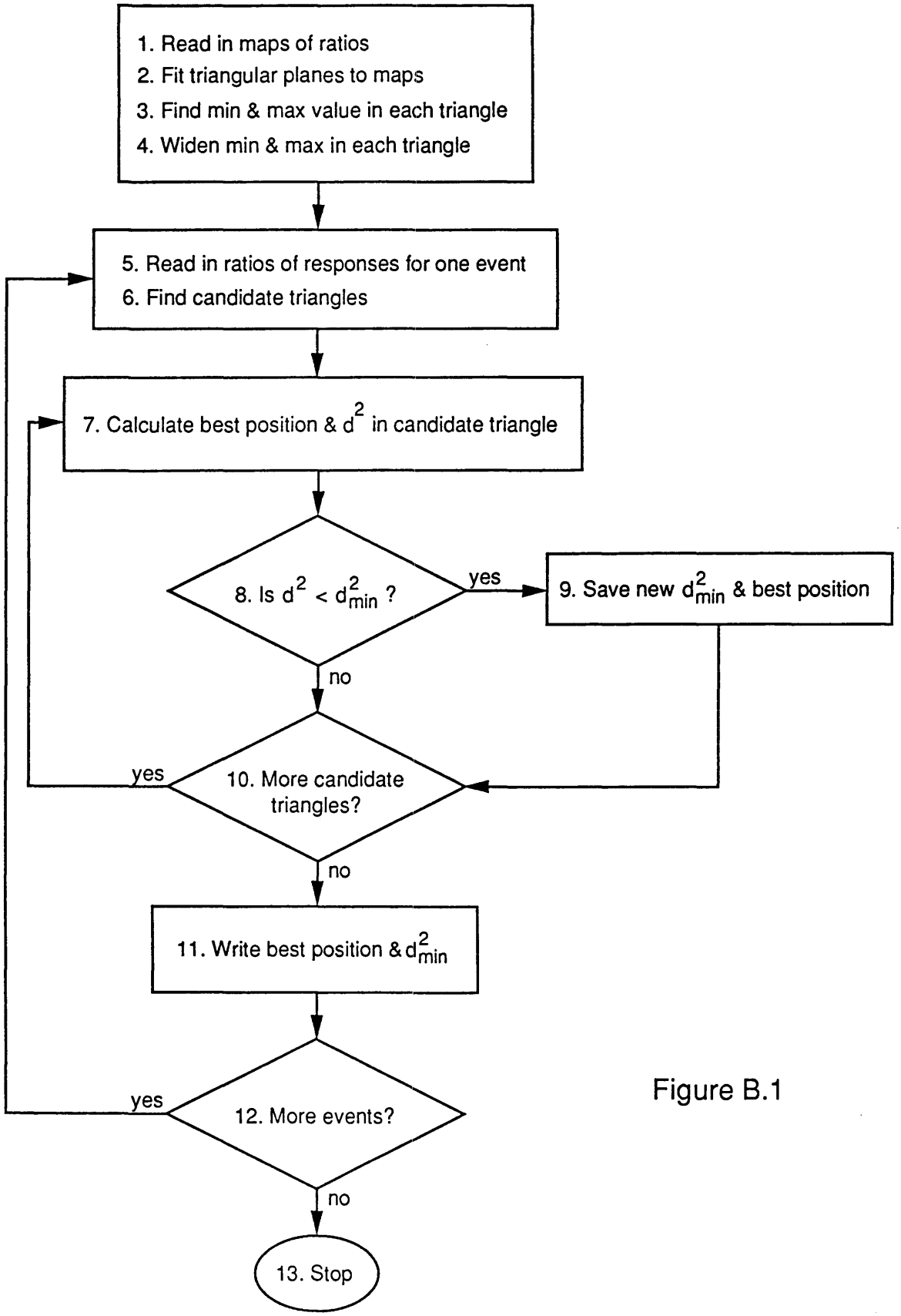
1. Read in maps of ratios
2. Fit triangular planes to maps
3. Find min & max value in each triangle
4. Widen min & max in each triangle
5. Read in ratios of responses for one event
6. Find candidate triangles
7. Calculate best position & d^2 in candidate triangle
8. Is $d^2 < d^2_{min}$?
yes
9. Save new d^2_{min} & best position
no
yes
10. More candidate triangles?
no
11. Write best position & d^2_{min}
yes
12. More events?
no
13. Stop

Figure B.1

Figure B.2

Array of 1 cm^2 square bins of the photomultiplier response maps and the triangular grid used to interpolate from the maps. The dashed lines mark the limits of the square bins. The bin centers form the vertices of the isosceles right-angle triangles, which are indicated by the solid lines.

Figure B.2

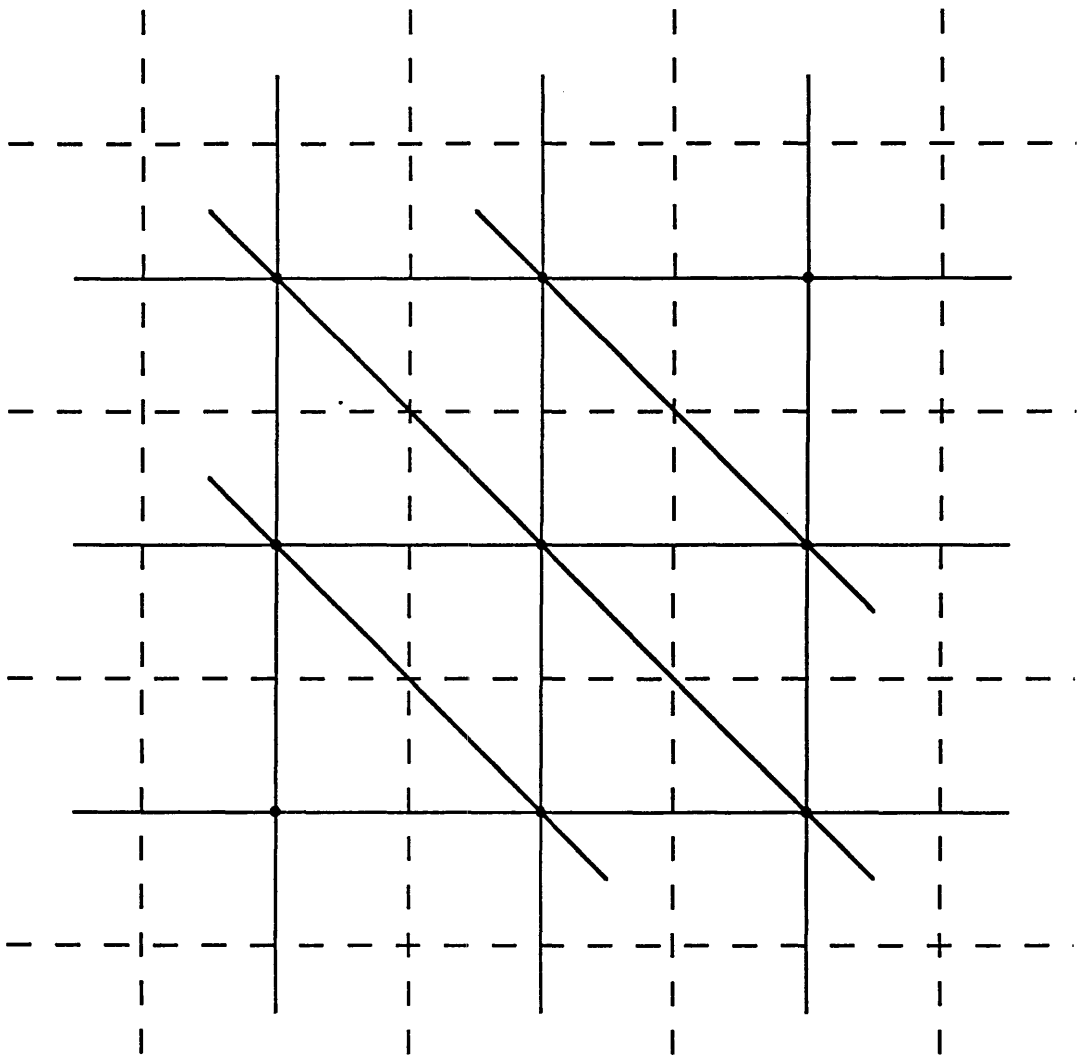

orientation of the triangles relative to the coordinate axes does not affect the position resolution. The bin centers, which form the vertices of the isosceles triangles, define 7200 unique triangular planes, which will be used to interpolate map values between bin centers.

3. Find min and max in each triangle. The program finds the two vertices of each triangle of each Σ_3 map that have the extreme values. The span of the minimum and maximum in a typical triangle is $\sim$0.05 in the logarithm. The minimum and maximum values will be used in the search for candidate triangles through which a particle might have passed.

4. Widen min and max in each triangle. The program adds a constant widening correction W to each minimum and maximum value to increase the probability that the true triangle will be among the candidate triangles selected in step 6. Without this correction, the algorithm fails to select the correct triangle as a candidate for $\sim$10% of events. We have found that a widening correction of W = 0.05 is satisfactory. Note that this is comparable to the span of the minimum and maximum in a typical triangle.

5. Read in ratios of responses for one event. The program reads in the logarithms of the six ratios of responses for a single event.

6. Find candidate triangles. The program searches through the widened map values for triangles which span the observed logarithms of ratios. Since the true particle position must be on the disk of the scintillator if the summed response of the six photomultipliers is above the pedestal value, the program searches only those triangles located on or adjacent to the disk. A triangle is considered a candidate if the observed logarithm satisfies the following relation for at least two of the three Σ_3 maps:

$$\min[\Sigma_3(t)] - W \;<\; \mathrm{obs}[\Sigma_3] \;<\; \max[\Sigma_3(t)] + W \qquad \text{(B.1)}$$

where $\mathrm{obs}[\Sigma_3]$ is the observed logarithm, $\min[\Sigma_3(t)]$ is the minimum value in triangle t, and $\max[\Sigma_3(t)]$ is the maximum value in triangle t. The widening correction W = 0.05 gives typically $\sim$300 candidate triangles, about three times as many as are selected with no widening correction. The program searches only the Σ_3 maps because we found that the balance between selecting too many candidate triangles and missing the correct

candidate triangle was more difficult to maintain when all six ratios were searched.

7. Calculate best position and d^2 in candidate triangle. The program finds the position $\vec{r}$ in the candidate triangle that minimizes the difference parameter d^2, which measures the difference between the observed logarithms and the interpolated map values, and is defined by

$$d^2 = \sum_i (R_i - M_i^0 - \vec{r}\cdot\nabla M_i)^2 , \tag{B.2}$$

where R_i is the observed logarithm, M_i^0 is the map value at the right-angle vertex of the candidate triangle, $\vec{r}$ is the particle position relative to the right-angle vertex, and ∇M_i is the gradient of the mapped logarithm, which is given by the x and y slopes of the triangle. The sum runs over all six maps. For example, the x position that minimizes d^2 is

$$r_x = \frac{\sum(\frac{\partial M_i}{\partial x}\frac{\partial M_i}{\partial y})\sum[\frac{\partial M_i}{\partial y}(M_i^0 - R_i)] - \sum(\frac{\partial M_i}{\partial y})^2\sum[\frac{\partial M_i}{\partial y}(M_i^0 - R_i)]}{\sum(\frac{\partial M_i}{\partial x})^2\sum(\frac{\partial M_i}{\partial y})^2 - \sum(\frac{\partial M_i}{\partial x}\frac{\partial M_i}{\partial y})^2} . \tag{B.3}$$

Positions outside the boundary of the triangle are accepted if they lie within 1.0 cm of the centroid of the triangle.

8. Is $d^2 < d^2_{min}$? The program tests the value of d^2 from the candidate triangle against the minimum value from all previous candidate triangles for this event. If the new d^2 is less than the minimum value d^2_{min}, the program proceeds to step 9, "Save new d^2_{min} and best position." If not, the program proceeds to step 10, "More candidate triangles?".

9. Save new d^2_{min} and best position. If the difference d^2 in the current candidate triangle is smaller than the minimum difference in all previous candidate triangles, the program saves the new d^2_{min} and the best position in the current triangle for comparison with further candidate triangles.

10. More candidate triangles? The program checks to see whether more candidate triangles remain to be considered. If so, it returns to step 7, "Calculate best position and d^2 in candidate triangle." If not, it proceeds to step 11, "Write best position

and d^2_{min}."

11. Write best position and d^2_{min}. Having found the position with the minimum difference d^2_{min} from among all candidate triangles, the program writes this best position and d^2_{min} in a file.

12. More events? The program checks to see whether more events remain for which positions have not been found. If so, it returns to step 5, "Read in ratios of responses for one event." If not, the program stops.

References

Abramowitz, M. and I. A. Stegun, *Handbook of Mathematical Functions* (National Bureau of Standards: Washington, D.C., 1964).

Ahlen, S. P., and M. H. Salamon, *Physical Review A*, **19**, 1084 (1979).

Ahlen, S. P., *Reviews of Modern Physics*, **52**, 121 (1980).

Ahlen, S. P., *Physical Review A*, **25**, 1856 (1982).

Althouse, W. E., A. Buffington, W. Campbell, K. Lau, S. M. Schindler, and J. South, *SRL Technical Report 81-1* (1981).

Anders, E. and M. Ebihara, *Geochimica et Cosmochimica Acta*, **46**, 2363 (1982).

Arens, J. F., *Nuclear Instruments and Methods*, **120**, 275 (1974).

Arens, J. F., V. K. Balasubrahmanyan, J. F. Ormes, F. Siohan, W. K. H. Schmidt, M. Simon, and H. Spiegelhauser, NASA Technical Memorandum 79677 (1978).

Arnett, W. D., D. N. Schramm, J. W. Truran, *Astrophysical Journal (Letters)*, **339**, L25 (1989).

Barkas, W. H., and M. J. Berger, "Tables of Energy Losses and Ranges of Heavy Charged Particles," NASA SP-3013 (1964).

Berger, M. J., and S. M. Seltzer, "Table of Energy Losses and Ranges of Electrons and Positrons," NASA SP-3012 (1964).

Binns, W. R., T. L. Garrard, M. H. Israel, M. D. Jones, M. P. Kamionkowski, J. Klarmann, E. C. Stone, and C. J. Waddington, *Astrophysical Journal*, **324**, 1106 (1988).

Bloch, F., *Annalen der Physik (Leipzig)*, **16**, 285 (1933).

Bodansky, D., D. D. Clayton, and W. A. Fowler, *Astrophysical Journal Supplement*, **16**, 299 (1968).

Buffington, A., unpublished HEIST internal memo, 19 September 1980.

Buffington, A., unpublished HEIST internal memo, 1981.

Buffington, A., K. H. Lau, and S. M. Schindler, *Proceedings of the 17th International Cosmic Ray Conference (Paris)*, **8**, 117 (1981).

Buffington, A., K. H. Lau, S. Laursen, I. L. Rasmussen, S. M. Schindler, and E. C. Stone, *Proceedings of the 18th International Cosmic Ray Conference (Bangalore)*, **2**, 49 (1983).

Burbidge, E. M., G. R. Burbidge, W. A. Fowler, and F. Hoyle, *Reviews of Modern Physics*, **29**, 547 (1957).

Burkhardt, H., P. Koehler, R. Riethmuller, B. H. Wiik, R. Fohrmann, J. Franzke, H. Krasemann, R. Maschuw, G. Poelz, J. Reichardt, J. Ringel, O. Romer, P. Schmuser, R. van Staa, J. Freeman, P. Lecomte, T. Meyer, Sau Lan Wu, and G. Zobernig, *Nuclear Instruments and Methods*, **184**, 319 (1981).

Cameron, A. G. W., *Space Science Reviews*, **15**, 21 (1973).

Cantin, M., J. J. Engelmann, P. Masse, and M. Rotenburg, *Proceedings of the 17th International Cosmic Ray Conference (Paris)*, **8**, 59 (1981).

Cassé, M., *Astrophysical Journal*, **180**, 269 (1973).

Cassé, M., and A. Soutoul, *Astrophysical Journal (Letters)*, **200**, L75 (1975).

Cassé, M., and P. Goret, *Astrophysical Journal*, **221**, 703 (1978).

Cassé, M., J. P. Meyer, and H. Reeves, *Proceedings of the 16th International Cosmic Ray Conference (Kyoto)*, **12**, 114 (1979).

Cassé, M., and J. A. Paul, *Astrophysical Journal*, **258**, 860 (1982).

Christian, E. R., J. E. Grove, R. A. Mewaldt, S. M. Schindler, T. Zukowski, J. C. Kish, and W. R. Webber, *Proceedings of the 20th International Cosmic Ray Conference (Moscow)*, **2**, 382 (1987).

Clayton, D. D., *Principles of Stellar Evolution and Nucleosynthesis* (University of Chicago Press: Chicago, 1968).

Comstock, G. M., *Astrophysical Journal*, **155**, 619 (1969).

Crawford, H. J., Ph.D. Thesis, University of California, Berkeley, LBL-8807 (1979).

de Loore, C., and A. Willis (eds.), *Wolf-Rayet Stars: Observations, Physics, Evolution* (D. Reidel: Dordrecht, 1982).

Dwyer, R., and P. Meyer, *Astrophysical Journal*, **294**, 441 (1985).

Dwyer, R., and D. Zhou, *Nuclear Instruments and Methods in Physics Research*, **A242**, 171 (1985).

Dye, S. T., Ph.D. Thesis, University of Hawaii, UH-511-667-89 (1989).

Enge, W., *Nuclear Instruments and Methods*, **147**, 211 (1977).

Engelmann, J. J., P. Goret, E. Juliusson, L. Koch-Miramond, P. Masse, A. Soutoul, B. Byrnak, N. Lund, B. Peters, I. L. Rasmussen, M. Rotenberg, and N. J. Westergaard, *Proceedings of the 18th International Cosmic Ray Conference (Bangalore)*, **2**, 17 (1983).

Engelmann, J. J., P. Goret, E. Juliusson, L. Koch-Miramond, N. Lund, P. Masse, I. L. Rasmussen, and A. Soutoul, *Astronomy and Astrophysics*, **148**, 12 (1985).

Evans, R. D., *The Atomic Nucleus* (McGraw-Hill: New York, 1955).

Fermi, E., *Physical Review*, **56**, 1242 (1939).

Fermi, E., *Physical Review*, **57**, 485 (1940).

Fernandez, C., K. E. Johansson, M. Schouten, S. Tavernier, P. Ladron de Guevara, P. Herquet, J. Kesteman, and O. Pingot, *Nuclear Instruments and Methods in Physics Research*, **225**, 313 (1984).

Ferrando, P., W. R. Webber, P. Goret, J. C. Kish, D. A. Schrier, A. Soutoul, and O. Testard, *Physical Review C*, **37**, 1490 (1988).

Fowler, W. A., and F. Hoyle, *Astrophysical Journal Supplement*, **9**, 201 (1964).

Garcia-Munoz, M., G. M. Mason, and J. A. Simpson, *Astrophysical Journal*, **217**, 859 (1977).

Garcia-Munoz, M., J. A. Simpson, T. G. Guzik, J. P. Wefel, and S. H. Margolis, *Astrophysical Journal Supplement*, **64**, 269 (1987).

Gleeson, L. J., and W. I. Axford, *Astrophysical Journal*, **154**, 1011 (1968).

Hainebach, K. L., D. D. Clayton, W. D. Arnett, and S. E. Woosley, *Astrophysical Journal*, **193**, 157 (1974).

Henning, S., and L. Svensson, *Physica Scripta*, **23**, 697 (1981).

Henning, S., G. Jarlskog, U. Mjoernmark, A. Nilsson, and L. Svensson, *Physica Scripta*,

23, 703 (1981).

Jackson, J. D., and R. L. McCarthy, *Physical Review B*, **6**, 4131 (1972).

Jelley, J. V., *Cerenkov Radiation and its Applications* (Pergamon: New York, 1958).

Kelly, R. L., *et al.*, Particle Data Group, *Reviews of Modern Physics*, **52** (1980).

Kobetich, E. J., and R. Katz, *Physical Review*, **170**, 391 (1968).

Koch, L., J. J. Engelmann, P. Goret, E. Juliusson, N. Petrou, Y. Rio, A. Soutoul, B. Byrnak, N. Lund, B. Peters, I. L. Rasmussen, M. Rotenburg, and N. Westergaard, *Astronomy and Astrophysics (Letters)*, **102**, L9 (1981).

Koch-Miramond, L., J. Engelmann, P. Goret, E. Juliusson, P. Masse, A. Soutoul, C. Perron, N. Lund, and I. L. Rasmussen, *Proceedings of the 18th International Cosmic Ray Conference (Bangalore)*, **9**, 275 (1983).

Lau, K. H., Ph.D. Thesis, California Institute of Technology (1985).

Landau, L., *Journal of Experimental Physics (USSR)*, **8**, 201 (1944).

Lezniak, J. A., *Nuclear Instruments and Methods*, **136**, 299 (1976).

Maza, J., and S. van den Bergh, *Astrophysical Journal*, **204**, 519 (1976).

McKlveen, J. W., and W. J. McDowell, *Transactions of the American Nuclear Society*, **22**, 149 (1975).

Mewaldt, R. A., J. D. Spalding, E. C. Stone, and R. E. Vogt, *Astrophysical Journal (Letters)*, **236**, L121 (1980).

Mewaldt, R. A., unpublished HEIST internal memo *RAM1* (1985).

Mewaldt, R. A., *Symposium on Cosmic Abundances of Matter (Minneapolis)*, AIP Conference Proceedings (1988).

Mewaldt, R. A., and E. C. Stone, *Astrophysical Journal*, **337**, 959 (1989).

Meyer, J. P., in *Origin and Distribution of the Elements*, ed. G. J. Mathews (World Scientific: Singapore, 1987).

Newport, B. J., Ph.D. Thesis, California Institute of Technology (1986).

Nomoto, K., F.-K. Thielemann, and K. Yokoi, *Astrophysical Journal*, **286**, 644 (1984).

Olive, K. A, and D. N. Schramm, *Astrophysical Journal*, **257**, 276 (1982).

Ormes, J. F., and P. Freier, *Astrophysical Journal*, **222**, 471 (1978).

Ormes, J. F., and R. J. Protheroe, *Astrophysical Journal*, **272**, 756 (1983).

Pierce, T. E, and M. Blann, *Physical Review*, **173**, 390 (1968).

Poelz, G., in *Aerogels*, ed. J. Fricke (Springer-Verlag: Berlin, 1986).

Prantzos, N., *Advances in Space Research*, **4**, 109 (1984).

Press, W. H., B. P. Flannery, S. A. Teukolsky, and W. T. Vetterling, *Numerical Recipes: The Art of Scientific Computing* (Cambridge University Press: Cambridge, 1986).

Protheroe, R. J., J. F. Ormes, and G. M. Comstock, *Astrophysical Journal*, **247**, 362 (1981).

Rasmussen, I. L., S. Laursen, A. Buffington, and S. M. Schindler, *Proceedings of the 18th International Cosmic Ray Conference (Bangalore)*, **8**, 77 (1983).

Rasmussen, I. L., accepted for publication in *Journal de Physique*, (1989).

Raisbeck, G., C. Perron, J. Toussaint, and F. Yiou, *Proceedings of the 13th International Cosmic Ray Conference (Denver)*, **1**, 534 (1973).

Rogers, E. H., J. F. Arens, and H. Whiteside, *Nuclear Instruments and Methods*, **121**, 599 (1974).

Rossi, B., *High Energy Particles* (Prentice-Hall: New York, 1952).

Salamon, M. H., *Lawrence Berkeley Laboratory Publication No. 10446* (1980).

Salamon, M. H., and S. P. Ahlen, *Physical Review B*, **B24**, 5026 (1981).

Schindler, S. M., A. Buffington, K. H. Lau, and I. L. Rasmussen, *Proceedings of the 18th International Cosmic Ray Conference (Bangalore)*, **8**, 73 (1983).

Shea, M. A., and D. F. Smart, *Journal of Geophysical Research*, **80**, 1202 (1975).

Shea, M. A., and D. F. Smart, *Proceedings of the 18th International Cosmic Ray Conference (Bangalore)*, **3**, 415 (1983).

Silberberg, R., and C. H. Tsao, *Astrophysical Journal Supplement*, **25**, 315 (1973a).

Silberberg, R., and C. H. Tsao, *Astrophysical Journal Supplement*, **25**, 335 (1973b).

Silberberg, R., and C. H. Tsao, *Proceedings of the 15th International Cosmic Ray Conference (Plovdiv)*, **2**, 84 (1977).

Simpson, G. A., J. Kish, J. A. Lezniak, and W. R. Webber, *Astrophysical Letters*, **19**, 3 (1977).

Soutoul, A., M. Cassé, and E. Juliusson, *Astrophysical Journal*, **219**, 753 (1978).

Stone, E. C., *Proceedings of the 13th International Cosmic Ray Conference (Denver)*, **5**, 3615 (1973).

Stone, E. C., Invited paper presented at the ESRO workshop on "Research Goals for Cosmic Ray Astrophysics in the 1980's," Frascati, Italy (1974).

Tammann, G. A., in *Supernovae: A Survey of Current Research*, eds. M. J. Rees and R. J. Stoneham (D. Reidel: Dordrecht, 1982).

Tarlé, G., S. P. Ahlen, and B. G. Cartwright, *Astrophysical Journal*, **230**, 607 (1979).

Thielemann, F.-K., K. Nomoto, K. Yokoi, *Astronomy and Astrophysics*, **158**, 17 (1985).

Thielemann, F.-K., K. Nomoto, K. Yokoi, in *Nucleosynthesis and Its Implications on Nuclear and Particle Physics*, eds. J. Audouze and N. Mathieu (D. Reidel: Dordrecht, 1986).

Tsao, C. H., and R. Silberberg, *Proceedings of the 16th International Cosmic Ray Conference (Kyoto)*, **2**, 202 (1979).

Tsao, C. H., R. Silberberg, and J. R. Letaw, *Proceedings of the 18th International Cosmic Ray Conference (Bangalore)*, **2**, 194 (1983).

van Sciver, W. J., and L. Bogart, *Bulletin of the American Physical Society*, **2**, 142 (1957).

Waddington, C. J., P. S. Freier, and D. J. Fixsen, *Physical Review A*, **A28**, 464 (1983).

Waddington, C. J., D. J. Fixsen, and P. S. Freier, *Proceedings of the 19th International Cosmic Ray Conference (La Jolla)*, **6**, 104 (1985).

Wallace, R. K., and S. E. Woosley, *Astrophysical Journal Supplement*, **45**, 389 (1981).

Webber, W. R., J. A. Lezniak, and J. Kish, *Astrophysical Journal (Letters)*, **183**, L81 (1973).

Webber, W. R., *Proceedings of the 17th International Cosmic Ray Conference (Paris)*, **2**, 80 (1981).

Webber, W. R., *Proceedings of the 18th International Cosmic Ray Conference (Bangalore)*, **2**, 198 (1983).

Webber, W. R., and J. C. Kish, *Proceedings of the 18th International Cosmic Ray Conference (Bangalore)*, **8**, 40 (1983).

Webber, W. R., *Proceedings of the 20th International Cosmic Ray Conference (Moscow)*, **2**, 463 (1987).

Westfall, G. D., Lance W. Wilson, P. J. Lindstrom, H. J. Crawford, D. E. Greiner, and H. H. Heckman, *Physical Review C*, 19, 1309 (1979).

Wheeler, J. C., in *Supernovae: A Survey of Current Research*, eds. M. J. Rees and R. J. Stoneham (D. Reidel: Dordrecht, 1982).

Wiedenbeck, M. E., Ph. D. Thesis, California Institute of Technology (1977).

Wiedenbeck, M. E., and D. E. Greiner, *Astrophysical Journal (Letters)*, **239**, L139 (1980).

Wiedenbeck, M. E., *Proceedings of the 18th International Cosmic Ray Conference (Bangalore)*, **9**, 147 (1983).

Willis, A. J., and R. Wilson, *Monthly Notices of the Royal Astronomical Society*, **182**, 559 (1978).

Wilson, L. W., Ph.D. Thesis, University of California, Berkeley, LBL-7723 (1978).

Woosley, S. E., W. D. Arnett, and D. D. Clayton, *Astrophysical Journal Supplement*, **26**, 231 (1973).

Woosley, S. E., *Astrophysics and Space Science*, **39**, 103 (1976).

Woosley, S. E., and T. A. Weaver, *Astrophysical Journal*, **243**, 651 (1981).

Woosley, S. E., *Annual Reviews of Astronomy and Astrophysics*, **24**, 205 (1986).

Woosley, S. E., and T. A. Weaver, in *Radiation Hydrodynamics in Stars and Compact Objects*, ed. D. Mihalas and K.-H. A. Winkler, (D. Reidel: Dordrecht, 1986).

Woosley, S. E., *Astrophysical Journal*, **330**, 218 (1988).

Yost, G. P., *Lectures on Probability and Statistics*, LBL-16993 (1984).

Young, J. S., P. S. Freier, C. J. Waddington, N. R. Brewster, and R. K. Fickle, *Astrophysical Journal*, **246**, 1014 (1981).

Zych, A. D., R. E. Wilson, E. Zanrosso, R. S. White, B. Dayton, and J. Simone, *IEEE Transactions on Nuclear Science*, **NS-26**, 506 (1979).